STUDIES ON GRAIN REFINEMENT AND ALLOYING ADDITIONS ON THE MICROSTRUCTURE AND MECHANICAL PROPERTIES OF Mg-8Zn-4Al ALLOY

Thesis submitted to
Cochin University of Science and Technology
in partial fulfillment of the requirements
for the degree of

DOCTOR OF PHILOSOPHY
in the Faculty of Technology

By

N. BALASUBRAMANI

MATERIALS AND MINERALS DIVISION
NATIONAL INSTITUTE FOR INTERDISCIPLINARY SCIENCE AND TECHNOLOGY (CSIR)
THIRUVANANTHAPURAM – 695019 INDIA

JUNE – 2009

DECLARATION

I hereby declare that the thesis entitled "**Studies on grain refinement and alloying additions on the microstructure and mechanical properties of Mg-8Zn-4Al alloy**" embodies the results of bonafide research work done by me for the degree of **Doctor of Philosophy** in Faculty of Technology of the ***Cochin University of Science and Technology, Cochin*** under the guidance of **Dr. U.T.S. Pillai**, National Institute for Interdisciplinary Science and Technology (CSIR), Trivandrum. I further declare that this thesis or part thereof has not previously been formed the basis for the award of any degree or diploma.

N. Balasubramani

N. BALASUBRAMANI

राष्ट्रीय अंतर्विषयी विज्ञान तथा प्रौद्योगिकी संस्थान NATIONAL INSTITUTE FOR INTERDISCIPLINARY SCIENCE & TECHNOLOGY
वैज्ञानिक तथा औद्योगिक अनुसंधान परिषद् COUNCIL OF SCIENTIFIC AND INDUSTRIAL RESEARCH
इंडस्ट्रियल इस्टेट-डाक घर, पाप्पनंकोड, तिरुवनंतपुरम्, भारत - 695 019
Industrial Estate P. O., Pappanamcode, Thiruvananthapuram, India - 695 019

CERTIFICATE

This is to certify that the thesis entitled "**Studies on grain refinement and alloying additions on the microstructure and mechanical properties of Mg-8Zn-4Al alloy**" that is being submitted by **Mr. N. Balasubramani** for the award of the degree of **Doctor of Philosophy in Technology**, in the Faculty of Technology of the **Cochin University of Science and Technology, Cochin,** is a record of bonafide research work carried out by him under my guidance and supervision. The results embodied in this thesis have not been submitted to any other University or Institute for the award of any other degree or diploma.

Dr. U. T. S. Pillai
Scientist
Materials and Minerals Division
National Institute for Interdisciplinary
Science and Technology (CSIR)
Trivandrum-695 019

ACKNOWLEDGEMENTS

A journey is easier when you travel together. Interdependence is certainly more valuable than independence. This thesis is the result of my four years of research work wherein I have been accompanied and supported by many people. It is a pleasant aspect that I have now the opportunity to express my gratitude to all of them.

The first person I would like to thank is my supervisor **Dr. U.T.S. Pillai,** Scientist, Materials and Minerals Division, National Institute for Interdisciplinary Science and Technology (CSIR), Trivandrum. During these years I have known Dr. U.T.S. Pillai as a sympathetic and principle-centered person. I owe him much gratitude for having shown me this path of research. I am really glad that I have come to know Dr. Pillai in my life.

I wish to thank my well-wisher **Dr. B.C. Pai**, Director, NIIST, Trivandrum, for his persistent encouragement and advice during the course of this work.

I am grateful to **Prof. T.K. Chandrashekar,** Former Director**,** NIIST for the support during the course of this research work.

I would like to thank **Dr. R.M. Pillai,** Former Head, MMD, Senior Deputy Director, for his valuable advice and encouragement.

I am thankful to the Council of Scientific and Industrial Research (CSIR), New Delhi, for granting Senior Research Fellowship to carry out this research work.

I express my gratitude to **Dr. A. Srinivasan** for his constructive ideas and support throughout my course. I thank **God** for having given me such a good friend.

Acknowledgements

I am very grateful to Mr. K. Sukumaran and Mr. K.K. Ravikumar, NIIST, for their help in mechanical testing, Mr. S.G.K. Pillai, NIIST, for optical metallography, Dr. V. John, Dr. M. Ravi, and Mr. M.C. Shaji, NIIST, for foundry facilities, Dr. Peter Koshy, Dr. P. Prabhakar Rao and Mr. M.R. Chandran, NIIST, for SEM and EDS facilities, Dr. Prasad and Mr. C. Narendraraj for TEM and EDS facilities and Dr. U. Syamaprasad and Mr. P. Guruswami, NIIST, for the XRD work.

I wish to place on record my sincere thanks to Dr. J. Swaminathan, Scientist, NML, Jamshedpur, for his valuable help in carrying out the creep testing work.

I am extremely grateful to Mr. M. Suresh, Mr. G. Jagannathan and Mr. S.B. Shiju NIIST, for the technical discussions and their restless help in my experimental work. I also thank all members of Light Metals, Alloys and Composite Group, NIIST, for their help throughout my work.

I express my sincere thanks to Dr. T.P.D. Rajan, Dr. S. Sreeja Kumari and Dr. V.M. Sreekumar NIIST for the technical discussions and the help given to me during the course of this research work.

My special thanks to Dr. K.R. Ravi for his valuable support and suggestions in carrying out experiments.

My sincere thanks to Prof. K.P. Vijayakumar, Department of Physics, Cochin University of Science and Technology, for his periodic evaluation of my research work.

My sincere thanks to Mr. T. Soman and Mr. V. Antony, NIIST for the help received from them throughout the research work. I thank Mr. P. Balan, Mr. S. Ramakrishnan, Mr. N. Narayanan, Mr. T.A. Balakrishnan, Mr. P. Sisupalan and P. Soman, NIIST for the machining, fabrication and other works at the workshop.

My grateful thanks to my friends Mr. R. Pannerselvam, Mr. R. Sabarinathan, Mr. Babu Nallusamy, Mr. Nithyanantha Vasagam, Mrs. Sethu, Mr. Prem E.J Babu, Dr. Jegan Roy, Dr. Raja Singh, Dr. Starwin, Dr. Sundararajan, Dr. Prabhu, Dr. Gokul, Mr. U. Dharanipathy, Mr. M. Saravanan, Mr. K. Sureshkanan, Mr. G. Nagasrinivasu, Mr. V. Vaithiyanathan, Mr. Prasad, Mr. V. Vishnuvardhan, Mr. K. Selvakumar and Mr. Thirumalai Kumaran for their help and support. I am also very thankful to Mr. Ravi Subramanian and Mr. S. Govindraj their help and support.

I would like to thank my friend Mr. S. Vivekanandan for his entire support during my stay in Trivandrum.

I am extremely grateful to my Guruji, Professor Dr. K. Raghukandan, Head, Department of Manufacturing Engineering, Annamalai University, who always encourage my thoughts and offered me wonderful opportunity. His word only changed my dream into reality.

Finally, I would like to share this moment of happiness with my wife Mrs. Vennila Balasubramani and parents Mr. D. Nandagopal and Mrs. N. Thilagavathy, and my brother Mr. N. Thanigaivel and sister-in-law Mrs. T. Sangeetha, my brother Mr. N. Thandavamoorthy and my sister N. Hemalatha, who always encourages me to achieve my goals.

I am **dedicating** this thesis to my beloved son soul; he is no more with us.

Last but not least, I thank **GOD** for giving me the knowledge and helping me throughout my life.

N. Balasubramani

ABSTRACT

MAGNESIUM ALLOYS have strong potential for weight reduction in a wide range of technical applications because of their low density compared to other structural metallic materials. Therefore, an extensive growth of magnesium alloys usage in the automobile sector is expected in the coming years to enhance the fuel efficiency through mass reduction. The drawback associated with the use of commercially cheaper Mg-Al based alloys, such as AZ91, AM60 and AM50 are their inferior creep properties above 100ºC due to the presence of discontinuous $Mg_{17}A1_{12}$ phases at the grain boundaries. Although rare earth-based magnesium alloys show better mechanical properties, it is not economically viable to use these alloys in auto industries. Recently, many new Mg-Al based alloy systems have been developed for high temperature applications, which do not contain the $Mg_{17}Al_{12}$ phase. It has been proved that the addition of a high percentage of zinc (which depends upon the percentage of Al) to binary Mg-Al alloys also ensures the complete removal of the $Mg_{17}Al_{12}$ phase and hence exhibits superior high temperature properties.

ZA84 alloy is one such system, which has 8%Zn in it (Mg-8Zn-4Al-0.2Mn, all are in wt %) and shows superior creep resistance compared to AZ and AM series alloys. These alloys are mostly used in die casting industries. However, there are certain large and heavy components, made up of this alloy by sand castings that show lower mechanical properties because of their coarse microstructure. Moreover, further improvement in their high temperature behaviour through microstructural modification is also an essential task to make this alloy suitable for the replacement of high strength aluminium alloys used in automobile industry. Grain refinement is an effective way to improve the tensile behaviour of engineering alloys. In fact, grain refinement of Mg-Al based alloys is well documented in literature. However, there is no grain refiner commercially available in the market for Mg-Al alloys. It is also reported in the literature that the microstructure of AZ91 alloy is modified through the minor elemental additions such as Sb, Si, Sr, Ca, etc., which enhance its high temperature properties because of the

formation of new stable intermetallics. The same strategy can be used with the ZA84 alloy system to improve its high temperature properties further without sacrificing the other properties. The primary objective of the present research work, "**Studies on grain refinement and alloying additions on the microstructure and mechanical properties of Mg-8Zn-4Al alloy**" is twofold:

1. To investigate the role of individual and combined additions of Sb and Ca on the microstructure and mechanical properties of ZA84 alloy.

2. To synthesis a novel Mg-1wt%Al_4C_3 master alloy for grain refinement of ZA84 alloy and investigate its effects on mechanical properties.

The contents of the thesis have been organized in five chapters. **Chapter 1** deals with the overall idea about the thesis. The applications of magnesium alloys in various industries and their importance are discussed in this chapter. The major problem of ZA84 alloy is identified as insufficient mechanical properties especially in respect of tensile strength and creep properties. Effective ways to improve the properties are also given. The grain refinement and alloying additions mechanism are discussed in brief.

Chapter 2 presents a comprehensive review of available literature. Based on a thorough study of the literature, the detailed methodology for achieving the objectives of the present work has been derived. A great deal of attention has been devoted to the various grain refinement methods, grain refining mechanisms and alloying additions effect on the tensile and creep properties of magnesium alloys.

Chapter 3 deals with the detailed experimental procedure followed for alloy preparation and characterization in the present research work. Magnesium alloys were prepared using the flux melting technique. To identify the phases present in the alloys, XRD studies were carried out using a PHILIPS PW1710 powder diffractometer with CuKα radiation. The microstructures were characterized using an optical microscope

(OM), scanning electron microscope (SEM) and transmission electron microscope (TEM) equipped with energy dispersive spectroscopy and the solidification behaviour by differential thermal analyzer (DTA). Macrohardness and microhardness were measured on INDENTEC and CLEMEX instruments under standard test conditions. Room temperature and 150ºC tensile properties were evaluated using an INSTRON Universal Testing Machine at a crosshead speed of 2mm/min. Creep properties at 150ºC with an initial stress of 50 MPa were evaluated using a 3 ton 'MAYES' creep testing machine.

Chapter 4 presents the results and discussion of individual and combined additions of Sb, Ca and Al_4C_3 on the microstructure and mechanical properties of ZA84 alloy.

An X-ray diffraction pattern of the as-cast ZA84 alloy confirmed that the alloy consisted of α-Mg matrix and $Mg_{32}(Al,Zn)_{49}$ phase. However, the microstructure of base ZA84 alloy consists of α-Mg matrix with two different morphologies of precipitates (continuous and isolated phases). The continuous τ-$Mg_{32}(Al,Zn)_{49}$ phase, which has the cubic crystal structure (a=1.416nm), and the other is isolated ϕ-$Mg_5Zn_2Al_2$ phase having a primitive orthorhombic structure (a=0.8979nm, b=1.6988nm and c=1.9340nm). These results are confirmed using SEM and TEM.

Additions of antimony (0.2, 0.5 and 1wt%) to base alloy introduce thermally stable Mg_3Sb_2 (823ºC) intermetallics at the grain boundaries and refine the ternary phase effectively. The morphology of Mg_3Sb_2 intermetallics has changed from fine phase to needle shape with increase in the Sb content. For all wt% of Sb addition, the strength (yield and ultimate tensile strengths) properties are found to increase both at ambient and elevated temperatures with slight reduction in the ductility as compared to that of ZA84 base alloy. However, the maximum strength properties are obtained with 0.2 wt% Sb addition. The improvement in strength properties owing to the Sb addition is attributed to the following: (1) refinement of the $Mg_{32}(Al,Zn)_{49}$ precipitates, (2) strengthening owing to the secondary Mg_3Sb_2 precipitates, and (3) strengthening by grain refinement. The 500

hr short-term creep test has revealed that the addition of Sb is also capable of improving the creep properties.

The addition of Ca (0.25, 0.5 and 1wt%) to ZA84 alloy has modified the precipitation behaviour with the formation of a new Mg-Zn-Al-Ca phase at 405ºC in the grain boundaries. As a result, improved mechanical properties, especially creep properties, are obtained. The creep extension of ZA84 alloy is reduced from 0.6678 % to 0.4172 % with 0.5wt% Ca addition, which is lower than the base alloy. The improvement in creep resistance of Ca-added alloys is attributed to the following reasons: (1) Formation of new thermally stable quaternary precipitates along the grain boundaries (2) The diffusion of solute atoms of Al and Zn at elevated temperature is minimized as the amount of Al and Zn in solid solution of Mg matrix is to be lowered. The change in microstructure that accompanies Ca addition results in an alloy having a stable matrix with well-fortified grain boundary precipitates. The tensile properties decrease beyond 0.5wt% Ca addition because of an increasing number of brittle precipitates at the grain boundaries.

The combined addition of Sb and Ca to ZA84 alloy increases the stability of quaternary phase with Mg_3Sb_2 intermetallics and improves the tensile behaviour of ZA84 alloy. Besides giving better performance than the individual additions, the creep extension for 500 hr has been reduced by approximately 50%.

Al-5wt%SiC composites held at 750ºC for 2 hrs after particle addition is found to be necessary to make the reaction between liquid Al and SiC_p to form Al_4C_3 particles completely. The microstructure of composites consists of α-Al matrix, eutectic silicon and interfacial reaction products. The reacted Al_4C_3 particles have been separated out from the composites by salt (equimolar NaCl-KCl-5%NaF) flux addition and skimmed as fine particles. Those reclaimed Al_4C_3 particles (5-8 μm in size) are introduced into the magnesium melt to make Mg-1wt%Al_4C_3 master alloy.

The potency of Al_4C_3 as a nucleating substrate for primary Mg can be demonstrated by crystallographic matching between hcp magnesium matrix of lattice parameters (a=3.208ºA, c=5.200ºA and γ=120º) the nucleating particle having hcp of a=3.338ºA, c= 24.996ºA and γ=120º. Theoretically, the interfacial free energy at the nucleating interface is believed to be a key factor controlling heterogeneous nucleation efficiency. It is hence reasonable to suggest that Al_4C_3 itself is a potent nucleating substrate for primary Mg, and addition of Al_4C_3 into the melt is expected to increase the nucleation frequency, therefore leading to a refined microstructure. In addition, it is further explained that the hypothesis for grain refinement of Al_4C_3 compound with magnesium is considering a high melting point. The stable fine particles exist at normal melting temperature act as an effective nucleant for Mg grains. Among the hypotheses proposed to explain the mechanism of carbon inoculation refining method to Mg-Al based alloys, Al_4C_3 nuclei hypothesis is the most commonly accepted theory. Besides, the size of heterogeneous nuclei is a vital factor deciding nucleation potency. It is proposed that 5-8μm or less is optimum mean particle size for high performance heterogeneous nuclei using a model based on free growth control of grain initiation.

The microstructure of combined added Sb, Ca and Al_4C_3 in ZA84 alloy shows the three morphologies of precipitates, such as continuous bone-like coarse phase called $Mg_{10}Al_6Zn_4Ca_2$ and the continuous without bone-like structure phase, called $Mg_{32}(Al,Zn)_{49}$ and fine black Mg_3Sb_2 phases at the grain boundaries. This alloy led to a greater improvement in the tensile properties (room as well as elevated at 150ºC) and creep resistance than that of base alloy without drop in elongation.

Chapter 5 presents a summary of the findings of this investigation, along with the contributions made to the knowledge and the avenues for further work.

CONTENTS

Page No.

Page No.

Page No.

Page No.

Page No.

LIST OF TABLES

LIST OF FIGURES

1.1 BACKGROUND OF MAGNESIUM

LIGHT ALLOYS with superb specific strength find increasing applications in the aerospace and automotive industries. With oil prices at a historic high and global concern about vehicle emission, the focus on car manufacturing is shifting in turn to light weight materials to reduce the fuel consumption [1]. The growth of light alloys in automotive applications has been estimated at 12% over the last decade and is expected to increase at the rate of 15% in the coming decade. According to information provided by the agency for natural resources and energy in 2004, passenger vehicles accounted for about 60% of the total energy in transport sector, which ultimately led to an increase in CO_2 emission and green house gas effect [2-3]. Therefore, it is essential and important to increase the usage of lighter alloys in automobiles, which can reduce environmental problems.

Among the lightest elements, magnesium has the 8^{th} highest Clark number (the amount of an element in the surface layer of the earth's crust), which is $2/3^{rd}$ lighter than that of aluminium and $1/4^{th}$ that of iron [4]. Apart from the density, magnesium alloys offer other advantageous properties such as high stiffness, excellent machinability, good dimensional stability, damping capacity and excellent casting properties [5-6]. The first commercial production of magnesium was recorded in Germany in 1916 [7]. By the end of 1945, magnesium production had increased to 237K tons worldwide [8]. In the year 2000, 366K tons of magnesium were consumed for different applications. The worldwide primary magnesium production in 2004 was 584K metric tons according to the U.S. Geological Survey Minerals Yearbook 2004 [9]. Recently, the American Foundry Society Magnesium Division has developed the Magnesium Casting Industry Technology Roadmap [10]. According to that report, in 2004, the U.S. magnesium casting industry culminated ten years of remarkable growth by shipping nearly 100K tons of castings to a wide range of markets [11] for several industrial applications. Among the numerous developed alloy systems, Mg-Al alloys are

widely used in different applications and are classified on the bases of Mg- Al (Zn or Mn) and Mg-Al (RE or Si).

1.1.1 Mg-Al (Zn or Mn)

These alloys have superior room temperature strength and ductility but do not exhibit good creep resistance [12-13]. Almost all of the automobile components are made up of such alloys. The addition of aluminium or zinc generally improves the room temperature strength and Mn leads to an improvement in the corrosion resistance [14]. Table 1.1 presents some of the major alloys and their chemical compositions.

Table 1.1: Chemical compositions of AZ and AM series alloys [12-13]

Alloy	Al	Zn	Mn	Si	Cu	Fe	Ni	others
AZ91	8.5-9.5	0.45-0.9	>0.17	<0.05	<0.015	<0.004	<0.001	<0.01
AZ61	5.5-6.5	0.45-0.9	>0.20	<0.05	<0.008	<0.004	<0.001	<0.01
AM50	4.5-6.3	<0.1	>0.27	<0.1	<0.008	<0.004	<0.001	<0.01
AM60	5.7-6.3	<0.2	>0.27	<0.05	<0.008	<0.004	<0.001	<0.01
AM20	1.7-2.2	<0.1	>0.27	<0.1	<0.008	<0.004	<0.001	<0.01

1.1.2 Mg-Al (RE or Si)

The other group of alloy systems based on AE and AS alloys has been developed for high temperature applications. The additions of RE and Si lead to the formation of thermally stable precipitates that have limited applications because of difficulties in die casting [15]. The beneficial role of rare earth on the strength and creep performance of magnesium alloys has led to the development of AE41, AE42 and AE21 alloys [16-18]. Those alloys are widely used in the aerospace industry but have limited use in the automobile industry because of enhanced cost. The AS series alloys have superior properties; however, the problem associated in casting is due to the metal sticking on the mould and fluidity problems. Table 1.2 gives the major systems and their chemical compositions.

Table 1.2: Chemical compositions of AE and AS series alloys [16-18]

Alloy	Al	Zn	Mn	RE	Si	Cu	Fe	Ni	others
AE42	3.6-4.4	< 0.2	>0.27	2.0-3.0	<0.05	<0.04	<0.004	<0.004	<0.01
AE41	3.6-4.4	< 0.2	>0.27	0.7-1.5	<0.05	<0.04	<0.004	<0.004	<0.01
AS42	3.6-4.4	< 0.2	>0.27	2.0-3.0	<0.05	<0.04	<0.004	<0.004	<0.01
AS41	3.6-4.4	< 0.2	>0.27	0.7-1.5	<0.05	<0.04	<0.004	<0.004	<0.01

Among them, AZ91 (Mg-9Al-0.8Zn-0.2Mn) is one of the most favoured magnesium alloys used in approximately 90% of all cast products [19-22]. It has good castability and excellent room temperature mechanical properties; in its high purity form, (AZ91-E) shows good corrosion resistance. However, the range of applications of this alloy is limited because of the poor strength and creep resistance when the temperature exceeds of 120°C, which makes it unsuitable for high temperature applications in the automotive industry [23-24]. The major reason proposed in this alloy is microstructure instability. The microstructure of AZ91 alloy is characterized by α-Mg and $Mg_{17}Al_{12}$ eutectic at the grain boundaries. $Mg_{17}Al_{12}$ is incoherent with the magnesium matrix, and exists in a wide composition range of 48-50 wt% of Al. This intermetallic has a low melting point and poor metallurgical stability, which contribute to poor creep resistance of the alloy at high temperature [25-27].

In 1970s, it was first reported that alloys with zinc as a major alloying element and a small amount of aluminium, called ZA alloys, might be the alternative to the commonly used aluminium-rich alloys [28-31]. These alloys showed better creep resistance, good castability and great resistance to hot cracking. No further investigations, however, have been carried out since then. However, the last few years have seen great interest in the Mg-Zn-Al system where new possible applications of those magnesium castings in automobiles have emerged. Recently, several Mg-Zn-Al alloys, such as ZA(10,14)2, ZA(10,14)4, ZA(10,14)6, ZA52, ZA84 and ZA85, have been developed with the evaluation of as-cast microstructure and properties [32-36].

Anyanwu *et al* [37] have studied the broad composition range of 6-14% Zn and 2-8% Al with total element content less than 13%. However, the phase constituents in the microstructure of ZA alloy are not clear. It is important to predict the microstructural constituents of a certain composition, as the ternary phase diagram is very complex and not well established. Although several studies on the phases present in high zinc alloys are reported, no consensus has yet been reached [38-39].

Previous research works indicate that ZA85, ZA102 and ZA104-0.15Ca magnesium alloys show better creep resistance than does the commercial AZ91 alloy [34, 40-41]. Zhang *et al* [42] reported that when the Zn/Al ratio is about 2:1, there are no β- $Mg_{17}Al_{12}$ and ε-$MgZn_3$ phases present in the microstructure, which is detrimental to creep properties in Mg-Al-Zn alloys. Therefore, it is highly essential not only to investigate the microstructure and mechanical properties of ZA84 alloy but also extremely important to improve its methods of performance to render it suitable for many applications in the transport sector.

Table 1.3: Mechanical properties of different Mg-Al and Mg-Zn-Al based alloys [12]

Alloy	Condition	Yield strength (MPa)	Tensile strength (MPa)	Elongation (%)
AZ91	Die cast	150	230	3
AM60	Die cast	115	205	6
ZA102	Permanent mould	90	140	2
ZA104	Permanent mould	100	108	2
ZA84	Permanent mould	104	148	4

1.2 ZA84 MAGNESIUM ALLOY

ZA84 alloy is one such system, which has 8%Zn, 4%Al with 0.2%Mn (all are in wt %), shows excellent casting properties, corrosion resistance and moderate room temperature tensile properties. This alloy provides superior creep resistance compared to AZ and AM series alloys. Zinc in this alloy offers better castability and strength. Aluminium improves the strengthening, whereas Mn provides corrosion resistance. However, ZA84 alloy does not exhibit sufficient tensile strength and creep resistance above 150ºC, which is a major setback in the engine parts where the operating temperature is in the range of 150 to 175ºC [31, 43].

1.2.1 TENSILE BEHAVIOUR OF ZA84 ALLOY

The thin-walled ZA84 alloy castings, such as electronics products, are produced using high pressure die casting showing good tensile performance. However, more complicated thick walled castings under development, such as engine blocks, are produced by sand casting, where a fine-grain structure cannot be achieved. It is well established that the general relationship between yield stress (and other mechanical properties) and grain size was proposed by Hall and greatly extended by Petch equations. The yield strength of fine grain size alloy increases as per the Hall-Petch equation [44]. Therefore, grain refinement is one of the most powerful metallurgical tools to improve the tensile properties of alloys. For magnesium alloys, the aluminium-free alloys are mainly refined by zirconium [45]. This refiner is not suitable for the Mg-Al system because of the formation of Al_4Zr intermetallics. Since the late 1930s, a number of approaches have been developed to obtain grain refinement in magnesium alloy containing aluminium. The comparatively few effective techniques including Mg-Al alloys are superheating, the Elfinal process and carbon inoculation [46-47]. Among them, carbon inoculation is an effective approach for grain refinement of Mg-Al alloys. The major challenge is how to introduce the carbon into molten magnesium while, on the other hand, having excess settling of carbon left in the melt. But a successful grain refiner has not been achieved so far in the foundry practice.

1.2.2 CREEP PROPERTIES

Creep is the permanent deformation of material that occurs when the material is loaded at elevated temperature for a prolonged time. The load is very much low compared to its yield strength. Although the deformation is not mainly due to the applied load, temperature plays a major role. However, there is very limited knowledge about the high temperature properties of ZA84 alloy [31]. The thermal stability of phases in ZA84 alloy is better than that of $Mg_{17}Al_{12}$ phase in the Mg-Al alloys. As a result, the creep properties are better than AZ91 alloy, but further enhancing the properties is well suited for different applications. Modification of the microstructure is an effective way to improve the creep properties of alloys [48-49].

1.3 ROLE OF MINOR ELEMENTAL ADDITIONS

Many new Mg-Al based alloy systems have been developed for high temperature applications [50-51]. However, no conclusions have been arrived at as yet. The idea of modifying the alloy chemistry of existing alloys by the addition of minor alloying elements has been found to be an effective way to improving the creep resistance and it has become popular.

In general, the mechanical properties of alloys are enhanced by trace elemental addition which changes the grain size, modifying the existing phases present in the microstructure and introducing a new thermally stable precipitate. There is a lack of works related to the Mg-Zn-Al system. It is well established and reported in the earlier studies [49, 53-53] that the addition of Sb, Ca, Bi, RE, Si, Sr and Sn to AZ91 alloys showed improved properties either because of suppression of the formation of $Mg_{17}Al_{12}$ phase and/or the formation of thermally stable intermetallics in the microstructure. Zhang *et al* [28] have reported that the Ca addition to ZA144 and Sr addition to ZA142 alloys yield superior elevated temperature mechanical properties and creep resistance compared to those of the base alloy. This is due to the presence of significant amounts of Ca and Sr in the complex phases, which effectively refines the microstructure and

increases the stability of precipitates to improve the properties. Yingxin *et al* [31] have stated that the RE addition to ZA84 alloy effectively refines the microstructure and improves the mechanical properties owing to the formation of quaternary Mg-Zn-Al-RE phase, which is very stable at a higher temperature. C.J. Bettles *et al* [54] have also studied the effect of 0.35 wt% of Ca addition to Mg-4Zn alloy and reported that the significant improvement in the creep properties is because of the refined precipitate structure, which is very stable for prolonged periods at a higher temperature. Even though some studies have been carried out to understand the effects of alloying additions in ZA84 alloy system, the effects of other alloying elements such as Sb, Si, Sr, Sn and Ca etc. have not been reported yet.

The grain refinement process that the fine grain boundaries, is in contrast to their low temperature behaviour. At low temperature, they do not flow viscously, which provides an effective obstacle to the dislocation motion. At a higher temperature, the grain boundaries facilitate the deformation process by sliding, whereas at low temperature, they increase the yield strength by inhibiting the dislocation. There is a controversy regarding grain refinement and creep properties improvement. Also, the alloying addition stops the grain boundary sliding because of the presence of stable phases along the grain boundaries. As a result, the combination of grain refiner and alloying addition improves the tensile properties as well as the creep resistance.

1.4 OBJECTIVE OF THE THESIS

ZA84 alloy is one such system, which has 8%Zn in it (Mg-8Zn-4Al-0.2Mn, all are in wt %), and shows superior creep resistance compared to AZ and AM series alloys. These alloys are mostly used in die casting industries. However, there are certain large and heavy components, made up of this alloy by sand castings that show lower mechanical properties because of coarse microstructure. Moreover, further improvement in its high temperature behaviour through microstructural modification is also an essential task to make this alloy suitable for the replacement of high strength

aluminium alloys used in the automobile industry. Grain refinement is an effective way to improve the tensile behaviour of engineering alloys. In fact, grain refinement of Mg-Al based alloys is well documented in the literature. However, there is no grain refiner commercially available in the market for Mg-Al alloys. It is also reported in the literature that the microstructure of AZ91 alloy is modified through the minor elemental additions such as Sb, Si, Sr, Ca etc, which enhance its high temperature properties because of the formation of new stable intermetallics. The same strategy can be used with the ZA84 alloy system to improve its high temperature properties further without sacrificing the ductility of the alloy. Therefore, the primary objective of the present research work "**Studies on grain refinement and alloying additions on the microstructure and mechanical properties of Mg-8Zn-4Al alloy**" is twofold:

1. To investigate the role of individual and combined additions of Sb and Ca on the microstructure and mechanical properties of ZA84 alloy.

2. To synthesis a novel Mg-1wt%Al_4C_3 master alloy for grain refinement of ZA84 alloy and investigate its effects on mechanical properties.

2.1 INTRODUCTION OF MAGNESIUM

The lavishness and safety features of recent cars have witnessed an increase in vehicle weight, which enhances the fuel consumption and CO_2 emission. The weight of the vehicles has increased by an average of over 20% in the two decades [55]. Most of the increased weight constituents increased the engine size along with the addition of safety features, especially the use of steels. The last two decades have witnessed significant increases in the use of light metals such as titanium, aluminium and magnesium alloys. Furthermore, the consumption rates of these materials are continually increasing because of the ever increasing pressures for higher performance and fuel economies. So, the greater importance of weight reduction posed a crucial challenge for automobile producers that led to improvement in the fuel economy, in addition to reducing the green house effects and other environmental issues [2]. Figure 2.1 shows the representation of fuel efficiency on vehicle weight, the fuel consumptions of vehicle increase with increase in overall weight of the vehicle. Therefore, it is necessary to reduce the vehicle weight. The weight reductions have been made possible by the replacement of steel by light metal alloys [56]. Most of the low strength room temperature applications move towards the plastic and polymer composites, especially in the frames and interior body covering of all passenger cars [57]. However, most of the engine components made from ferrous material are now being replaced by aluminium and magnesium alloys [58]. The major aim of the researchers is to find suitable material that is more efficient than Al so as to reduce the weight of automobiles still further. Mg and its alloys are one such promising material whose light weight advantage could be used for the abovesaid purpose.

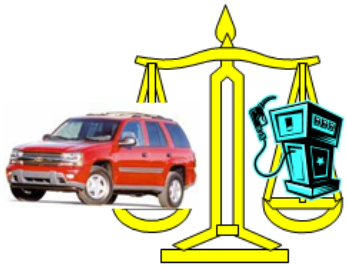

Figure 2.1: Representation of fuel efficiency on vehicle weight [56]

Owing to its low density (1.74g/cm^3), magnesium alloys offers distinct advantages for weight saving in automotive applications. It has two-third of aluminium density (2.74g/cm^3) and one-fourth of steel density (7 g/cm^3) [59]. The other advantageous properties include high specific strength and stiffness, superior damping capacity, electromagnetic shielding capacities, excellent machinability and good castability. It has high specific strength compared with its counterpart, aluminium alloys. Today, magnesium is cast for a variety of components, including steering wheels, body panels, body frame sections, seat frames and valve covers. For weight reduction, however, applications must migrate to the drive train and its higher operating temperatures of 150-175ºC. Many diecasters have searched for alloys to help reduce vehicle component weight without sacrificing material property [14]. Although magnesium alloy use in light vehicles has grown from 8 lb./vehicle in 2000 to a forecast of 30 lb. by 2008, the problem is whether existing alloys can meet the material required for particular applications [7]. While the light weight is certainly the major reason for the renewed interest in magnesium castings, there are a number of other properties that make magnesium the preferred choice for components in industrial applications. Table 2.1 compares some of the typical physical properties of commercial magnesium alloy (AZ91), aluminium alloy (LM 24) and glass-reinforced plastics moulding material

Table 2.1: Comparison of physical and mechanical properties of magnesium alloy with aluminium alloy and plastic [60-63]

Properties	Magnesium alloy (AZ91)	Aluminium alloy (LM 24)	Nylon 66/6
Yield strength (MPa)	160	150	65
Tensile strength (MPa)	230	320	105
Elongation (%)	0.5-3	1-3	50
Shear strength (MPa)	140	185	NA
Elastic modulus (GPa)	45	71	2.4
Density (g/cc)	1.81	2.79	1.14
Specific heat (J/Kg/^{o} K)	1050	963	NA
Expansion Co. eff .(x10^{-4}/^{o}K)	26	22	NA
Thermal Conductivity (W/M^{o}K)	72	96	NA

2.2 APPLICATIONS

2.2.1 AEROSPACE INDUSTRY

Magnesium alloys are extensively used in aircraft engines, air frames and landing wheels. Figure 2.2 gives some of the aerospace components made from magnesium alloys. Alloys such as ZE41 (Mg-4.2% Zn-0.7% Zr-1.3% MM), QE22 (Mg-0.7% Zr-2.5% Nd-2.5% Ag) and particularly WE43 (Mg-4% Y-3.25% Nd-0.5% Zr) are commonly used for aircraft applications [64-67] because of their improved corrosion, creep resistance fatigue and impact properties, always with good machinability.

Figure 2.2: ZE41 Mg fan housing in aerospace application [65]

2.2.2 NUCLEAR INDUSTRY

The higher electromagnetic shielding effect of magnesium is widely attractive in the nuclear industry. Most of the covering components are made of magnesium because (a) of its low tendency to absorb neutrons, (b) it does not alloy with uranium, (c) of its adequate resistance to carbon dioxide up to the highest service temperatures envisioned, and (d) its good thermal conductivity [68].

2.2.3 AUTOMOBILE INDUSTRY

Automobile industry, the latest beneficiary of magnesium, is currently exploring its maximum usage. Figure 2.3 gives a number of applications of magnesium that are currently being addressed by the automotive industry. Components at the top of this list, such as steering wheel armatures, cylinder head covers, seat frame, door panel and instrument panel beams, are already in significant production, whereas items at the bottom of the list, especially transmission case and intake manifold, require several years of intensive development before they can be implemented [69-71].

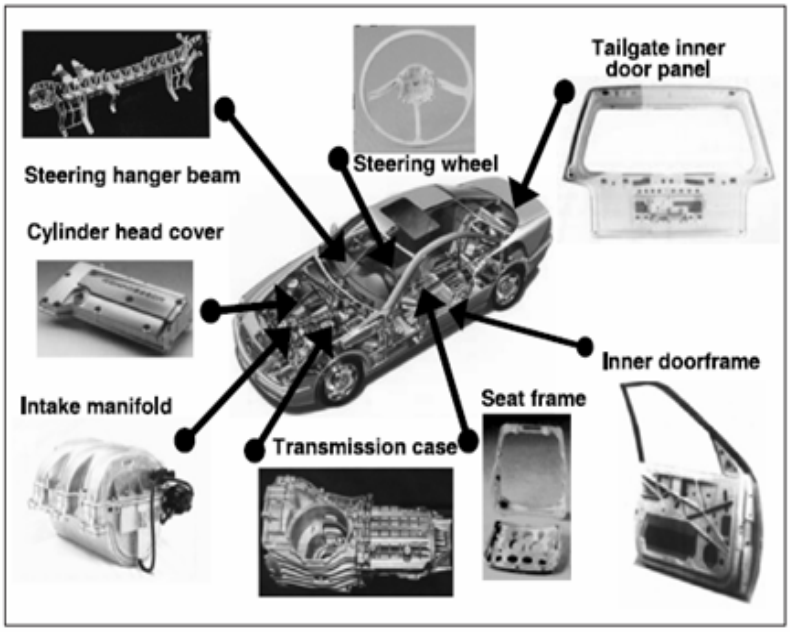

Figure 2.3: Important automobile components [70]

2.2.4 ELECTRONIC AND DOMESTIC INDUSTRIES

Apart from transport and missile components, magnesium also finds application in electronics and household items. Some of the examples are computer housing and mobile telephone cases, where lightness, suitability for thin wall casting and the characteristic of electromagnetic shielding are the particular advantages [72-73].

2.3 LIMITATIONS

In spite of all the advantageous properties and applications, there are some limitations responsible for the lack of magnesium product applications in different firms. The challenges in different areas listed in table 2. 2 are focused to develop the alloys that enhance the applications [74-75].

Table 2.2: Limitations of magnesium alloys

1.	Low elevated temperature properties
2.	Corrosion problem
3.	Low stiffness
4.	High cost of recycling
5.	Environment problem during melting
6.	Lack of joining technologies
7.	Poor workability
8.	High cost

2. 4 MELTING PRACTICE

Melting practice is the process of converting the cast ingots into molten metal, which can be ready to cast. When magnesium and its alloys are melted, they tend to oxidize and explode, unless care is taken to protect the molten metal surface against oxidation. Magnesium melting can be classified as follows: (i) flux treatment and (ii) Flux-less melting [13, 76-77].

2.4.1 FLUX MELTING AND REFINING

Molten magnesium alloys behave differently from aluminium alloys, which tend to form a continuous, impervious oxide skin on the molten bath, limiting further oxidation. Magnesium alloys, on the other hand, form a loose, permeable oxide layer on the molten metal surface. This allows oxygen to pass through and support burning

below the oxide surface. There are two main reasons that lead to the ignition of magnesium during melt process [78-79].

1. The volume of magnesium shrinks after oxidation to magnesia (MgO) , and a loose and porous layer on the melt surface. This layer cannot be prevent further passage of oxygen into magnesium melt resulting in more oxide.

2. The heat of formation magnesia is so large that the local area temperatures can reach even 2850˚C during the oxidation process**.**

The rate of oxidation in moist air at different temperatures is illustrated in figure 2.4. It can be observed from the figure that the drastic mass enhancement takes place during oxidation from 300 to 500ºC.

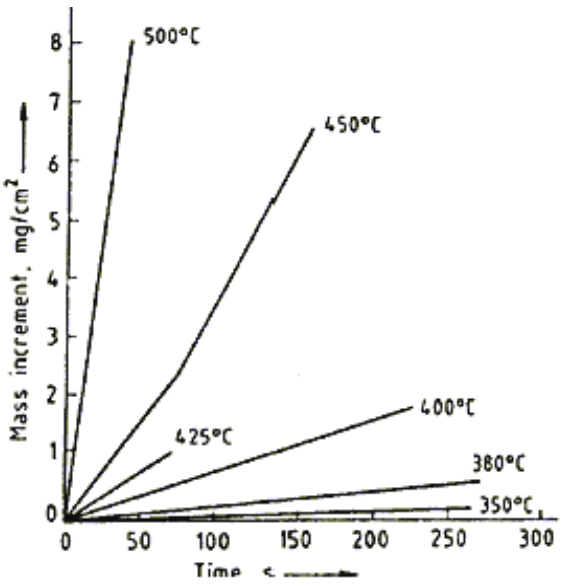

Figure 2.4: Rate of oxidation of magnesium in moist air [78]

Protection of the molten alloy using either a flux or a protective gas cover to exclude oxygen is therefore necessary. Flux process uses salt as a cover. Molten magnesium oxidizes readily to form a magnesium oxide (MgO) film. This film is easily disturbed and discontinuous MgO liquid film inclusions readily wet and coat solid charge materials and can also entrain liquid metal. Fluxes are therefore used to protect the melt for further oxidation, to agglomerate non-metallic inclusions originating with the charge, and to break up and collect the oxide inclusions and skins that may form during melting. These fluxes are usually low-melting mixtures of halide salts capable of wetting both solid and liquid metal surfaces. Most alkali chloride and magnesium chloride fluxes wet and coat the surface of the impurity particles. The higher density of the chlorides causes the impurities to sink to the bottom of the melt as sludge. Fluxes are composed to maintain a minimum difference in density compared with that of the metal of 0.15-0.20 g/cm^3. A typical flux composition [80] (see Table 2.3) includes $MgCl_2$, KCl, $BaCl_2$, CaF_2 and MgO. The magnesium and potassium chloride salts provide the low-melting eutectic; the fluoride provides good surface wetability and chemical reactivity with magnesium oxide; and the heavy barium chloride salt constituent provides the density component to effect mixing and sludging capability for separation.

Table 2.3: Compositions of fluxes used in melting and refining [81]

Purpose	**$CaCl_2$**	**NaCl**	**KCl**	**$MgCl_2$**	**CaF_2**	**MgO**
Melting	40	30	20	10	-	-
Melting and refining	20	10	10	35	15	10
Refining	15	10	10	35	20	10

2.4.2 FLUX-LESS MELTING

Although extremely effective in controlling oxidation, fluxes create corrosive fumes in the foundry and are difficult to separate from the metal, contributing to a high incidence of corrosive inclusions in magnesium casting parts. The quest for technology to protect magnesium from oxidizing without the negative ramifications associated with flux led to flux-less melting. It is a very effective way of melting in which inert gases are used to protect the molten metal. The most common gas used in flux-less melting is SF_6 mixed with dry air and CO_2 [82]. To maintain an adequate and homogeneous level of SF_6 at all areas of the melt surface, it is usually desirable to supply a protective atmosphere through a manifold with several outlets to enable the gas to spread out over the melt surface. The gas mixtures shields the melt from oxygen hence provide an oxygen- free atmosphere for melting.

The SF_6-based shielding gas is non-toxic, odourless and corrosion-free. However, SF_6 is having a heavy green house effect. It has a Global Warming Potential (GWP) 23900 times higher than CO_2 and will be banned from industrial use [83]. Therefore, researchers in magnesium industries are trying to find alternatives. Recently, the International Magnesium Association (IMA) found out suitable substitutes for SF_6. These are HFC-134, HFE-7100 and HFE-7200, and Novec^{TM} 612 (FKs) [16]. These alternatives are all fluorides and their protective effects are no less than that of SF_6, but their GWP values are much less than that of SF_6 [84-85].

2.5 CASTING PROCESSES

Normally smaller components of magnesium are cast by die casting, sand mould, permanent mould and low-pressure casting, etc [86-88]. The choice of a particular casting method depends on many factors, e.g., the number of castings required, the properties required, the dimensions and shape of the part and the castability of the alloy.

Normally, the magnesium alloy's smaller components are cast by die-casting method [89].

2.5.1 SAND CASTING

Magnesium alloy sand castings are used in aerospace applications because they offer a clear weight advantage over aluminium and other materials [90]. A considerable amount of research and development on these alloys has resulted in some spectacular improvements in their general properties compared with the earlier AZ types. A large volume of magnesium alloy castings for aerospace applications are being using conventional AZ-type alloys. The trend is changing with the use of zirconium alloyed grades. Although the magnesium-aluminium and magnesium-aluminium-zinc alloys are generally easy to cast, they are limited in certain respects. They exhibit micro shrinkage when sand-cast, and they are not suitable for applications in which temperatures of over 120°C are experienced. The magnesium rare earth-zirconium alloys were developed to overcome these limitations. Sand castings in the EZ33A alloy do in fact show excellent pressure tightness. The greater tendency of the zirconium-containing alloys to oxidize is overcome by the use of specially developed melting processes. The two magnesium-zinc-zirconium alloys originally developed, ZK51A and ZK61A, show high mechanical properties, but suffer from hot-shortness cracking and are non-weldable.

For normal, fairly moderate temperature applications (up to 160°C), the two alloys ZE41A and EZ33A are finding the greatest use. They are highly castable and can be used to make very satisfactory castings of considerable complexity. In addition, they have the advantage of requiring only a T5 heat treatment (precipitation treatment). When a demand arose in some aerospace engine applications for the retention of high mechanical properties at higher elevated temperatures (up to 205°C), thorium was substituted for the rare earth metal content in alloys of the ZE and EZ type, giving rise to the alloys of the types ZH62A and HZ32. Not only were there substantial

improvements in mechanical properties at elevated temperatures in these alloys, but also good castability and welding characteristics were retained. The thorium-containing alloys, however, showed a greater tendency for oxidation, requiring greater care in meltdown and pouring [90].

A further development aimed at improving both room temperature and elevated-temperature mechanical properties produced an alloy designated QE22A. In this alloy, silver replaced some of the zinc, and the high mechanical properties were obtained by grain refinement with zirconium and by a heat treatment to the full T6 condition (solution heat treated, water quenched and precipitation aged). However, problems were experienced with both of these alloys. The use of thorium has become increasingly unpopular environmentally, and the price of silver has become very unstable in recent years. Hence, there has been a considerable amount of research and development work on alternative alloy types. The most recent alloy emerging from this research was an alloy containing about 5.0% Y in combination with other rare earth metals (that is, WE54A), replacing both thorium and silver. This alloy has better elevated-temperature properties and a corrosion resistance almost as good as the high-purity magnesium-aluminium-zinc types (AZ91C). The alloys used for investment casting are very similar to those used for the sand-casting process.

2.5.2 DIE-CASTING

The 90s saw renewed activity in the development of elevated-temperature magnesium die-casting alloys. Table 2.4 shows a review of recent patent applications and patents on magnesium die-casting alloys. Among these, the Mg-Al-Ca, Mg-Zn-Al-Ca, Mg-Al-RE-Ca, Mg-Al-RE-Ca-Mn and Mg-Ca-Mn-RE systems can be cited. The less expensive Mg-Al-Ca alloy [91] has die-castability problems (susceptibility to hot-tearing when prototyping an automatic transmission case). This alloy has been considered subsequently for semi-solid forming applications. A subsequent version of

the alloy, Mg-Zn-Al-Ca, had some promise in eliminating the die-castability problems [92], but the alloy seems to work only in an extremely narrow composition range and also to show variation in properties. It is obvious that more work is needed to develop an optimum magnesium die-casting alloy for an application such as the automatic transmission case.

Noranda **[93-99]** has recently taken up this challenge by targeting the development of a new magnesium diecasting alloy with elevated-temperature properties equal to or better than the AE42 alloy but with acceptable cost to the automotive industry. This has led to the development of the new Noranda alloys (Noranda-A and Noranda-N, the chemical compositions not released anywhere), which are currently undergoing patent application process. The properties based on die-cast test specimens are extremely encouraging as seen in Figures 2.5 & 2.6 and Table 2.4.

Table 2.4: Recent magnesium die-casting patent alloy applications [93-99]

Chemical composition					Claims	Patent Number	Year of application
Al	Zn	Mn	RE	Ca			
1.5-10	-	-	2	0.2-5.5	Compares with AE42 but reduced RE. May also contain 0.2-2.5Zn or Ca	UK Appn 2296256A	1994
0.1	0-0.04	0-0.5	2-5	0-1	Alloys with creep resistance superior to AE42 or other currently available alloys.	W09624701	1996
2-6	-	0-0.25	-	0.1-0.8	Alloys with composition give Al_2Ca precipitation, good creep resistance	EP 0791662A1	1997
2-6	-	-	-	0.5-4.0	Alloys for semi-solid casting with better creep resistance than AS21	EP 0799901A1	1997
2-9	6-12	0.2-0.5	-	0.1-2.0	Superior elevated temperature properties such as creep and tensile and good diecastability	US 1997000861056	1997

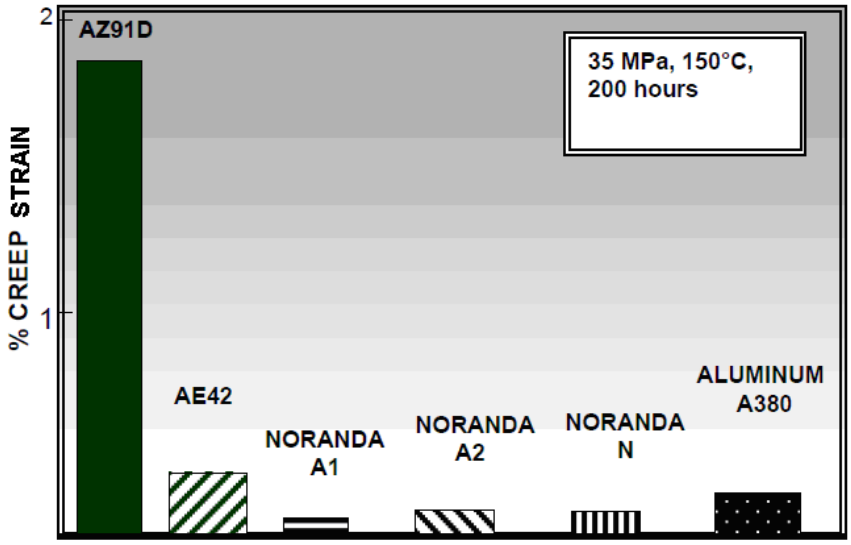

Figure 2.5: Creep properties of commercial and Noranda alloys [93-99]

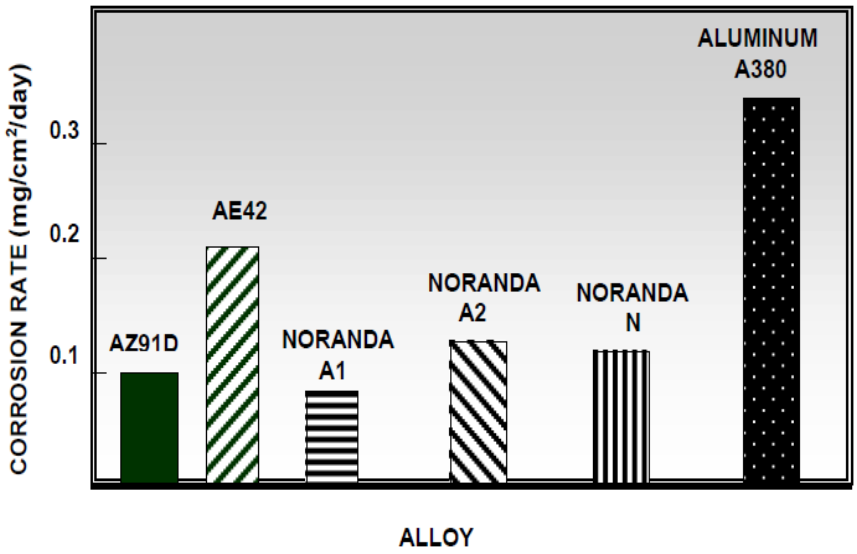

Figure 2.6: Salt spray (200 h) corrosion resistance of die-cast magnesium alloys [93-99]

2.5.3 LOW PRESSURE CASTING

This is a pressure-assisted casting technique in which very low pressure is applied for filling the mould cavity, which is placed above the casting furnace [100].

Normally [101], the high-pressure applied in die casting leads to the related filling problems such as turbulence and spraying effects, which reduce the mechanical properties. By filling the mould very slowly, these problems could be avoided. Normally, Mg-Al and Mg-Al-Zn systems can be cast. The tensile properties obtained are superior to other casting processes and other advantages such as defect free, exceptionally good, standard casting of smaller thickness can be cast.

2.5.4 SQUEEZE AND OTHER CASTINGS

Squeeze casting and semi-solid processing such as Reho casting and thixo casting are well advanced developments of magnesium casting in aerospace applications [102-103]. The components produced through these methods show fewer defects and porosity and can be heat treated to get maximum mechanical properties. These casting methods are also suitable for thick and thin sections.

2.6 ALLOY DESIGNATION AND MAJOR ALLOYING SYSTEM

The method of codification used to designate magnesium alloys is taken from ASTM Standard Practice. It gives an immediate, approximate idea of the chemical composition of an alloy, with letters representing the main constituents and figures representing the percentages of these constituents [104].

- Part 1: Indicates the two principal alloying elements and consists of two code letters representing the two main alloying elements arranged in order of decreasing percentage. These letters are the following:

    - A-Aluminium
    - E-Rare Earth
    - C-Copper
    - H-Thorium

- K-Zirconium
- L-Lithium
- M-Manganese
- Q-Silver
- S-Silicon
- T-Tin
- W-Yttrium and
- Z-Zinc.

❖ Part 2: Indicates the amounts of the two principal elements and consists of two whole numbers corresponding to the alphabets.

❖ Part 3: Distinguishes alloys with the same percentages of the two principal alloying elements. It consists of one of the following letters: A-First compositions, B-Second compositions, C-Third composition registered as ASTM, D-High purity, and E-High corrosion resistance.

Magnesium alloys can be classified into two major groups: zirconium-free alloys and zirconium-containing alloys. Zr is an effective grain refiner for Mg alloys. However, in the presence of Al, the efficiency of Zr decreases because Al reacts with Zr to form Al-Zr intermetallics. Hence, in zirconium-free alloys, Al is present as the major alloying element along with zinc and manganese (Mg-Al-Zn, Mg-Al-Si, Mg-Al-RE, etc.), whereas alloy systems such as Mg-Zn-Zr and Mg-RE-Zr are examples of zirconium-containing alloys**.**

2.6.1 ZIRCONIUM CONTAINING ALLOYS

The maximum solubility of zirconium in molten magnesium is 0.6%**.** As binary Mg-Zr alloys are not sufficiently strong for commercial applications, the addition of

other elements is necessary. The ability to refine the grains in Mg-Zn alloys with zirconium led to the introduction of ternary alloys such as ZK51 (Mg-4.5Zn-0.7Zr). However, these alloys are susceptible to micro porosity and are not weldable, and thus have found little practical application [105-106]. However, Zn along with RE addition provides high strength and finds many applications.

Magnesium forms solid solutions with a number of RE elements. The addition of cheaper mischmetal based on cerium or neodymium to magnesium gives good casting characteristics and mechanical properties. These properties are improved by adding Zr to refine the grain size, and further increases in strength occur if zinc is added as well. EZ33 (Mg-3RE-2.5Zn-0.6Zr) is one such alloy that retains strength and creep resistance at temperatures up to 250^{o}C [107]. Recently, Mg-Y age-hardenable alloy systems have been developed to use the benefit of high solid solubility of yttrium in magnesium. A series of Mg-Y-Nd-Zr alloys have been produced that provide high strength at ambient temperature and good creep resistance up to 300^{o}C temperature [108-109]. Maximum strength combined with an adequate level of ductility is found to occur in an alloy containing approximately 6% Y and 2%Nd and the commercially available alloy in this category is WE54 (Mg-5.25Y-3.5RE-0.45Zr).

The addition of thorium also confers increased creep resistance in magnesium alloys, and these alloys have been used in service temperatures up to 350^{o}C. Ternary compositions such as HK31 (Mg-3Th-0.7Zr) are developed for high temperature applications. However, in spite of their application in missiles and spacecraft, the alloy usage is reduced because of environmental considerations Also, silver is added to magnesium and Mg-Ag-RE-Zr alloys are developed with improved room and high temperature mechanical properties [110]. The alloy QE22 (Mg-2.5Ag-2RE-0.7Zr) has been used for a number of aerospace applications including landing wheels, gear box housings and rotor heads for helicopters.

2.6.2 ZIRCONIUM FREE ALLOYS (Mg-Al ALLOYS)

Aluminium is the principal element alloying with magnesium. The binary Mg-Al system is the basis for the first magnesium casting alloys but most current compositions also contain small amounts of zinc and manganese. The most widely used alloys in this group are AZ91 and AM50 [105]. These alloys have a wide range of mechanical properties and good castability and are mostly used in die-casting application. However, the drawback of using these alloys is its poor elevated temperature tensile and creep properties above 150^{o}C [19].

Alloys such as AS21 and AS41 (Mg-Al-Si), which contain Si in them, are developed for better creep properties compared with AZ91 [87]. Later on, the solubility of rare earth (RE) in magnesium led to the development of AE alloys systems, which contain less amount of aluminium and a small percentage of RE [111]. One such alloy system, AE42 (Mg-4Al-3RE-0.3Mn)) has a good combination of properties including creep strength, which is superior to the Mg-Al-Si alloys [112]. The major drawback of these alloys is that the addition of RE increases the alloy cost drastically [87]. Recently, it was also found that the thermal stability of Al_4RE intermetallic in RE containing Mg alloys does not extend beyond 150^{o}C and hence the AE42 alloy loses creep strength above this temperature**.**

The addition of calcium to Mg-Al-based alloys for improved creep resistance has been reported in a British patent [113]. This patent disclosed that calcium additions of 0.5-3% provide creep resistance to magnesium alloys containing up to 10% Al. However, the patent also revealed that calcium-containing alloys are prone to hot cracking**.** Volkswagen attempted the use of Mg-Al-Ca alloys in the 1970s and claimed an improvement in creep resistance with the addition of about 1% Ca to magnesium alloy AZ81. However, the application of this alloy to die-casting was not possible because of die sticking and hot cracking**.** Later, a through investigation on the optimum

amount of Ca addition to Mg-Al alloy to avoid these problems was carried out by the Institute of Magnesium Technology (ITM) in Canada and by General Motors [114-115]. It was found that Mg-Al-Ca-based alloys, which contain more than 1%Ca, are susceptible to the hot cracking problem.

Mg-Al-Sr (AJ) alloys are a new addition to the creep-resistant Mg-Al-based alloys [116]. Various alloy compositions such as AJ51 (Mg-5Al-1Sr), AJ52 (Mg-5Al-2Sr) and AJ62 (Mg-6Al-2Sr) have been developed. The creep resistance of these alloys is found to be better than that of many Mg-Al alloys [117-118]. However, the microstructure and its creep mechanism are not yet fully understood.

The current commercial magnesium alloys developed for die-casting applications fall into two classes [26]. The first group is based on the Mg-Al system and Mg-Al-Zn sytems (AM and AZ alloys). These alloys have been developed for good room temperature strength and/or ductility but do not show good creep resistance. They make up the bulk of the magnesium alloys used in automotive applications. The second group of alloys has been developed for improved elevated-temperature performance and is based for the most part on the Mg-Al-RE and Mg-Al-Si systems (AE and AS alloys) [119-120]. These second group alloys offer either borderline improvement in creep resistance, as in the case of AS alloys, or have cost or other disadvantages (e.g. poor die-castability, high oxidation rate, low fatigue properties) despite their good creep resistance as in the case of AE alloys.

Among the various alloy systems developed, Mg-Al and Mg-Al-Zn with 0.2 Mn combinations are widely used because of their moderate tensile strength at ambient temperature they are prone to excessive creep when exposed to above 100ºC [14, 121]. One approach involves the addition of a large amount of Zinc to Mg-Al alloys so as to get the composition of microstructure consisting of α-Mg and Mg-Zn-Al ternary precipitates.

2.7 EFFECT OF ALLOY ELEMENTS

2.7.1 ZINC

Zinc is one of the major elements alloying with magnesium. Zinc has a very good solid solubility in magnesium. The Mg-Zn binary phase diagram given in Figure 2.7 shows that the maximum solubility of Zn in Mg at 345^{o}C (eutectic temperature) is around 6.2% [122]. The solid solubility of zinc in magnesium at room temperature is around 2%. So the excess zinc forms $Mg_{51}Zn_{20}$ intermetallic with Mg. This phase is hard and brittle and hence acts as a strengthening element at room temperature. Zinc also improves the fluidity of the alloy, but a higher amount of Zn added to Mg-Al alloys can lead to hot cracking problems. The selection of zinc content into magnesium-aluminium alloy is based on the content of wt% of Zn and Al in the castable region, which is shown in Figure 2.8. The presence of zinc decides the type of eutectic (completely or partially divorced) during the final stage of solidification. It is further reported that the addition of zinc reduces the ductility of the alloy [76].

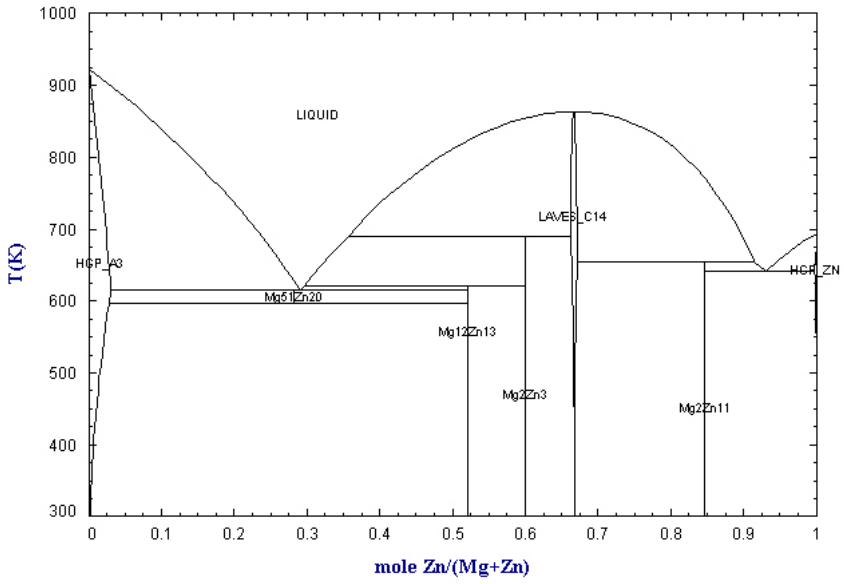

Figure 2.7: Phase diagram of Mg-Zn alloy [122]

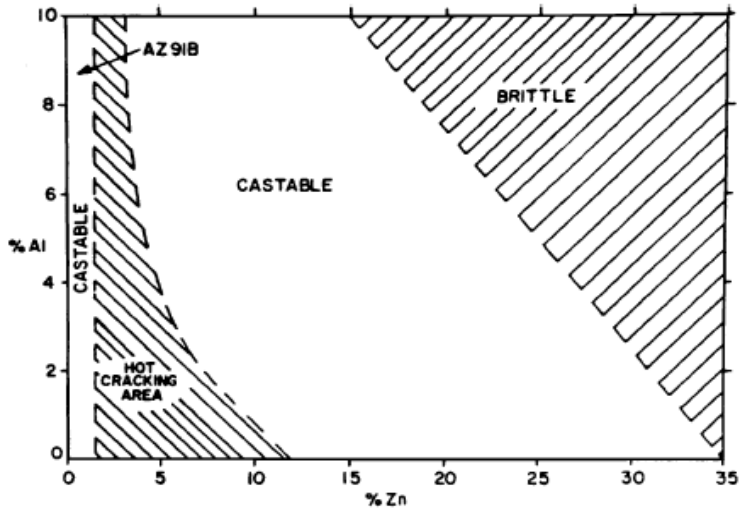

Figure 2.8: Castability region of Mg-Zn-Al alloy [123]

2.7.2 ALUMINIUM

Aluminium has very good solid solubility in magnesium. Al in this alloy improves the castability [123]. The yield strength increases with the addition of Al, whereas UTS increases up to 4% and then decreases. However, the ductility increases initially up to 3% of Al addition and then starts decreasing steeply. Studies have reported that with the additions of Al greater than 2%, the entire solidification of Mg-Zn alloy changes and form the Mg-Zn-Al ternary phase in the microstructure. It also increases the corrosion behaviour of Mg-Zn alloys and tends towards micro-porosity [124].

2.7.3 MANGANESE

The main purpose of adding Mn to Mg alloy is to improve the corrosion properties. The role of manganese in the improvement of corrosion resistance is twofold.

1. When manganese is added to Mg-Al alloys, several types of AlMnFe intermetallics particles are formed [125]. These particles settle at the bottom of the melt, by which the iron content in the melt is reduced.

2. Manganese also renders the iron-containing particles left in the melt during solidification less harmful by making them less efficient as cathodes, compared with the Al-Fe intermetallics, which are formed in Mn-free Mg-Al alloys.

2.8 DEVELOPMENT OF ZA ALLOYS

In the last decade, there have been tremendous of renewed interest on the development of Mg–Zn–Al systems (Zn-rich alloys) having better creep resistance, good castability and excellent resistance to hot cracking [28-31]. Recently, several Mg–Zn–Al-based alloys such as ZA104 [34, 126], ZA84 [31] and ZA52 [127] have been developed. Jing *et al* [128] have studied the microstructural constituents and the crystallographic morphology of the primary intermetallic phases in cast Mg-Zn-A1 alloys with having high zinc content. Figure 2.9 represents the phase constituent of the alloy with respect to Zn/Al ratio and Al content. It is reported that three kinds of primary compounds with distinct morphology has been identified, viz τ-$Mg_{32}(Al,Zn)_{49}$, ε-$MgZn_2$ and a ternary icosahedral quasi-crystalline compound (denoted with Q). These constituent is found to change with Zn and Al content and their concentration ratio. Alloys with equivalent mass ratio of Zn to A1 and Al content consist of α-Mg and τ-phase. Although alloys with high mass ratio of Zn to A1 and low A1 are composed of α-Mg, and ε phase a small amount of τ phase, those with low ratio of Zn to Al and high A1 consist of α-Mg with Q. The solidification ranges decreases with increasing Zn and A1 content for τ and Q-type alloys, whereas ε-type alloy shows the reverse. The second phase transformation moves to higher temperature range when A1 content increases and ratio of Zn to A1 decreases.

High-zinc Mg alloys (zinc content over 5% in general, mass fraction) are newly developed heat-resistant alloys that are strengthened mostly by ternary intermetallics compound τ-$Mg_{32}(Al,Zn)_{49}$, with good creep-resistant property, and a little φ-$Mg_5Al_2Zn_2$ phase. It is reported that the Mg–Zn–Al alloy systems having Zn:Al

composition in the ratio of 2:1, in particular ZA84 (Mg–8Zn–4Al–0.2Mn) alloy, have moderate mechanical properties, good creep resistance, satisfy the requirement of other corrosion and casting properties as compared with AZ91 alloy [28]. The creep-detrimental $Mg_{17}Al_{12}$ or Mg_2Zn_3 [31] precipitates are completely eliminated in the ZA84 alloy. However, there is need to improve the castability of this alloys and the elevated-temperature mechanical properties obtained in this alloy are highly suitable for several applications.

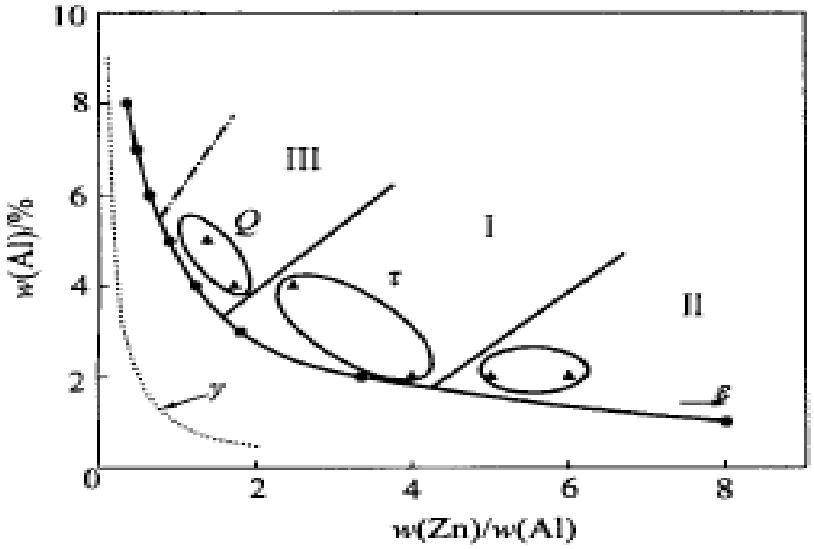

Figure 2.9: **Phase constituent with respect to Zn/Al ratio and Al content [128]**

It can be observed from Figure 2.10 that YS values increase with an increase of Al content of 8 %Zn contents. The UTS reaches its highest value at 4% Al with 8% Zn. [129]. The most economic use of magnesium in the automotive industry presently is in die-cast applications because of the high productivity of the die-casting process, which upsets the relatively high cost of the magnesium metal.

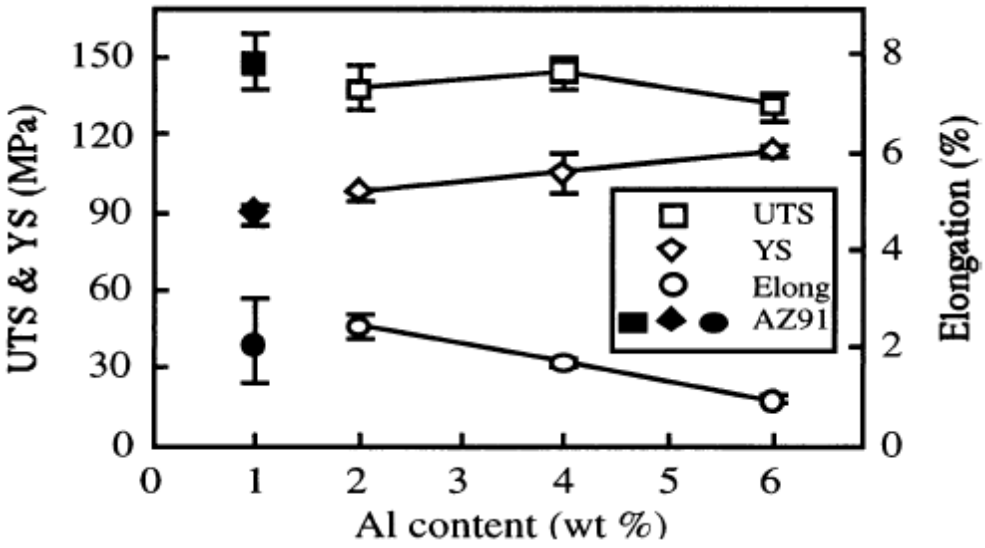

Figure 2.10: Mechanical properties of Mg- 8% Zn-x% Al alloys tested at room temperature [28]

The magnesium components produced by die-cast process have good room temperature mechanical properties. Whereas, sand cast alloys show lower mechanical properties because of the coarse microstructure [130].. Moreover, further improvement in high temperature behaviour through microstructural modification by alloying additions is also an essential task to make this alloy suitable for the replacement of high strength aluminium alloys used in automobile industries. Minor alloying additions and grain refinement combination have effective way to improve the tensile behaviour of engineering alloys.

2.9 ROLE OF MINOR ALLOYING ADDITIONS

Surface active elements such as Sb, Ca, Bi, Sr, RE, etc. are added to the AZ91 alloy to improve its mechanical and corrosion properties. It has been reported that the addition of minor alloying elements such as X (Sb, Ca, Sr and RE, etc.) to AZ91 alloy not only refines the primary β-$Mg_{17}Al_{12}$ phase effectively but also forms new secondary precipitates (Mg_xX_y and/or Al_xX_y, where *x* and *y* represent the whole number depending on the stoichiometry of the stable intermetallics) at the grain boundary, which alter the microstructural stability to improve creep properties [26, 48, 130-132]. Some elements such as Ca and Sr are effective in refining the grain size of AZ91 alloy. Ca and RE are also found to improve the corrosion resistance of AZ91 alloy. Table 2.5 summarizes the advantages and limitations of alloying elements with AZ91 alloy.

Improve the properties of ZA alloys for high temperature applications is through by alloying additions .. It is reported that the properties of ZA alloy systems can be improved by the addition of minor alloying elements, such as Ca, Sn, Sr and Si, which effectively modify the precipitates in the microstructure [28, 133]. Zhang *et al* [28] have reported that the Ca addition to ZA144 and Sr addition with ZA142 alloys yield superior elevated temperature mechanical properties and creep resistance compared to those of the base alloy. This is due to the presence of significant amounts of Ca and Sr in the complex phases, which effectively refine the microstructure and increase the stability of precipitates to improve the tensile and creep properties. Those studies are proof that the minor alloying additions to ZA alloys show the effective modification of the microstructure, which in turn increases the elevated properties.

Table 2.5: Advantages and limitations of trace alloy element additions to AZ91 alloy

Elements	Optimum addition, wt %	Precipitates	Advantages	Limitations
Sb[49, 131]	0.5	Mg_3Sb_2 (rod shaped hexagonal $D5_2$ structure)	Leads to grain refinement Improved strength and elongation at room and elevated temperature Improved fracture toughness	Impairs plasticity
Bi [131]	2	Mg_3Bi_2 (rod shaped hexagonal D52 structure)	Leads to grain refinement. Improved creep resistance Improved yield strength and elongation at elevated temperature	Reduces the ductility at elevated temp.
Ca[48-134]	2	Al_2Ca & Mg_2Ca phases	Improved yield strength and elongation at elevated temperature Ignition proof during melting	Leads to hot tearing Poor mechanical properties at ambient temperature
Au[135]	0.5	Mg-Al-Au phase	Improved creep resistance	Lower primary creep rate Highly expensive
Sr[133, 135,	0.5	Mg_2Sr (needle shape)	Leads to superior grain refinement	Poor mechanical properties, hardness and fracture toughness worse than AZ91 alloy
Y[135, 136]	1	Al_2Y (rod shaped)	Improved creep resistance Improved fracture toughness	Reduces the ductility and castability Highly expensive
Nd[135-137]	0.5	Al_2Nd phase (rod shaped)	Leads to grain refinement. Improved creep resistance Improved fracture toughness	Slightly reduces the castability

The solubility of Ca in Mg is approximately 0.8% and that of Sr is about 0.11–0.15% at 450–570°C [76]. Some experimental alloys containing 14% Zn and 2–4% Al were alloyed with Ca or Sr. The higher Zn content alloys were selected in this study because of their higher volume fraction of intermetallics compound. Figure 2.11 shows the effect of Ca and Sr on the total creep strain of ZA142 and ZA144 alloys. Results indicate that both Ca and Sr are effectively improving the creep resistance. The improvement is more significant when the Al content is 2% and Ca is more effective than Sr for both compositions.

Figure 2.12 shows the effect of Ca and Sr on tensile properties. The effect of Ca is hardly noticeable, whereas Sr additions lead to a slight decrease in tensile properties. An EDS analysis of the Ca and Sr-bearing alloys was undertaken and Table 2.6 shows the distribution of these two additions in the Mg matrix and in the complex $Mg_xZn_yAl_z$ phase. These results show that although some Ca and Sr are in solid solution in the Mg matrix, a very significant amount of Ca and Sr has also entered the complex phase. Consequently, Ca and Sr additions could be influencing the creep behaviour of ZA alloys in two different ways.

1. First, as solutes, they could contribute to the slowing down of the dislocation climb process, which has been established as the rate-controlling process in secondary creep [28].
2. Second, the modification of the complex $Mg_xZn_yAl_z$ phase may also play a role on the creep behaviour of these alloys. It is inferred from the study that Ca and Sr can improve further the creep resistance of ZA alloys and that Ca is more effective than Sr for that purpose. Ca and Sr additions are present to some extent in the Mg matrix as solutes, but a significantly larger amount is found in the complex phase $Mg_xZn_yAl_z$ leading to great improvement in the properties of ZA alloys.

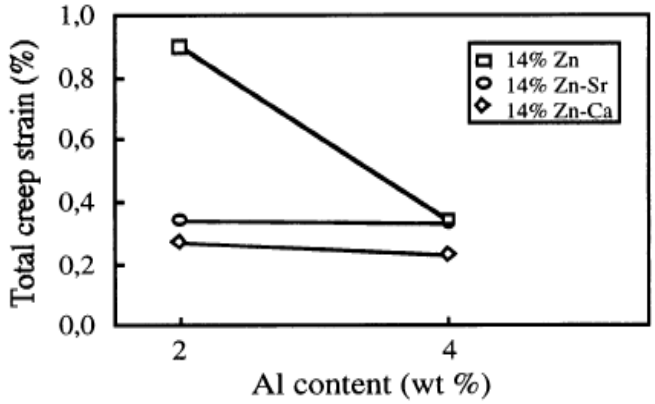

Figure 2.11: Influence of Ca and Sr on the creep properties of Mg-14%Zn-x%Al alloys [28]

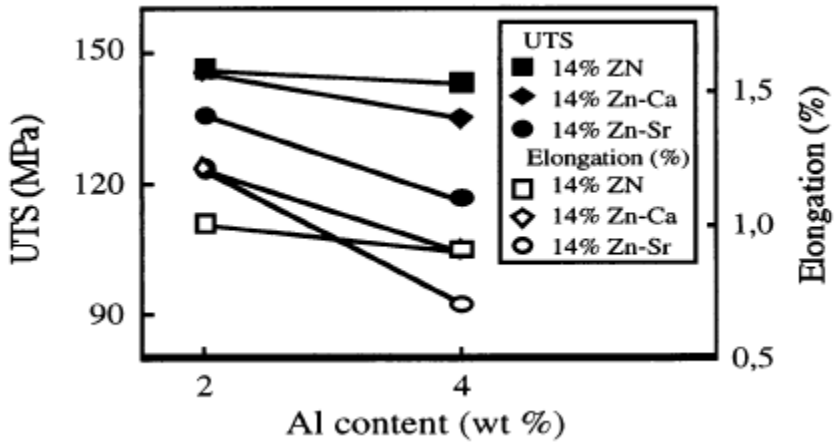

Figure 2.12: Influence of Ca and Sr on the tensile properties of Mg-14%Zn-x%Al alloys [28]

Table 2.6: Chemical analysis of Ca and Sr-bearing experimental alloys (in wt %) [28]

Alloy	Zn	Al	Mn	Ca	Sr
ZA142Ca	14.1	2.13	0.30	0.53	-
ZA144Ca	14.4	4.15	0.31	0.47	-
ZA142Sr	14.5	2.19	0.28	-	0.77
ZA144Sr	14.2	4.25	0.25	-	0.69

C.J. Bettles *et al* [54] have also studied the effect of 0.35 wt% of Ca addition to Mg-4Zn alloy and report a significant improvement in the creep properties because of the refined precipitates structure, which is very stable for prolonged periods at elevated temperatures. Yingxin *et al* [31] have stated that the RE addition to ZA84 alloy effectively refines the microstructure and improves the mechanical properties owing to the formation of the quaternary Mg-Zn-Al-RE phase, which is very stable at a higher temperature. Figure 2.13 shows the cooling curves for ZA84 and RE-containing ZA84 alloys at the speed of 3 K/min. As can be seen from Figure 2.13(a), two phase transformation temperature points (571ºC, liquidus temperature and 334ºC, solidus temperature) are present in the curve of ZA84 alloy results in the solidification range of 230ºC. With the RE addition of 1.5 wt%, the cooling curve changes distinctly, showing three phase transformation temperatures of 566ºC (liquidus temperature), 413ºC and 329ºC (solidus temperature) (Figure b) and the solidification range is 237ºC.

During the solidification, the segregation of RE on the grain boundaries leads to an increase in the solute distribution coefficient *K*. Consequently, neck shrinkage and crystal multiplication [138] occurred, which resulted in the detachment of dendrite and formation of fine nuclei. These fine nuclei can act as a heterogeneous nucleus for the primary (α-Mg) crystals, which leads to the decrease of grain size of ZA84 alloy. With a small amount of RE addition, only the detachment of dendrite occurs. With increasing RE, new $Mg_3Al_4Zn_2RE$ phases form. The structure of the $Mg_3Al_4Zn_2RE$ phase is similar to that of the φ phase, in which no other phases appear, and no reduction in the quantity of φ phase indicates that the $Mg_3Al_4Zn_2RE$ phase comes from the φ phase dissolving the RE element. Intergranular interdiffusion of Al and Zn atoms hindered by the RE segregation on the grain boundaries makes the reaction L→α-Mg+φ happen early and the RE dissolving to the φ phase results in the formation of the $Mg_3Al_4Zn_2RE$ phase. Therefore, the reaction can be hypothesized to be L→α-Mg+φ + $Mg_3Al_4Zn_2RE$ at 413ºC.

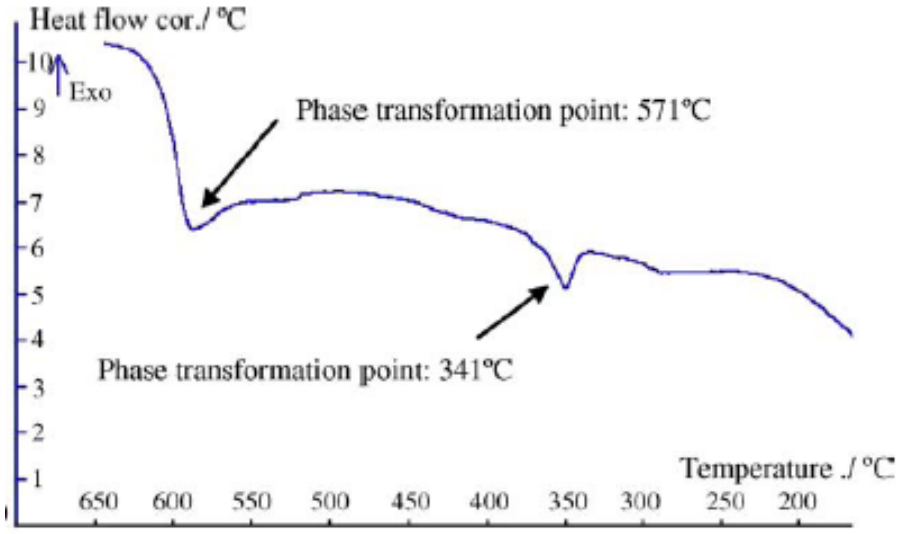

(a)

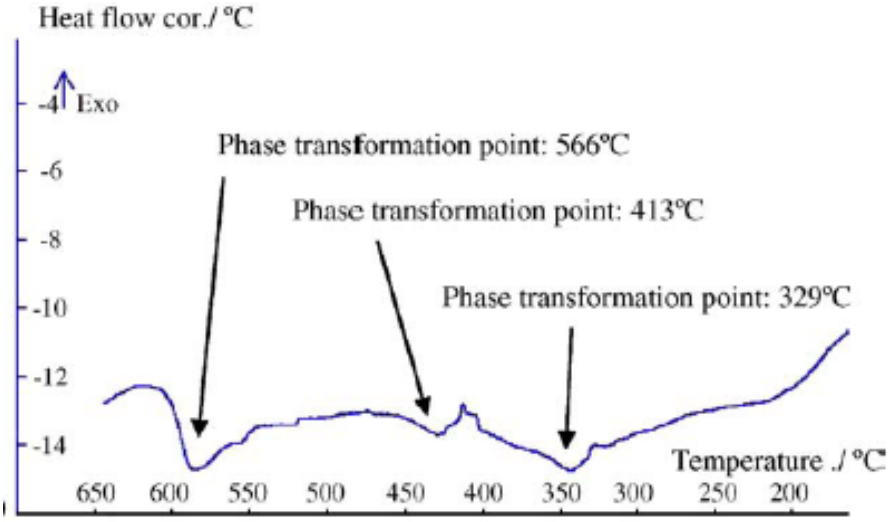

(b)

Figure 2.13: DSC curves of (a) ZA84 and (b) ZA84+1.5RE alloys [31]

Guan *et al* [139] studied the phase selection of ternary intermetallic compounds during solidification of high zinc magnesium alloy. The XRD patterns of without and with Si are shown in Figure 2.14. The presence of τ-$Mg_{32}(Al,Zn)_{49}$ and φ-$Mg_5Al_2Zn_2$ phases without Si containing ZA84 alloy can be clearly observed from Figure 2.14a. Addition of Si in Mg-8Zn-4Al-0.3Mn (ZA84) alloy (Figure 2.14 b), φ-$Mg_5Al_2Zn_2$ phase is promoted, whereas τ-$Mg_{32}(Al,Zn)_{49}$ phase is inhibited. The Chinese script-type Mg_2Si and matrix microstructure are greatly refined; in addition, the formation of τ phase is facilitated and that of φ phase is restrained when modifier Al-AlP master alloy is added in ZA84 alloy containing Si. The steady-state nucleation rate of τ-$Mg_{32}(Al,Zn)_{49}$ and φ-$Mg_5Al_2Zn_2$ phases vs temperature in ZA84 melt is shown in figure 2.15. The silicon addition into ZA84 alloy is a dynamic process of the phase selections based on the chemical composition of critical undercooling of the melt. If the undercooling exceeds the critical value, τ phase preferentially forms whereas φ phase is restrained; otherwise, φ phase preferentially forms whereas τ phase is restrained. The order of phase selection serves as a scientific basis for the selection of strengthening phases in high-zinc magnesium alloys.

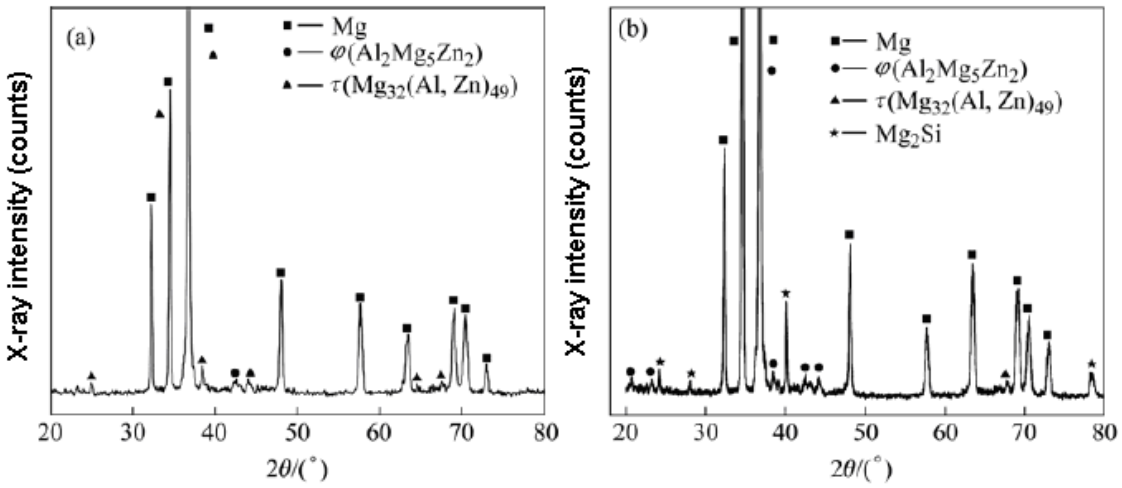

Figure 2.14: XRD pattern of (a) ZA84 and (b) ZA84+Si added alloys [139]

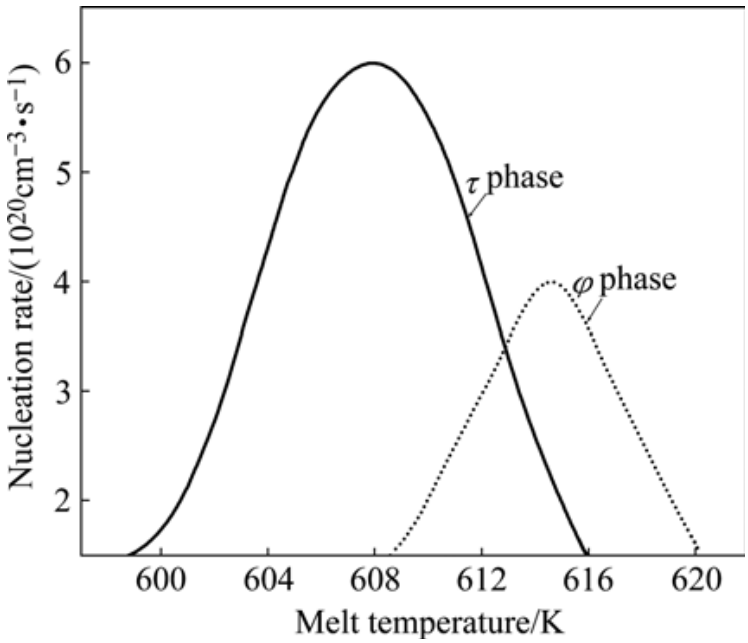

Figure 2.15: **Steady-state nucleation rate of τ-$Mg_{32}(Al,Zn)_{49}$ and φ-$Mg_5Al_2Zn_2$ phases vs temperature in ZA84 melt [139]**

Recently, Yang *et al* [140] have reported the effects of TiC additions on as-cast ZA84 alloy on the microstructure and mechanical properties. The results show that on the addition of TiC to ZA84 alloy, the as-cast microstructure of the alloy is refined. At the same time, the distribution of the second phase in the alloy becomes relatively uniform and the quasi-continuous networked second phases in the alloy become discontinuous. As a result, the as-cast tensile properties of the alloy are improved. In addition, after solutionization at 345ºC, parts of the $Mg_{32}(Al,Zn)_{49}$ phases in the ZA84 alloy without TiC modification still show quasi-continuous distribution. The $Mg_{32}(Al,Zn)_{49}$ phases in the alloy treated with 0.5%TiC change to disconnected particles with an angular morphology and gradually spheroids. Under the optimum heat treated conditions, the ZA84 alloy treated with 0.5%TiC shows higher heat treated properties than the base alloy without TiC modification.

Even though some studies have been carried out to understand the effect of alloying additions in ZA alloy systems, the effect of other alloying elements such as Sb, Si, Sr, Pb, etc. has not been studied. Moreover, studies have been reported that the Sb addition to AZ91 alloy has led to a favourable microstructure by distributing the fine

Mg_3Sb_2 particles (melting point around 1228^oC) at the grain boundary and refining the $Mg_{17}Al_{12}$ precipitates, thus improving the room and high temperature properties. Ca additions to magnesium alloys effectively refine the microstructure and improve the elevated temperature properties, especially creep. Hence, the present investigation aims to study the effect of individual and combined additions of Sb and Ca on the microstructure and mechanical properties of ZA84 alloy.

2.10 GRAIN REFINEMENT

It is well known that the metallic alloys usually solidify with coarse columnar grains structure under normal casting conditions unless the mode of solidification is carefully controlled. One possible way is to produce fine equiaxed grains in the microstructure either by controlling the cooling rate or by introducing a heterogeneous nucleant during solidification. There are also other methods, such as melt agitation/vibration during solidification or use of a mould coating, which result in the formation of fine equiaxed grain structure in the casting. Among all the techniques, the common grain refinement practice in metal casting industries is obtained by introducing nucleating agents, known as inoculation [141]. ***Such fine grain structure alloys improve the mechanical properties and ensure consistent performance of the cast products***.

Grain refinement of alloy shows uniform distribution of secondary phases and solute elements on a fine scale, which results in better machinability, good surface finish, excellent resistance to hot tearing and superior extrudability [142]. Apart from these established benefits of grain refinement, it has been shown by a recent work [143], that fine and spherical primary crystals are obtained directly from the liquid state by grain refinement without any liquid agitation, which enhances the structural uniformity of alloys. Grain refinement also favours corrosion resistance as a result of improved structural uniformity, including a more continuous phase. Therefore, it is appropriate to say that grain refinement is an important factor for the further development of alloys from all aspects.

The present review will confine itself to the literature on grain refinement achieved by heterogeneous nucleation through inoculants. The existing literature in this field is reviewed under the following sections:

- ***Concept of grain refinement by heterogeneous nucleation***
- ***Mechanism of grain refinement by different nucleating particles***
- ***Types of grain refiners and methods of production***
- ***Grain refiners***

2.10.1 HETEROGENEOUS NUCLEATION CONCEPT [141, 143-144]

The mechanism of grain refinement can be related to nucleation and growth process of grains. This is based on the nucleation ideas of Volmer and Weber [143]. The theory involves both homogeneous and heterogeneous nucleation. In pure metal solidification, the critical nucleus size for survival is given by

$$r^*_{\text{hom}ogenous} = -2\nu_{sL} / \Delta G_v \quad \text{---------- (1)}$$

The free energy barrier is given by

$$\Delta G^*_{\text{hom}ogenous} = 16\pi\gamma^3_{sL} / 3\Delta G_v^2 \quad \text{---------- (2)}$$

where γ_{sL} is the interface surface energy of a solid–liquid interface in J/m^2, assuming the specific heats of liquid and solid are similar and ΔG_v is the driving force for solidification

$$\Delta G_v = \Delta T \Delta S = \Delta H_f \Delta T / T_m \quad \text{————————— (3)}$$

ΔT is the undercooling below the liquidus temperature K,

ΔS is the entropy change for liquid to solid phase transformation, J/K/m^3,

ΔH_f the enthalpy of solidification and

T_m the melting temperature

If the origin of the solid is greater than critical radius, $r^*_{\text{homogeneous}}$, the embryo will survive and become a nucleus.

In heterogeneous nucleation, the critical nucleus size is

$$r^*_{hetrogenous} = -2\gamma_{sL} / \Delta G_v \text{ ---------- (4)}$$

(1) and (4) are identical for both homogeneous and heterogeneous nucleation, and the free energy barrier is

$$\Delta G^{*}_{hetrogenous} = 16\pi\gamma^{3}_{sL} / 3\Delta G_{v}^{2} f(\theta) \text{ ---------- (5)}$$

where $f(\theta)$ is a function of the contact angle and θ is an angle between the nucleant and the liquid substrate. Figure 2.16 shows the solid nucleating in a liquid substrate. It shows the variation of $f(\theta)$ with θ and as $f(\theta)$ is always ≤ 1, the critical free energy for heterogeneous nucleation is always less than or equal to that for homogeneous nucleation. However, it is clear that potent heterogeneous substrates are those with θ close to zero.

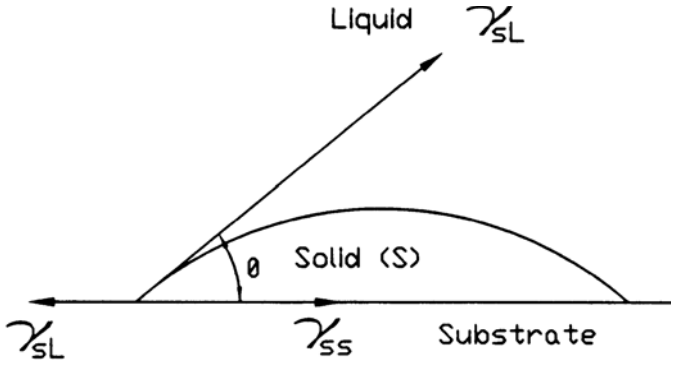

Figure 2.16: Equilibrium of interfacial energies during heterogeneous nucleation [141]

The value of undercooling, ΔT is of the order of 1–2 K for observable nucleation rates in commercial aluminium alloys with grain refiners. Therefore, clearly heterogeneous nucleation is taking place. The following simplified expression for heterogeneous nucleation rate per unit volume in m^3/s is

$$I^{v}_{hetrogenous} = 10^{18} N_{v}^{p} e[-16\pi\gamma^{3}_{sL} f(\theta) / 3K_{B}\Delta S^{2}\Delta T^{2}] \text{ ---------- (6)}$$

Where K_B is the Boltzmann constant, J/K, N_v^p is the number of nuclei/m^3, and $I^{v}_{hetrogenous}$ the heterogeneous nucleation rate of nuclei/m^3.sec. Therefore, it can be seen that if the contact angle is close to zero, wetting of the substrate for nucleation is promoted and the nucleation rate increases.

The requirement of inoculants acting as effective nucleating sites is as follows:

1. *It should have a melting point higher than that of the alloy being solidified.*
2. *It should be able to initiate freezing at very small undercooling.*
3. *A sufficient number of nucleating particles should be uniformly distributed.*
4. *The nucleating particles should be larger than a critical size, which depends on the undercooling of melt.*

2.10.2 GROWTH OF NUCLEI [144-146]

Once nucleation takes place, more importantly heterogeneous nucleation, the growth front of the nuclei is seldom planar. The well-known constitutional super cooling occurs as the solute is rejected at the interface and the criterion is given by Kurz and Fisher (1984) [145].

$$G_L / R = -m_L C_o (1-k) / kD_L \quad \text{---------- (7)}$$

where G_L is the temperature gradient in the liquid ahead of the solid–liquid interface (K/m), R the growth rate of solid liquid interface (m/sec), m_L the liquidus slope of the phase diagram (K/wt%), C_0 the bulk alloy composition in the liquid (wt%), k the partition coefficient between solid and liquid, and D_L the diffusion coefficient of the solute in the liquid (m^2/sec).

2.10.3 SOLUTE THEORY [141, 147]

This theory was formalized by Johnson and co-workers [147]. It suggests that both the nucleants and the segregating solutes influence the grain refinement. The segregation power of an element is described in terms of growth restriction factor (GRF) during solidification. GRF is a measure of the growth restricting effect of solute elements on the growth of solid-liquid interface of new grains as they grow into the melt.

2.11 MECHANISMS OF GRAIN REFINEMENT IN MAGNESIUM ALLOYS

Depending on whether they are alloyed with aluminium, magnesium alloys can be generally classified into two broad categories:

(1) Aluminium-free alloy [148-159] and

(2) Aluminium-bearing alloy [160-182].

2.11.1 ALUMINIUM-FREE ALLOYS

Magnesium alloys containing zirconium or grain refined by zirconium, such as ZE41, ZK60, WE43 and AM-SC1 are referred to as aluminium-free alloys. These are an important high value-added class of alloys and are based on the exceptional grain-refining ability of zirconium when added to aluminium-free magnesium alloys.

Zirconium is a potent grain refiner for pure magnesium, [148-151] which is ineffective in magnesium alloys that contain ***Al, Mn, Si, Fe, Ni, Co, Sn and Sb*** as zirconium forms stable compounds with these elements [152]. The maximum solubility of zirconium in molten pure magnesium at 650^0C is ~ 0.45% Zr, which can readily reduce the average grain size to about 50μm from a few millimeters at normal cooling rates. Moreover, well-controlled grain refinement by Zr can lead to the formation of nearly round or nodular grains [153, 154], which further enhance the structural uniformity of the final alloy. This exceptional grain-refining ability of Zr has led to the development of a number of commercially important magnesium alloys, including a few recently developed sand-cast creep-resistant magnesium alloys that are aimed at automotive applications such as transmission cases and engine blocks [154, 155]. The most characteristic feature of the microstructure of a magnesium alloy containing more than a few tenths percent soluble Zr is the Zr-rich cores that exist in most magnesium grains. These Zr-rich cores are usually less than 15 μm in size at normal cooling rates. They are believed to be the products of peritectic solidification [156]. To know the mechanism of grain refinement by Zr and capitalize on the grain-refining ability of Zr, it is necessary to understand the characteristics of these Zr-rich cores.

At present, grain refinement of these alloys is commercially carried out by the addition of a Zr –rich Mg-Zr master alloy, which contains Zr particles ranging from sub-micron to 50 μm in size [157]. It has been found that grain refinement of magnesium alloys by Zr is dictated by both soluble and insoluble Zr contents [151, 157-158]. However, Zr particles settle very fast in molten magnesium because of the significant difference between the densities of Zr and molten magnesium. As a result, the average grain size increases, obviously with increasing residence time of the melt prior to pouring [158]. Moreover, once the Zr particles that are released from a Mg-Zr master alloy added

to the melt settle at the bottom of the alloying vessel, little dissolution can be expected of these particles in the absence of stirring. Hence, the particle size distribution in a Mg-Zr master alloy can be understood mainly from a settling point of view rather than from the nucleation point of view. The identification of effective nucleant particles is commonly based on the assumption that after nucleation of any particle added to the melt, latent heat release will decrease the likelihood of nucleation on neighbouring particles, which subsequently will be pushed to grain boundaries or into the interdendritic spaces. Therefore, an effective nucleant particle is always expected in the central regions of grains. Compared with the grain refinement of most other alloys, where it is usually difficult to find a large number of nucleant particles on polished sections, Zr-rich particles that have played a role as nucleation centers in a magnesium alloy can be readily distinguished using a SEM in the BSE image mode, because of the characteristic particle-core structures that form during solidification [150]. Certainly, any information about the size distribution of these particles will help understand the potency and efficiency of Mg-Zr master alloy grain refiner, providing an important basis for improving the design of a grain refiner.

To investigate the morphology, distribution and composition of the Zr-rich cores observed in Mg-0.56%Zr and the small particles present in them, the following experimental procedure is used [150]. A 600-g pure magnesium melt is prepared in a BN-coated mild steel crucible in an electrical resistance furnace using pure magnesium ingots (99.9% Mg). The cover gas 0.5%SF6 in dry air has been used. 1% zirconium is added to the melt at 730ºC in the form of Mg-33.3Zr ***Zirmax*** master alloy, which contains different sizes of pure zirconium particles ranging from sub-micron to approximately 50μm. Samples have been taken from the top of the melt both before the 1% Zr addition and after two minutes of manual stirring following the addition, using a BN-coated mild steel cone ladle (Ø30 mm x Ø 20 mm x 25 mm).

Figure 2.17 shows the typical views of the grain structures of the cone samples taken before and after the 1% Zr addition, showing the exceptional grain-refining ability of Zr when added to pure magnesium. Zr-rich cores have been observed on the three

different sections prepared from the zirconium-containing cone sample in the BSE mode and are found in general either elliptical or nearly circular morphology on all three polished sections. Also ellipsoidal morphology of several Zr-rich cores has been observed on an etched transverse section prepared from the same zirconium-containing cone sample, and most of the zirconium-rich cores that have been observed are smaller than 20μm. Many magnesium grains containing more than one Zr-rich core are shown in Figure 2.18. In addition, it is found that the Zr-rich cores are not always present inside the magnesium grains; they exist at the grain edges as well. Hence, it can be often observed that two different grains share a single Zr-rich core at the grain boundary. Many Zr-rich cores are found to be associated with a tiny bright particle. Though it is impossible to examine all the Zr-rich cores formed, the observations suggest that if the samples are continued to be polished, then the tiny bright particles observed in the cores will disappear, resulting in particle-free elliptical or nearly round cores. This is in agreement with Emley's [156] point of view that the central particles are visible only if the microsection happens to cut through them. Therefore, it is quite reasonable to believe that each Zr-rich core is associated with at least one particle. This coincides with the hypothesis that the Zr-rich cores are products of a peritectic reaction during solidification. To initiate such a peritectic reaction, the presence of a solid phase is necessary. To form as many Zr-rich cores as possible for excellent grain refinement, it is desirable to have a sufficient number of suitably sized particles in the melt prior to peritectic solidification. Electron microprobe analyses of the particles in the Zr-rich cores show that the majority are nearly pure Zr particles. On the other hand, little Zr has been detected in most traversed areas that surround the cores, indicating that almost all Zr in solid solution is concentrated in the Zr-rich cores. The distribution of Zr in these cores has been found to be inhomogeneous and to vary in a wide range, for example, from 0.5 to 3%. From the detailed examination of the size distribution of active Zr particles that are observed at the centres of Zr-rich cores, it has been shown that the majority of the particles are in the range of 1 to 5 μm in size when measured on polished sections, and that the most active group of particles are ~2μm.

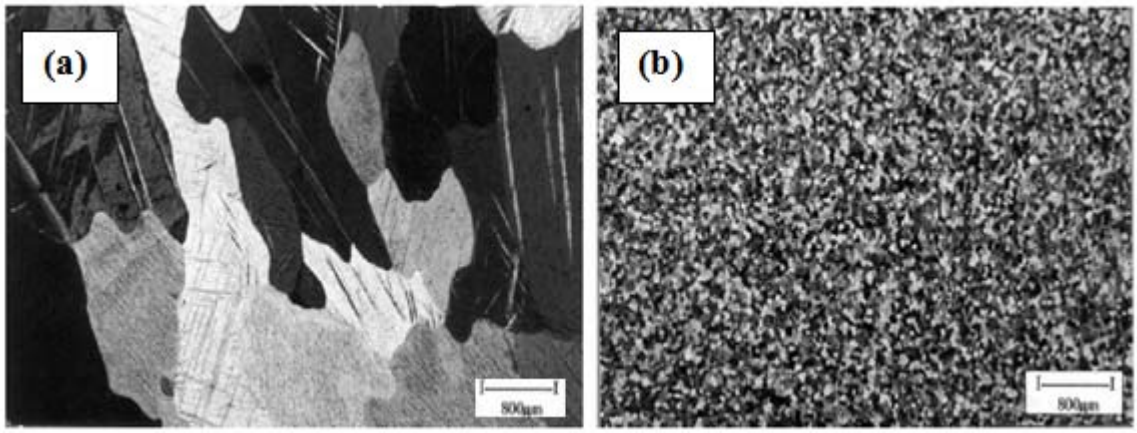

Figure 2.17: Microstructures showing grain size of (a) pure magnesium (b) Mg-0.56Zr alloy [150]

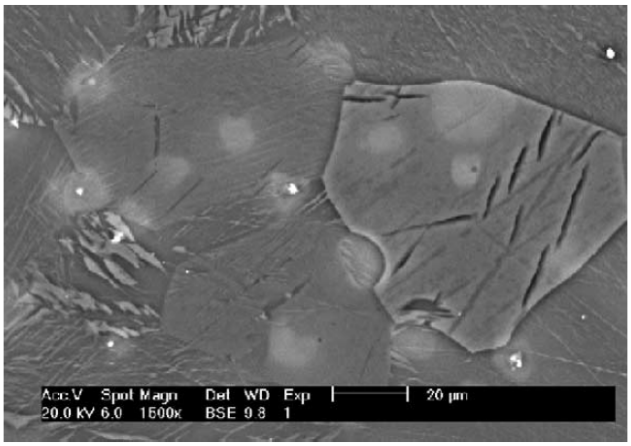

Figure 2.18: A BSE image of Mg-0.56Zr alloy showing Zr-rich cores [150].

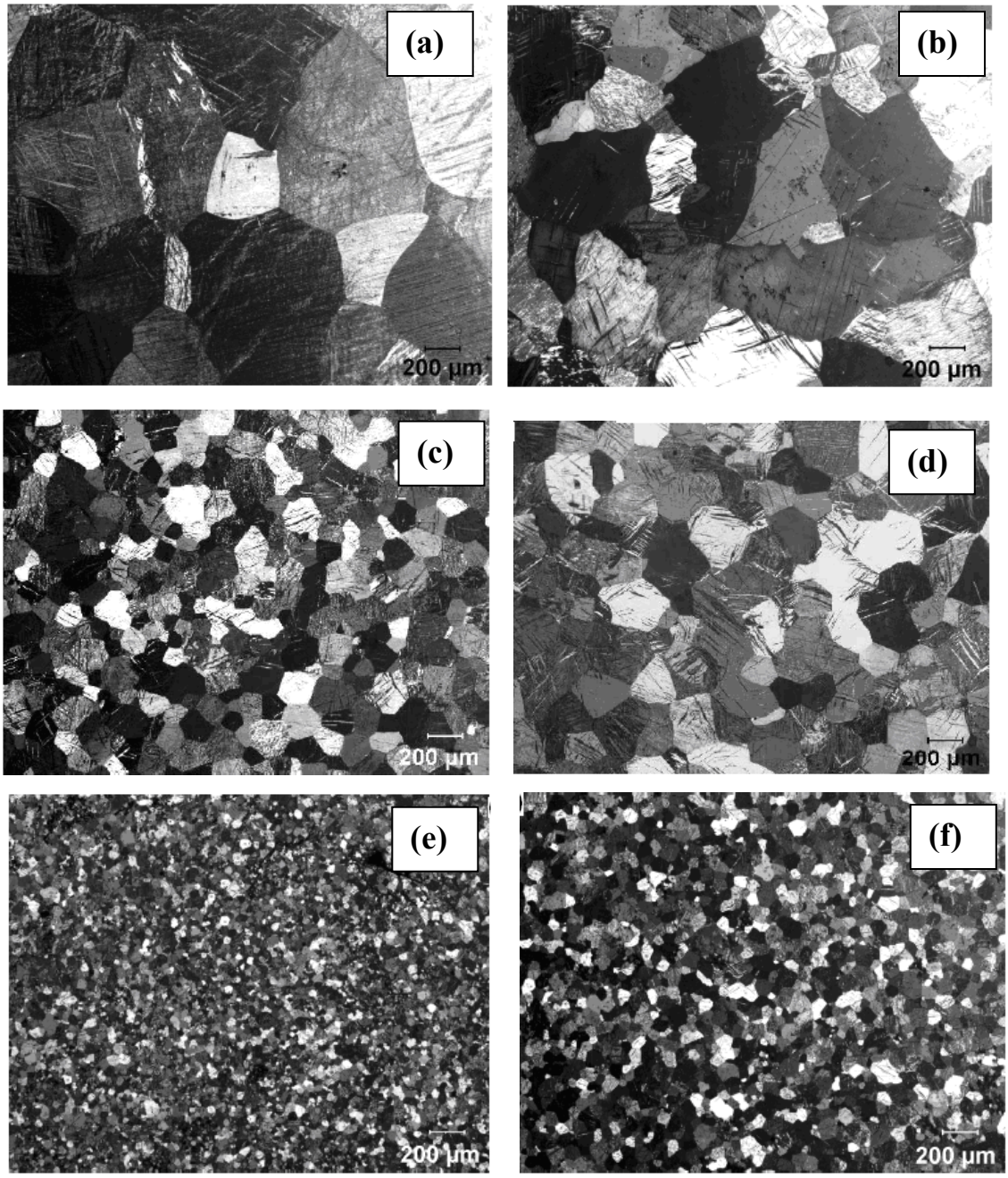

Figure 2.19: Micrographs of Mg-0.5%Zn showing grain size (a) without grain refiner (b) with 0.5% Zr and without stirring (c) 0.5% Zr added with 2 min stirring (d) 0.5% Zr added and holding for 2 hours without stirring (e) 1% Zr added alloy (f) 2% Zr added alloy [150].

Experiments have been conducted [159] on Mg-0.5%Zn alloy to study the effect of stirring, settling and Zr loss on grain size. In this study, Mg-0.5%Zn alloyed with Zr as Zr master alloy has been melted in an aluminium titanite crucible and the sampling temperature is 730ºC. The above study relies on nucleation on Zr particles in the size range between 1 and 5 μm (more favourably around 2 μm in size) and on the formation of the maximum number of Zr-rich cores during solidification. The steps from (a) to (f) have been carried out as described in the caption for Figure 2.19. It has been proved by the work that restirring the melt improves the grain-refining effect as some undissolved Zr particles have been stirred up from the bottom of the crucible. After 2 min of stirring, the grain size has been further reduced to 110μm as shown in micrograph (c), owing to dissolution of Zr and a more even distribution of Zr particles. Micrograph (d) is the result of a further addition of 0.5%Zr (total 1%Zr), reducing the grain size to 54μm and micrograph (e) results from another 1% Zr addition (total 2%Zr), further reducing the grain size to 27μm. Micrograph (f) shows the effect of holding the melt that produced (c) for 2 hours without stirring.

2.11.2 ALUMINIUM-BEARING ALLOYS

Aluminium-bearing magnesium alloys such as AM50, AM60 and AZ91 comprise the core of the magnesium business today and are mainly used in high pressure die-casting (HPDC) applications. As aluminium and zirconium form stable intermetallic phases that are ineffective as nucleants for magnesium grains, the exceptional grain-refining ability of zirconium does not occur in these alloys [160, 161]. Though much research work has been conducted to achieve fine grains in magnesium alloys [162-168], currently, a suitable grain refiner that is reliable and easy to apply for Mg-Al alloys does not exist [169, 170] and it has long been anticipated that such a grain refiner would allow alloys such as AZ91 and AZ31 to be used more extensively in non-HPDC applications, as there is a great demand for high quality extrusion billets. This is because of grain refinement can effectively reduce hot tearing susceptibility during direct chill billet casting and provide fine-grained billet with improved extrusion properties, ensuring a uniform fine-grained recrystallized microstructure in the extruded product. Such a

microstructure can lead to both optimum mechanical and cosmetic properties of extruded profiles. Grain refinement results in improved creep resistance for alloys that contain a hard divorced eutectic phase, as has been shown by the AM-SC1 alloy [171]. This is because in the fully grain-refined state, the hard divorced eutectic phase exists at triple points and along the grain boundaries to help lock the grain boundaries and reduce grain boundary sliding.

In the last few decades, magnesium-based alloys exemplified by AZ (Mg-Al-Zn) and AM (Mg-Al-Mn) series alloys have been rapidly developed and applied in the automobile industry [170,172]. Moreover, magnesium alloys are also used widely in electric and aerospace industries [173]. The grain refinement of Mg based alloys has become a particularly active topic and deserves more and more attention. This necessity has provoked an interest in understanding the mechanisms by which grain refinement takes place, and the present research work seeks to investigate the mechanisms of grain refinement in magnesium alloys using the approach based on the experimental results in conjunction with microstructural investigations. From the knowledge this research work generates, the potential for the discovery of new or improved refiners is significantly enhanced, so that the benefits of fine grain size on mechanical properties and structural uniformity in magnesium alloys can be readily achieved.

For castings that impose fast cooling rates, such as squeeze casting, constitutional undercooling can be effectively used to obtain a homogeneous and fine microstructure, whereas for slow cooling rates in case of continuous casting, there is a lack of potent methods for grain refinement, especially for aluminium-bearing magnesium alloys [174]. Owing to the importance of grain refinement to a broad range of Mg-Al alloys, considerable work has been carried out to determine the mechanisms by which grain refinement occurs. Methods that have been used with varying degrees of success to grain-refine Mg-Al alloys include [159] carbon inoculation [175-177] using various systems, for example carbon-containing organic compounds, direct additions of C-containing particles and bubbling of carbonaceous gases through melts or superheating [175, 178]. Also, by controlling the impurity levels that affect the grain size of Mg-Al alloys, high purity Mg-

Al alloys have a significantly finer grain size than those of commercial purity alloys [159, 179], referred to as native grain refinement. Another grain-refining method developed for Mg-Al-based alloys is the Elfinal process, [159,180] which involves the addition of anhydrous $FeCl_3$ to a molten magnesium alloy. Apart from the above, other additives such as Sr, RE, Th, Si, Ca, B, AlN, MgO, TiB_2 and TiC have also been tried [181-182]. In the following, a brief discussion on the mechanisms underlying the grain refinement of Mg-Al based alloys is made.

2.11.2.1 SUPERHEATING

Aluminium-bearing magnesium alloys benefit from high-temperature treatment in terms of grain refinement. This high-temperature treatment is usually termed as superheating [183] and the process involves heating the melt to a temperature well above the liquidus of the alloy, often in the range 453K to 573K for a short time, followed by rapid cooling to, and short holding at, the pouring temperature. Although the grain refinement efficiency of superheating is subjected to many factors, there are some basic characteristics of this technique [170]. A significant grain-refinement response can be achieved in Mg-Al alloys only with a minimum addition of Mn/Fe content. A specific temperature range above the pouring temperature is then required to maximize the grain-refining effect. Finally, rapid cooling from the overheating temperature to the pouring temperature and the short holding time are also crucial requirements to produce fine grains.

Though the study on grain refinement by superheating [184] from various perspectives has been carried out, the exact mechanism is not fully understood and there are discrepancies in the explanations put forward. The first group of researchers basing their theory on ***temperature solubility*** proposed that the particles at normal pouring temperatures are not small enough to serve as heterogeneous nucleation sites, but that at higher temperature they may dissolve and re-precipitate as fine particles required for nucleating small grains [184-185]. However, this approach fails to address the species of these particles and clarify the key roles of Mn/Fe in the melt. The second approach tends to imply that the formation of one or more Al-Mn or Al-Mn-Fe intermetallic compounds

may take place at high temperatures, which act as an effective grain refiner after the subsequent cooling [186-187]. However, from the crystallographic viewpoint, the actual atomic row matching across the interface between the $Al_8(Mn,Fe)_5$ compound and the magnesium matrix has been examined and concludes that the crystallographic matching at the interface is so poor that the $Al_8(Mn,Fe)_5$ phase cannot provide an effective nucleation site for the Mg grains, and this conclusion is found to be supported by a work of Cao et al [188]. The third major hypothesis proposed is the nucleation of magnesium grains on Al_4C_3, based on the assumption that there is an obvious uptake of carbon from steel crucible walls at very high superheating treatment temperature [189].

A recent work [190] concludes that in Mg-Al alloys, Al_4C_3 heterogeneous nucleants are formed and primary Mg crystals have grown from them as the alloy has been super-heated. For this study, a crucible for melting the alloy made from Fe to 18%Cr stainless steel that has corrosion resistance at elevated temperatures has been used. The crucible is lined with pure aluminium by dipping it into a molten aluminium bath, then inside with magnesia to prevent interaction with impurities from the crucible. An AZ91E alloy is used in the experiment. The molten alloy has been superheat-treated at 850ºC for 900s, then cooled at 2.5C/s and poured at the desired temperature for obtaining quenched samples. The casting temperatures are 750, 700, 650 and 600ºC. During pouring, the molten alloy has been quenched by using two chilled copper blocks. A mixture of SF_6 and CO_2 gas has been used to prevent the molten alloy from burning during heating and pouring into the mold.

Figure 2.20 represents the microstructures of superheat-treated and untreated AZ91E alloy samples obtained through quenching from 600ºC. The samples that are superheat-treated reveal that there is an existence of foreign substances at the centre of each dendrite crystal shown in Figure 2.21. The foreign substances include Al, C and O or Al, C, Mn, Si and O. C, Mn and Si are impurities in the AZ91E alloy. During superheat treatment there is a possibility of formation of Al_4C_3 or Al_2CO compound. As water has been used for polishing the sample, the following chemical reaction could have taken place.

$$\mathbf{Al_4C_3(s) + 12H_2O(l) = 4Al(OH)_3(s) + 3CH_4(g)}$$

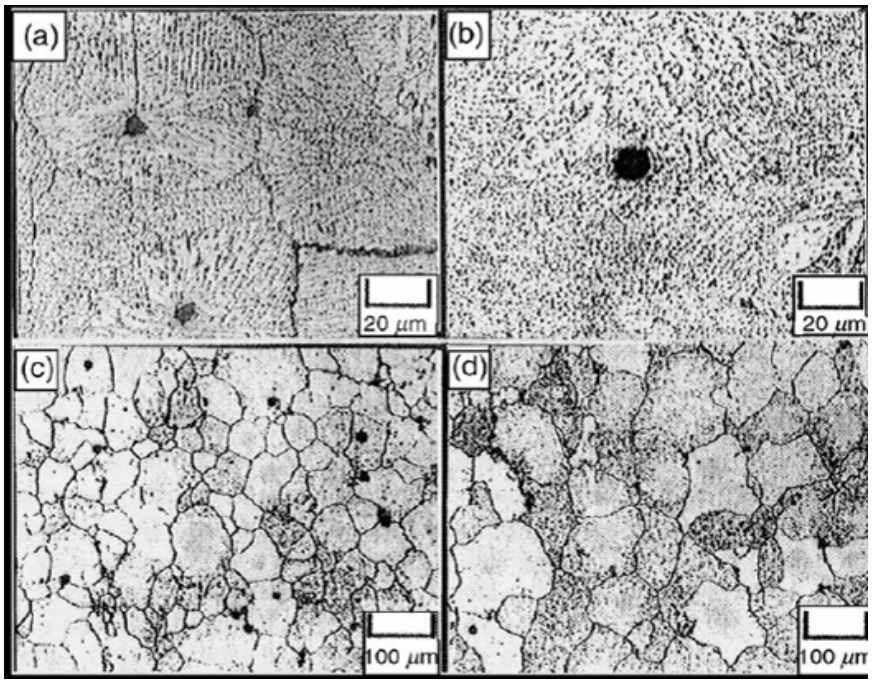

Figure 2.20: Microstructure showing Mn compound of (a) quenching at 600ºC (b) quenched coarse particle (c) as-cast sample (d) non-superheat treated [190]

AZ91E alloy samples quenched from 600, 650 and 700ºC have revealed the existence of Al, Mn, C, O and Si elements. Mn-free and Si-free Al-C-O compounds have appeared only in the sample from 800ºC. Crystallization of Mn and Si may have taken place on the Al_4C_3 compound or only on Mn compound formed below 700ºC and Al, Mn and Si are probably solute in the molten magnesium during superheat-treating. However, compounds consisting of Al, Mn and Si have also existed in non superheat-treated alloy that made no magnesium dendrite crystals to nucleate. Other mechanisms that have been proposed include nucleation on magnesium oxides aluminium oxides or similar nonmetallic inclusions that form during the superheating process. It is likely that there is more than one mechanism functioning in superheating [159].

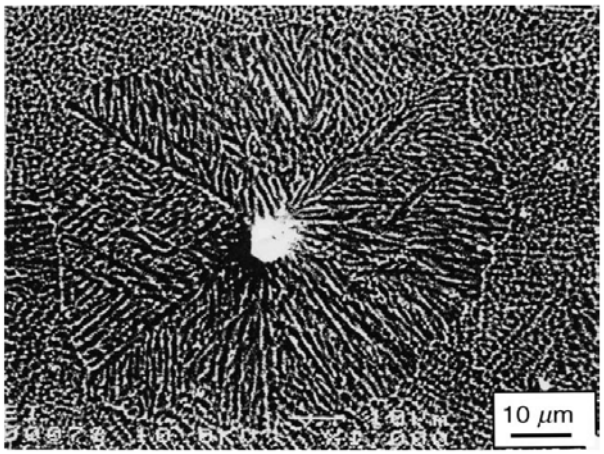

Figure 2.21: Microstructure of AZ91E sample, quenched from 750ºC, showing the presence of Al_4C_3 compound [190].

2.11.2.2 NATIVE REFINEMENT

An interesting observation that has been made about the grain refinement of Mg-Al type alloys is the influence of the source magnesium impurity level. This native refinement in Mg-Al type alloys is said to have occurred when the native grain size is finer than that of commercial purity alloys [191]. It is unclear whether native grain refinement of high purity Mg-Al alloys is conditional on the C and Al contents. The difficulty of clarifying the role of carbon lies in the difficulty of how to accurately determine a trace level of carbon in magnesium alloy [159].

In a recent work [191] carried out to understand the mechanism of native grain refinement in Mg-Al alloys, the raw materials used are high-purity aluminium, commercial purity zinc and calcium, and two different sources of magnesium metal, which include sublimed high purity magnesium (99.98%) and commercial purity magnesium (99.7%). Table 2.7 represents the chemical composition of magnesium metals from two sources in wt%. Three groups of Mg-Al alloys have been prepared: the first group using high purity magnesium, and the second group using commercial purity magnesium metal. Seven different compositions of Mg-Al alloys in the range of 0.5-9%Al have been prepared in each of these two groups. The Al content in the third group has been fixed at 9.0% and is made using a mixture of high purity and commercial purity

magnesium metals in different proportions. Mg-Zn and Mg-Ca alloys with different impurity levels are also used to confirm the occurrence of native grain refinement particularly in Mg-Al alloys. To avoid the uptake of iron and carbon that often accompanies the use of a mild steel crucible, the melting of raw materials has been conducted in aluminium-titanite (Al_2TiO_5) crucibles at 730ºC. Grain size measurements have been carried out on the central regions of the conical samples that have been taken from the top of the melt using a BN-coated ladle with the dimensions of Ø 20 mm x Ø 30 mm x 25 mm.

Table.2.7 Chemical composition of magnesium metals from two sources (wt%) [191].

Purity	Fe	Mn	Ni	Si	Zn	Al	Mg
Hydro Mg (CP)	0.01	0.016	<0.001	0.01	<0.005	0.01	Bal.
Timminco Mg (HP)	<0.001	<0.002	<0.001	<0.01	0.008	<0.005	Bal.

CP- Commercial Purity HP- High Purity

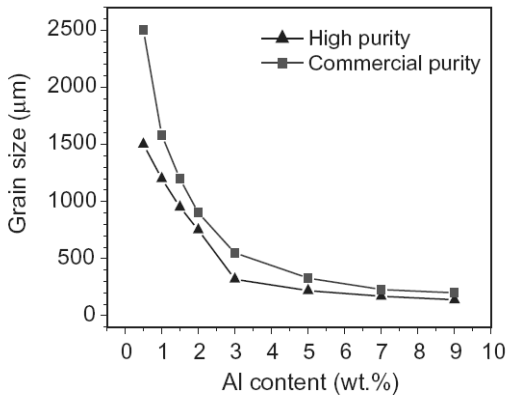

Figure 2.22: Effect of purity on the grain refinement of Mg-Al alloys [191].

It has been found that Mg-Al alloys with the same basic composition, but made of different sources of magnesium metal, showed an obvious difference in grain size, which is represented in figure 2.22. High purity alloys have consistently proved a finer grain size than commercial purity alloys in all cases across the composition range 0.5-9%Al. In figures 2.23 and 2.24, microstructural observations show native grain refinement in Mg-9%Al and Mg-0.5%Al samples, respectively. Results that have been obtained from the Mg-9%Al samples prepared using a mixture of high purity and commercial purity

magnesium metals at different proportions are shown in figure 2.25. With the increasing proportion of commercial purity magnesium metal, a gradual increase in grain size has been observed that is in agreement with a work on Mg-3%Al alloy [191]. The observations made for Mg-Al alloys, both high purity Mg-Zn alloys and high purity Mg-Ca alloys show a coarser grain size than do their commercial purity counterparts, particularly when the Zn or Ca content is low, or in other words these results indicate that native grain refinement occurs only in Mg-Al type alloys.

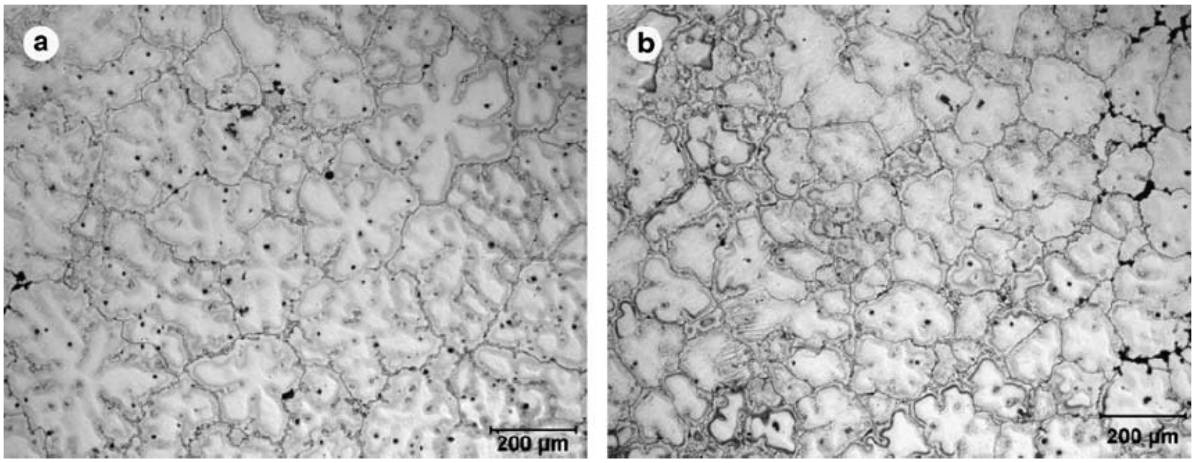

Figure 2.23: Microstructures showing grain size of Mg-9%Al alloy made of (a) commercial purity magnesium and (b) high purity magnesium metal [191].

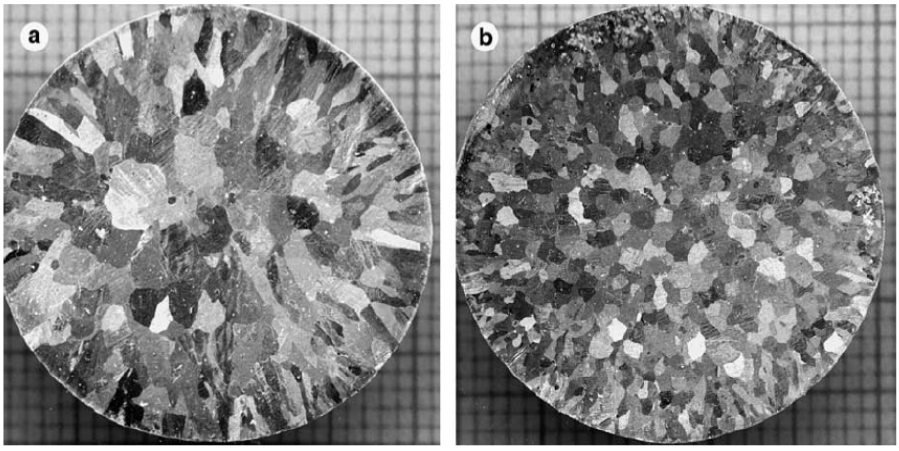

Figure 2.24: Microstructures showing grain size of Mg-0.5%Al sample made of (a) commercial purity magnesium metal and (b) high purity magnesium metal [191].

Although there is a belief in the existence of particles comprising Al, C and O in the centre of many magnesium grains, through calculation of the activity of Al_2OC, it is suggested that the formation of Al_2OC phase is thermodynamically less favourable than the formation of Al_4C_3 phase [192]. The presence of oxygen is very likely due to contamination caused during sample polishing, and the nucleant particles observed are more likely to be Al_4C_3.

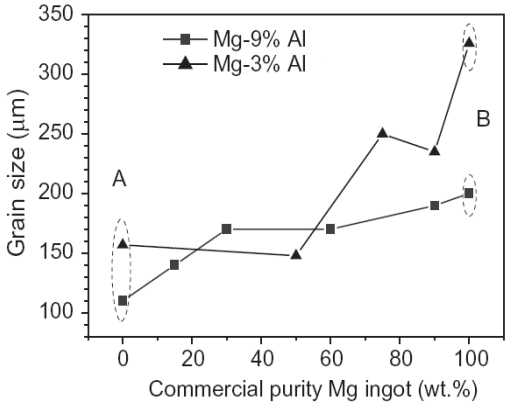

Figure 2.25: Dependence of grain size on impurity level in Mg-9%Al and Mg-3%Al alloys. Composition 'A' corresponds to 100% high purity, whereas composition 'B' corresponds to 100% commercial purity [191].

Based on the fact that native grain refinement is a unique characteristic feature of Mg-Al alloys, it is hypothesized that Al_4C_3 particles act as nucleation centres that are responsible for native grain refinement. In the commercially available Mg-Al type alloys, the presence of Fe or Mn degrades the potency of Al_4C_3 by forming Al-C-Fe or Al-C-Mn ternary particles, which are considered less potent than Al_4C_3.

2.11.2.3 ELFINAL PROCESS

The Elfinal process has been invented by the metallurgists of a pioneering German magnesium company based on the hypothesis that iron particles can act as nucleation sites for magnesium grains. It has been reported that Mg-Al-Zn alloys (Al: 4 to 8.5 pct; Zn: 0.5 to 3 pct; no other elements have been mentioned) can be grain-refined by the addition of 0.4 to 1.0 pct of anhydrous $FeCl_3$ at a temperature range of 740ºC to 780 ºC [193]. Though the approach has worked satisfactorily in terms of grain

refinement, the inventors have failed to convince other metallurgists about the mechanism behind it. Different mechanisms have been proposed subsequently. It has been suggested that Fe- containing intermetallic particles or aluminium carbide (Al_4C_3) particles are possibly the nucleants. According to Emley, [189] hydrolysis of $FeCl_3$ in the magnesium melt gives rise to copious hydrogen chloride (HCl) fumes, which then attack steel crucibles to liberate some carbon into the melt. The other major hypothesis proposed is that Mg grains nucleate on Fe-Mn-Al particles. A detailed examination of this process has been performed [194] to clarify a number of key issues: (i) whether Fe is a grain refiner or an inhibitor for Mg-Al alloys; (ii) whether iron only grain-refines Mg-Al alloys that contain Mn; and (iii) the mechanism by which the Elfinal process works.

For the work stated above, sublime high-purity magnesium ingots (99.98%) and commercial high-purity aluminium ingots (99.999%) have been used to prepare high-purity Mg-3%Al and Mg-9%Al alloys. Melting has been conducted in an electrical resistance furnace under a protective cover gas of 1.0%SF_6 in 49% dry air and 50% CO_2. Aluminium titanite crucibles have been used for the reason that they are free of carbon. Anhydrous $FeCl_3$ has been plunged into the melt at 750ºC. Cone samples have been taken from the top of the melt using a boron nitride-coated cone ladle (Ø 20mm x Ø 30mm x 25 mm), 10 min following the addition of $FeCl_3$. No stirring has been applied in each test. The average grain size of each cone sample has been measured from the central region of a longitudinal section of the cone cut through the axis.

Figures 2.26(a) and (b) show the results obtained from the grain refining tests of Mg-3%Al and Mg-9%Al alloys, respectively, conducted at 750ºC. The results show that with an increase in the amount of $FeCl_3$ addition, the grain size decreases. Figures 2.27(a) and (b) show the typical views of the grain structures of samples taken prior to and after 1% of $FeCl_3$ addition at 1023K to Mg-3%Al alloy, respectively, and figures. 2.28(a) and (b) show that of Mg-9%Al alloy samples taken prior to and after 2% of $FeCl_3$ addition, respectively. From the results, it is clear that when introduced in the form of anhydrous $FeCl_3$, the addition of iron results in obvious grain refinement of both Mg-3%Al and Mg-9%Al alloys. It is also clear that iron can readily grain refine high-purity

Mg-Al alloys that contain little Mn (<10 ppm). An effective nucleant particle is always expected in the central regions of grains as its identification is commonly based on the assumption that, after nucleation on any particle existing in the melt, latent heat release will decrease the likelihood of nucleation on neighbouring particles, which will subsequently be pushed to grain boundaries or into the interdendritic spaces. Detailed microscopic examination made on grain refined samples using an SEM in the backscattered electron (BSE) imaging mode has also revealed the presence of tiny particles in the magnesium grains of each sample examined.

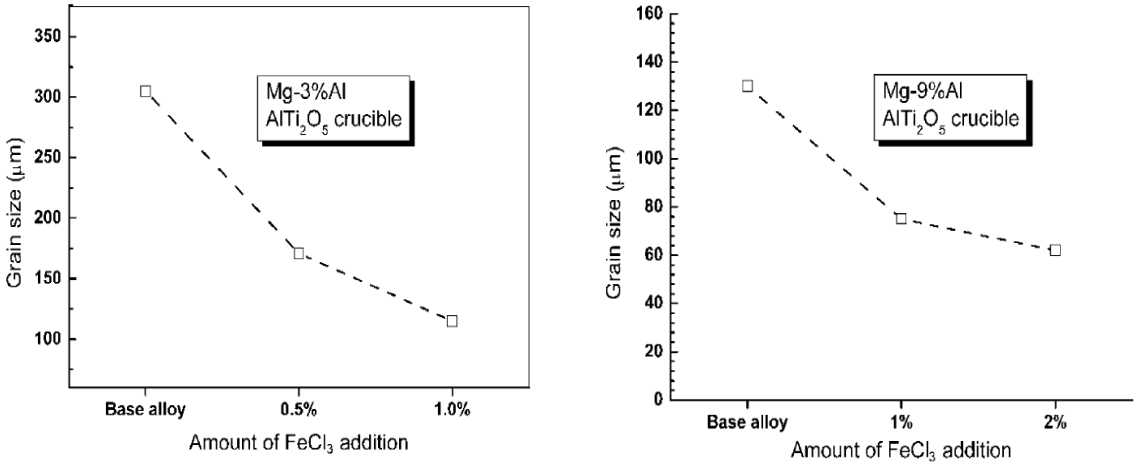

Figure 2.26: Grain refinement of (a) Mg-3%Al alloy and (b) Mg-9%Al alloy, by addition of $FeCl_3$ at 750ºC [194].

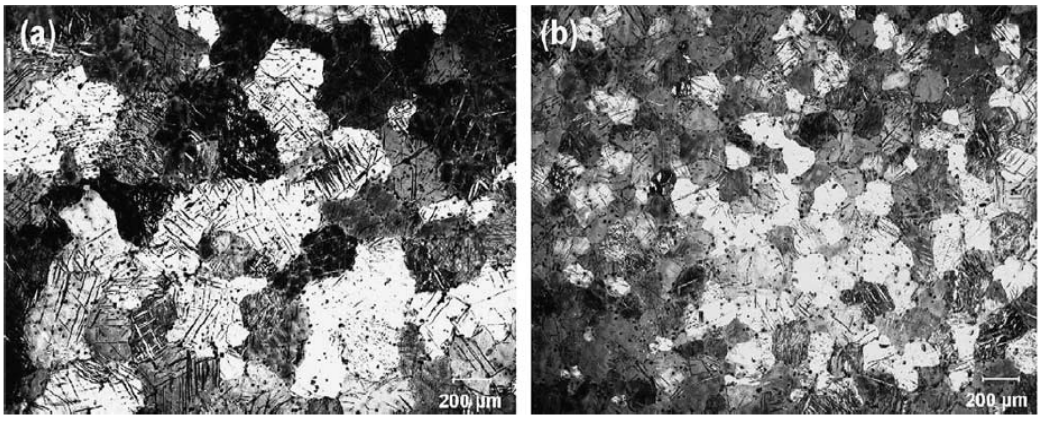

Figure 2.27: Grain refinement of Mg-3%Al by $FeCl_3$ at 650ºC (a) base alloy (b) **1% $FeCl_3$ addition and 10 min holding at 750ºC** [121].

`

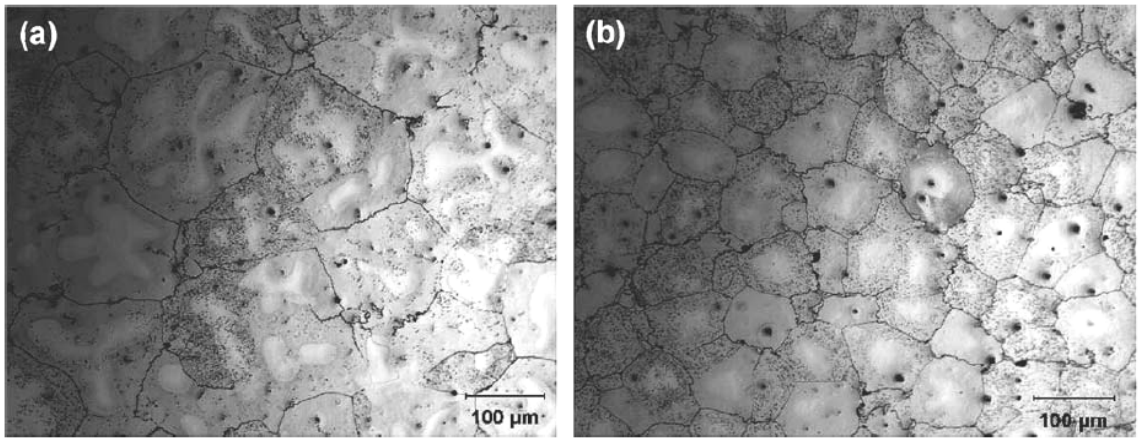

Figure 2.28: Grain refinement of Mg-9%Al by $FeCl_3$ at 750ºC (a) base alloy (b) after 2% of $FeCl_3$ addition and 10 min holding [194].

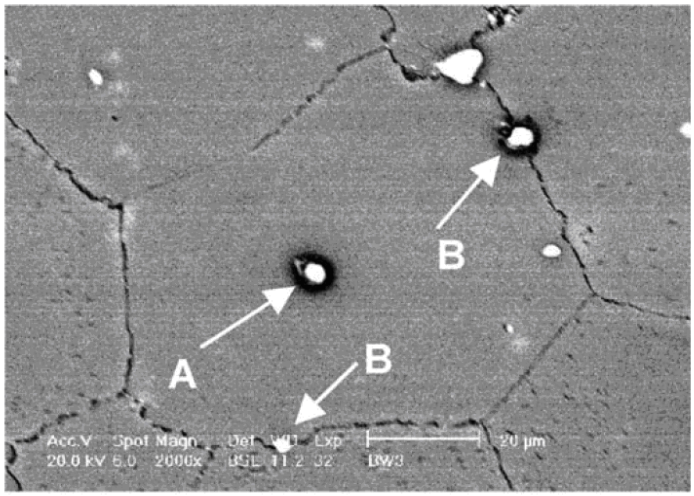

Figure 2.29: Intermetallic particles observed in Mg-9%Al sample solution treated with 2% of $FeCl_3$ addition at 750ºC [194].

Figure 2.29 shows an example of the Fe- and Al- rich intermetallic particles observed in a Mg-9%Al sample that has been treated with 2% of $FeCl_3$ addition at 750ºC. EDX analyses of these particles show that these are Fe and Al-rich intermetallic particles. Weak signals of O and C are also detected that are probably due to contamination during sample preparation. It has also been observed that not all of the Fe- and Al- rich particles observed are present in the central regions of grains (arrow A) and that some are found at the grain boundaries (arrow B). This is similar to observations made from the grain refinement of other alloys [195]. The above work conducted in carbon-free aluminium titanite crucibles clearly shows that the Elfinal process has little to do with the Al_4C_3 hypothesis.

2.11.2.4. OTHER ADDITIVES

For grain refinement of Mg-Al alloys, apart from the use of carbon or carbonaceous substances and $FeCl_3$, many other additives have also been tried, which include Sr, RE, Th, Si, Ca, B, AlN, MgO, TiB_2 and TiC [181-182, 196]. It has been reported that of the abovementioned additives, Sr is found to be effective only for pure magnesium or for low aluminium content magnesium alloys. Other additives have reportedly led to grain refinement of Mg-Al alloys, but none has yet been made available commercially. It has also been claimed that the use of microcrystalline TiB_2 and TiC particles of particle size 0.5 to 30μm gives rise to grain refinement of Mg-Al alloys, but no experimental details have been disclosed yet [181].

2.11.2.5 CARBON INOCULATION

Carbon inoculation is another major and effective grain-refining approach developed to date for Mg-Al based alloys. The key step of this process is the introduction of carbon into the molten magnesium. Or, in other words, the major challenge is how to consistently introduce carbon into molten magnesium while on the other hand having no excess carbon left in the melt from a corrosion point of view [159]. However, carbon inoculation offers many practical advantages such as low operating temperature and less fading with long holding times for applications in mass production [197]. Reported

methods of introducing carbon include graphite, paraffin wax, lamp-black, organic compounds such as hexachloroethane (C_2Cl_6) and hexachlorobenzene (C_6Cl_6), carbides such as Al_4C_3, SiC, CaC_2 and bubbling the melt with carbonaceous gases such as CO, CO_2 and CH_4. Even though calcium carbide and hexachloroethane appear to work more satisfactorily than the other means, the use of hexachloroethane causes environmental problems. The elements Be, Zr, Ti and RE are found to interfere with this process [189].

It is often called carbon inoculation as it is suggested [175-176, 189] that carbon reacts with aluminium in the melt to form a large number of fine Al_4C_3 particles dispersed in the melt, which in turn act as the nucleating substrates for primary Mg crystals. Though a number of hypothesis have been proposed to explain the mechanism by which carbon addition causes grain refinement in aluminium-bearing magnesium alloys, it is quite reasonable to suggest that Al_4C_3 hypothesis is an effective mechanism. Grain refinement achieved by carbon inoculation is in general comparable to that achieved by superheating [72]. It has long been recognized that carbon inoculation is effective only with magnesium alloys that contain aluminium. Mg-Al type alloys that can be effectively grain-refined by carbon inoculation normally contain more than 2%Al. This dependence on aluminium content provides a strong support to the Al_4C_3 hypothesis [198]. As such, there is a general consensus about the mechanism of carbon inoculation, that is, Al_4C_3 particles are effective nucleants for magnesium grains. This is further supported by a recent study [199] that shows the experimental results using Al_4C_3 as a potential grain refiner for Mg-Al alloys and the mechanism involved.

For this study, Mg-3%Al alloy has been selected as a base alloy and prepared from sublime high-purity magnesium (99.98%) and high-purity aluminium (99.97%) ingots in an electrical resistance furnace under a protective cover gas (AM-cover). Aluminium titanate ($AlTi_2O_5$) crucibles have been used to avoid introducing C and Fe into the melts through the crucible. Table 2.8 summarizes the relevant properties of the synthetic Al_4C_3 powder used in the study. Seven grams of freshly ground Al_4C_3 powder, corresponding to 1 wt.% of the melt, has been wrapped in an aluminium foil and plunged into the melts at about 735ºC and 785 ºC, which is about 100 and 200ºC above the

liquidus of the base alloy. The melts have been stirred using Ø 20 mm aluminium titanite rod after each addition and periodically during holding. It has been found that the powder is well wetted by the melt. Samples have been made just before addition and 10, 20 and 30 min after addition from the centre of the melt using a BN-coated ladle of Ø 38 x Ø 20 mm x 40 mm, and have been submerged into the melt for 5 secs before being withdrawn from the melt.

Both samples, as seen from the microstructure (Figure 2.30), clearly display a similar equiaxed dendritic structure. In addition to the rosette-like primary Mg, the β phase is found distributed in the interdendritic region because of non-equilibrium solidification. It can be observed from the figure that the decreased grain size is observed after the addition of Al_4C_3. As the addition of Al_4C_3 is the only process performed, it is believed that Al_4C_3 is responsible for the grain-refining effect observed in figure 2.30 (b)

Table 2.8: **Relevant properties of Mg and Al_4C_3 powder** [199]

Potential catalyst	Density [g/cm^3]	Thermo-chemical property	Pearson symbol	Space group	Prototype	Crystal system	Lattice parameters			Planar disregistry [%]
							a [Å]	c [Å]	γ [°]	
Mg	1.738		hP2	$P6_3/mmc$	Mg	H	3.2088	5.2099	120	
Al_4C_3	2.972	Decomp. at about 2475 K	hR7	R-3m	Al_4C_3	R(unimolecular)	8.552	–	22.51	
						H(trimolecular)	3.3388	24.996	120	4.05

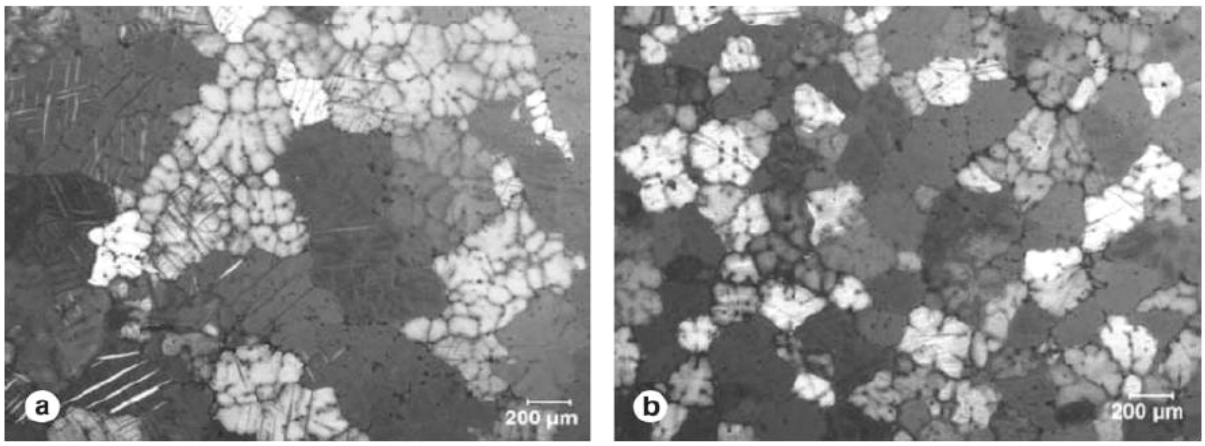

Figure 2.30: Grain refinement efficiency of ground Al_4C_3 in Mg-3%Al at 735ºC (a) base alloy and (b) 20 min after addition of Al_4C_3 [199].

The microstructure of a casting can be refined by increasing the number of potent nuclei in the melt and the thermal and constitutional undercooling at the advancement of S/L interface [200-201]. From Table 2.8, it is clear that Al_4C_3 is thermally stable up to a temperature of about 2200ºC, and hence the addition of Al_4C_3 will not introduce any solute into the melt to facilitate a strong constitutional undercooling required for the grain-refining effect observed in Figure 2.30. Therefore, it is reasonable to suggest that Al_4C_3 itself is a potent nucleating substrate for primary Mg and that the addition of Al_4C_3 into the melt is expected to increase the nucleation frequency, which leads to a refined microstructure.

Comparison of the microstructure of a sample treated by Al_4C_3 at 750ºC with the base alloy is shown in Figure 2.31. Many partially or fully opened pores are observed in the primary Mg grains in Figure 2.31 b, which are not found in the base alloy in Figure 2.31 a. These pores are likely to be left by Al_4C_3 particles, which are extremely hydroscopic.

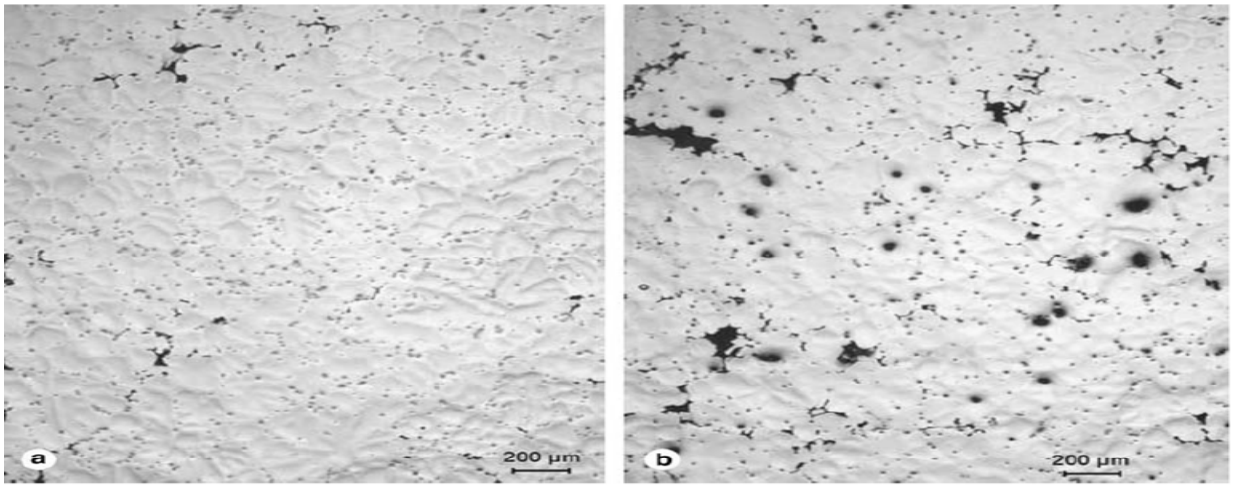

Figure 2.31: Micrographs of unetched samples from the melts held at 735ºC (a) without and (b) with Al_4C_3 addition [199].

Hence, the Al_4C_3 particles cannot survive through the sample preparation procedure and react with water, leaving behind many partially or fully opened pores. In figure 2.31b, although most of the pores are empty, partially reacted particles are found in

the centre of some pores, which shows that a chemical reaction has taken place. This is further evidenced in the high magnification SEM images.

Figure 2.32 represents a typical SEM secondary electron image of the sample treated with Al_4C_3 at 735ºC, revealing a partially reacted particle with a diameter of about 3μm. Figures 2.32 (a) and (b) are the two EDS spectra obtained from this particle and from the matrix surrounding it, respectively. This particle contains higher C, O and Al concentrations compared with the matrix, and the Mg peak in Figure 2.32 (a) is believed to be contributed by the matrix. This partially reacted particle mainly consists of Al, C and O, and it is suggested that it is thermodynamically impossible to form Al-C-O compounds in the melt. Hence, it is believed that these particles are originally Al_4C_3 particles and that the oxygen is introduced during the sample preparation as per the reaction in the section 2.11.2.1. Similar particles are often observed in the primary Mg grains. Detailed optical and SEM observations further support the suggestion that Al_4C_3 is a potential substrate for nucleating primary Mg crystals.

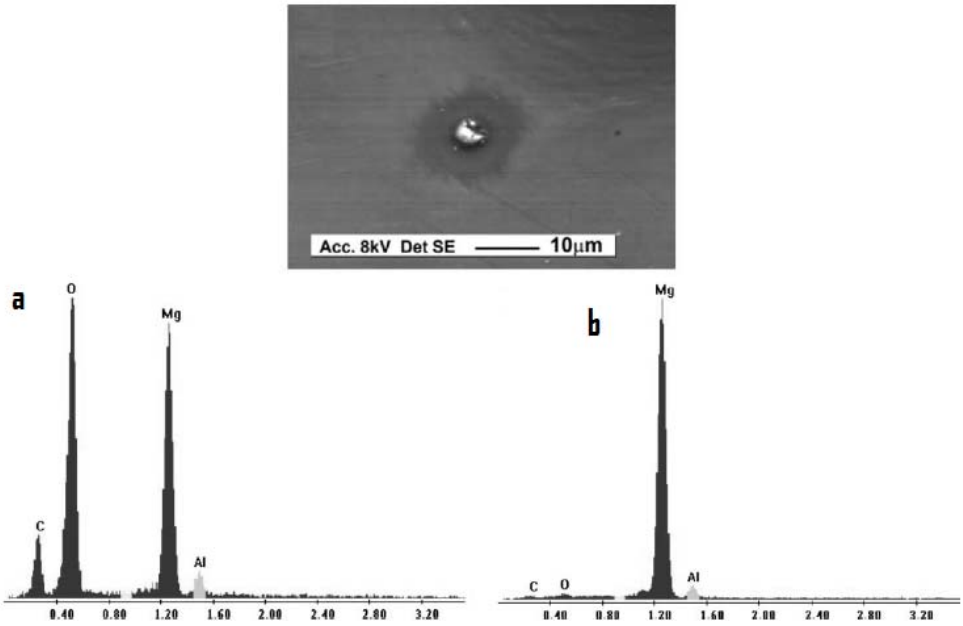

Figure 2.32: **SEM and EDS spectra of sample treated with Al_4C_3 at 735ºC (a) particle and (b) matrix** [199].

For aluminium alloys, various compositions of ternary Al-Ti-B and binary Al-Ti master alloys with different composition of elements have been developed by a number of investigators. However, for magnesium alloys, no such master alloys for commercial products in the foundry industries have been developed. The aim is to develop a new master alloy from Al-SiC composites to form an Mg-1%Al_4C_3 master alloy and the literature are shown in the following sections.

Carbon inoculation is one of the most powerful systems highly suitable for Mg-Al alloys. However, the major problem in the casting method is "How to introduce aluminium carbide (Al_4C_3) particles into the magnesium melt?" The Al_4C_3 reaction in the melt creates a lot of complications such as reaction between aluminium and carbon, distribution and melts loss. The major drawback associated in the fabrication of aluminium composites is the formation of aluminium carbide during the melting process with this drawback in aluminium composites in the formation of Al_4C_3 is transformed into an advantageous process of magnesium alloys for grain refinement.

2.12 Al-SiC COMPOSITES

In Al-SiC composites, a direct reaction between Al and SiC can occur during the fabrication stage forming Al_4C_3 and Si according to the reaction [202-209]

$$4Al + 3SiC \rightarrow Al_4C_3 + 3Si \quad (1)$$

This reaction is well known to have undesirable effects on the overall Al - SiC composite properties such as (i) Degradation of mechanical properties due to the formation of Al_4C_3, (ii) Reduction in corrosion resistance in water, methanol, HCl, etc., because of the unstable nature of the reaction product, Al_4C_3, in such environments, [210-212] and (iii) Changing the matrix alloy composition by Si released during interfacial reaction. As a result, composite interface plays an important role in determining the resultant composite properties. Most studies carried out to identify the structures and morphologies of the interfacial reaction products of composites have used transmission electron microscopy (TEM), although the same goals can be achieved by X-ray diffraction (XRD) crystallography and scanning electron microscopy (SEM). It has been clearly stated in the reports [213-217] that the interfacial reaction products such as Al_4C_3

and free Si are formed during composites fabrication. Therefore, the separation of interfacial from the composites to make magnesium-based Al_4C_3 master alloy is important.

2.12.1 THEORETICAL ASPECTS OF SEPARATION

MMCs consist of a matrix metal and reinforcement, which have their own crystal structure and interfaces between them. The entropy of mixing in the fabrication of MMCs does not change much because MMCs are not mixtures at the atomic level. This indicates that there should be a way to separate reinforcements from the matrix [218-224].

During the fabrication of MMCs, the minimum work, W, required is given by

$$W = (\gamma_{rm} - \gamma_{ra})\, dA \qquad [1]$$

where γ_{rm} is the interface energy between reinforcement and matrix metal, γ_{ra} is the surface energy of the reinforcement surrounded by air before the fabrication of the MMCs, and dA is the total interface area between the matrix metal and reinforcement of a unit weight of MMCs (Figure 2.33 (a)). When ceramic fibres or particles are used as the reinforcement, γ_{rm} is much larger than γ_{ra}, because the contact angle between the molten matrix metal and the reinforcement is larger than 90^o. Hence, when some stimulus is given to the interface, the separation of the reinforcement might occur because the interface has a driving force. However, the separation occurs spontaneously only when the interface free energy (ΔG_1) is negative.

$$\Delta G_1 = \gamma_{ra}\, dA_1 + \gamma_{ma}\, dA_2 - \gamma_{rm}\, dA \qquad [2]$$

where γ_{ma} is the surface energy of the matrix surrounded by air during fabrication of the composite and dA_1 and dA_2 are surface area of reinforcement and matrix metal at the interface, respectively, after separation (Figure 2.33 (b)). For metal – ceramic system, ΔG_1 is always positive, because the driving force available according to the equation 1 is compensated by the energy required to create two new surfaces. Hence, the separation of reinforcements from composite does not occur spontaneously.

To separate the matrix alloy and reinforcement, it is important to find a material that makes an interface having smaller interface energy than the matrix metal, when the material contacts the reinforcement. The salt fluxes are found to be candidate material for the separation process. When it comes into contact with the interface between the reinforcement and matrix metal at the molten state (Figure 2.34 (a)), it infiltrates into the interface instead of the matrix metal as shown in Figure 2.34 (b). The interface-free energy of this case is given by

$$\Delta G_2 = \gamma_{rf}\, dA_3 + \gamma_{mf}\, dA_4 - \gamma_{rm}\, dA \qquad [3]$$

where γ_{rf} is the interface energy between the reinforcement and the flux, γ_{mf} is the interface energy between the metal and the flux, dA_3 is the total interface area between reinforcement and flux, and dA_4 is the total interface area between the matrix and flux. Assuming $dA = dA_3 = dA_4$, as the difference between these three interface areas is very small,

$$\Delta G_3 = (\gamma_{rf} + \gamma_{mf} - \gamma_{rm})\, dA \qquad [4]$$

When ΔG_3 is less than zero and the salt fluxes have only little solubility in the matrix metal, separation of the matrix metal and the reinforcement from composite is spontaneous.

When the contact angle between the two materials is rather low, it is possible to estimate the interface energy by Girifalco and Good's equation [225]

$$\gamma_{rf} = \gamma_{ra} + \gamma_f - 2\phi\, (\gamma_{ra}.\gamma_f)^{1/2} \qquad [5]$$

where γ_f is the surface tension of molten salt flux and ϕ is a constant that is determined by the characteristics of the system.

When the interfacial tension changes because of the adsorption of surface active elements, Girifalco and Good's equation [226] in conjunction with expressions for the surface coverage of surface active species can be used to estimate the interfacial tension. In this present work, interfacial tension between molten aluminium and various salt flux systems has been taken from the plot showing the variation of interfacial tension between aluminium and equimolar NaCl – KCl as a function of NaF addition (Roy and Utigard 1998 [227]). Based on the salt flux separation of interfacial from composites, the fine treated Al_4C_3 is introduced into the magnesium melt and converts the Mg-1% Al_4C_3 master alloy.

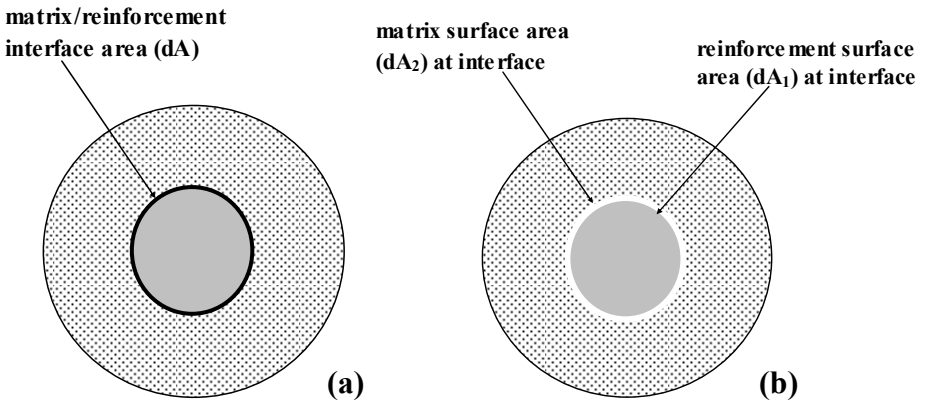

Figure 2.33: Surface area at the interface prior to flux addition (a) Before separation (b) After separation

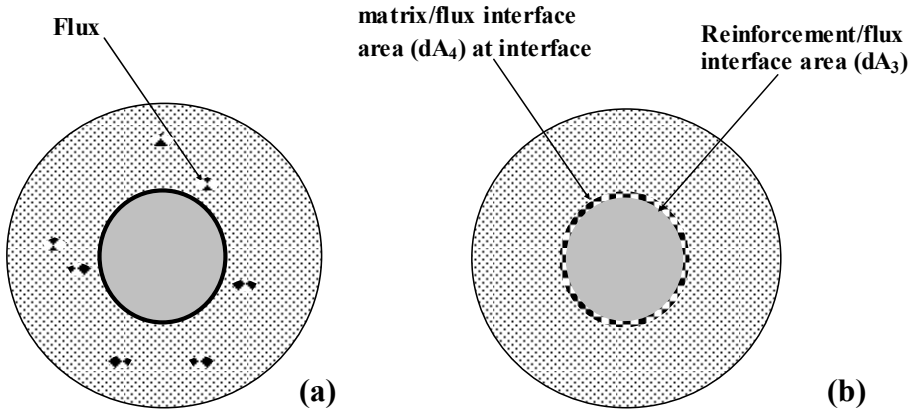

Figure 2.34: Surface area at the interface after flux addition (a) Before separation (b) After separation [229]

2.13 SHORTCOMINGS IN THE Mg DEVELOPMENT

The importance of magnesium alloys is extensively reported in literature. It is well understood from literature that the poor creep resistance of Mg-Al alloys is attributed to the presence of $Mg_{17}Al_{12}$ precipitates at the grain boundaries. By the systematic reduction in the volume or by the removal of $Mg_{17}Al_{12}$ precipitates, the elevated temperature behaviour of Mg-Al-Zn alloys can be improved. Recent studies are focused on designing the microstructures of Mg-Al alloys that do not contain $Mg_{17}Al_{12}$ precipitates so as to improve the high temperature properties. ZA84 alloy is one such system that has 8%Zn in it (Mg-8Zn-4Al-0.2Mn, all are in wt %) and shows superior creep resistance compared with AZ and AM series alloys.

These alloys are highly suitable for die-casting industries. However, there are certain large and heavy components, made up of this alloy by sand castings, that show lower mechanical properties because of coarse microstructure. Moreover, further improvement in its high temperature behaviour through microstructural modification is also an essential task to make this alloy suitable for the replacement of high strength aluminium alloys used in the automobile industry. Grain refinement is an effective way to improve the tensile behaviour of engineering alloys. In fact, grain refinement of Mg-Al based alloys is well documented in the literature. However, there is no grain refiner commercially available in the market for Mg-Al alloys. Furthermore, it is also reported in the literature that the microstructure of AZ91 alloy is modified through the minor elemental additions such as Sb, Si, Sr, Ca, etc, which enhance its high temperature properties because of the formation of new stable intermetallics. The same strategy can be used with the ZA84 alloy system to improve its high temperature properties further without sacrificing the ductility of the alloy. The grain refiner master alloy has been developed for common use in Mg-Al alloys and the ***Structure-Property*** relations for alloying additions and grain refinement are extensive detailed in this investigation.

2.14 THEME OF THE THESIS

MAGNESIUM ALLOYS have strong potential for weight reduction in a wide range of technical applications because of its low density compared to other structural materials. Therefore, an extensive growth of magnesium alloys usage in automobile sector is expected for in coming years to enhance the fuel efficiency through mass reduction. The drawback associated with use of commercially cheaper Mg-Al based alloys, such as AZ91, AM60 and AM50 is its easy creep deformation above 100ºC, which is due to the presence of discontinuous $Mg_{17}A1_{12}$ phases at the grain boundaries. Rare earth based magnesium alloys show better mechanical properties but it is not economically viable to use these alloys in auto industries. Recently many new Mg-Al based alloy systems are developed for high temperature applications, which does not contain $Mg_{17}Al_{12}$ phase. It has been proved that the addition of high percentage of zinc (depends upon the percentage of Al) to binary Mg-Al alloys also ensures the complete removal of $Mg_{17}Al_{12}$ phase and hence exhibits superior high temperature properties.

ZA84 alloy is one such system shows superior creep resistance compared to AZ and AM series alloys. These alloys are normally used in die-casting industries. Besides, there are certain large and heavy components, made up of this alloy by sand castings that show lower mechanical properties because of coarse microstructure. In addition, further enhancing the high temperature behaviour through microstructural modification is also an essential task to make this alloy suitable for several applications. Grain refinement is an effective way to improve the tensile behaviour of engineering alloys. In fact, grain refinement of Mg-Al based alloys is well documented in the literature. However, there is no grain refiner commercially available in the market for Mg-Al alloys. It is also reported in the literature that the microstructure of AZ91 alloy is modified through the minor elemental additions such as Sb, Si, Sr, Ca etc, which enhance its high temperature properties because of the formation of new stable intermetallics. The same strategy can be used with the ZA84 alloy system to improve its high temperature properties further without sacrificing the ductility of the alloy.

Therefore, the primary objective of the present research work "**Studies on grain refinement and alloying additions on the microstructure and mechanical properties of Mg-8Zn-4Al alloy**" is twofold:

1. To investigate the role of individual and combined additions of Sb and Ca on the microstructure and mechanical properties of ZA84 alloy.

2. To synthesis a novel Mg-1wt%Al_4C_3 master alloy for grain refinement of ZA84 alloy and investigate its effects on mechanical properties.

3.1 MATERIALS

3.1.1 METALS AND MASTER ALLOYS

The alloys were prepared in the present laboratory by melting the following metals together:

1. Pure magnesium ingots (purity >99.988)
2. Pure aluminium ingots (purity >99.98)
3. Pure zinc granules (purity >99.99)
4. Al-10Sb master alloy
5. Al-10Ca master alloy
6. Pure calcium granules
7. Pure antimony metal
8. Al-10Mn master alloy
9. Mg-1wt%Al_4C_3 master alloy

The required amount of alloying elements such as Sb, Ca and Al_4C_3 were added in the form of master alloys. Some pure elements such as Sb and Ca were added in the alloys when wt. pct. of alloys was greater than 0.5%. The chemical composition (as analyzed by an Optical Emission Spectrometry) of the experimental alloys used in the present work is summarized in Table 3.1.

3.1.2 CLEANING OF MATERIALS

To remove the oxides attached to the wall and at the bottom of the crucible from the previous melting, the crucible was filled with water and kept for one day for the oxides to get mixed with water. Then, it was cleaned with an MS wire brush. All the steel tools used for melting and pouring purposes such as skimmer, starrier, etc., and the metal ingots were cleaned by a metal wire brush. The metal ingots were then cleaned with acetone. All the tools and metal ingots were preheated before use. The properly

cleaned mould was given a graphite coat and preheated to 250^{o}C in a heating oven for 1 hr just before the pouring.

3.1.3 FLUX

Fluxes are composed to maintain a minimum difference in density of 0.15-0.20 g/cm^3 compared to that of the metal. Single flux was used for both the covering and refining of molten metal during melting. **MAGREX-60** supplied by ***Foseco*** industries was used for the melting. The flux mainly consists of $MgCl_2$, $CaCl_2$, NaCl, MgO, CaF_2, etc. Fine sulphur powder was used for dusting around the melt to remove the oxygen and hence avoid the oxidization of molten metal during pouring.

3.1.4 MOULD

The rectangular cast iron mould having cavity dimensions 240mmx220mmx40mm is shown in Figure 3.1, which was specially designed for bottom pouring in order to avoid the blocking of air and porosity in the casting during the pouring of liquid metal.

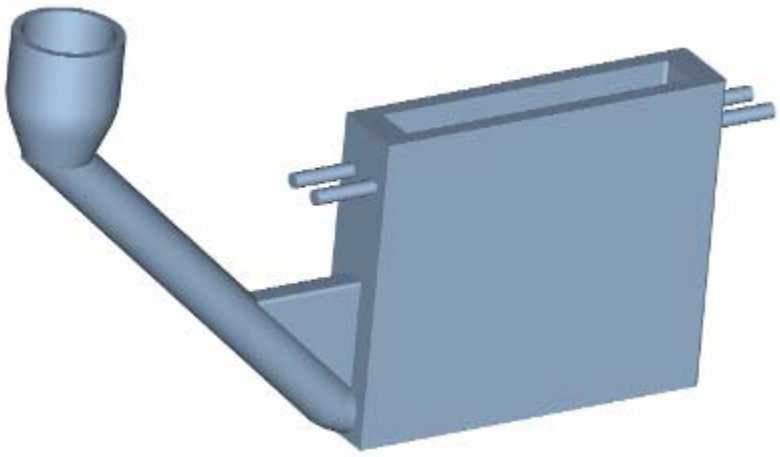

Figure 3.1: Schematic diagram of rectangular mould

3.1.5 CRUCIBLE

A cylindrical steel crucible of dimensions 225 mm diameter and 300 mm length of capacity around 12-15 kg of liquid metal was used. Around 75% of liquid metal was poured into mould and cast this cast was used for material characterization. The remaining 25% of metal was poured with into other mould, which has scrap because of the flux settling at the bottom of the crucible.

3.1.6 MELTING

The melting arrangement for magnesium alloys is presented in Figure 3.2. A resistance box furnace was used for melting. The preheated flux was sprinkled in the bottom and at the side of the cleaned crucible and kept inside the furnace. After the crucible reached the red hot condition (750^0C), the preheated ingots were charged into the crucible. Initially part of the total magnesium ingots were charged. After melting of charged ingots was completed, the remaining ingots were then immersed into the molten metal. This kind of charging practice of metal ingots avoids the excessive oxidation during melting. The crucible was covered with a furnace lid to minimize the air contact with the molten metal. Flux was sprinkled over the metal throughout the melting. Before the addition of alloying elements, the top layer of oxides was completely removed and a fresh layer of flux was applied. The required amount of master alloys were weighed and wrapped in aluminium foil and slowly immersed into the melt. After the additions, the melt was gently stirred for dissolution of the added elements. Again, the top oxide layer was removed and a fresh layer of flux was applied. The melt was held for 10 min to ensure the complete dissolution of elements into the melt.

3.1.7 REFINING

After the complete melting of the metals in the crucible, the refining of melt was carried out at a temperature of $\approx 720^o$C. Initially, the top layer (oxide layer) of the melt

was removed and the melt was rigorously stirred for 2-3 min. Flux was applied during stirring. This stirring helps to mix the added flux with the melt uniformly. After thorough mixing, the top surface of molten melt was removed and a fresh layer of flux was applied. The melt was then held for 10-15 min without disturbance, which enabled the added flux to react with oxide inclusions present in the melt, become heavier and settle down at the bottom of the crucible.

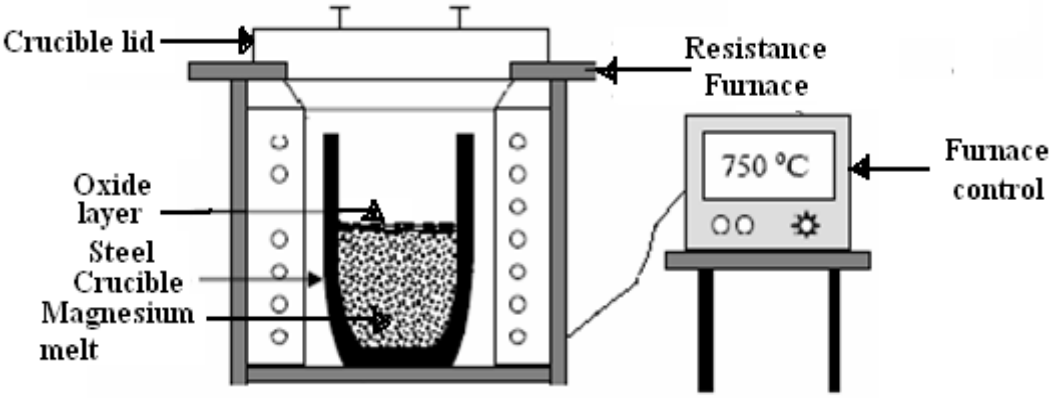

Figure 3.2: Schematic diagram showing the melting arrangement for magnesium

3.1.8 POURING AND CASTING

After the refining and settling process was over, the molten metal was poured into the preheated moulds. During the pouring, much care was taken to avoid the breakage of the top flux protective layer. The pouring was carried out gently without any jerk in the melt, as excessive jerk disturbs the settled oxide inclusions at the bottom. The flux layer near the lip of the crucible was pulled back gently by using a skimmer for the smooth flow of molten metal. Sulphur powder dusting was carried out to remove the oxygen around the melt jet. Three-fourths of the melt in the crucible was poured into the preheated mould. The remaining metal was poured separately as a scrap. Figure 3.3 shows a photograph of one such casting. Figure 3.4 shows a schematic diagram of casting, indicating the locations from where samples for different testing were taken.

3.1.9 ALLOY PREPARATION

The alloys used for this study were prepared using the abovementioned procedure and are presented in figure 3.5. To find out the chemical composition of the castings, chemical analysis was carried out using an inductively coupled plasma spectrometer (ICP Plasmascan, Model LABTAM 8410). The chemical compositions of the prepared alloys are given in Table 3.1.

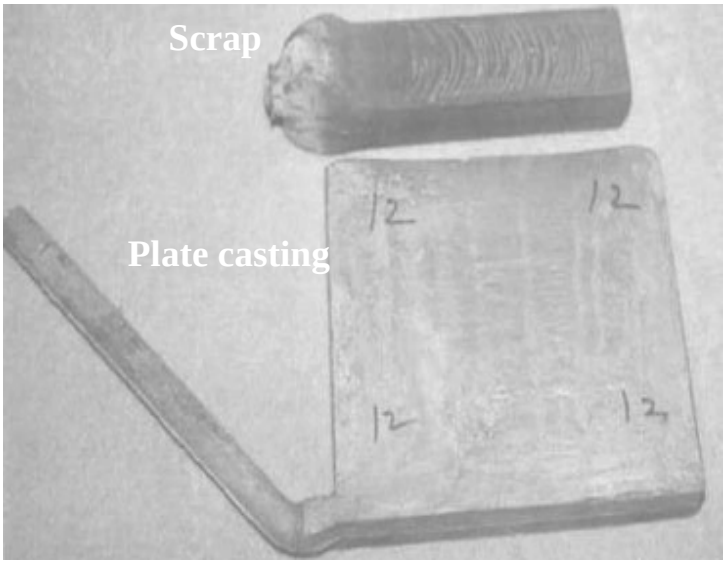

Figure 3.3: Photograph of the magnesium alloy castings

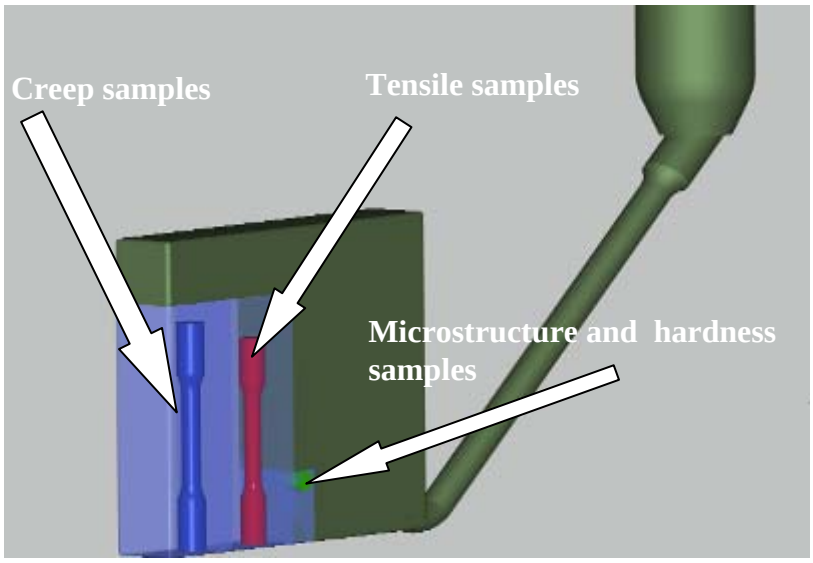

Figure 3.4: Schematic diagram showing the magnesium alloy casting and sample locations

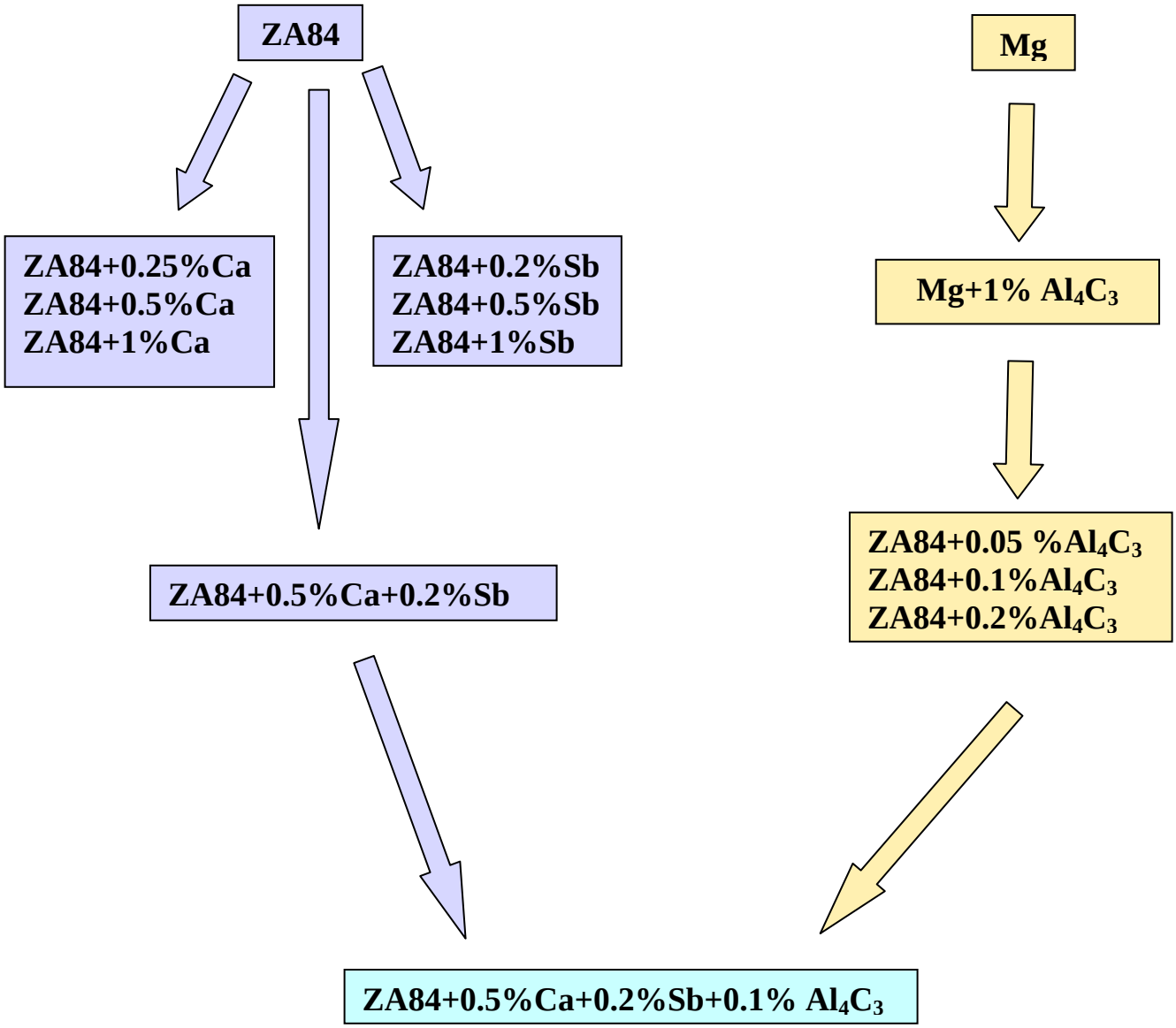

Figure 3.5: Flow chart for alloys prepared

Table 3.1 Chemical compositions (wt%) of the experimental alloys and their code

Alloy Code	Designed Composition (wt%)					Analyzed Composition (wt%)				
	Zn	Al	Sb	Ca	Al_4C_3	Zn	Al	Sb	Ca	Al_4C_3
Z1	8	4	0	0	0	7.71	3.68	0	0	0
Z2	8	4	0.2	0	0	7.49	4.15	0.18	0	0
Z3	8	4	0.5	0	0	8.21	4.02	0.41	0	0
Z4	8	4	1.0	0	0	7.68	3.61	0.82	0	0
ZC1	8	4	0	0.25	0	7.88	3.97	0	0.18	0
ZC2	8	4	0	0.5	0	7.92	4.01	0	0.42	0
ZC3	8	4	0	0.75	0	8.23	3.54	0	0.60	0
ZC4	8	4	0	1.0	0	8.56	3.65	0	0.82	0
ZG1	8	4	0	0	0.05	7.68	3.71	0	0	0.05
ZG2	8	4	0	0	0.1	7.69	3.91	0	0	0.1
ZG3	8	4	0	0	0.2	7.98	4.21	0	0	0.2
ZCG	8	4	0.2	0.5	0.1	8.21	3.91	0.16	0.39	0.1

3.2 MICROSTRUCTURAL OBSERVATION

3.2.1 SAMPLE PREPARATION

3.2.1.1 POLISHING

Initially, the cylindrical samples of 15mm diameter X 10 mm height were drawn from the castings. The section surfaces so obtained were initially polished with emery papers of progressively fine grade 80, 220, 400 and 600 grits. The samples were turned through 90^o between the papers and washed thoroughly with distilled water before proceeding from one paper to another. During paper polishing, water was used as a cleaning agent. After completing the paper polishing, the samples were polished in a rotating disc of proprietary cloth (selvyte cloth) charged with a diamond paste of 6, 3 and 0.25 μm particle size in sequence. Filtered kerosene was used as lubricant during cloth polishing. Samples were gently pressed against the rotation wheel. As magnesium

is a soft material, much care was taken during polishing to avoid scratches and excessive surface contamination. Cleaning the samples with water (even with distilled water) was found to be ineffective in removing surface contaminants of the polished samples. So, after the final polishing was over, the same surface was cleaned with ethanol using an ultrasonic cleaner.

3.2.1.2 CHEMICAL ETCHING

Picric acid-based etchant was found to be an efficient one, which clearly revealed the microconstituents of magnesium alloys. The chemical composition of the etchant used in the present study is given below:

Picric acid (Solid form)	–	6 grams
Acetic acid	–	5 ml
Ethanol	–	100ml
Distilled water	–	10 ml

Etching time of 2-3 seconds was found to be an optimum. Much care was taken during etching to avoid over-etching, which would otherwise have spoilt the surface of the samples.

3.2.2 OPTICAL MICROSCOPE

Microstructural specimens (after polishing and etching) were observed under a LEICA DMRX optical microscope. Photographs were taken at different locations with various magnifications.

3.2.3 IMAGE ANALYSIS

Quantitative analysis of the microstructure was carried out using a Leica 2001 Image Analyzer in conjunction with the optical microscope. Sizes of various intermetallics and the grain sizes of various castings were measured by the linear

intercept method. The fields of observations were selected randomly at different locations of the sample.

3.3 X-RAY DIFFRACTION (XRD)

The various microstructural constitutes of castings were identified using XRD. 15 mm Φ and 3mm thick samples were cut from the castings and the surface scales were removed by rough polishing. XRD spectrums were obtained using Phillips PW 1710 Powder Diffractometer with Cu-K_{α} radiation.

3.4 SCANNING ELECTRON MICROSCOPE (SEM)

To identify the type of precipitates in various castings and to study the micro-mechanisms of fracture during tensile and creep, samples were cleaned in ethanol using an ultrasonic vibrator and the surfaces were examined in a JEOL, JSM 35C Scanning Electron Microscope operating at an accelerating voltage of 15-30 KeV. The same optical microstructural samples were used for SEM studies. The compositions of various phases and intermetallics were analyzed using Energy Dispersive Spectroscope (EDS) attached to SEM. An average of ten EDS measurements was used to approximate the composition of phases. For fracture studies, 5 mm height samples cut from near the fractured surface were used. Most SEM images were taken using secondary electrons (SE) although some images have been acquired from back scattered electrons (BSE).

3.5 HIGH RESOLUTION TRANSMISSION ELECTRON MICROSCOPY

The as-cast composites "E" were polished with 1000 grit size emery paper up to 10 μm thickness with the help of a double header sticker. The samples were washed with 1/3HNO_3 and with ethanol to remove the sticky layer on the surface of the sample. The specimens were then ion milled using the precision ion polishing system, **BAL-TEC model RES 101,** with a low angle of 15º that was maintained throughout the experiments. HRTEM studies were carried out using **FEI T30 S-TWIN** modernized equipment, which was operated at 150 KV attached with an EDS.

3.6 DIFFERENTIAL THERMAL ANALYZER (DTA)

To study the phase transformation, samples weighing ≈ 7-12 mg were cut from the respective castings and kept in an alumina crucible placed inside the SETARAM TG-DTA1600 instrument. The photograph of the DTA instrument is shown in Figure 3.6. To maintain the inert atmosphere, the argon gas was flushed for 10 minutes before start of the experiment. Both heating and cooling curves were recorded at a scanning rate of 10 K/min. At least three runs were carried out for every sample to confirm the repeatability of results.

Figure 3.6: Photograph of DTA instrument

3.7 MECHANICAL PROPERTIES

3.7.1 HARDNESS MEASUREMENT

Both the macrohardness and microhardness measurements were carried out for the prepared alloy specimens, Macrohardness was measured using Brinell's hardness method and microhardness using Vickers hardness method.

3.7.1.1 MACROHARDNESS

The Brinell hardness measurements were carried out in an INTENDEC hardness machine with a 2.5mm steel round ball indenter and an applied load of 62.5 Kg with a dwell time of 30 secs. At least five symmetrical readings were taken from each sample to get representative data. The specimens for hardness measurements were paper polished with different grit sizes. Sufficient care was taken to ensure that the opposite surfaces were parallel to each other to ensure accurate measurements.

The Brinell Hardness Number (BHN) is given by the formula:

$$BHN = 2P / [\pi D(D-(D^2-d^2)^{1/2})]$$

Where P - applied load (kgf)

D - diameter of the indenter ball (mm)

d - diameter of the impression (mm)

3.7.1.2 MICROHARDNESS

To identify the hardness of the matrix and the precipitates with respect to elemental addition, microhardness was measured on a polished sample. The samples were etched with acetic picral as per microhardness tester fitted with diamond pyramid indenter and the angle between the opposite face was 136º. A 50g constant load was maintained throughout the experiments with 10 sec dwell time. The Vicker hardness may be determined from the following equation:

$$VHN = 1.854P/L^2$$

Where P - Applied load in Kgf

L - Average length of diagonal in mm

3.7.2 TENSILE TESTING

Room as well as high temperature (150ºC) tensile testing was carried out using the fully computer-controlled **INSTRON 8801** universal testing machine. Ultimate tensile strength, yield strength and elongation were obtained. For room temperature test, an extensometer was used to measure the elongation %, whereas for high temperature tests, ductility was measured manually by measuring before and after the test, the distance between marks made on the GL. Samples for tensile testing were prepared according to ASTM E8 Standard. Figure 3.7 shows the schematic diagram of a tensile specimen. For high temperature testing, the samples were heated in an oven attached to the INSTRON machine and soaked for 15 min after the required test temperature is reached to homogenize the test temperature along the test sample length.

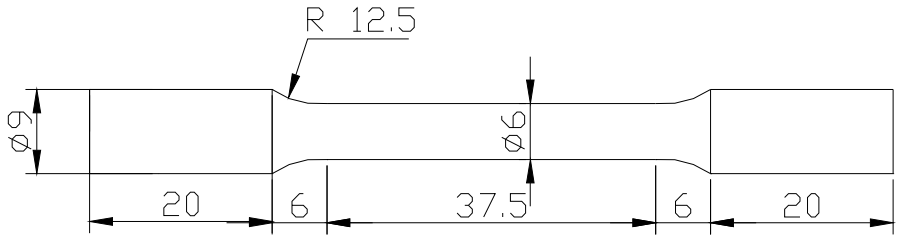

Figure 3.7: Schematic diagram showing standard test sample

3.7.3 CREEP TESTING

The photograph of the creep testing machine is shown in Figure 3.8. Creep testing was carried out using a 3 ton MAYES creep testing machine with a lever ratio of 15:1. The standard creep test samples presented in Figure 3.9 were machined out from the castings according to ASTM 138. The displacement during creep was measured

using two LVDTs mounted on the extensomenter attached on the GL (gauge length) of the test specimen. The required load was calculated according to the specimen diameter and lever ratio. The sample was heated using a three zone coil furnace. Specimen temperature was controlled within ± 2º C of the set point using a Eurotherm-make three zone temperature controller. Two thermocouples were attached: one near the top ridge and another near the bottom ridge of the test specimen to ensure uniform temperature throughout the GL. The testing temperature was reached within 1 hr and 30 mins soaking time was given for stabilization of temperature along the sample length. Both the displacement and temperature were monitored and recorded automatically at regular intervals (30 minutes) through a Yokogawa-make data logger.

Figure 3.8: Photograph of creep testing machine

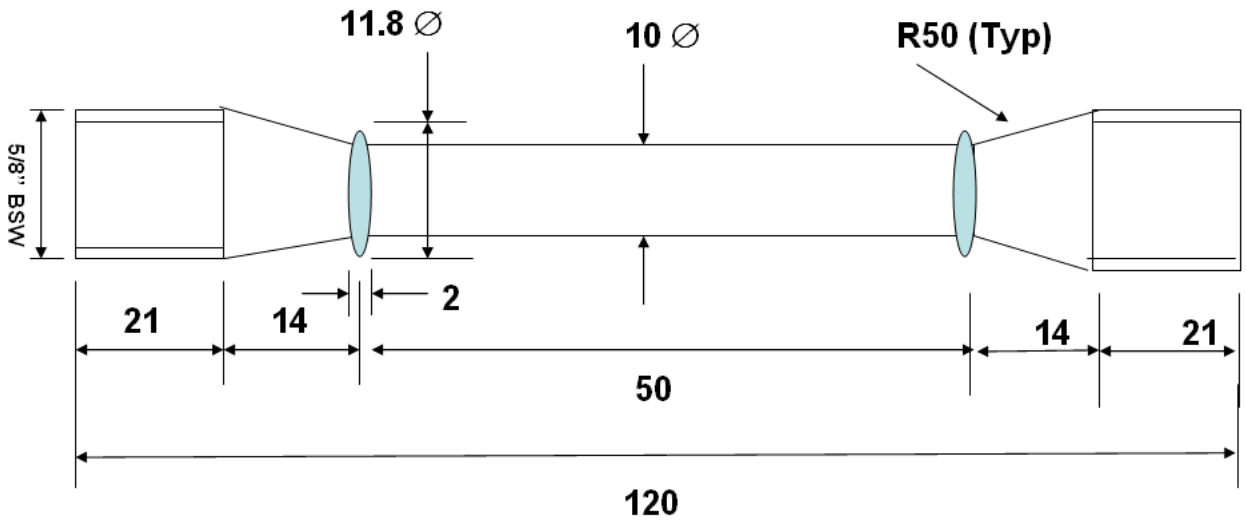

Figure 3.9: Schematic diagram showing standard creep testing specimen

3.8 PREPARATION OF MASTER ALLOY

3.8.1 PROCESSING METHOD

The Al-SiC composites used in the present study were fabricated by liquid stir cast method, which was indigenously developed in our laboratory with about 600 gms casting size. The schematic diagram of composite synthesis is shown in Figure 3.10. The mild steel impeller was specially designed for creating a uniform vortex in the liquid metal, which was coated with graphite to avoid the dissolution of iron atoms into the composites. The alloy melt was mechanically stirred by an electrical motor and the stirring speed was controlled by an electrical dynamometer.

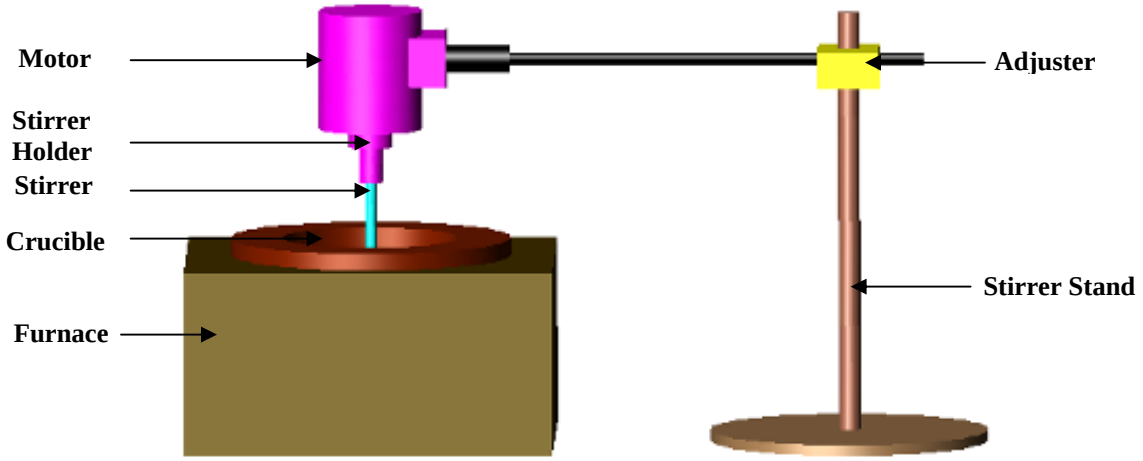

Figure 3.10: Schematic representation of experimental setup for composite Fabrication

3.8.2 STIR CAST COMPOSITES

The composite selected for this study was Al-5wt%SiC. The following materials were used for the experiments:

- Inconel pure aluminium ingots
- Pure magnesium ingot
- SiC particle (14 μm average particle size)
-

3.8.3 CRUCIBLE

A clay graphite crucible of capacity 800 grams was used for these experiments. Separate crucibles were used for melting and the Al_4C_3 particle reclamation.

3.8.4 MOULD

A standard cast iron round mould was used to maintain uniform solidification and the schematic diagram is shown in Figure 3.11.

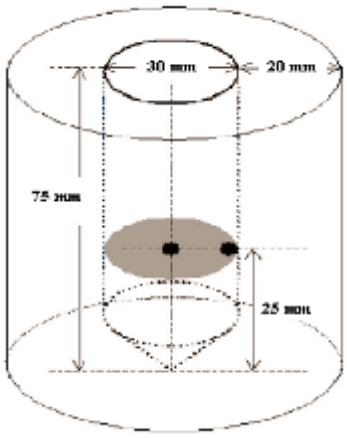

Figure 3.11: Schematic representation of cast iron mould

3.8.5 PROCESSING OF COMPOSITES

The required amount of pure aluminium was melted in a clay graphite crucible using electrical resistance furnaces and the melt temperature was maintained at 730-750ºC. The composites were fabricated in 500 grams level of melt. To increase the wetability of liquid melt, an average of 1wt% of Mg was added into the melt which leads to avoidance of the particle rejection during addition. After melting, the liquid metal was mechanically stirred using an impeller driven by an electrical motor and the preheated particles at 500ºC for 4 hrs were introduced in the vortex of the liquid metal. The particles were added into the melt with a known average feed rate (2.5 grams/min), stirring speed (500rpm) and the abovementioned melt temperature. The liquid metal was poured into the preheated mould which allows solidifying.

3.8.6 Al_4C_3 SYNTHESIS ROUTE

In Al/SiC_p composites, a direct reaction between Al and SiC occurs to form hexagonal platelet-shaped Al_4C_3 crystals and elemental Si. Such an interfacial reaction in Al/SiC_p composites depends upon the processing route and the experimental parameters. To complete the reaction between Al and SiC_p, the different processing parameters were used and the details are listed in Table 3.2. For the melt holding

studies, every 15 minutes the melt was stirred vigorously using a graphite rod to distribute the particles uniformly into the melt.

Table 3.2: Processing parameters for optimum reaction between particle and matrix with respect to time

Code	Composites	Temperature in deg C	Time of holding after particle addition in min
A	Al-5wt%SiC	750	0
B	Al-5wt%SiC	750	5
C	Al-5wt%SiC	750	30
D	Al-5wt%SiC	750	60
E	Al-5wt%SiC	750	120

3.8.7 RECLAMATION OF INTERFACIAL PRODUCTS

In this method, interfacial reaction products and unreacted SiC particles reclaimed from Al-5wt%SiC composite processed by different processing parameters are mentioned in Table 3.2. The small amount of salt flux containing an equimolar mixture of NaCl-KCl-5%NaF was added through the vortex, which was created by a mechanical stirrer. After mixing for 30 to 120 seconds, separation of reaction products along with reinforcement particles starts leading to their floating on the melt surface and skimming off. The powders extracted by this process are named as reclaimed powder. The reclaimed particles were sieved in a 75 μm spacing wire mesh and the final sieve at 10 μm. The leftover matrix melt in the crucible was poured into a cast iron mould. The flow chart shown in Figure 3.12 describes the entire processing route.

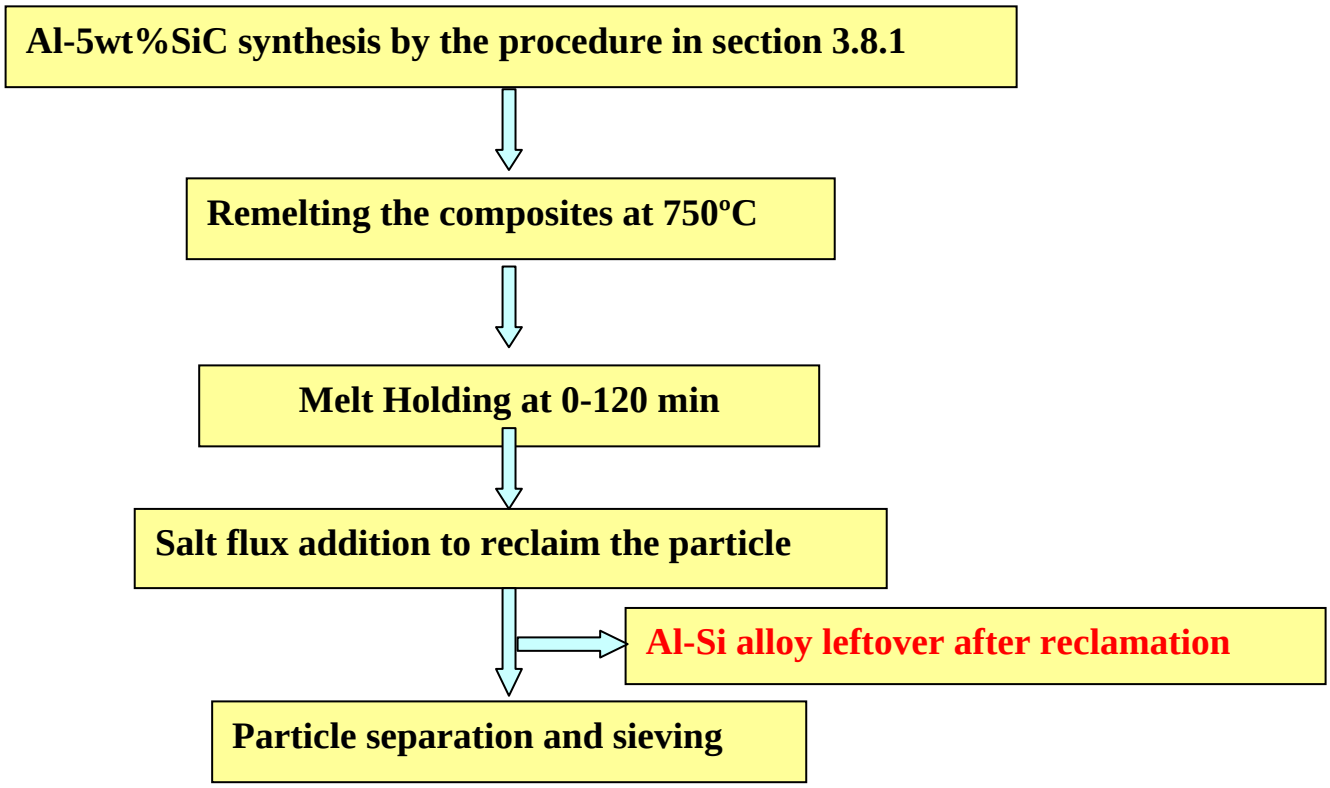

Figure 3.12: The flow chart of particle synthesis route

From the results of DTA, SEM and HRTEM investigations, optimum temperature and time required for the interfacial reaction products have been found out.

4.1 MICROSTRUCTURE AND PHASE IDENTIFICATION

This chapter deals with the microstructural features of individual and combined additions of Sb and Ca on ZA84 alloy. X-ray diffraction analysis was conducted to find out the phases present in the alloys. Optical, scanning electron and transmission electron microscopy studies were conducted to examine the microstructural features of various alloys. EDS analysis of both SEM and TEM were used to analyze the stoichiometry of the phases. To study the phase transformation in the alloys, differential thermal analysis (DTA) was conducted at a scanning rate of 10 K/min.

4.1.1 ZA84 ALLOY

X-ray diffraction pattern of as-cast ZA84 alloy is shown in Figure 4.1. It can be observed from the figure that the peaks correspond to two phases:

(i) α-Mg corresponds to the peaks of (hkl) planes (100), (002), (101), (102), (110), (103), (200), (112), (201), (004) and (202) at 2θ angle 32.99, 34.99, 37.16, 48.22, 58.32, 63.95, 67.92, 69.31, 70.42, 72.49 and 78.82, which exactly matches with the International Diffraction Data of JCPDS for magnesium peaks [229].

(ii) The other peaks of planes (611), (631), (550), (770), (1031) and (1060) at 2θ angle 38.99, 43.16, 45.92, 65.52, 70.22 and 79.18 match with the $Mg_{32}(Al,Zn)_{49}$ phase [230].

The maximum intensity peak corresponds to $Mg_{32}(Al,Zn)_{49}$ at (530) for 36.62 angle is not clearly seen in the pattern because of its overlapping with the Mg matrix. This phase has a cubic crystal structure ***a=1.416nm*** with the space group $\boldsymbol{Im\bar{3}}$. Slight shift (+1º±0.25º) in the X-ray diffraction peaks of the phases from the JCPDS diffraction data indicates small change in the lattice parameters. These differences can be ascribed to the variable concentrations of solutes in the α-Mg matrix and the wide range of compositions in the ternary phases. The intensity area from the XRD pattern is used to calculate the volume fraction of the matrix and the precipitates. According to a planimetric estimation of the X-ray diffraction pattern, α-Mg matrix occupies 92±2 vol.

% of the sample volume and the ternary $Mg_{32}(Al,Zn)_{49}$ phase occupies around 8±2 vol. %.

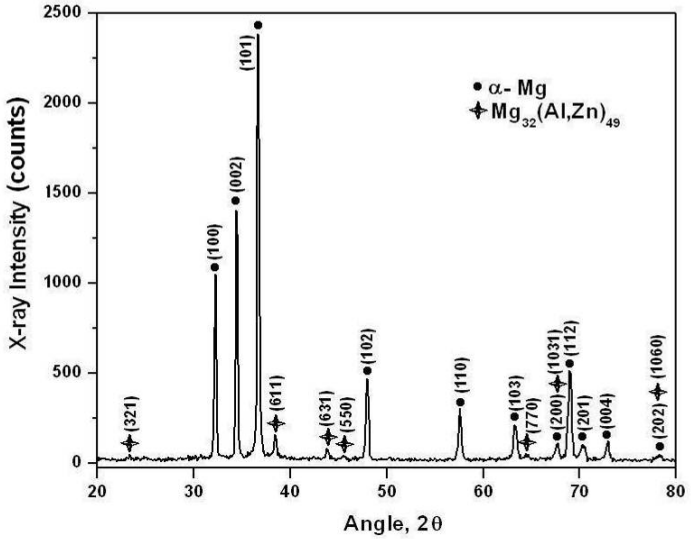

Figure 4.1: XRD pattern of ZA84 alloy

The optical microstructure of the as-cast ZA84 alloy at different magnifications is presented in Figure 4.2. It can be observed from the figure that precipitates exist at the grain boundaries. Further, the precipitates have two morphologies: continuous phase (marked as A) and the isolated phase (marked as B) in the microstructure. The dark grey region that is surrounded by the intermetallic region called the supersaturation of Zn and Al. The average grain size of the ZA84 alloy under the permanent mould casting condition is 62µm. The measured length of the continuous precipitates varies from 70 to 140µm with an average of around 105µm, and the width is from 3 to 6 µm with the average reported as 4.5µm. In ZA84 alloy, mainly two ternary precipitates are reported in the literature [28, 31]. One is identified as the τ-$Mg_{32}(Al,Zn)_{49}$ phase which has a long chain in a wide range of homogeneity in the structure and the other has an isolated phase called the ϕ-$Mg_5Zn_2Al_2$ phase. The microstructure observations are well in line with the previous investigation [31]. The minor $Mg_5Zn_2Al_2$ phase is not observed in the XRD pattern because the volume fraction of the phase is very much below the detectable level.

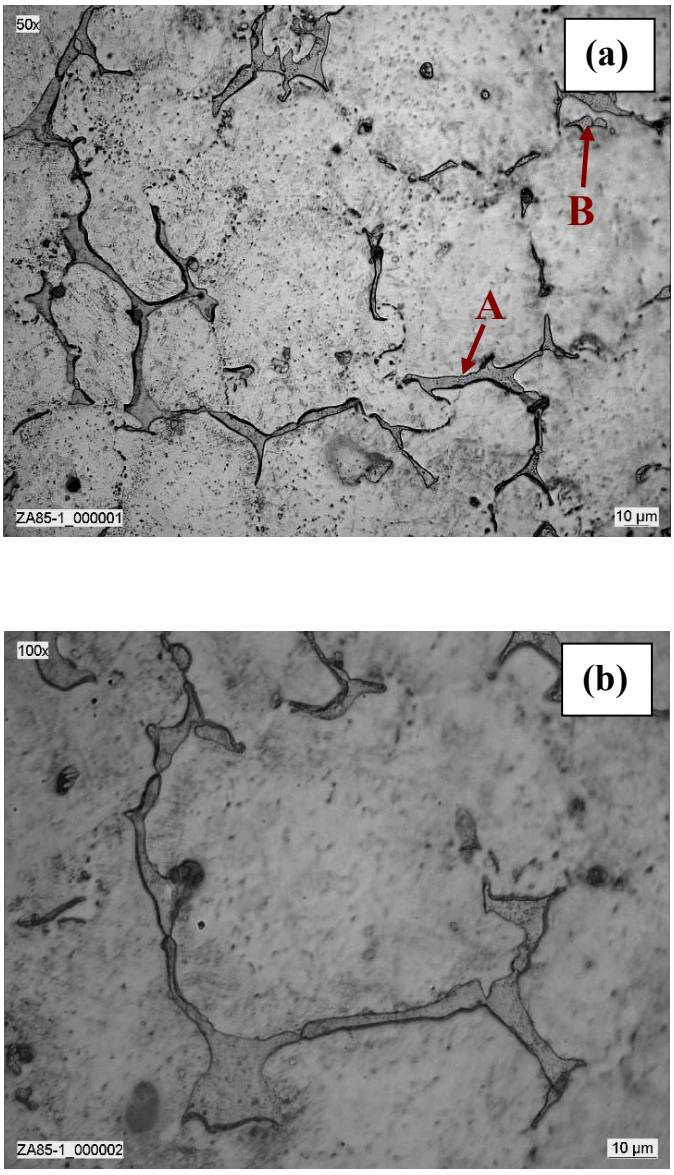

Figure 4.2: Optical microstructure of ZA84 alloy (a) 50x (b)100x

In ZA alloys, normally three types of phases are identified and characterized. They are the $Mg_{32}(Al,Zn)_{49}$ phase, known as the τ phase; the MgZn phase, known as the ε phase; and the ternary icosahedral quasi-crystalline phase, denoted as the Q phase. A schematic phase relationship with respect to change in the Zn/Al ratio to wt% of aluminium is shown in Figure 4.3. The diagram reveals that the microstructural constituent is influenced by both the content of Al and the Zn/Al mass ratio: (i) alloys with a high Zn/Al ratio and a low Al content fall into the ε-type; (ii) alloys with an intermediate Zn/Al ratio and an intermediate Al content favour the τ -type and; (iii) alloys with a low Zn/Al ratio and a high Al are dominated by the icosahedral quasi-crystalline phase. There is no $Mg_{17}Al_{12}$ phase reported in the ZA series of alloys [128].

In the present study, in the Zn 7.71% and Al 3.68% alloy both the τ-type and ϕ-type phases are formed which is clearly evidenced from the micro constituent's and X-ray analyses. The results reported are very much in line with the earlier work reported for the same alloy [31]

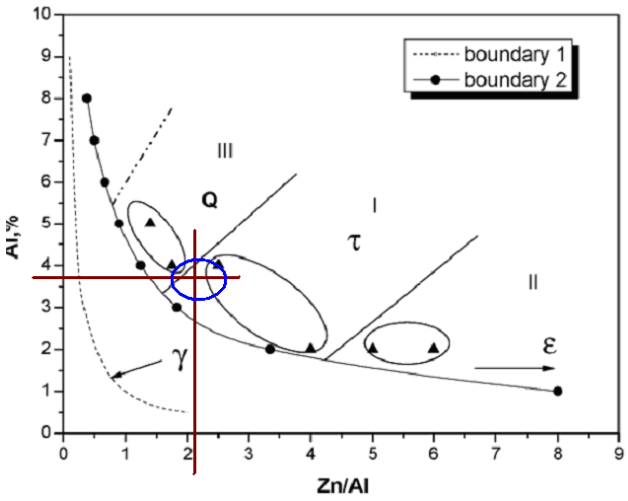

Figure 4.3: Phase relationship with respect to change in phase constituents of aluminium and zinc [128]

Further, the micro constituents of ZA84 alloy are clearly seen in a scanning electron microstructure along with EDS pattern presented in Figure 4.4. It can be observed from the figure that the precipitates have two different morphologies. One has a continuous network (marked as B) and the other has an isolated phase (marked as C) in the microstructure. The dark grey phases randomly present in the alloy structures are α-Mg matrix (marked as A). Other phases marked as B,C and D were also presented in Fig.4.5 along with the EDS spectra. The spectrum analysis revealed the dark region(A) corresponds to the Mg matrix with solid solution of Zn and Al solute elements. The elemental composition of phase marked as 'B' corresponds to $Mg_{32}(Al,Zn)_{49,}$ although more magnesium atoms are found in the phase than in the suggested stoichiometric composition. The isolated phase marked as C corresponds to $Mg_5Zn_2Al_{2.}$. This phase has been reported [38] to have an orthorhombic structure of space group Pbcm, a= 0.8979nm, b=1.6988nm, c=1.934nm.

The distribution of major chemical elements, including Mg, Zn and Al within the microstructure, was traced by EDS to detect differences in the chemistry of micro-regions between the matrix and the ternary phase. It is clearly seen that the centre of the α-Mg grain contains small traces of Zn and Al while moving towards the grain boundary phases as the constituents of Zn and Al increase. The compounds are almost the stoichiometric proportion of the ternary phase, which contains the elements of Mg, Zn and Al. The variation in the exact proportion of the phase stoichometry is due to the interaction between the Mg matrix and the electron beam.

Apart from the $Mg_{32}(Al,Zn)_{49}$ and $Mg_5Zn_2Al_2$ phases, the fine particles are also seen from the SEM microstructure presented in Figure 4.6. This is because the addition of 0.2 wt% of Mn forms the Al_8Mg_5 precipitate along with the major phases. The volume fraction of the precipitate is very less because most of the added Mn reacts with Fe by forming Al-Mn-Fe heavy intermetallic, which normally settles at the bottom of the crucible.

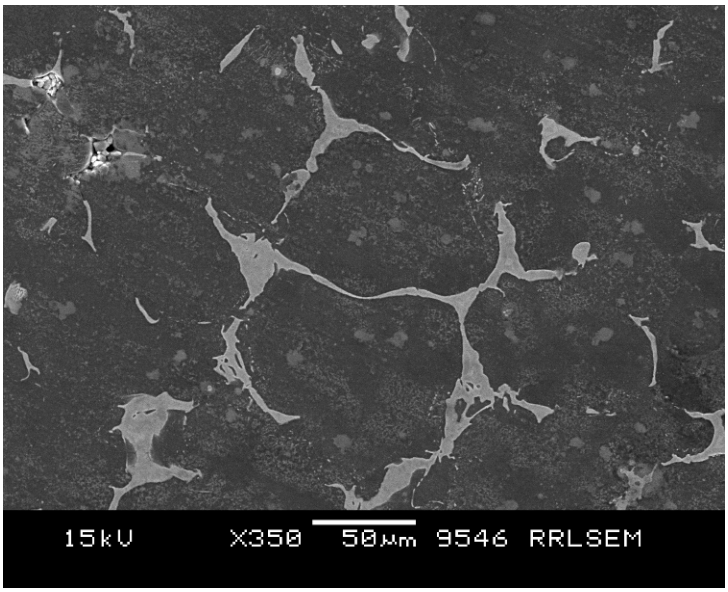

Figure 4.4: SEM microstructure of ZA84 alloy

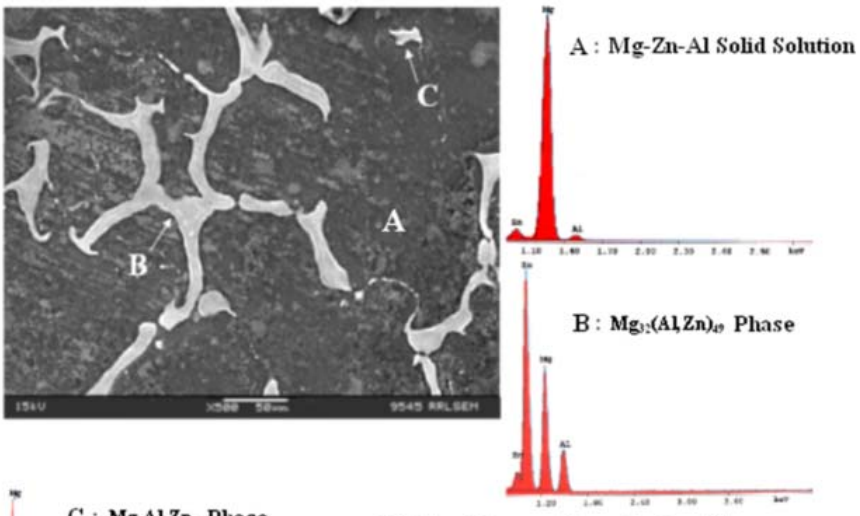

EDS elemental compositions of A, B and C

Elements	A		B		C	
	Wt %	at %	Wt %	at %	Wt %	at %
MgK	90.46	92.17	16.39	31.98	38.76	55.40
Al K	5.81	5.17	23.11	27.50	15.95	20.53
Zn K	3.73	2.66	60.50	40.52	45.29	24.07
Total	100	100	100	100	100	100

Figure 4.5: SEM-EDS of ZA84 alloy

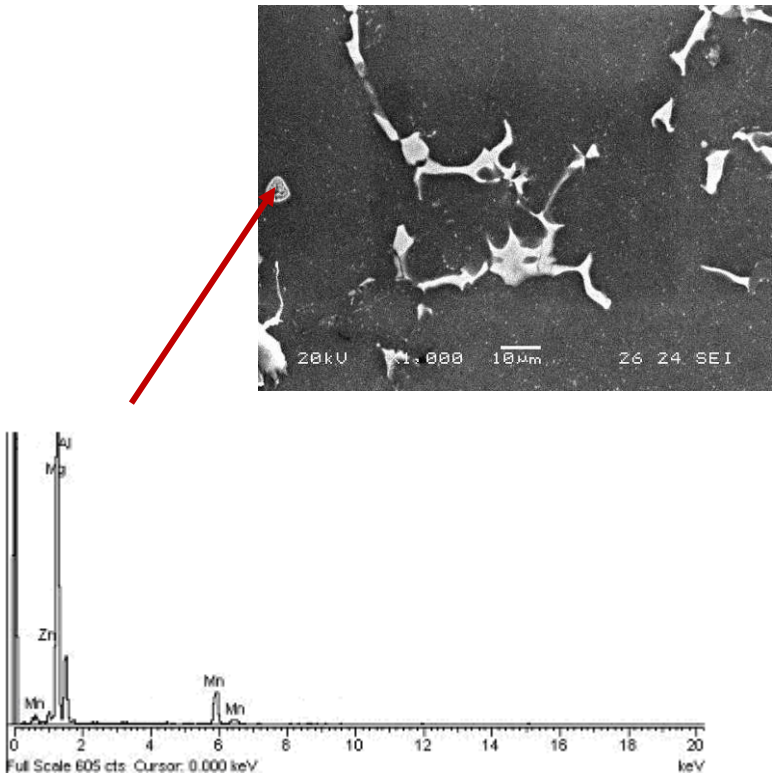

Figure 4.6: SEM microstructure shows the presence of Al_8Mn_5 phase

The as-cast TEM microstructure of ZA84 alloy at continuous phase is shown in Figure 4.7. It is inferred from the microstructure that the grain is a single phase of the α-Mg matrix with precipitation of the second phases. It is further quantified from the EDS results that the Mg has 28.22 atom percent (at%), zinc 41.24 at% and aluminium 30.54 at%, which are equivalent to the atomic stoichiometry of the ternary $Mg_{32}(Al,Zn)_{49}$ precipitates. The results obtained from the TEM results confirm well with the XRD and SEM results.

The as-cast TEM microstructure of the ZA84 alloy at the isolated region is depicted in Figure 4.8. The matrix is seen as the white region from the figure, whereas

the corresponding SAD pattern confirms the hcp magnesium matrix and the calculated value of **a=1.414** nm is slightly lower than that of pure magnesium. This may be due to the solid solution effect of other alloying elements such as zinc and aluminium. The SEM-EDS results also confirm the presence of considerable solid solution of alloying elements (see Figure 4.5). The region adjacent to the matrix is the ternary phase of Mg-Zn-Al and the elemental composition varies with respect to the change in the location within the sample. However, the EDS results of elements give Mg with 55.64 at%, zinc 21.72 at% and aluminium 22.64 at%, which are equivalent to the atomic stoichiometry of the ternary $Mg_5Al_2Zn_2$ precipitates. This phase has an orthorhombic structure of space group Pbcm, a= 0.8979nm, b=1.6988nm, c=1.934nm, matching with the SAD pattern reported in the literature [38].

4.1.2 ZA84+XSb (X=0.2%, 0.5% and 1%)

Figure 4.9 shows the Mg-Sb binary phase diagram. According to the Mg-Sb phase diagram, antimony has negligible solid solubility with magnesium at room temperature [231]. It is clearly seen from the phase diagram that all the added Sb goes to the formation of precipitates rather than of solid solution. Mg-Sb, Al-Sb and Zn-Sb intermetallics are capable of forming in the Sb-added ternary ZA84 alloy. However, the priority of the phase formation depends on the electronegativity difference between the alloying elements (Δ_x A,B where A and B represent alloying elements). As per Hume-Rothery rule, higher the electronegativity differences, easier the formation of intermetallics. The electronegativity of different elements with respect to Sb is given in Table 4.1.

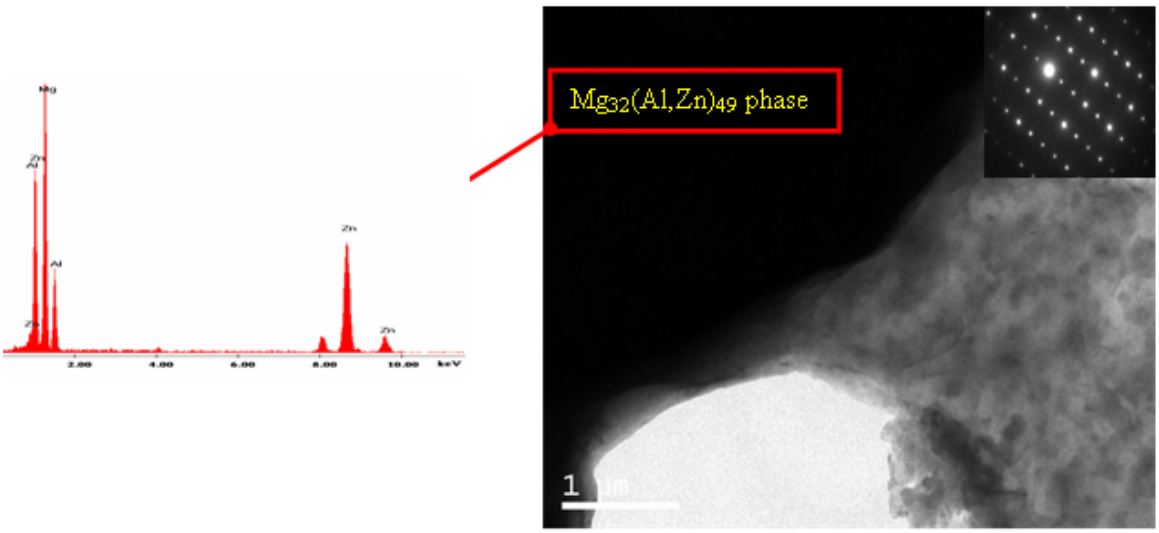

Figure 4.7: TEM microstructure, EDS and SAD pattern for ZA84 alloy showing the presence of $Mg_{32}(Al,Zn)_{49}$

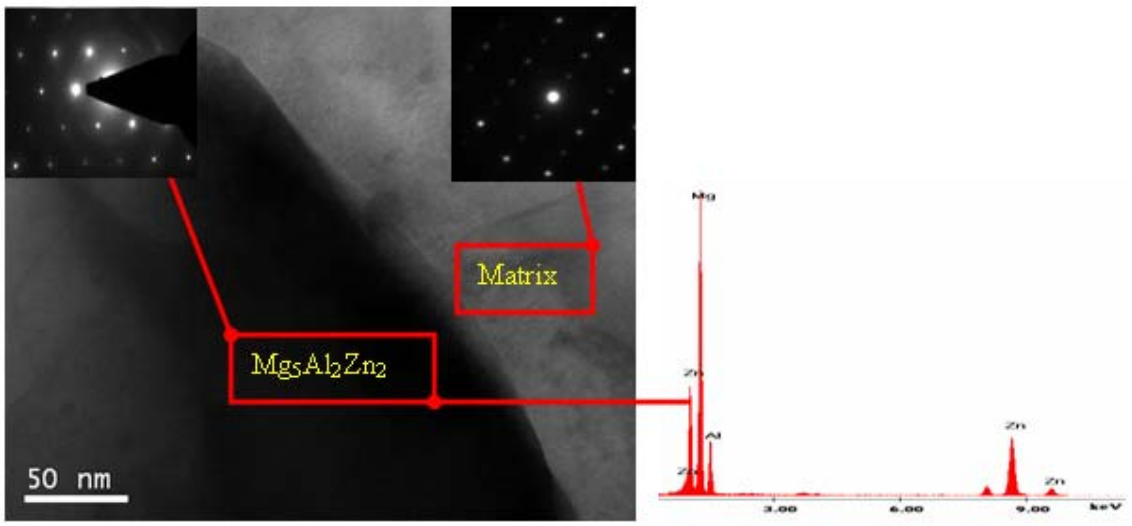

Figure 4.8: TEM microstructure, EDS and SAD pattern for ZA84 alloy showing the presence of $Mg_5Al_2Zn_2$

The electronegativity differences of the possible phases Mg-Sb, Al-Sb and Zn-Sb are 0.74, 0.44 and 0.40 respectively. From these results, the value of the Mg-Sb electronegativity difference is higher than those of Al-Sb and Zn-Sb intermetallics. Therefore, the possible phase formed during Sb addition with Mg-Zn-Al alloys is Mg-Sb intermetallics.

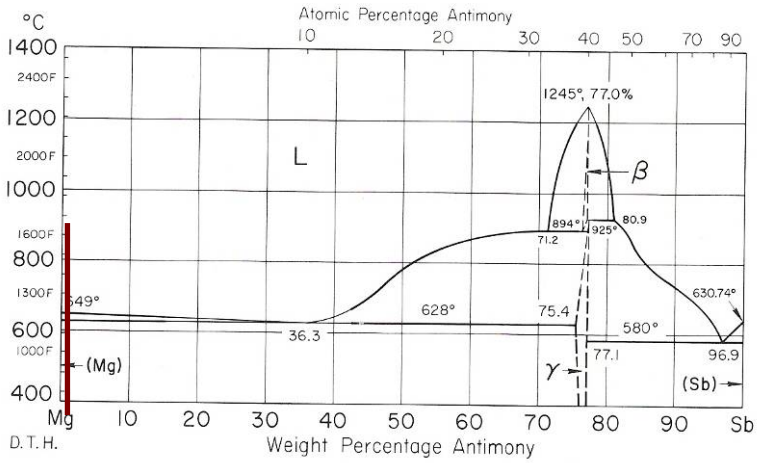

Figure 4.9: Mg-Sb phase diagram [12]

Table 4.1: Electronegativity analysis of Mg, Zn, Al and Sb

Elements	Electronegativity values of individual elements	Electro negativity difference (Δx A,B)			
		Mg	Zn	Al	Sb
Mg	1.31	0	0.34	0.30	***0.74***
Zn	1.65	0.34	0	0.04	0.40
Al	1.61	0.30	0.04	0	0.44
Sb	2.05	***0.74***	0.40	0.44	0

The XRD pattern of 1wt% Sb-added ZA84 alloy solution-treated at 335^{o} C for 48 hrs is shown in Figure 4.10. The sample was solution treated in order to get dissolved the ternary phases so as to avoid overlapping of the α-Mg and Mg-Sb peaks. It can be observed from the figure that the peaks correspond to two phases:

(i) α-Mg, peaks of (hkl) planes at 2θ angle matching exactly with the International Diffraction Data of JCPDS for magnesium peaks [229].

(ii) The maximum intensity peak of (hkl) planes at 2θ angle (25.79) matching with Mg_3Sb_2 phase [232].

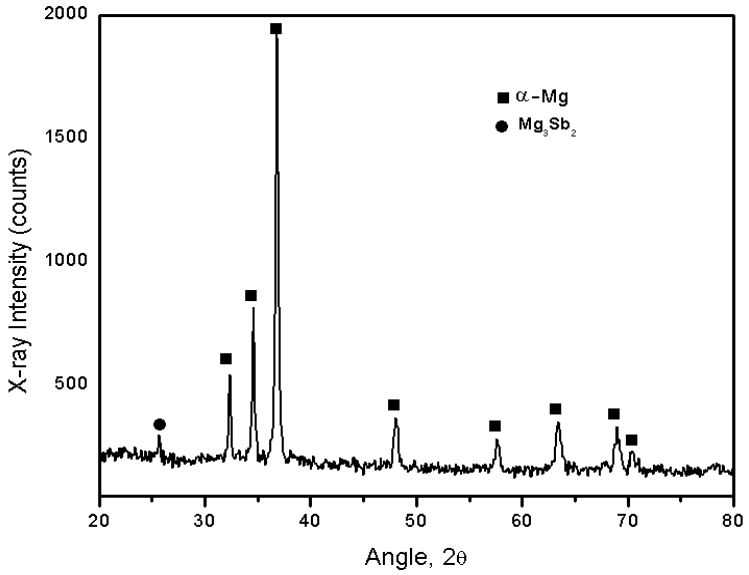

Figure 4.10: XRD pattern of ZA84+1%Sb

Figure 4.11 shows the optical microstructure of base and Sb (0.2, 0.5 and 1 in wt%) added ZA84 alloys. It can be seen from these figures that the ternary $Mg_{32}(Al,Zn)_{49}$ precipitates in the Sb added alloys appears to be broken into smaller sizes, which are finer than that of base alloy structure in which ternary precipitates are more continuous and longer. The growth of the ternary phase is restricted by the presence of the Mg_3Sb_2 binary phase. Moreover, it is observed from the figure that in the Sb added alloys, the length of the ternary phase (from continuous 105 μm to discontinuous 30 μm) is much reduced and they are distributed uniformly throughout the matrix and the width increases from 6.5 to 8 μm when compared with the base alloy.

The growth of the continuous $Mg_{32}(Al,Zn)_{49}$ phase is restricted from 105 to 30 μm length by the mechanism shown in Figure 4.12. The thermally stable phase formed at the earlier stage of solidification was distributed uniformly throughout the matrix. The cubic crystal growth of ternary lattice has been restricted by the presence of Mg_3Sb_2 phase with change in their lattice. The growth restrictions in length also lead to an increase in the width of the precipitate to a certain extent. Under equilibrium conditions, the solidification sequence of 0.5wt% of Sb added alloy is as follows: Mg_3Sb_2 formation at the earlier stage, primary α-Mg formation followed by peritectic reaction to form τ and ϕ-type precipitates. The final microstructure contains α-Mg, $Mg_{32}(Al,Zn)_{49}$, $Mg_5Zn_2Al_2$ and Mg_3Sb_2 with the presence of minor Al_8Mn_5 phases at the grain boundaries. Besides, all the Sb added alloys show the same sequence with an increase in the volume fraction of Mg_3Sb_2 with increase in the wt% of Sb.

It is seen that black rod-shaped particles are distributed at the grain boundaries in the Sb added alloy microstructure. The EDS pattern of the black region corresponds to the elemental composition of Mg_3Sb_2 phase (see Figure 4.13). Moreover, an increase in Sb addition has led to an increase in the volume of Mg_3Sb_2 phase besides changing its morphology from finer to a thicker needle shape (see Figures 4.11 c & d). However, an increase in Sb addition does not change the quantity of $Mg_{32}(Al,Zn)_{49}$ precipitates; this is because (1) the solubility of Sb in Mg is very low and (2) no other Sb-bearing compound such as Al-Sb or Zn-Sb is formed with Sb addition.

Figure 4.14 presents the effect of Sb addition on grain size of ZA84 alloy. It is also observed from the figure that the addition of Sb refines the grain to a certain extent, i.e. from 62 μm grain size of base alloy to 35μm for ZA84+1wt% Sb-added alloy. The grain size was measured using the linear intercept method in an image analyzer. The grain size difference seen with the addition of alloying elements does not suggest an effective grain refinement such as carbon inoculation. However, there are reports [47] which suggest that grain refinement could be obtained with elemental additions such as Si, Ca and Sr. Even though these alloying elements form micron-sized intermetallics at

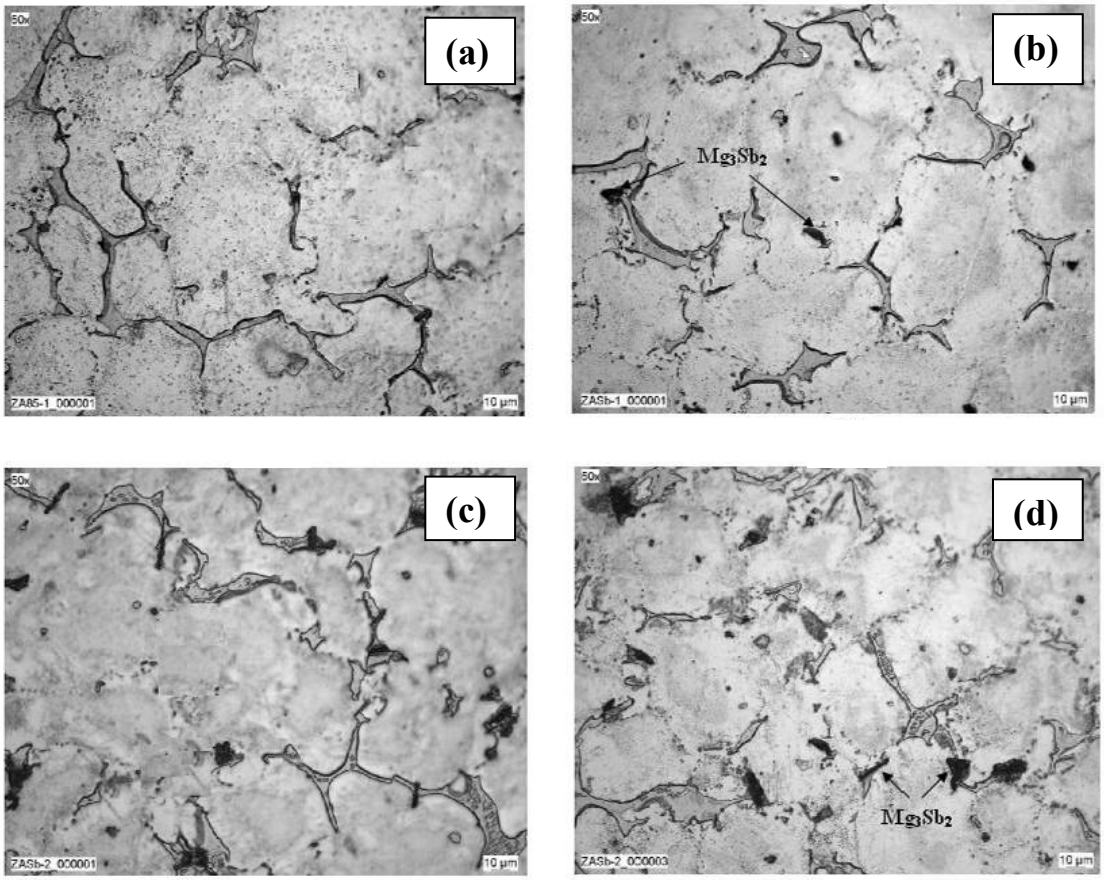

Figure 4.11: Microstructure of (a) ZA84 (b) ZA84+0.2Sb, (c) ZA84+0.5Sb (d) ZA84+1Sb

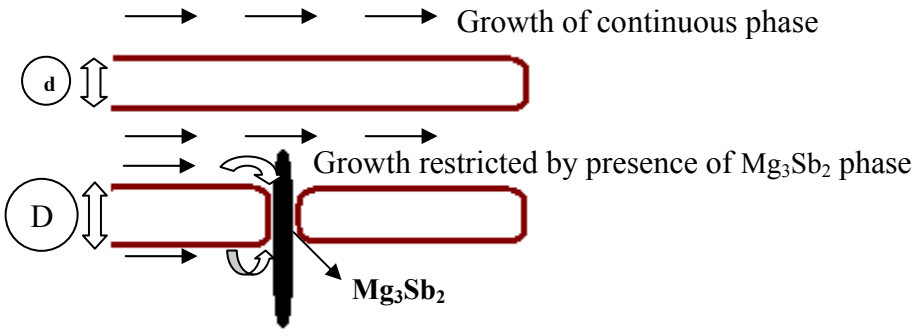

Figure 4.12: Growth restriction mechanism of ternary phase

the grain boundary, the grain refinement obtained with these elements could be explained by constitutional under cooling caused by the intermetallics during solidification. The constitutional undercooling was simplified as the growth restriction factor (GRF). GRF can be defined as

$$GRF = \Sigma_i m_i C_o(K_i-1)$$

where m is the slope of the liquidus line, C_o the initial composition, and k_i the equilibrium partition coefficient for element i. A large GRF can result in effective grain refinement. Based on the Mg-Sb phase diagram, the slope of liquidus line (m) calculated for antimony is 0.53 as shown in Table 4.2.

Table 4.2: Slope of liquidus line m, Equilibrium distribution coefficient K for antimony

Element	m	k	m(K-1)	system
Sb	-0.53	0.00	0.53	eutectic

Table 4.3 gives the GRF values of Sb with respect to the different weight pct. of alloying addition. It is well known that the lower GRF of Sb with magnesium leads to small effect on the grain refinement. The grain size reduction obtained from 62 to 35 μm is well proven in this study. This is attributed to the presence of more number of Mg_3Sb_2 particles in the Sb-added alloy, which might have restricted the grain growth during solidification.

Table 4.3: GRF values of Sb-added alloys

wt % of Sb	$mC_o(K-1)$
$GRF_{0.2Sb}$	0.106
$GRF_{0.5Sb}$	0.265
GRF_{1Sb}	0.530

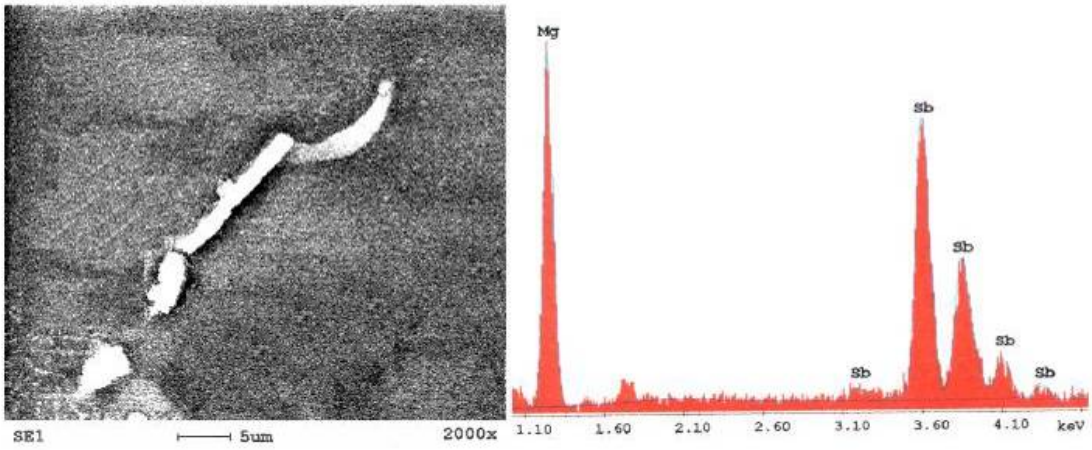

Figure 4.13: EDS pattern of Mg_3Sb_2 in ZA84+0.2%Sb

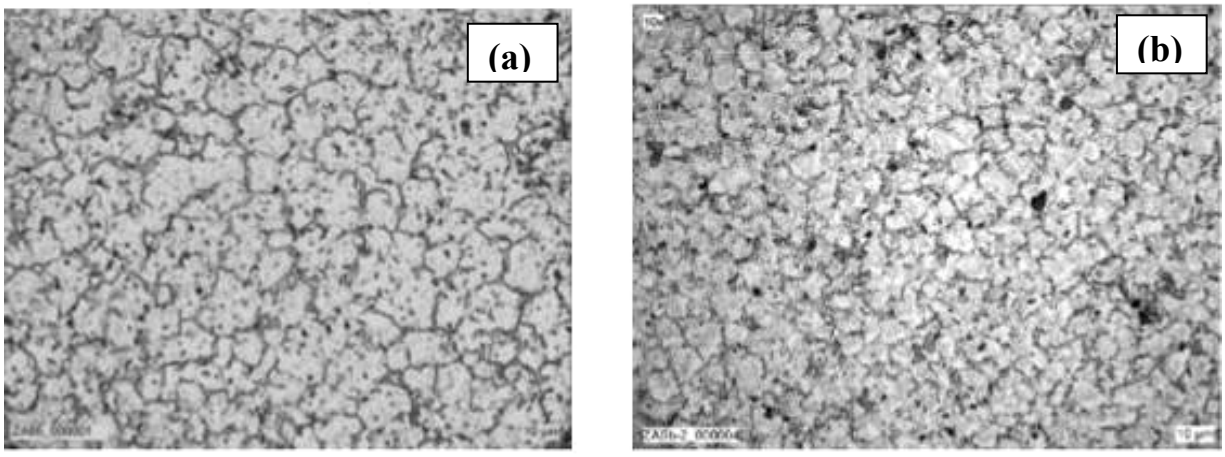

Figure 4.14: Grain size of (a) ZA84 (b) ZA84+1%Sb

4.1.3 ZA84+XCa (0.25%, 0.5% and 1%)

From the Mg-Ca phase diagram shown in Figure 4.15, all the added calcium goes into the formation of precipitates rather than the solid solution with Mg at room temperature [233]. In the ternary system, Mg-Ca, Al-Ca and Zn-Ca precipitates are possible to form in the ZA84+XCa added alloys and the electronegativity differences are 0.31, 0.61 and 0.65 respectively. The possible precipitates are Al-Ca, Zn-Ca and combination with Mg, which forms at an earlier stage of solidification of ZA84 alloy and later formation of ternary phase can grow from the primary α-Mg. However, the key obstacle is the lack of well defined Mg-Zn-Ca and Mg-Al-Ca phase diagrams.

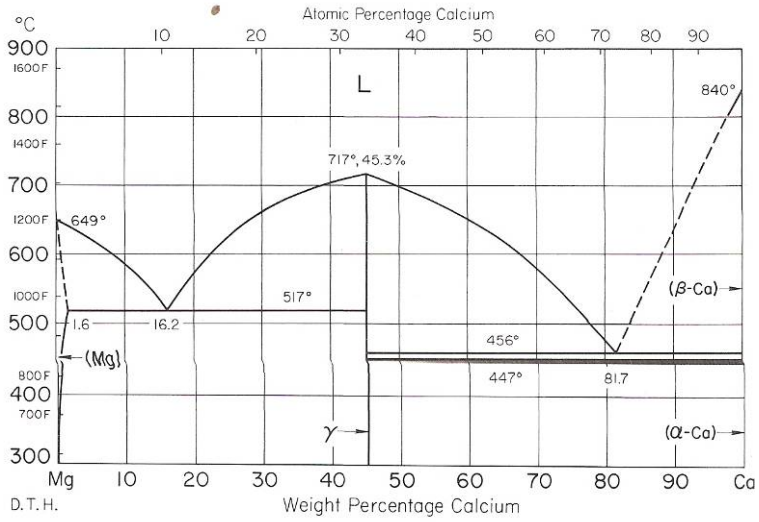

Figure 4.15: Mg-Ca phase diagram [12]

The XRD analysis of ZA84, ZA84+0.25%Ca and ZA84+1%Ca alloys is shown in Figure 4.16. The presence of a new peak at 31.67º for Ca-added alloys compared to the base alloy can be observed from the figure. The intensity of the peak increases with increase in the percentage of Ca-additions. According to a planimetric estimation of base alloy X-ray diffraction pattern, α-Mg matrix occupies 92±2 vol.% of the sample volume and the ternary $Mg_{32}(Al,Zn)_{49}$ phase occupies around 8±2 vol.%, whereas the

addition of 0.25%Ca-added alloy decreases the volume percentage of ternary phase with the appearance of a new phase at 31.67 and occupies 3±2 vol. %. However, no standard data are available in JCPDS International diffraction data for Mg-Zn-Al-Ca phase. Further, clear microstructure studies were carried out to confirm the stoichiometry of the phase.

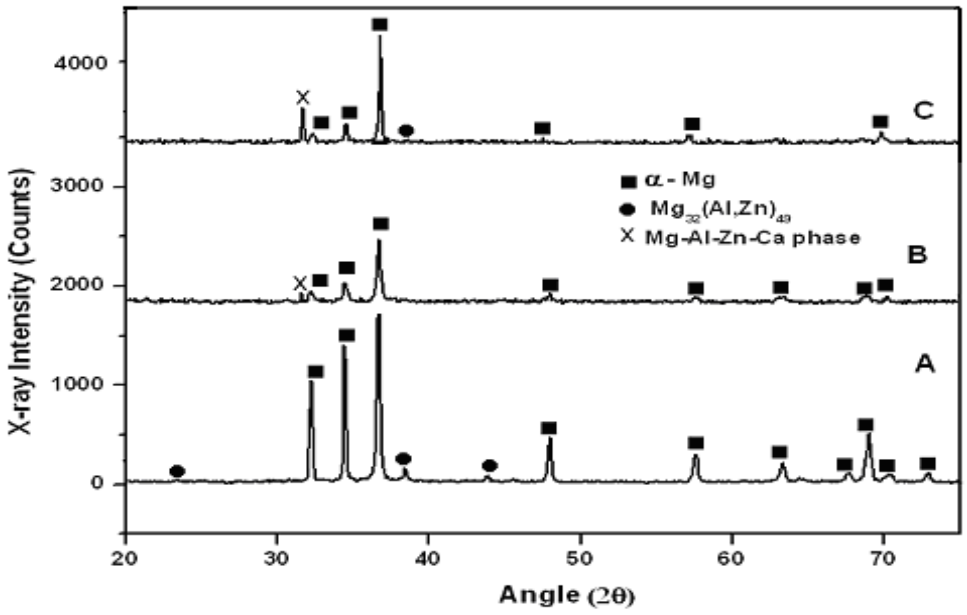

Figure 4.16: XRD pattern for (A) Base alloy (B) 0.25% Ca added alloy (C) 1%Ca added alloy

The optical microstructure of 0.25%Ca added ZA84 alloys is shown in Figure 4.17. In comparison with the as-cast microstructure of the base alloy, it seems that the addition of 0.25%Ca causes apparent changes in the microstructure. The microstructure of 0.25wt% Ca-added ZA84 alloy entirely changes the morphology of the precipitates from continuous phases into bone-like phases along with fine particle-like precipitates, which are shown in the magnification representation of Figure 4.17 (b). Calcium react with ternary phase forms quaternary phase at the earlier stage of solidification with

different crystal structure. With increase in Ca concentration, however, more lamellar eutectic appears in the as-cast microstructure.

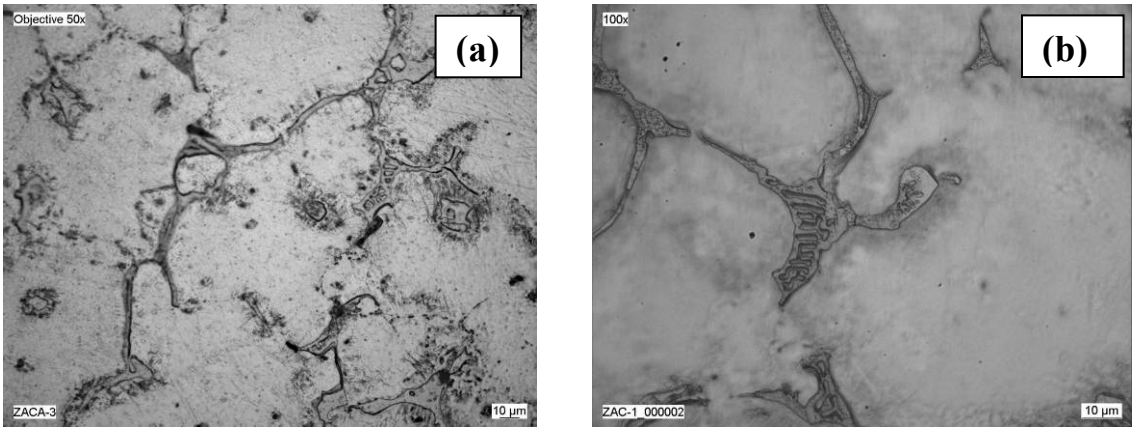

Figure 4.17: Optical microstructure of ZA84+0.25Ca (a) lower and (b) Higher magnification

The SEM microstructure of Ca-added ZA84 alloys is presented in Figure 4.18. In comparison with the as-cast microstructure of base alloy, it seems that the addition of 0.25%Ca does cause apparent changes in the microstructure. With the increase of Ca concentration, however, more lamellar eutectic appears in the as-cast microstructure as shown in the figures 4.18 (a) to (e). The results of microanalysis show that the presence of Ca in the ternary phase is due to segregation of Ca on the grain boundaries, which leads to increase in the solute distribution coefficient, which consequently forms a neck shrinkage and crystal multiplication of the new quaternary phase called as γ. With the increase of Ca concentration from 0.25 to 0.5%Ca, the volume fraction of γ-phase increases, while the τ-phase decreases.

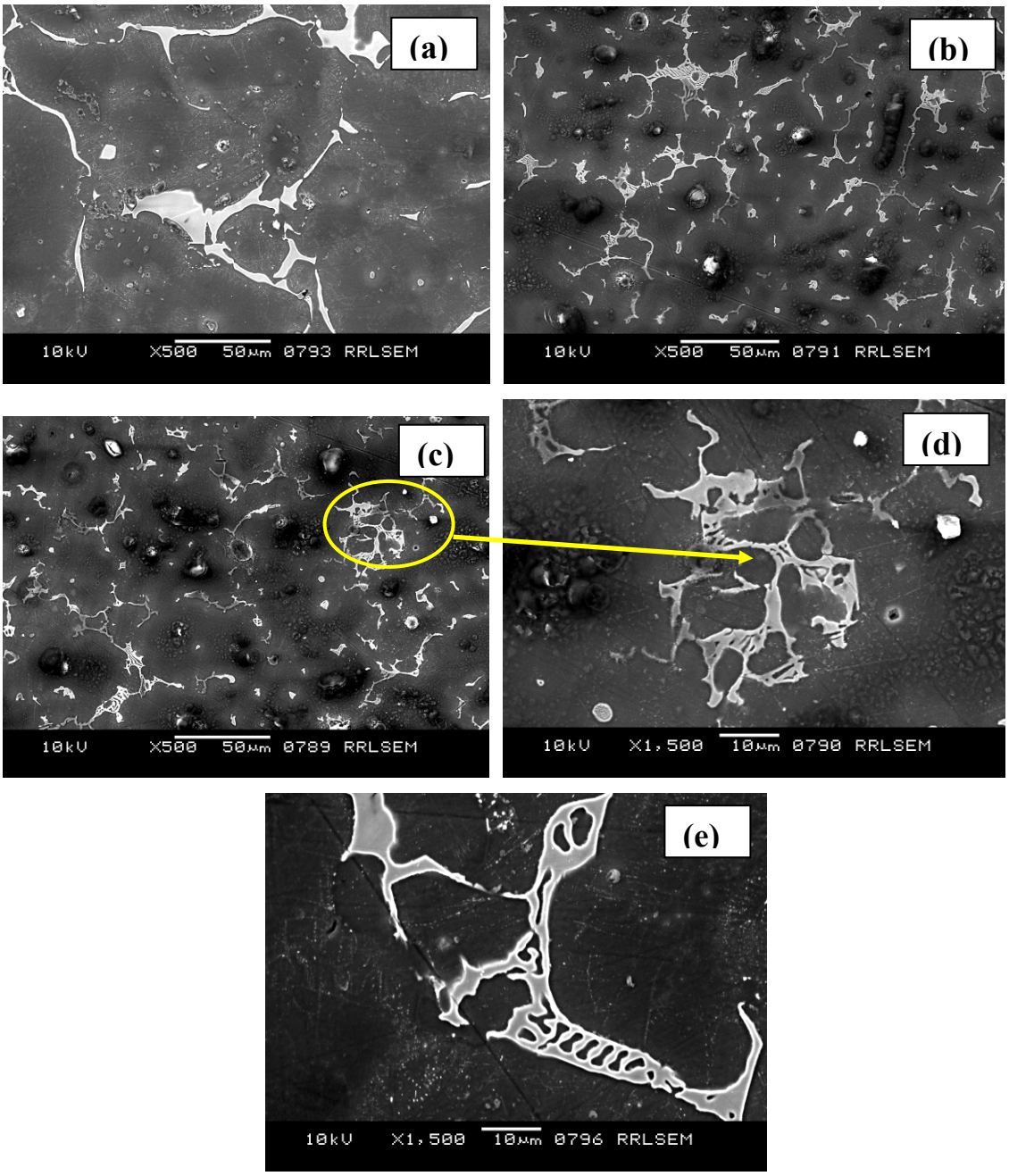

Figure 4.18: SEM microstructure of (a) ZA84 (b) ZA84+0.25Ca (c) ZA84+0.5Ca (d) higher magnification of (c); (e) shows quaternary phase bone-like structure in 1%Ca-added alloy

The SEM microstructure and EDS pattern of ZA84+0.5Ca-added alloy is shown in Figure 4.19. It can be seen from the microstructure that the following three morphologies of intermetallics phases are present: (i) a bone-like precipitate (marked as A); (ii) $Mg_{32}(Al,Zn)_{49}$ (marked as B) and; (iii) fine Al_8Mn_5 phase. The microanalysis result of A corresponds to the stoichiometric proportion of $Mg_{10}Al_6Zn_4Ca$ phase. In addition, the microanalysis of the ternary phase corresponds to the $Mg_{32}(Al,Zn)_{49}$ phase with some fine particles called the Al_8Mn_5 phase. In the Mg-Al-Ca system, the eutectic compounds have been reported to be C14-Mg_2Ca and C15-Al_2Ca, which are types of hexagonal and cubic structure. This behaviour has been diminished by the presence of ternary reactivity of zinc alloying elements change in the formation of the quaternary phase of Mg-Zn-Al-Ca. However, the crystal structure and the stoichiometry proportion of this quaternary phase are important to identify for further mechanism in phase transformation.

The EDS spectrum reported for the Ca-added alloys correspond to the stoichiometry composition equivalent to $Mg_{10}Al_6Zn_4Ca$. It is reported that the addition of Ca to AZ91 alloy resulted in change in the the valence electron structures (VES) of $Mg_{17}Al_{12}$ by using the empirical electron theory and the Ca dissolved in $Mg_{17}Al_{12}$ enhances the strengths of $n_C^{Al–MgIII}$ and $n_D^{Al–MgIII}$ bonds controlling the stability of $Mg_{17}Al_{12}$. Additions of Ca also make the distribution of valence electrons on the dominant bonds and the whole unit cell more uniform, which is considered to be the mechanism accounting for the increase of melting point of $Mg_{17}Al_{12}$ [48]. The same mechanism also involves in this ZA84-Ca added alloys to increase the stability of the ternary phases.

The TEM microstructure of 0.25% Ca-added ZA84 and ZA84+1%Ca alloy is shown in Figures 4.20 and 4.21. It is inferred from the figure that the structure contains the black region of phases uniformly distributed throughout the figure. The EDS analysis of the phase contains Mg, Zn, Al and Ca alloying elements and the precipitates are equivalent to the quaternary phase of Mg-Zn-Al-Ca precipitates.

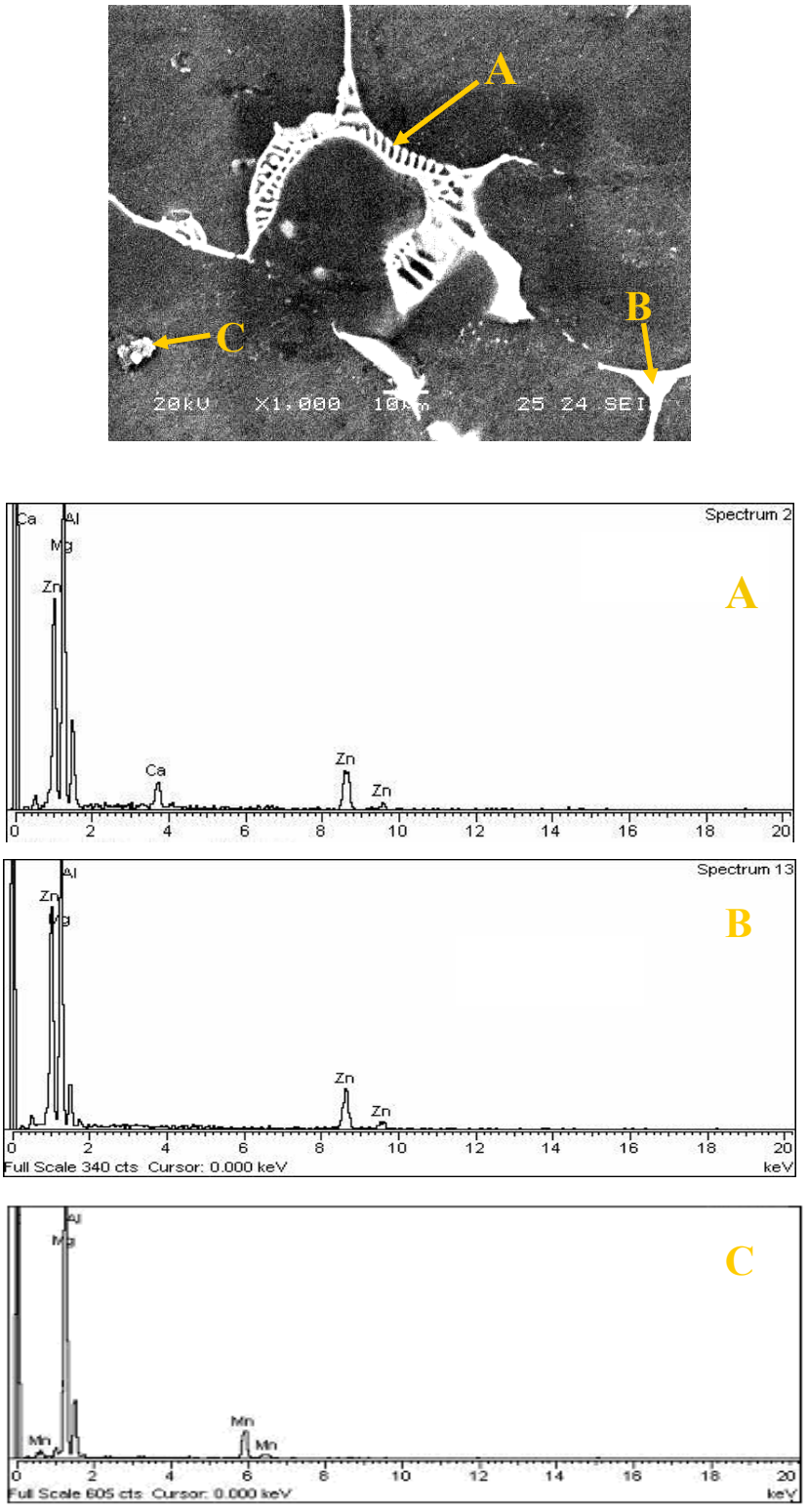

Figure 4.19: SEM microstructure and EDS pattern of ZA84+0.5Ca added alloy

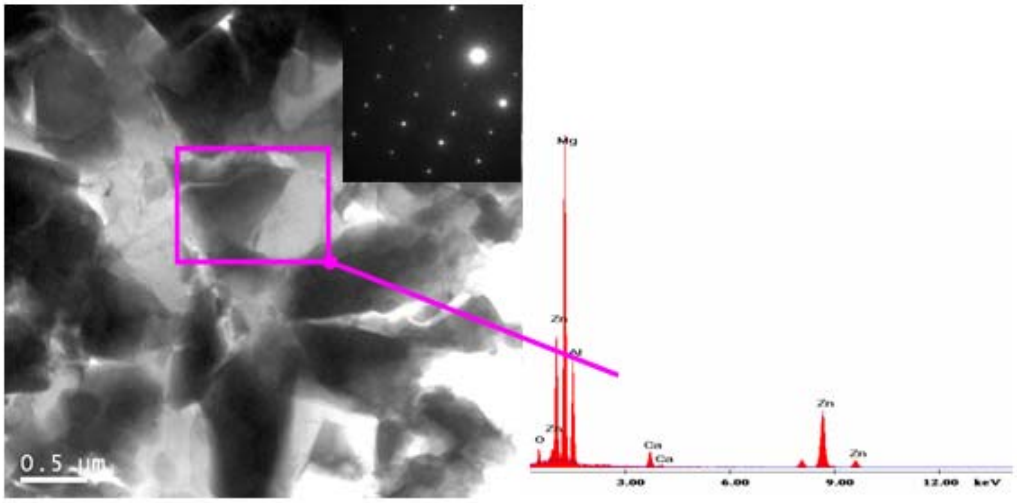

Figure 4.20: TEM microstructure, EDS and SAD pattern for the quaternary Mg-Zn-Al-Ca phase of ZA84+0.25Ca alloy

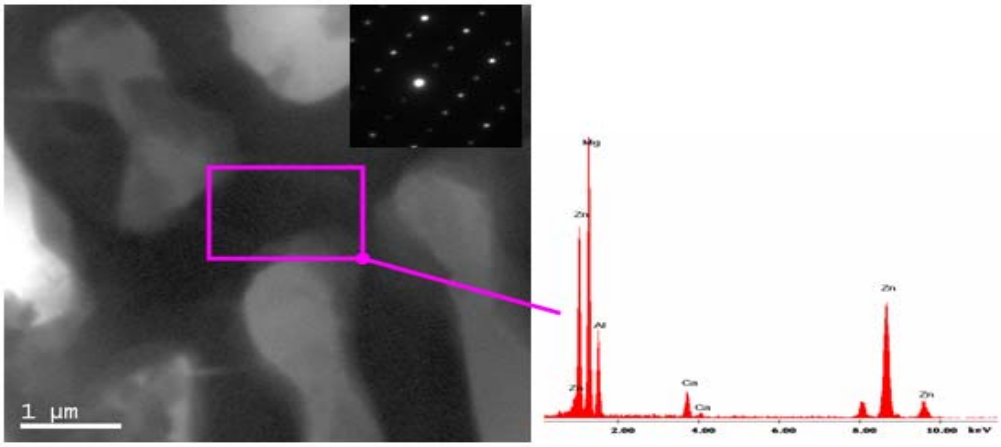

Figure 4.21: TEM microstructure, EDS and SAD pattern for the quaternary Mg-Zn-Al-Ca phase of ZA84+1Ca alloy

The EDS results of elements show that Mg has nearly 38.22 at%, aluminium 24.54 at%, zinc 21.23 at% and calcium 16.01 at% of elements, which are equivalent to the atomic stoichiometry of the $Mg_{10}Al_6Zn_4Ca$ precipitates. The SAD pattern of the phase is shown in the same figure. It is observed from the SAD pattern that the atoms are arranged in a cubic structural manner of the precipitates.

4.2 SOLIDIFICATION BEHAVIOUR

4.2.1 ZA84 ALLOY

The typical DTA thermograms characteristic values of peak, onset temperatures and enthalpy required for the phase transformation, and other details are summarized in Table 4.4 and Figure 4.22. It can be inferred from the figure that there are two peaks, one corresponding to a α-Mg matrix and the other to a second phase transformation. The primary α-Mg starts nucleating at 593.44ºC, which corresponds to monotectic reaction L (liquid)$\rightarrow$ L_1 (Liquid) + α-Mg (solid) and then grows into the melt till the second phase transformation. The second phase transformation reaction in the temperature range of 346.62 ºC and 354.22ºC and the solidification range of this alloy is 245.19ºC. During second phase transformation, a mixed quasi-peritectic reaction occurs in the reaction zone, α-Mg + $L_1\rightarrow$ α-Mg + τ + $L_2\rightarrow$ α-Mg + τ + ϕ phases. It is further confirmed from the microstructure (marked as M1 in Figure 4.22) that the as-cast alloy consists of the τ and ϕ phases (τ-continuous and ϕ-isolated phases). In addition, from the equilibrium of DTA investigation, it is found that the liquidus and solidus temperatures of ZA84 alloy are 593.44ºC and 346.62ºC, respectively (from the equilibrium).

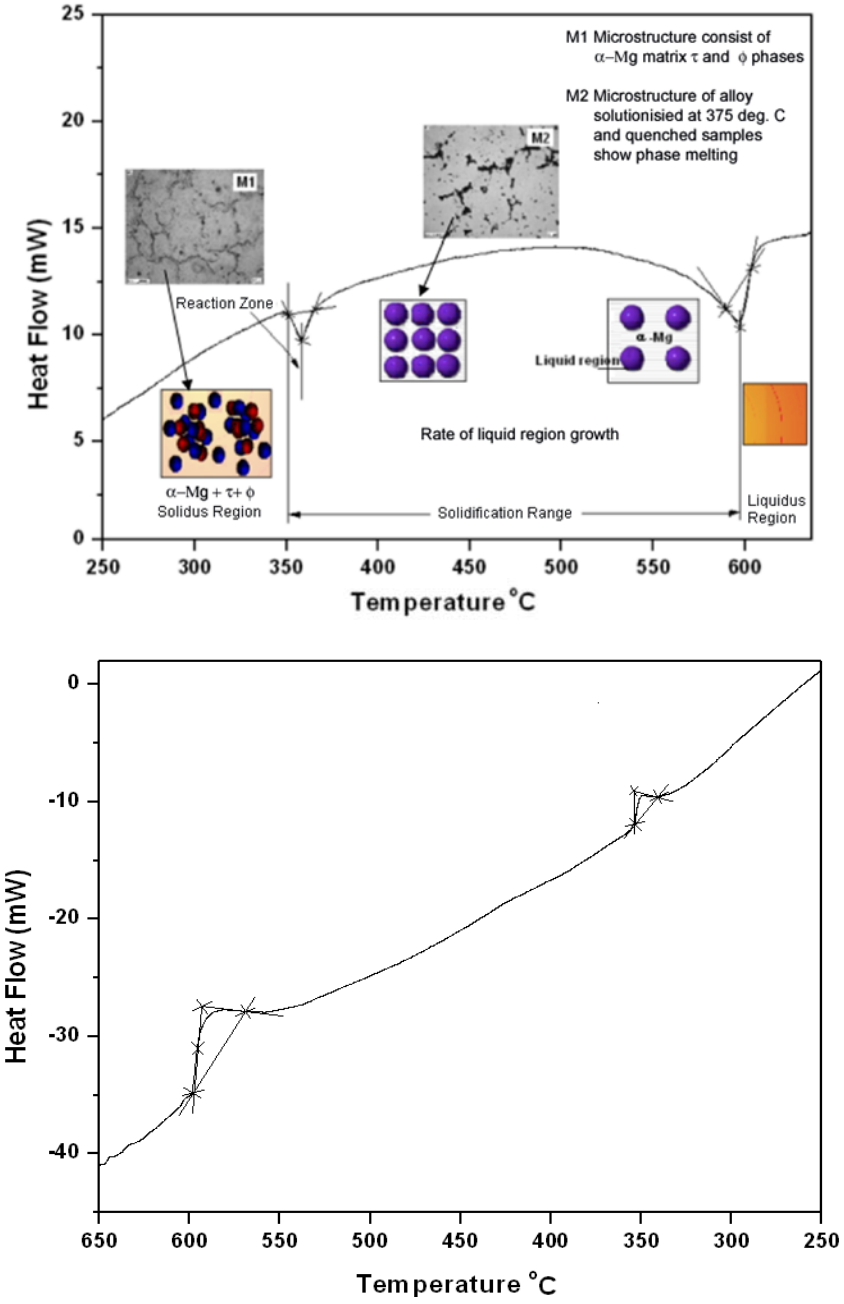

Figure 4.22: DTA thermograms of ZA84 alloy (a) heating curve (b) cooling curve

Table 4.4: Peak, onset temperatures and enthalpy required for phase transformation in as-cast alloy

Process	Matrix Melting			Second Phase Transformation			Solidification Range
	Peak Temp. in ºC	Onset Temp. in ºC	Enthalpy mW/mg	Peak Temp. in ºC	Onset Temp. In ºC	Enthalpy mW/mg	
Heating	596.78	572.56	+63.778	358.34	351.07	+12.2426	238.44
Cooling	590.11	567.81	-49.3771	350.11	338.17	-8.4839	251.94
Equilibrium	593.44	570.18	*	354.22	346.62	*	245.19

+ represent endothermic reaction, - represent exothermic reaction * Not considered

4.2.2 ZA84 + 1%Sb

The typical DTA heating thermogram of ZA84+1%Sb-added alloy is presented in Figure 4.23. It can be inferred from the figure that there are three peaks, corresponding to the melting of the Mg_3Sb_2 phase, melting of the α-Mg matrix and the second phase transformation. The Mg_3Sb_2 phase transformation observed in the early stage of solidification corresponds to the reaction Liquid $\rightarrow$L (liquid) + Mg_3Sb_2 because of formation at higher temperatures. Then, the primary α-Mg starts nucleating at 591.14ºC, corresponding to monotectic reaction L (liquid) + Mg_3Sb_2 $\rightarrow$ L_1 (Liquid) + α-Mg (solid) + Mg_3Sb_2, which then grows into the melt till the second phase transformation. The second phase transformation reaction in the temperature 351.62ºC and the solidification range of this alloy is 239.52ºC. During second phase transformation, a mixed quasi-peritectic reaction occurs in the reaction zone, α-Mg + L_1+ Mg_3Sb_2 $\rightarrow$ α-Mg + τ + L_2+ $Mg_3Sb_2$$\rightarrow$ α-Mg + τ + ϕ + Mg_3Sb_2 phases. It is further confirmed from the microstructure (shown in Figure 4.11) that the as-cast alloy consists of the τ and ϕ phases (τ-continuous and ϕ-isolated phases) with Mg_3Sb_2 phase.

4.2.3 ZA84+ XCa (0.25, 0.5 and 1%Ca)

Under the equilibrium condition, the solidification sequence of 0.25wt% Ca-added ZA84 alloy (Figure 4.24), there are three reaction temperatures: 591ºC (liquidus temperature, not shown in the figure) 406.66ºC and 343.6ºC (solidus temperature). During solidification, the α-Mg starts nucleating and grows into the melt up to 406.66ºC, when a new second transformation occurs corresponding to the reaction, L_1 + α-Mg→ α-Mg+ γ + L_2. Further phase transformation occurs in the temperature 349.92 ºC, corresponding to the reaction, L_1 + α-Mg + γ → α-Mg + γ + τ. There is no evidence in the formation of Al_2Ca phase; however, for AZ91 alloy, the Ca addition leads to the formation of this phase. In AZ91 alloy, the formation of Al_2Ca phase has occurred because of lower zinc content and high aluminium content to 9 wt% fact of the high electronegativity difference.

Besides, the enthalpy required for I-phase transformation for ZA84+0.25%Ca-added alloy is approximately 55% lower than that of base alloy which implies that the volume fraction of the ternary precipitates has decreased with the addition of a small amount of Ca. The characteristic values of peak, onset temperatures and enthalpy required for the phase transformation, and other details are summarized in Table 4.5. The complete elimination of ternary phase occurs when 1% Ca is added to the base alloy and the phase occurs in the temperature range from 380ºC to 408ºC (see Fig. 4.26). The higher volume percent of quaternary phases in the microstructure, the EDS, corresponds to $Mg_{10}Al_6Zn_4Ca$.

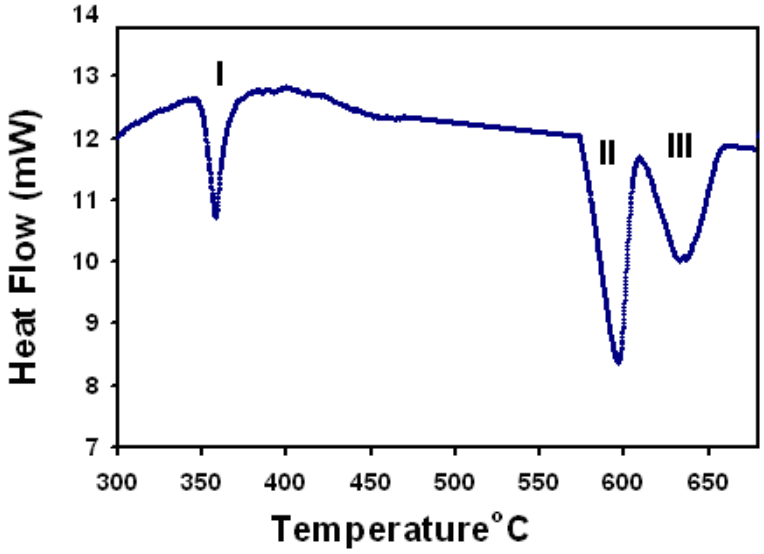

Figure 4.23: DTA heating curve of ZA84+1%Sb alloy

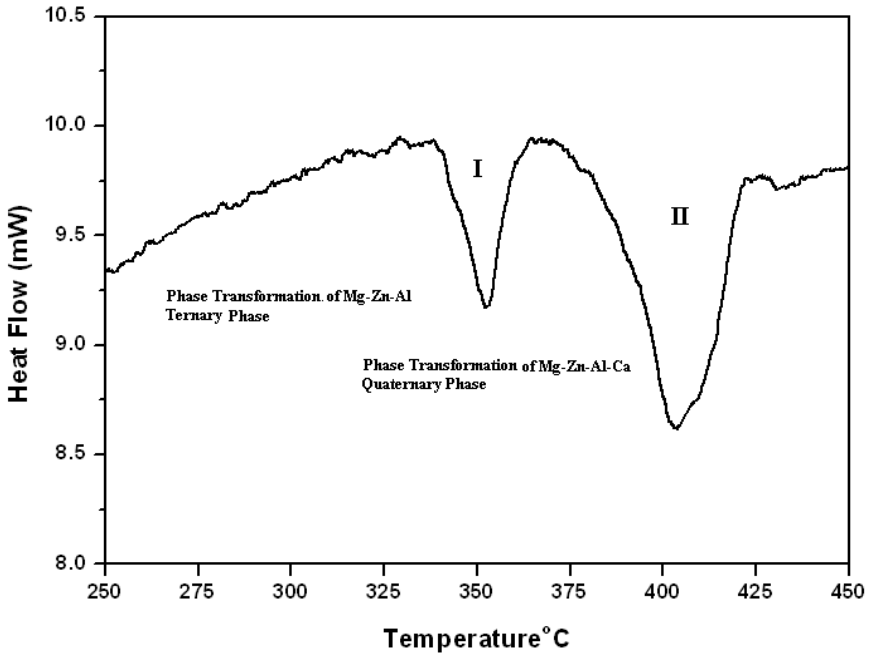

Figure 4.24: DTA heating curve of ZA84+0.25Ca alloy

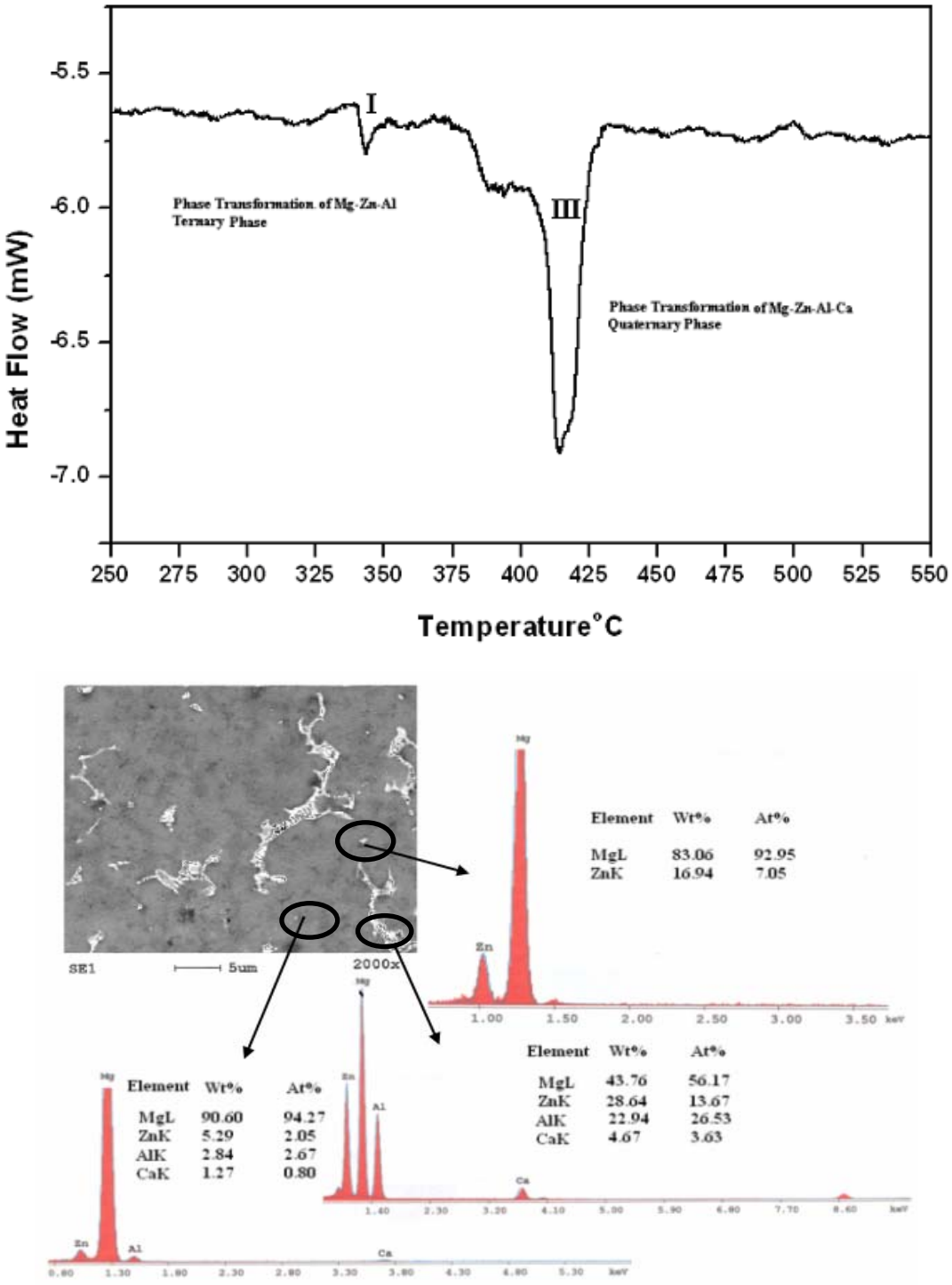

Figure 4.25: DTA curve and the SEM-EDS of ZA84+0.5Ca

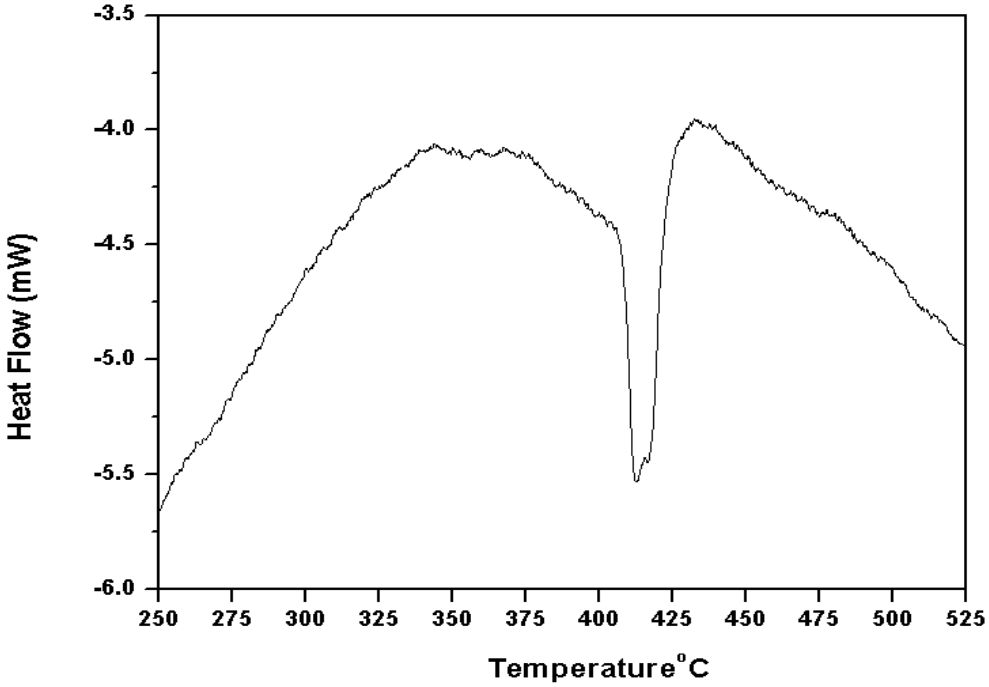

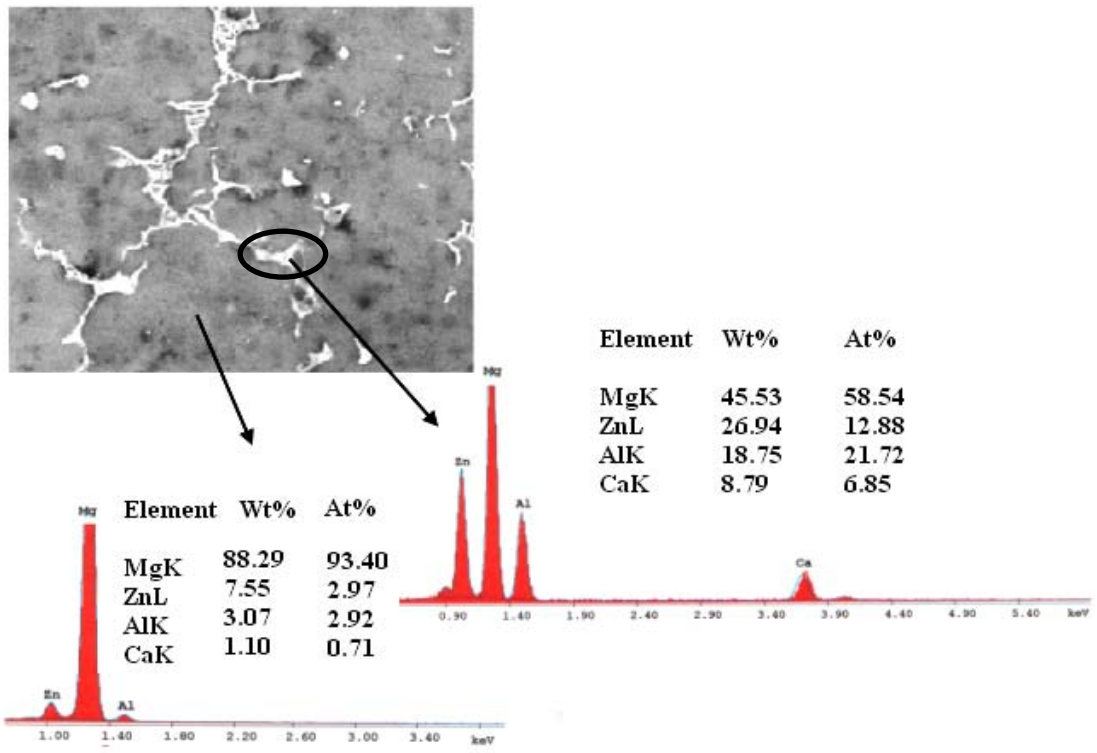

Figure 4.26: DTA curve and the SEM-EDS of ZA84+1Ca

Table 4.5: Peak, onset temperatures and enthalpy required for phase transformation in ZA84+XCa added alloys

Phase Formation Sequence	Onset Temp. in ºC	Peak Temp. in ºC	Enthalpy (µ.v.s/mg)
ZA84 alloy			
I Phase	344.50	349.92	12.33
ZA84+0.25Ca alloy			
I Phase	343.63	349.92	5.5764
II Phase	384.80	406.66	9.334
ZA84+0.75Ca alloy			
I Phase	382.79	385.12	0.42585
II Phase	408.59	413.73	10.2197
ZA84+1Ca alloy			
I Phase	407.52	414.82	11.3912

4.3 MICROHARDNESS

The role of elemental additions on the microhardness of the matrix and precipitate regions has been investigated using the CLEMEX microhardness indenter machine. The average of the five results is reported in this chapter.

4.3.1 ZA84 ALLOY

As discussed in section 4.1, the microstructure of ZA84 alloys shows the presence of the matrix region and of two different morphologies of precipitates having $Mg_{32}(Al,Zn)_{49}$ and $Mg_5Al_2Zn_2$. The micro-indentation at the different regions mentioned above is shown in Figure 4.27 and the results are reported in Table 4.6. Since the precipitate is black in color under optical microscope, it was found difficult to measure the indentation. Hence it is decided to make an indentation such a way that it lies on the matrix adjoining the precipitates making it clearly visibled. It is further inferred from the results that the precipitates are harder than the matrix region. The continuous phase τ-$Mg_{32}(Al,Zn)_{49}$ is slightly harder than the isolated phase $Mg_5Al_2Zn_2$ because of the different crystal structure and thermal stability of the precipitates.

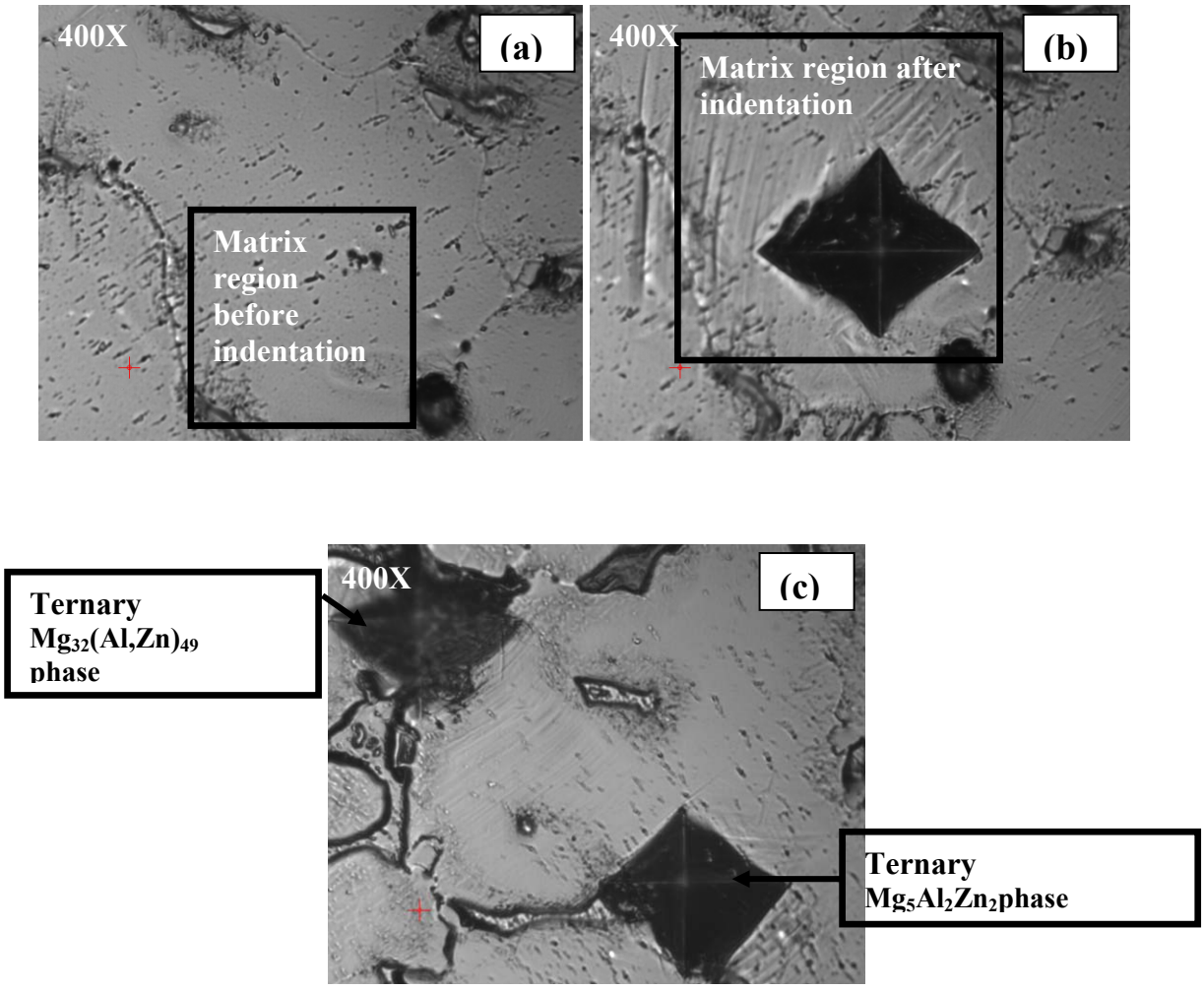

Figure 4.27: Microstructure of ZA84 alloy showing (a) the matrix region without indentation (b) with indentation on the matrix (c) with indentation on both the $Mg_{32}(Al,Zn)_{49}$ and $Mg_5Al_2Zn_2$ phases

Table 4.6: Microhardness of the matrix and phases in ZA84 alloy

Indentation area	Microhardness (HV_{100g})
Matrix	85± 5
$Mg_{32}(Al,Zn)_{49}$	163 ± 6
$Mg_5Al_2Zn_2$	140 ± 5

4.3.2 ZA84+0.5Sb

The microstructure of Sb-added alloy shows the presence of α-Mg**,** $Mg_{32}(Al,Zn)_{49,}$ $Mg_5Al_2Zn_2$ and Mg_3Sb_2. The mechanisms of phase formation of Sb added alloys are explained clearly in section 4.1.2. The indentation location of microstructure at different regions is presented in Figure 4.28 and the values are presented in Table 4.7. From tables 4.6 and 4.7, it is observed that the hardness values of microstructural constituents (**$Mg_{32}(Al,Zn)_{49}$ and $Mg_5Al_2Zn_2$**) are not much differ in both base and Sb added alloys.

Table 4.7: Microhardness of the matrix and phase in ZA84+1Sb alloy

Indentation area	Microhardness (HV_{100g})
Matrix	90± 5
$Mg_{32}(Al,Zn)_{49}$	170 ± 6
$Mg_5Al_2Zn_2$	145 ± 5

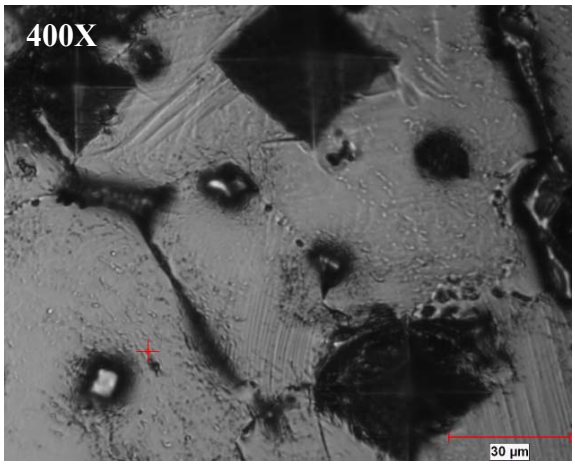

Figure 4.28: Microstructure of ZA84+0.5Sb showing indentation on the matrix and ternary phase

4.3.3 ZA84+0.5Ca

The microhardness and indentation location of Ca-added ZA84 alloy is shown in Figure 4.29 and the values are reported in Table 4.8. It can be observed from the values that the Ca addition effectively influences in increasing the hardness of the as-cast alloy. The modified microstructure of the Ca-added alloys shows the presence of the $Mg_{10}Al_6Zn_4Ca$ quaternary phase, which is thermally more stable than the ternary phase. The quaternary phase is harder (210±5 HV) than the matrix, which may influence more stability at higher temperature. The matrix region of the alloy is harder at 92±5 HV than the base alloy (85±5 HV) because of more segregation of Ca at the grain boundaries as well as inside the grains. The microstructural studies strongly support the microhardness results.

Table 4.8: Microhardness of the matrix and phase in ZA84+1Ca alloy

Indentation area	Microhardness (HV_{100g})
Matrix	92± 5
$Mg_{10}Al_6Zn_4Ca$	210±5

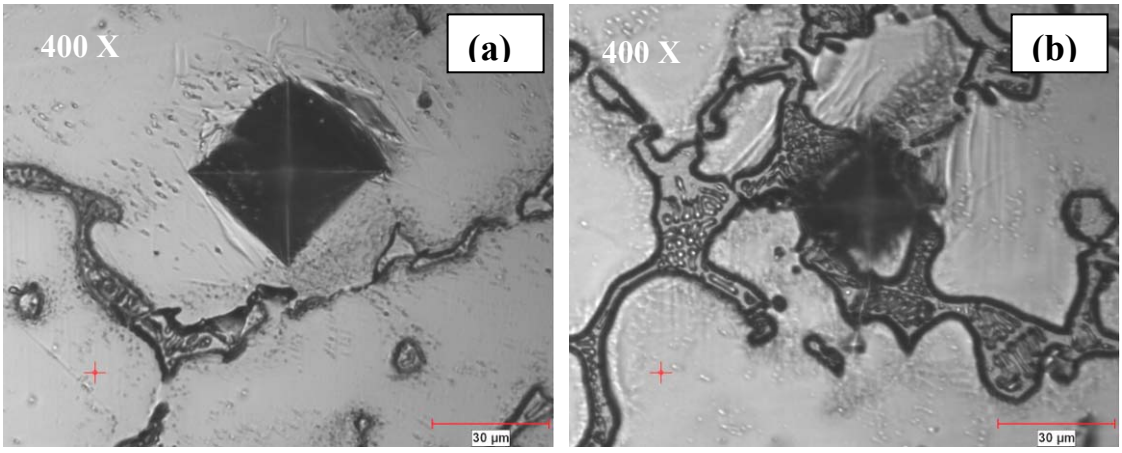

Figure 4.29: Microstructure of ZA84+1Ca alloy showing the (a) matrix region, (b) Mg-Zn-Al-Ca quaternary phase with indentation

4.4 TENSILE PROPERTIES

The effects of alloying addition on the tensile properties of ZA84 alloy have been investigated by tensile testing using the fully computerized INSTRON 1195 machine. Tensile samples prepared in accordance with the ASTM E8 standard were tested for room as well as at 150^{o}C temperature. Five samples were tested for each alloy and two-sided Student's "t" test at 95% of significance was used to analyze the reported results. Strain gauge was used to get the % elongation at room temperature testing, but at high temperature the % elongation values were manually calculated from the marking on the sample (25mm gauge length was used). Fractography studies were also carried out to identify the micro-fracture mechanism.

4.4.1 ZA84 ALLOY

The tensile properties reported in this base alloy are in fact marginally above the reported value of the earlier research article in the same alloy. Yang [49] recently reported that the location of the sample drawn makes the difference in the properties because of changes in thickness and cooling rate. Therefore, the samples drawn from all

the castings are maintained in the same location to enable uniform grain size, volume percentage of precipitates, cooling rate and porosity. Tensile properties, such as the ultimate tensile strength (UTS), yield strength (YS) and ductility (% of elongation) of the as-cast ZA84 alloy for room and elevated temperatures at 150ºC, are presented in Figure 4.30. From the figure, it can be seen that the strength properties of the alloy at room temperature are UTS=160 MPa, YS=115MPa and elongation at 5%. Within the margin of experimental errors a simple two-sided Student's "t" test can be used to analyze the results. At the higher temperature of 150ºC, the UTS value reduces from 160 to 135 MPa without change in YS along with increased elongation from 5 to 6.5%.

The improvement in elongation is attributed to the activation of slip system in the magnesium matrix. Normally, at room temperature, the basal slip planes are activated, whereas at higher temperatures the other slip systems such as prismatic and pyramidal planes are activated as shown in Figure 4.31. Moreover, the elevated temperature properties of commercial AZ91 alloy are drastically reduced at this temperature range because the presence of $Mg_{17}Al_{12}$ has more diffusivity and easily coarsens when the temperature exceeds 100ºC. Under the same conditions, ZA84 alloy yielded better strength properties at elevated temperature because the presence of $Mg_{32}(Al,Zn)_{49}$ phase has low diffusivity and requires more temperature to coarsen the phase. Besides, the mechanism for enhancing the elevated properties of the ZA alloys is still unclear.

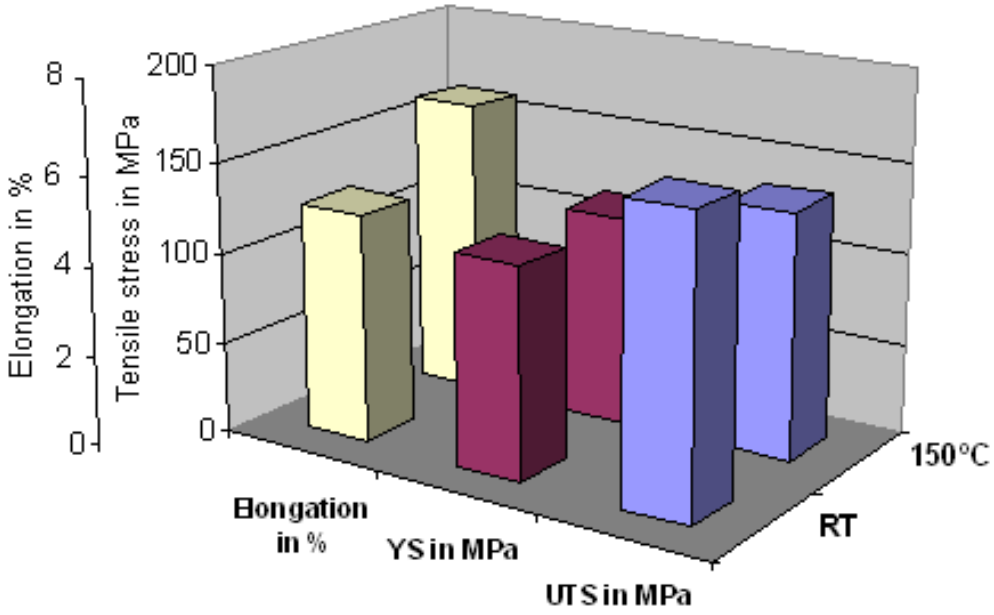

Figure 4.30: Tensile properties of ZA84 alloy at RT and 150ºC

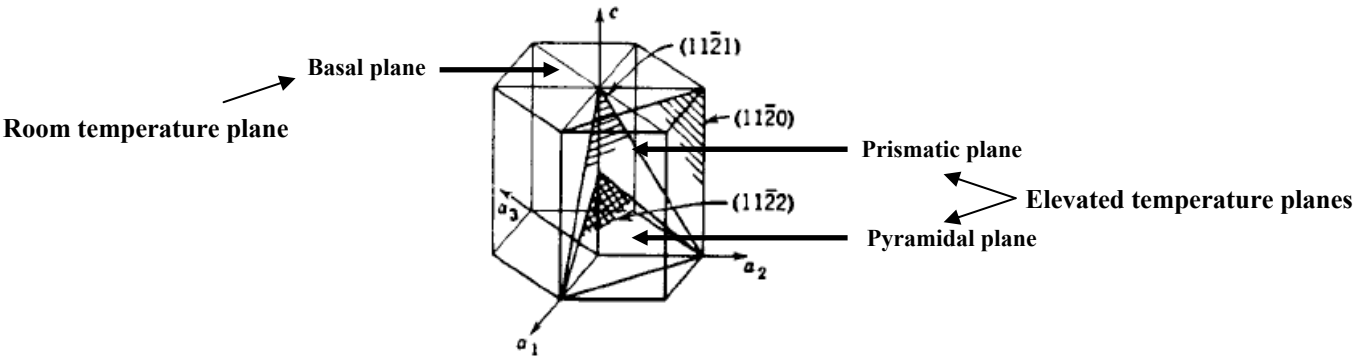

Figure 4.31: Schematic diagram showing different slip systems [90]

Normally, the failure of hcp-structured magnesium alloys is brittle through cleavage and quasi-cleavage fracture. The fractograph of the tensile-fractured surfaces of ZA84 alloy tested at ambient temperature is exhibited in Figure 4.32**.** It can be observed from the figure that the fracture surface of ZA84 alloy, which consists of intergranular fracture with some secondary cracks (A). The presence of more cleavage planes (B in Figure 4.32) with constrained plastic zone (C) noticed in the structure confirms the limited ductility. In cleavage fracture, micro-cracks develop along certain crystal planes, which are mostly in the basal plane (0001) of magnesium [52]. When the load is applied, micro-cracks are initiated that are readily connected to grain boundaries, thereby making the failure of ZA84 alloy brittle and intergranular.

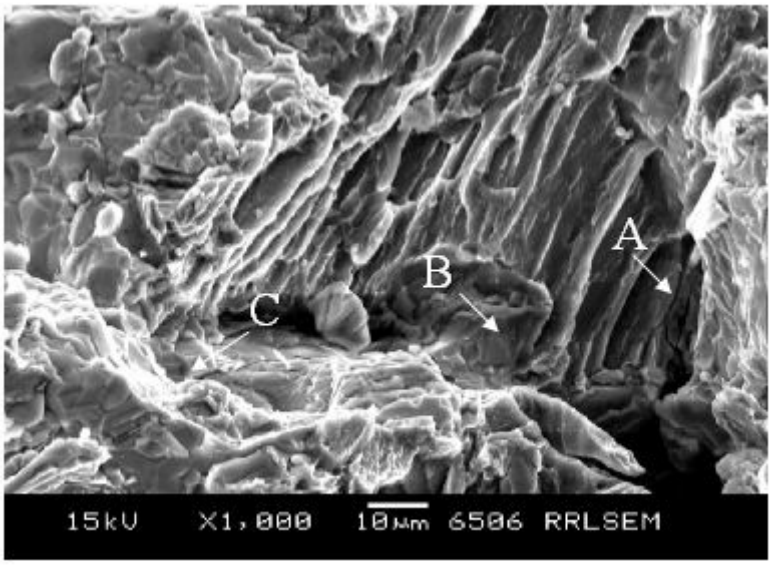

Figure 4.32: Tensile fracture surface of ZA84 alloy

4.4.2 ZA84+XSb (X=0.2%, 0.5% and 1%)

The room and the high temperature (150ºC) tensile properties evaluated for the alloys are given in Table 4.9. It can be inferred from the table that the Sb addition has a significant influence on the strength properties of ZA84 alloy. For all wt% of Sb

addition, the strength (yield and ultimate tensile strengths) properties are found to increase both at ambient and elevated temperatures as compared to the ZA84 base alloy strengths with slight reduction in the ductility. However, the maximum strength properties are obtained with 0.2 wt% Sb addition. The improvement in strength properties are attributed to the following: (1) refinement of the $Mg_{32}(Al,Zn)_{49}$ precipitates, (2) strengthening owing to the secondary Mg_3Sb_2 precipitates, and (3) strengthening by grain refinement. Moreover, the presence of a substantially greater number of fine ternary $Mg_{32}(Al,Zn)_{49}$ phase and stable secondary precipitates on a variety of planes with the matrix would have contributed to the superior strength properties. Owing to the finer microstructure of 0.2%Sb-added alloy, the size of ternary phase decreased from 105 μm to 30 μm, which distributes uniformly throughout the matrix along with Mg_3Sb_2 precipitates. The presence of high thermally stable (1228ºC) Mg_3Sb_2 precipitates have slow diffusion, which resist the dislocation motion and the grain boundary sliding during deformation at elevated temperatures. While increasing Sb beyond 0.2%, the size of the ternary phase (from 3 μm to 4.5 μm, diameter) increases when compared with the base alloy microstructure, in addition changing in the morphologies of secondary precipitates. The reduction noticed in the mechanical properties with the higher amount of Sb addition is due to the presence of a large number of thicker needle-shaped Mg_3Sb_2 phase (from 1.4 μm to 2.2 μm, diameter) along the grain boundaries, which cuts apart the Mg matrix during deformation.

Based on the microstructural analysis and the result of mechanical properties, three mechanisms contribute to the improvement of tensile strength of Sb-added ZA84 alloys. They are: solid solution strengthening (σ_{ss}), grain boundary strengthening (σ_{gb}) and precipitation strengthening (σ_{ppt}). As per the phase diagram and the microstructure analysis, the solid solution strengthening and grain boundary strengthening are almost negligible because of limited solid solubility and the negligible effect on the grain refinement. The major contribution is to the improvement of the mechanical properties of ZA84 alloy by precipitation strengthening. It is easier to determine the strengthening

sources of as-cast ZA84 alloy with 0.2% Sb, which by the precipitation strengthening contribution is approximately $180 - 160 = 20$ MPa and is presented in Table 4.10. Normally during plastic deformation, owing to the hardness difference between the hard intermetallics and the ductile matrix, an internal stress develops that acts as a back-stress for the dislocation movement and contributes to an improvement in the tensile strength of the alloy.

Table 4.9: Effect of Sb addition on tensile properties of ZA84 alloy

Alloy Code	RT			150 °C		
	UTS (MPa)	YS (MPa)	% of Elongation	UTS (MPa)	YS (MPa)	% of Elongation
ZA84+0.2Sb	180	135	4	162	130	4
ZA84+0.5Sb	165	128	2	150	112	3
ZA84+1Sb	162	124	1.5	140	102	2

Table 4.10: Strengthening mechanism of Sb in ZA84+0.2Sb alloy

Strengthening mechanism	Strength
Solid solution strengthening [Negligible solid solution]	-
Grain boundary strengthening [54 µm size (base 62 µm) Δ=12 µm]	-
Precipitation strengthening [Mg_3Sb_2 phase]	180-160 = 20 MPa

At higher temperature, the tensile strength of Sb-added alloys decreases because of the prismatic precipitate plates, which are thought to be less effective obstacles to dislocations gliding on the non-basal plane or cross slip activated at the elevated

temperature. As they are not perpendicular to the slip planes, the effective area decreases as an obstacle to dislocation slip.

The fracture surface of 0.2 %Sb-added alloy shows that the river pattern between different local cleavage facets of the same cleavage plane (see Fig. 4.33(b)) and the crack have propagated through the grains (transgranular T in Fig. 4.33(b)) and consumed more energy, which leads to an increase in the strength properties. This is due to the fact that the coarse precipitates at the grain boundaries are refined by the addition of Sb. With 1% Sb addition (Figure 4.33 (c)), the well-defined cleavage planes with multiple secondary cracks observed on the fracture surface suggest a reduction in ductility and strength. Cleavage planes observed without river patterns indicate that the grain may have been orientated at a right angle to the main tensile axis, causing the fracture to propagate very easily on a single plane [234]. Yet, the constrained plastic zone and coarse cleavage fracture observed can be correlated to the presence of the large and needle-shaped Mg_3Sb_2 phase. These results well corroborate the mechanical testing.

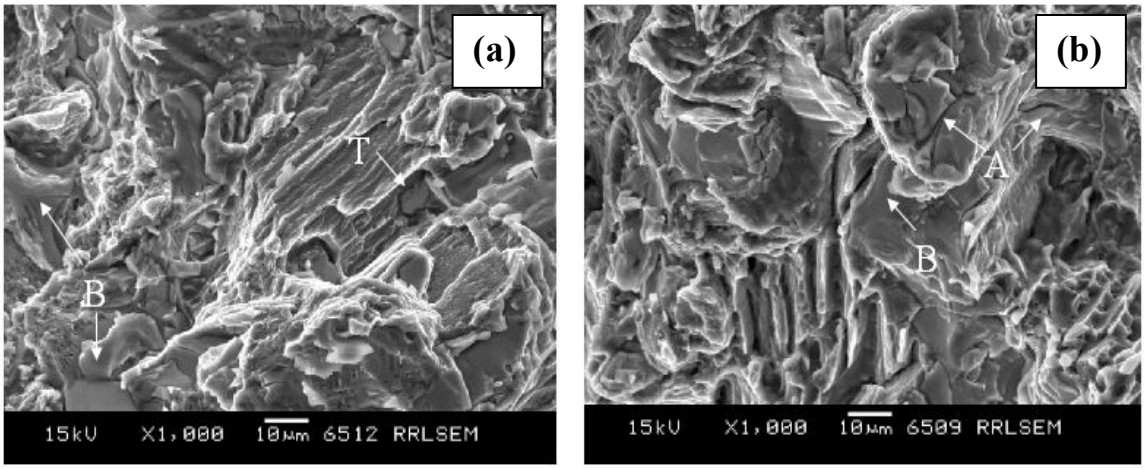

Figure 4.33: Effect of Sb on the tensile fractography of (a) ZA84+0.2Sb and (b) ZA84+1Sb alloys

4.4.3 ZA84+XCa (X=0.25%, 0.5% and 1%)

The effect of Ca additions on the tensile properties of ZA84 alloy is shown in Table 4.11. At room temperature, the Ca addition shows a marginal improvement in the tensile properties compared with ZA84 base alloy. The maximum strength properties were observed at 0.5% Ca addition with considerable reduction being observed in elongation. With 0.5%Ca addition, the UTS increases from 160MPa (base alloy) to 168MPa and the elongation decreases from 5% to 3% with marginal improvement in the yield strength of alloy. The ternary phase and quaternary Mg-Zn-Al-Ca phase are coarse and highly brittle, which greatly affect the ductility compared to the strength. With an increase in the Ca from 0.5% to 1wt%, the strength properties are marginally reduced because of the coarsening and formation of more quaternary coarse brittle phases at the grain boundaries. It is reported [48] in the Ca addition to AZ91 alloy that increased thermal stability of the β precipitates inhibited the grain boundary sliding and resulted in an improvement in creep resistance of the alloys. In addition, the discontinuous precipitation of β had a deleterious effect on the mechanical properties of Mg-Al alloys. The small amount of calcium addition to alloy AZ91 effectively suppressed the discontinuous precipitation of β. This was also an important factor in improving the mechanical properties of the alloys.

Table 4.11: Effect of Ca addition on tensile properties of ZA84 alloy

ALLOYS	RT			150ºC		
	YS (MPa)	(UTS MPa)	% of Elongation	YS (MPa)	UTS (MPa)	% of Elongation
ZA84+0.25Ca	110	162	5	108	140	7
ZA84+0.5Ca	116	168	3	102	160	5
ZA84+1Ca	101	154	2	96	138	6

The room temperature tensile fracture surface of the Ca-added ZA84 alloys is shown in Figure 4.34. A relatively ductile fracture is evident for all failed tensile specimens. The observation at a higher magnification showed that the fracture surfaces exhibit a mixed mode of features: small dimples around damaged intermetallics particles, ductile areas with numerous micro-voids associated with matrix precipitates, flat areas characterized by a fine population of shallow dimples containing coarse grain boundary precipitates and ridges at which the crack had changed its direction of propagation. This suggests that the fracture process is complex and involves different micro-mechanisms. Three main fracture micro-mechanisms contributing to the overall fracture are identified:

• Coarse primary voiding at large intermetallic particles, most of which are fractured or separated from the matrix;

• Ductile intergranular fracture, characterized by crack nucleation and propagation along the grain boundaries covered with coarse incoherent η precipitates accompanied by the PFZ much softer than the grain interior, promoting easier crack propagation within the PFZ;

• Ductile transgranular fracture through grain, generated by the micro-voids formation occurring by the interaction of dislocations with the precipitates in grain interiors.

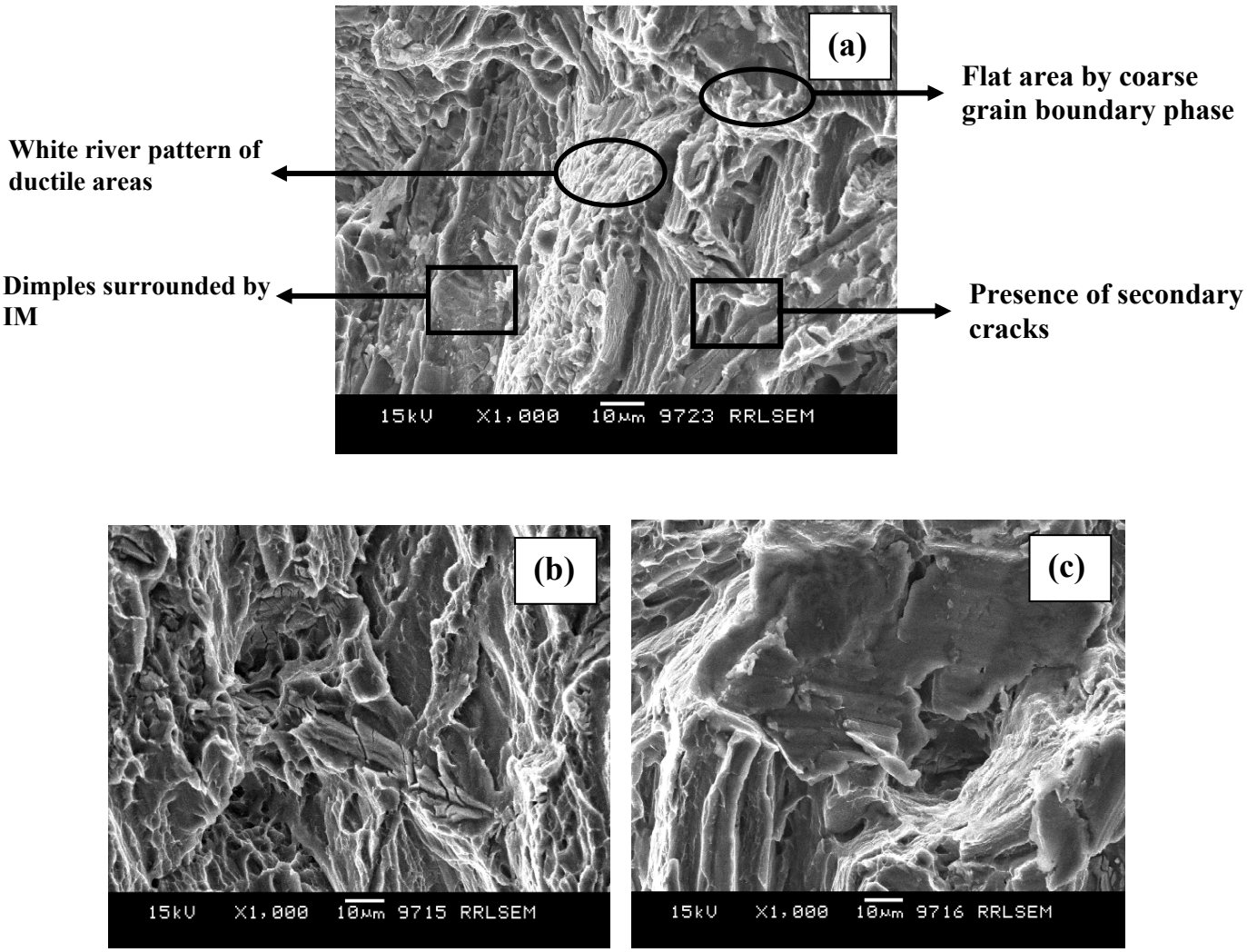

Figure 4.34: Tensile fractography of (a) ZA84+0.25Ca (b) ZA84+0.5Ca, and (c) ZA84+1Ca-added alloys

4.5 CREEP

4.5.1 ZA84 ALLOY

There is no creep data available in the literature for ZA84 alloy. The creep behaviour of as-cast ZA84 alloy has been carried out in a short-term test at 150ºC for 500 hrs with an initial stress of 50 MPa**.** It is found that in most of the cases, the steady-stage creep is not reached even after 500 hrs. The short term creep testing conducted on this alloy is to get an idea on the high temperature behavior. .

The creep curve of ZA84 alloy is shown in Figure 4.35. It can be observed from the figure that the region of short interval up to A is called primary creep and the long continuous region up to B is called secondary creep, followed by the tertiary region. The creep rate is continuously decreased during the primary stage to reach a constant creep rate and stabilized for a longer time during the secondary stage. Finally, the rate is increased drastically till failure during the tertiary stage. The minimum creep rate of ZA84 alloy is $8.24105X10^{-4}$ % h^{-1} and the creep strain is 0.6678 %, which is lower than the commercial AZ91 alloy [3]. There are various mechanisms postulated for improving the creep. One of the major mechanism is the presence of ternary $Mg_{32}(Al,Zn)_{49}$ at the grain boundaries, which pins the grain boundary migration and sliding during high temperature, impeding the dislocation movement. However, it is necessary to understand the micro mechanisms by analyzing the pre and post microstructure.

4.5.2 ZA84+0.2Sb

Figure 4.36 shows the creep behaviour of Sb-added alloys at 150^{o}C. The 500 h test indicates that the creep behaviour of 0.2% Sb added alloy exhibits superior behaviour to the base alloy. On the other hand, Srinivasan et al [3] reported that the presence of more volume fraction of needle shaped Mg_3Sb_2 brittle intermetallic acted as a stress raiser and is the reason for the poor creep performance of high percentage Sb added alloy especially for its volume greater than 0.2%. So, in this study, creep studies have been carried out only for 0.2Sb-added alloy, the other additions not being

beneficial for mechanical properties. The stable Mg_3Sb_2 intermetallic is the reason for the improvement in creep behaviour. Extended secondary creep regions along with low creep strain indicate that the alloy exhibits excellent creep resistance owing to the presence of thermally stable Mg_3Sb_2 intermetallic.

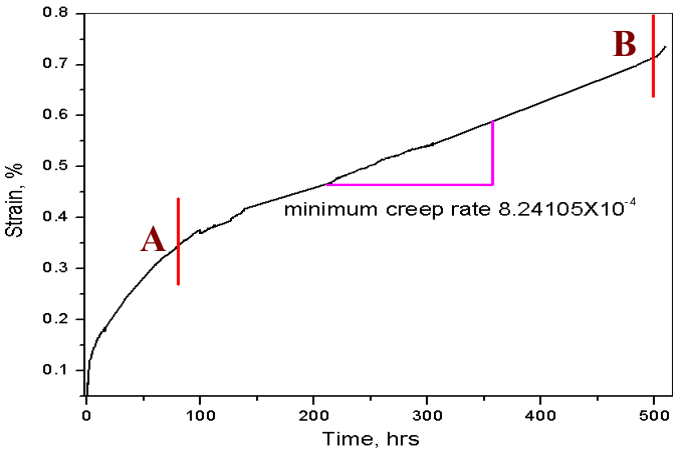

Figure 4.35: Creep curve of the ZA84 alloy tested at 150ºC with an initial stress of 50 MPa

4.5.2 ZA84+XCa(X=0.25% and 0.5%)

Figure 4.37 shows the creep curves of ZA84 alloy with and without Ca additions. The creep tests were conducted at 150ºC, with an initial stress of 50 MPa. It can be observed from the figure, the improvement in creep properties with calcium addition is evident. The creep rate of ZA84 alloy is 8.241×10^{-4} $\%h^{-1}$, whereas the creep rate of alloy B is 3.882×10^{-4} $\%h^{-1}$, respectively, which is approximately 60% lower than that of the ZA84 alloy. The improvement in creep resistance of Ca-added alloys is attributed to the following reasons: (1) Formation of new thermally stable quaternary precipitates along the grain boundaries, (2) Diffusion of solute atoms of Al and Zn at elevated temperature could be minimized if the amounts of Al and Zn in solid solution of Mg matrix are lowered. The change in microstructure that accompanies Ca addition results in an alloy having a stable matrix with well-fortified grain boundary precipitates.

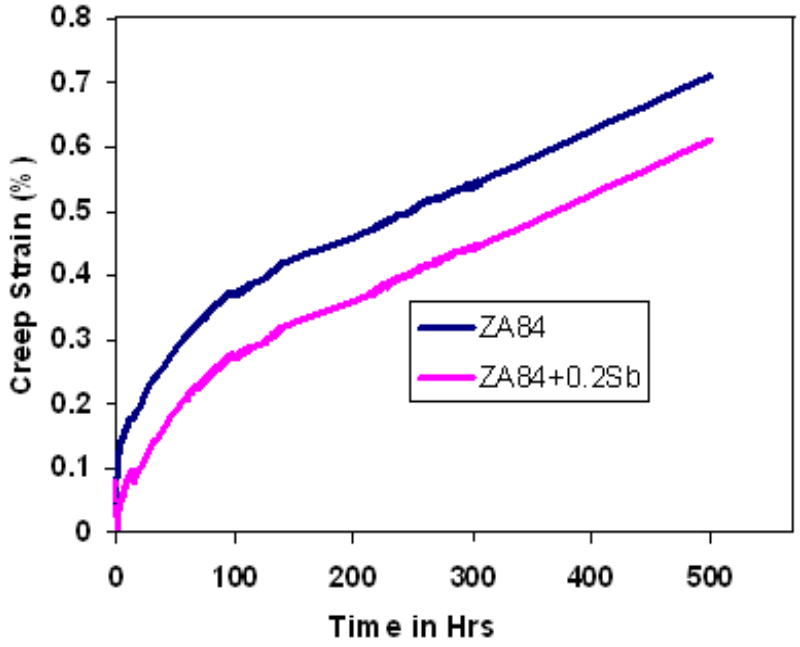

Figure 4.36: Creep curves of ZA84+0.2Sb and ZA84 alloys

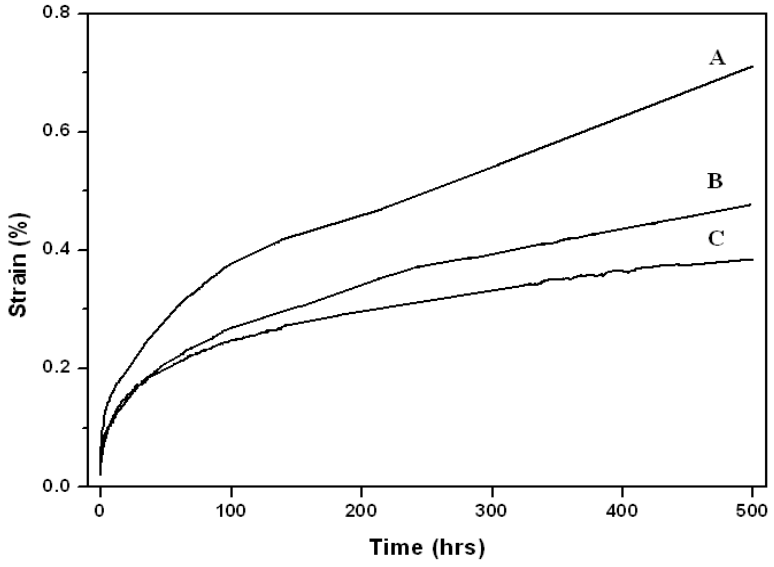

Figure 4.37: Creep curves of the Ca-added alloys A: ZA84, B: ZA84+0.25Ca, C: ZA84+0.5Ca

4.6 EFFECT OF COMBINED ADDITION OF Sb AND Ca

4.6.1 MICROSTRUCTURE

The scanning microstructure of ZA84+0.2Sb+0.5Ca alloy is shown in Figure 4.38. It can be observed from the figure that the microstructure consists of α-Mg, eutectic, quaternary $Mg_{10}Al_6Zn_4Ca$ and Mg_3Sb_2 phases in the presence of the $Mg_{32}(Al,Zn)_{49}$ ternary phase. The continuous τ-phases in the base alloy are suppressed by alloying addition and formation of new $Mg_{10}Al_6Zn_4Ca$ phases with hard Mg_3Sb_2 particles at the grain boundaries. Further, clear investigation on TEM analysis revealed that hard particles are present along with the quaternary phases. Those particles further strengthen the microstructure of the alloy with increase in the stability of the phases. The XRD analysis of ZA84+0.2Sb+0.5Ca alloy is presented in Figure 4.39 from which it can be inferred that the XRD identified only the α-Mg, and $Mg_{10}Al_6Zn_4Ca$ phases. No evidence of the ternary and Mg_3Sb_2 phases was observed because of lesser volume fraction. The Mg–Zn-Al and Mg_3Sb_2 phases could be identified in the SEM-EDX results is shown in Figure 4.40. The results are strongly supportive of the mechanism of alloying additions.

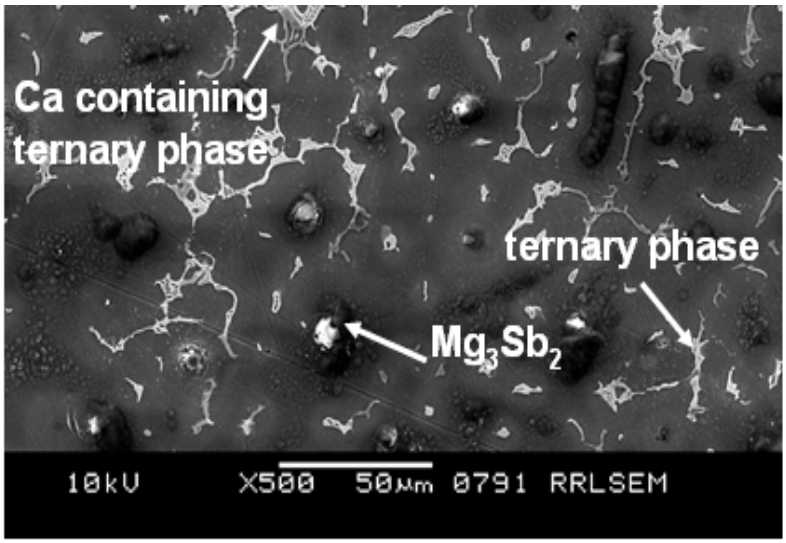

Figure 4.38: SEM Microstructure of ZA84+0.2Sb+0.5Ca alloy

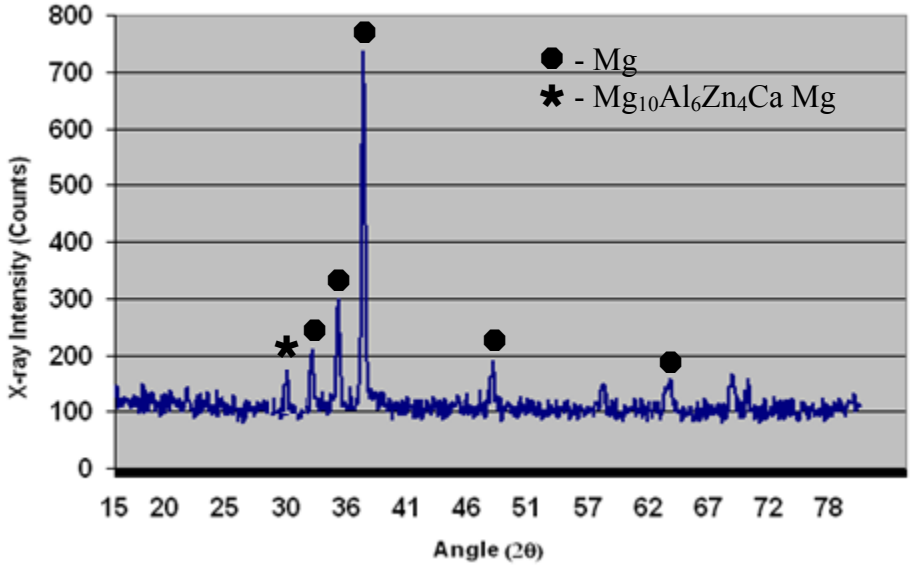

Figure 4.39: XRD analysis of ZA84+0.2Sb+0.5Ca alloy

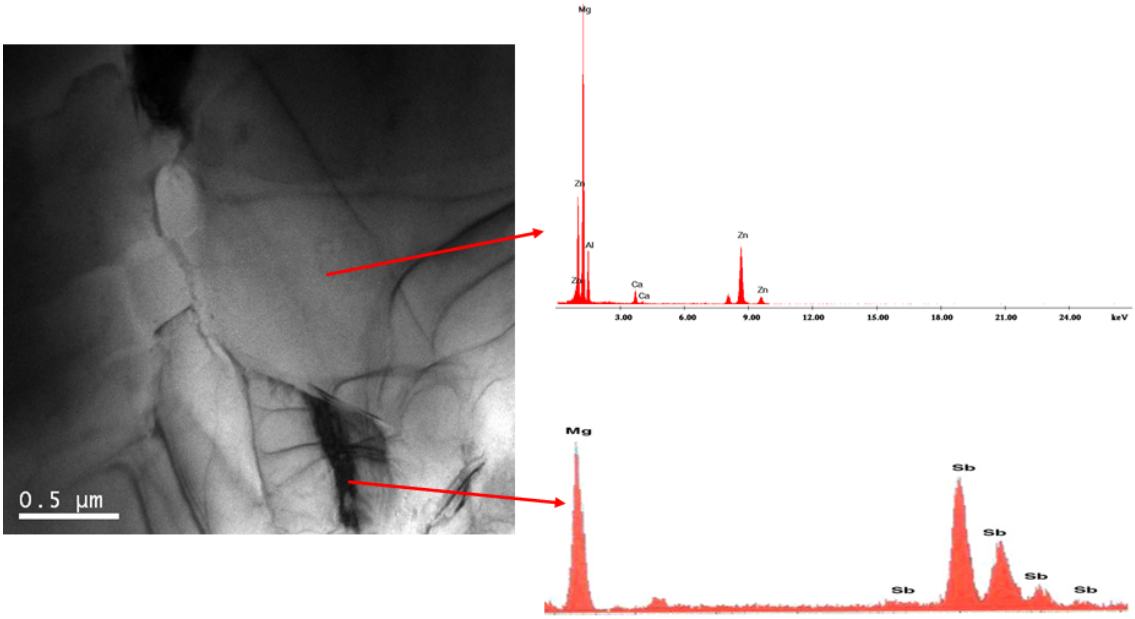

Figure 4.40: TEM Microstructure and EDS of ZA84+0.2Sb+0.5Ca alloy

4.6.2 TENSILE PROPERTIES

The room and the high temperature (150ºC) tensile properties evaluated for the alloys at an optimum percentage of Sb, Ca and a combination of (Sb + Ca) are given in Table 4.12. It can be inferred from the table that the Sb addition has a significant influence on the strength properties of ZA84 alloy as discussed in section 4.4.2. However, the maximum strength properties are obtained with 0.2 wt% Sb addition. The improvement in strength properties are attributed to the following: (1) refinement of the $Mg_{32}(Al,Zn)_{49}$ precipitates, (2) strengthening due to the secondary Mg_3Sb_2 precipitates, and (3) strengthening by grain refinement. Moreover, the presence of a substantially greater number of fine ternary $Mg_{32}(Al,Zn)_{49}$ phases and stable secondary precipitates on a variety of planes with the matrix would have contributed to the superior strength properties. At elevated temperatures, the Sb alloy shows better properties compared with the base alloy. This is due to the presence of high thermally stable (1228ºC) Mg_3Sb_2 precipitates, which are very stable, have slow diffusion (as compared with ternary precipitates) and resist the dislocation motion and grain boundary sliding during deformation. As discussed in section 4.4.3, the Ca addition shows marginal improvement in the tensile properties compared with the ZA84 base alloy. The maximum strength properties are observed at 0.5% Ca addition with a considerable reduction in elongation being observed. With 0.5%Ca addition, the UTS increases from 160MPa (base alloy) to 175 MPa and the elongation decreases from 4% to 2.5% without greatly affecting the yield strength of the alloy. The ternary and quaternary Mg-Zn-Al-Ca phases are coarse and highly brittle, which greatly affect the ductility compared with the strength.

The combined additions of (Ca+Sb) the tensile properties at both ambient and elevated, are superior to those of the base alloy. The improvement in strength properties are attributed to the following: (1) formation of new $Mg_{10}Al_6Zn_4Ca$ precipitates, (2) strengthening due to the secondary Mg_3Sb_2 precipitates, and (3) strengthening by grain refinement. The combined additions have little effect on the ductility of an alloy. The

tensile properties in this investigation are much closer to the commercial AZ91 alloy, which is weakened in the creep properties. The tensile fractograph surface of combined additions shown in the figure observed the presence of more cleavage plane as well as micro cracks initiated at the grain boundaries shown in figure 4.41. The tensile results are strongly support to the microfracture mechanism of combined alloying additions.

Table 4.12: Effect of individual and combined additions of Sb and Ca on tensile properties of ZA84 alloy

Alloy	RT			150 °C		
	YS (MPa)	UTS (MPa)	% of Elongation	YS (MPa)	UTS (MPa)	% of Elongation
ZA84	115	160	5	114	135	6.5
ZA84+0.2Sb	135	180	4	130	162	4
ZA84+0.5Ca	116	168	3	102	160	5
ZA84+0.2Sb+0.5Ca	146	192	3	138	182	5

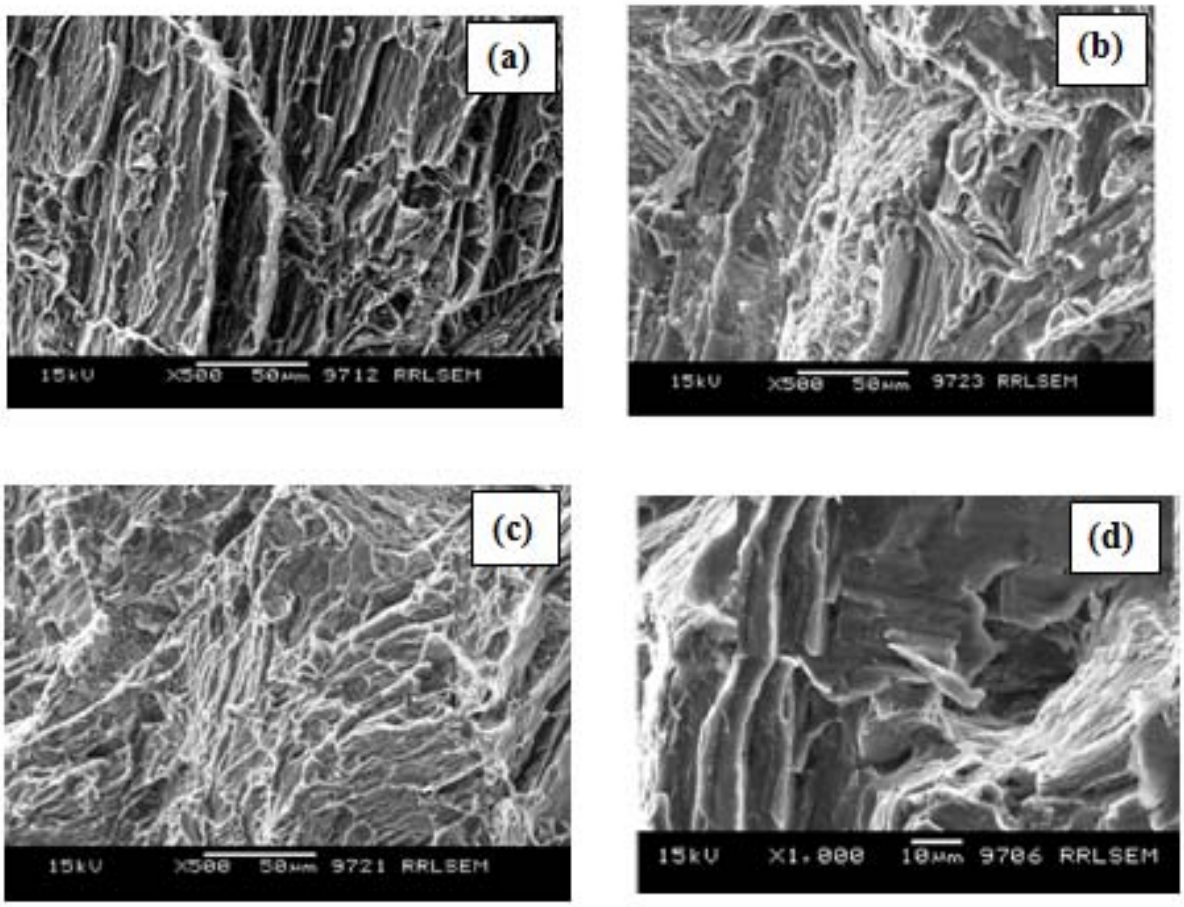

Figure 4.41: Tensile fractograph of (a) ZA84 (b) ZA84+0.2Sb, (c) ZA84+0.5Ca and (d) ZA84+0.2Sb+0.5Ca alloy

4.6.3 CREEP

The creep properties of individual and combined additions of Sb and Ca are shown in Figure 4.42. It can be observed from the Figure that the creep properties of base alloy minimum creep rate % h^{-1} ($8.24105X10^{-4}$) and creep extension % (0.6678) are higher than the combined addition of Sb and Ca minimum creep rate % h^{-1} (2.7142×10^{-4}) and creep extension % (0.3234); however, the ductility of an alloy has been reduced.

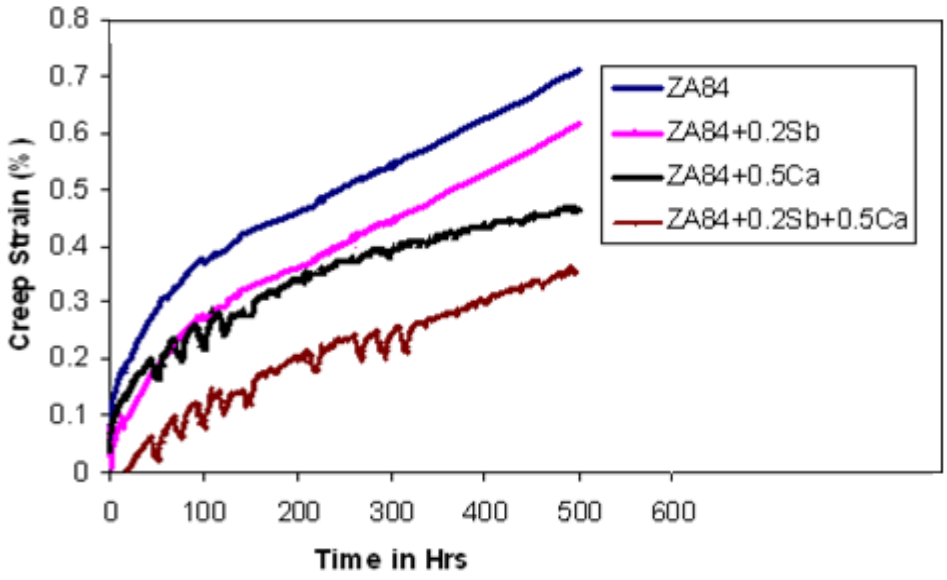

Figure 4.42: Creep curves of ZA84, ZA84+0.2Sb, ZA84+0.5Ca, ZA84+0.2Sb+0.5Ca alloys

Table 4.13: Creep properties of tested alloys

Testing condition	Alloy	Minimum creep rate, % h-1	Creep extension, %
150°C, 50 MPa 500 h	ZA84	$8.24105X10^{-4}$	0.6678
	ZA84+0.2Sb	$5.5454 X 10^{-4}$	0.6123
	ZA84+0.5Ca	3.882×10^{-4}	0.4172
	ZA84+0.2Sb+0.5Ca	2.7142×10^{-4}	0.3234

4.7 GRAIN REFINEMENT

As reported in Chapter 2, the literature on grain refinement of magnesium alloys is appraised with two broad groups: (1) Aluminum-free alloys and (2) aluminum-containing alloys. The aluminum-free alloys are generally well grain refined by Zr master alloys. On the other hand, aluminum-containing magnesium alloys are not suitable for Zr addition because of the formation of stable Al_4Zr phase. The carbon inoculation in the melt either by the *exsitu* addition or dissolution of carbon from crucible with aluminium forms Al_4C_3 heterogeneous nucleates, which act as an effective grain refiner. However, the process is complex and the formation of Al_4C_3 is not clearly stated in the literature [128]. In many cases, the debate is owing to the interaction between impurity elements and aluminum, which affect the formation of nucleant particles. Therefore, the new metallurgical process will provide a solution by introducing such particles in the form of a magnesium- based master alloy.

As a key point of the above statement, the present work is addressed to understand the grain-refining mechanism of Al_4C_3 nucleating particles in ZA84 alloy. The work plan is as follows:

- Synthesis of Al_4C_3 grain-refining particles from Al-SiC composites and the detailed characterization involving DTA, SEM and TEM studies
- Preparation and characterization of Mg-1wt%Al_4C_3 master grain refiner alloy
- To study the potency of Al_4C_3 grain refiner in ZA84 alloy and evaluation of the mechanical properties.

4.8 SYNTHESIS OF Al_4C_3 PARTICLES FROM Al-5wt%SiC

4.8.1 PROCESS OVERVIEW

The Al_4C_3 particles were synthesized from Al-5wt%SiC composites by stir casting route. Stir casting is a process that was adopted to prepare the composites. This process involves the introduction of preheated SiC powder (size 14μm) in liquid aluminium in the metal vortex. The amount of interfacial reaction product between Al and SiC forms Al_4C_3 and free Si by holding the liquid metal at 750ºC for different time intervals from 0, 5, 30, 60 and 120 min. The optimum interfacial product has been characterized by XRD, differential thermal analysis and microstructure investigations. A small amount (2 wt%) of salt flux having a composition of 48 wt%NaCl + 42 wt%KCl + 10 wt%NaF was added into the melt. It resulted in separation of interfacial products on the melt surface because of a change in the wetability of particles and liquid metal. The separated Al_4C_3 particles were reclaimed and skimmed out, which sleeve the wire mesh filter of 10 μm grid size. The unreacted SiC particles and some sort of sticky-free silicon were also filtered in the mesh. The resultant-reclaimed Al_4C_3 particles (5-8μm in size) are introduced into the magnesium melt to produce the Mg-1wt%Al_4C_3 master alloy.

4.8.2 SiC SUBSTRATES

X-ray powder diffraction spectrum recorded on as-received SiC crystals is shown in Figure 4.43. It can be observed from the figure that the α-hexagonal variety of 6H polytyp is largely predominant with the presence of a small quantity of β-group of 3C polytyp. The maximum intensity peak of the plane at 35.67º for 2θ angle is exactly matching with the International diffraction data of JCPDS for silicon carbide [235]. Further, microstructural characterization by scanning electron microscope (SEM) is shown in Figure 4.44, which reveals that the SiC particles of size varies from 10 to 16 μm size and the average mentioned in this chapter is 14 μm.

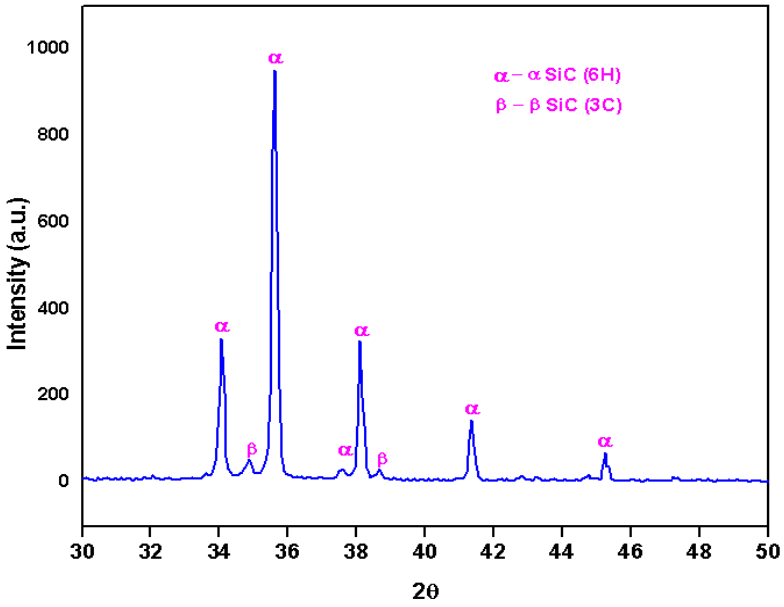

Figure 4.43: X-ray diffraction pattern of SiC particles

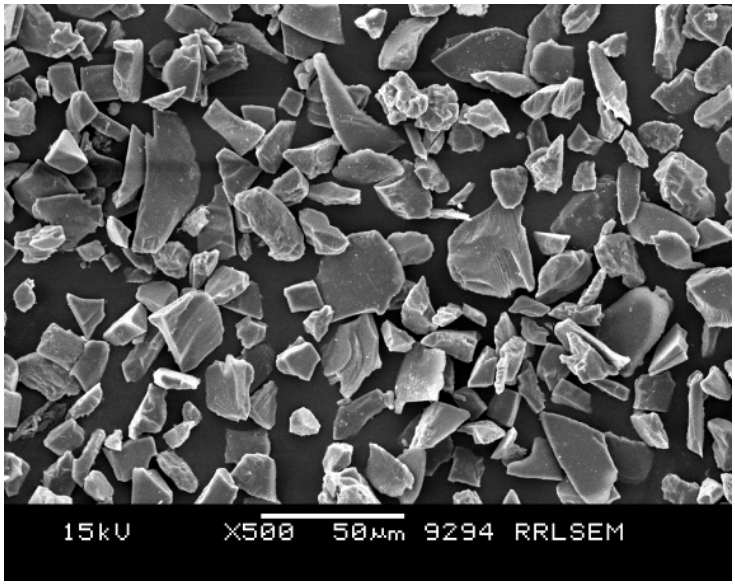

Figure 4.44: SEM microstructure of SiC particles

4.8.3 Al-5wt%SiC

The important steps involved in synthesizing the composite by stir casting method are: (i) melting the matrix (pure aluminium) and adding the wetting promoters such as 1wt% Mg; (ii) preheating the SiC particles at 400ºC for 2 hrs; (iii) mixing the matrix and reinforcement with the help of steel stirrer; and (iv) finally pouring the composites into the mould and allowing for normal solidification. The variation in the processing parameters is because of the alloy compositions; melt temperature and holding time, which influence on the final microstructure of the composites.

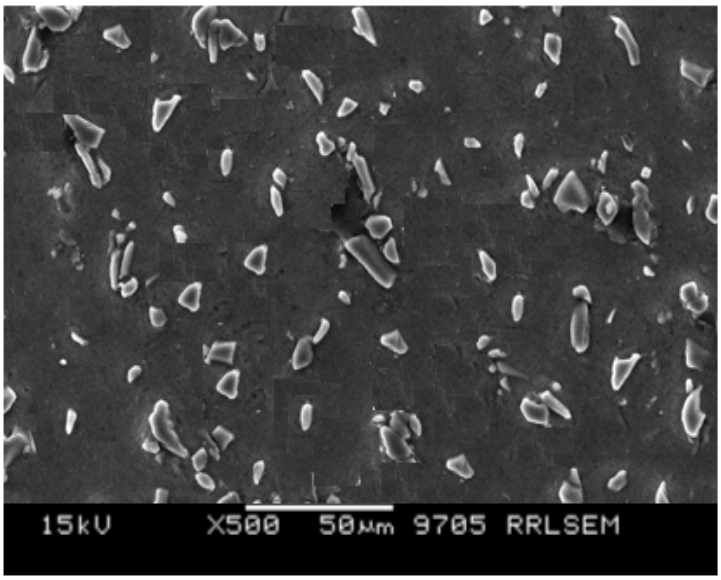

Figure 4.45: SEM microstructure of Al-5wt%SiC composite processed at 675ºC without holding

The scanning electron microstructure of Al-5wt%SiC composite processed at 675ºC without holding is presented in Figure 4.45. It is observed from the figure that the SiC particles are distributed well throughout the matrices with the interfacial region surrounded by a bright interface of SiC particles. Some particle-free zones (banding) and the clustering areas are also observed in the microstructure. The mechanisms

promoting interfacial bonding in MMCs, at the interface, can be chemical and/or mechanical. Bonding is chemical in nature when there is transport of charges across the interface as the metal and ceramic are brought into contact. Subsequent to the electronic interaction, a chemical reaction may also occur when there is transport of atoms from one or both of the components to the interface reaction site. On the other hand, bonding is mechanical when simple mechanical interlocking takes place between the adjacent component surfaces. In view of Figure 4.45 in the interfacial zone, the interface surfaces of the unreacted SiC particles can infer that the strength of interfacial bond in the composite was attributed to a combination of both mechanical and chemical bonding.

4.8.4 Al-SiC REACTION

Several investigations of phase equilibria in the ternary system Al-C-Si [204-206,236] have shown that silicon carbide is attacked by pure aluminium at temperatures higher or equal to 650ºC and up to about 1000ºC, according to the chemical reaction:

$$4Al\ (l) + 3SiC\ (s) \xrightarrow[650\text{-}1000^{o}C]{} Al_4C_3\ (s) + 3Si\ (s)$$

where (l) denotes the liquid state and (s) the solid state. The brittle Al_4C_3 is largely insoluble in the liquid aluminium and forms either as a continuous layer or as discrete precipitates around the SiC particles. The elemental silicon enters the remaining liquid aluminium to produce a binary liquid Al–Si alloy. Liquid-phase processing routes are particularly prone to this reaction because of the high temperatures employed and prolonged contact between the reinforcement and the matrix, especially in large-scale casting processes or when re-melting is involved. For the free energy changes of the reaction to be negative, the silicon produced by the reaction must dissolve in liquid aluminum to reduce the activity. The interfacial products are therefore Al_4C_3 and Al-Si liquid phase, which also contain a very small concentration of carbon. As discussed in the earlier section 4.8.3, heating a mixture of SiC and pure aluminium at temperatures below 650ºC is claimed to not produce any reactions, i.e., the two phases are in

thermodynamic equilibrium. At the abovementioned temperature, a reaction occurs, producing a three-phase monovariant equilibrium between SiC, Al_4C_3 and an Al-Si-C liquid phase. Such an interfacial reaction in Al-SiC_p composites is known to have several undesirable effects on the overall composite properties: (i) composites can be susceptible to corrosive environments owing to the presence of Al_4C_3, because Al_4C_3 is unstable in some environments such as water, methanol, HCl, etc. [204,211]; (ii) degradation of SiC itself occurs owing to the formation of Al_4C_3; and (iii) the elemental Si, formed as a result of the interfacial reaction, produces the Al-Si eutectic during fabrication or the heat-treating stage, resulting in undesired mechanical and physical properties of the matrix alloy. Therefore, fabrication of Al-SiC_p alloy composites devoid of Al_4C_3 has been one of the major concerns.

There are two widely accepted methods to control the interfacial reaction process: (i) addition of Si into the Al matrix; and (ii) artificial oxidation of SiC to produce SiO_2 layer on the surface of the SiC [206, 237]. The basic principle behind both methods is to enhance the Si activity by dissolving a certain amount of Si within the Al matrix. Such treatments, in turn, reduce the Al activity, resulting in suppression of the interfacial reaction between SiC and Al. Therefore, up to the selection of 5wt% SiC addition to Al alloy, the dissolved Si undergoes the maximum interfacial reaction beyond the wt% of SiC, and the microstructure of the composites contains unreacted SiC particles.

The rate of reaction between SiC and pure aluminium involves a long-term contact in the parameters such as the ***chemical composition of alloy and matrix***, ***melt temperature*** and ***time.*** The temperature selected in this study in the range of reaction zones in the interfacial products is 750ºC, whereas the time needs to be calculated for the complete reaction to form the Al-Si alloy with reacted Al_4C_3.

4.9 IDENTIFICATION OF INTERFACIAL PRODUCTS

When Al/SiC_p composite is exposed to elevated temperature, an interfacial reaction takes place to form Al_4C_3 and free the Si stated in Section 4.8.4. The amount of Si increases in the melt with respect to increase in interfacial reaction, which results in a decrease in the liquidus temperature of the composite. Therefore, the measurement of the liquidus temperature can be used to calculate the amount of Si dissolved into the matrix and quantify the amount of Al_4C_3 within the composite. For such purposes, a differential thermal analysis (DTA) was used and calibrated using various pure metals at a heating/cooling rate of 10^oC/min to measure the liquidus temperatures of the composites. The measured liquidus temperatures are converted into Si contents using the Al-Si phase diagram.

To find out the dissolved Si contents experimentally, it is necessary to decide how long the composites should be held at heat treating cycle to attain the equilibrium state. For such a purpose, variations in liquidus temperatures as a function of holding time at 750^oC were measured in pure Al/SiC_p composites. The design of experiments has been carried out on the basis of the literature as shown in Table 4.14.

Table 4.14: Design of experiments for composites

Material Code	Composites	Temperature in deg C	Time of holding after particle addition in min
as-processed	Al-5wt%SiC	675	0
A	Al-5wt%SiC	750	0
B	Al-5wt%SiC	750	5
C	Al-5wt%SiC	750	30
D	Al-5wt%SiC	750	60
E	Al-5wt%SiC	750	120

The amount of Si released from the SiC particles to form Al-Si alloy in holding at 750ºC for different time intervals from 0-120 min can be calculated using the solidus and liquidus temperatures. The solidus temperature would not be normally used for this purpose because it is less well defined than that of the liquidus.

The phase diagram of Al-Si alloy is presented in Figure 4.46. It is observed from the figure that the amount of Si increases with decrease in the liquidus temperature of the alloy. The DTA thermogram of composites as-processed condition at 675ºC without holding after particle addition is shown in Figure 4.47. It is inferred from the figure that the composite attributed to decrease the liquidus temperature to about 659.57ºC and the amount of calculated Si released from the SiC particle is nearly ≈ 0.5 wt%. However, holding at 675ºC for 0 minutes shows the lesser formation of interfacial reaction products in the vicinity of SiC, which is observed in the microstructure shown in Figure 4.45.

Figure 4.48 shows the DTA heating thermogram of Al-5wt%SiC_p composites during holding at 750^0C for 0 to 120 minutes. It can be observed from the figure that by holding at 750^oC for 0, 5, 30, 60 and 120 minutes, the liquidus temperature decreases to 659.49, 653.33, 636.64, 633.83 and 633.72^{o}C, respectively, and a peak corresponding to eutectic Si has been observed at 574.8^{o}C after 30 minutes of holding.

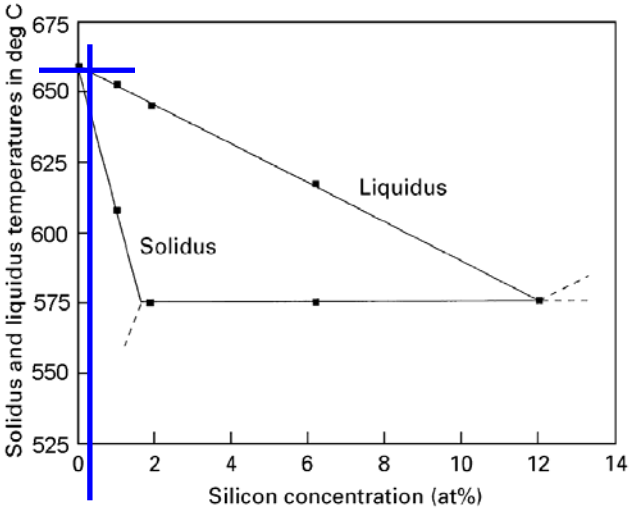

Figure 4.46: Phase diagram of Al-Si alloy [12]

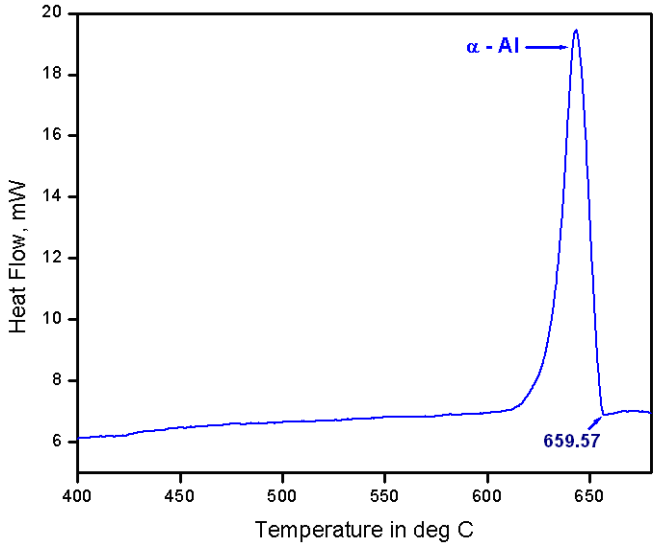

Figure 4.47: DTA thermogram of composites processed at 750ºC without holding

In composite, at Condition A, a strong endothermic peak appears at around 659.49ºC, corresponding to the melting of the matrix alloy. It is well known that the eutectic temperature of Al-Si alloy is 577ºC and maximum solubility of Si in solid Al at 577^{o}C is 1.65 at %. A very small decrease in liquidus temperature and the absence of eutectic Si peak indicated that the interfacial reaction between Al and SiC is small during composites fabrication of this condition. Considering that the melting of the pure Al occurs at 661.8ºC, the measured melting temperature of the Al-SiCp composite in its as-cast condition was somewhat lower. The reason for such observation is because of the presence of a small amount of impurities within the matrix or the incident interfacial reaction during the heating stage. In the case of the composite held for condition B, the general thermal response was observed to be similar to that observed from condition A except for a slightly lower melting temperature. With continued heating at the same temperature for 30, 60 and 120 min, the composite showed liquidus temperatures of 636.64, 633.83 and 633.72^{o}C for eutectic melting. Considering that 574.8ºC is the invariant reaction temperature of the Al-Si eutectic, it is evident that Si contents within the matrix alloy of the composite have reached the composition range of the

hypoeutectic Al-Si alloy. It is clearly noticed from the figure that the decrease in liquidus temperature and eutectic Si peak has been observed after just 5 minutes of holding. It indicates that the kinetics of interfacial reaction increases with the increase in the holding time.

There are two possible mechanisms that could explain this behaviour:

a. The reaction between Al and SiC is believed to follow the dissolution-diffusion-precipitation steps. The dissolution kinetics of SiC_p in Al has been suggested to be the rate-determining step in Al-SiC_p during the initial state of reaction. With the SiC_p dissolution, Al_4C_3 grows and Si will diffuse into the melt. With increasing time, a layer of Al_4C_3 forms around the SiC particle. It may act as a diffusion barrier for the diffusion of Si, C and Al. Hence, thereafter interfacial reaction kinetics decreases and follows the linear parabolic path shown in Figure 4.49 after reaching 60 minutes of holding.

b. On the other hand, during the initial state of reaction, Si originated from the interfacial reaction between SiC and molten Al diffuse away from interface at a faster rate as the Si concentration at interface is much higher than that of liquid Al. With increasing time, the diffusion distance of the Si atom from the interface is limited because of the: (a) active reactivity of Al-SiC_p at the interface reducing the concentration gradient of Si at the interface to the bulk; (b) the hydrodynamic interaction between liquid and the particles; (c) non-hydrodynamic interaction between the particles themselves [205]. Thus, the SiC particles were surrounded by an Si-rich band to form a local thermodynamical equilibrium adjacent to SiC particles and to reduce the kinetics of interfacial reaction drastically after 60 minutes of holding.

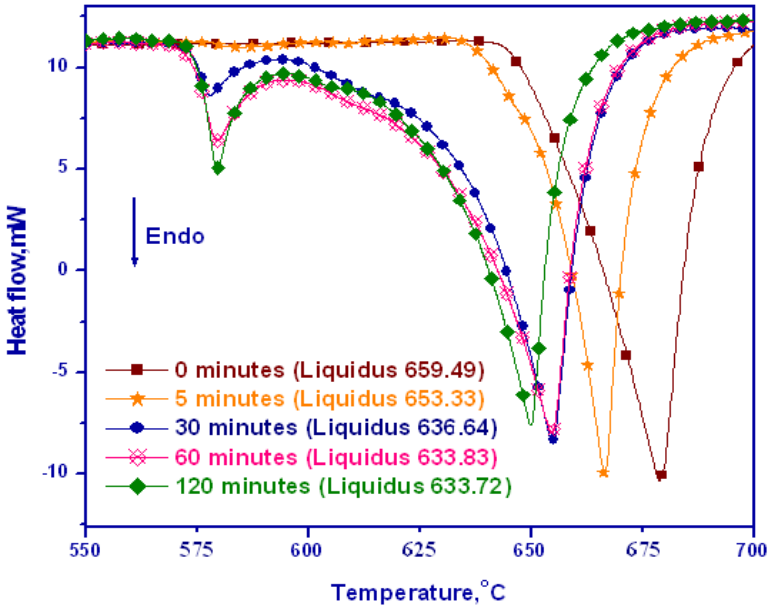

Figure 4.48: DTA heating thermogram of Al-5wt%SiC_p composites at 750°C for 0-120 min

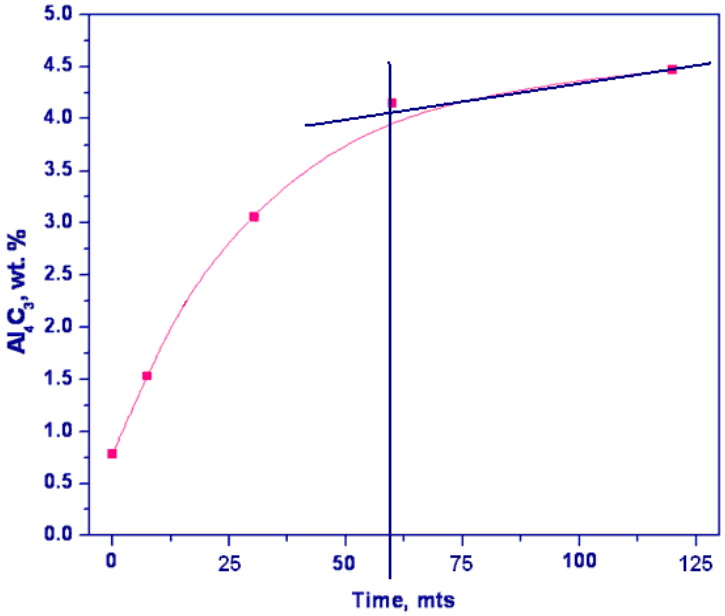

Figure 4.49: Al_4C_3 wt% with respect to holding time

4.9.1 TEM OBSERVATION

The transmission electron microstructure shown in Figure 4.50 helped to determine the nature of the Al-matrix/SiC_p interface during casting at 750ºC. In this case, formation of Al_4C_3 aggregates by reaction mentioned in section 4.8.4 and preferential precipitation of Si compounds nucleated from the interface were observed. In the first case, the Al_4C_3 formed discrete crystals, identified by EDS, growing not only inside the aluminium matrix but also into the SiC particle as clearly shown in the figure. However, care should be taken during specimen preparation to avoid the wet degradation of the Al_4C_3.

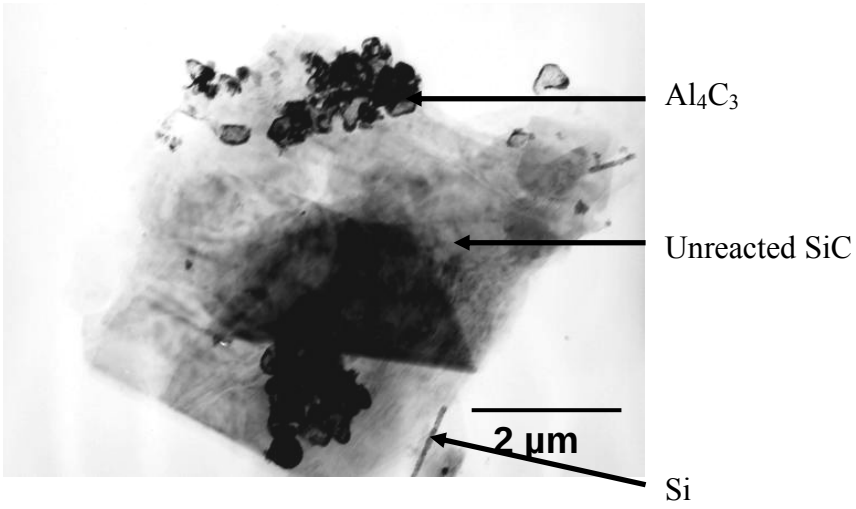

Figure 4.50: TEM observation of Al-5wt%SiC composite

4.10 RECLAMATION PROCESS

In this investigation, reclamation of interfacial particles by salt flux addition was used to extract interfacial Al_4C_3, reaction products, unreacted SiC and free Si from pure Al-SiC_p. In this process, after heat treating/holding at different intervals, the composites (including as processed), and 1wt % of salt flux (equimolar proportion of NaCl-KCl-5%NaF) were added to the composite melt through the vortex created by mechanical

stirring. After mixing for 30-60 seconds, the separation of reinforcement particles along with the reaction products starts leading to their floating because of a change in wetting on the melt surface and the interfacial products. Wetting is a term that describes the contact between a liquid and a solid surface. The amount of wetting is controlled by the thermodynamic tendency to minimize free energy. Atoms at surfaces possess higher energy because they have unsatisfied coordination numbers. They are attracted inwards by atoms in the bulk of the material, but by nature of being a surface, there are no atoms available to exert an outward force on the surface atoms and cause the net force to be zero. The addition of salt flux that creates surface atoms exerts stronger attractive forces on their surface neighbours, giving rise to surface tension. Surface atoms are also in a state of compression, thereby creating a new surface (moving additional atoms to the surface) on the interfacial products. The surface tension, γ, is expressed as energy per unit area, such as mJ/m^2. Liquids, with their ability to flow, can adjust their surface area and respond to these energetic demands by compressing themselves and minimizing the surface area. As a result, the interfacial products are floated on the melt surface.

The powders extracted by this process are termed reclaimed powder. The left over matrix melt in the crucible is poured into a cast iron mold and is termed reclaimed alloy. The flux introduced into the melt created the wetability changes between the particles and the melt. The fine particles of Al_4C_3 are surrounded by some fluxing agent; as a result, the low density particles are floated on the melt surface. The unreacted SiC particles cannot be reused as reinforcement because of the coexistence of the contamination; therefore, it is necessary to eliminate these contaminates or to find another use. XRD can be used as a qualitative means to monitor the extent of interfacial reaction in the Al-SiCp composite. Figure 4.51 shows the XRD results obtained from composites, showing how the extent of the interfacial reaction with temperature varies with holding time. As seen in the graphs, no evidence for the presence of interfacial reaction products could be seen from the as-processed composite. This is believed to be due to the short exposure time, although the process temperature was low and did not

occur in the interfacial reactions. It can also be observed from the figure (750ºC for 2 hrs) that the presence of Al_4C_3 phase as expected, besides SiC, and free Si from reaction between SiC and Al according to equation in section 4.8.4 was found. The diffraction peaks showing the incipient formation of Al_4C_3 and Si could be observed.

Detailed 3D morphologies of interfacial reaction products in the reclaimed powders are examined using SEM instrument at an operating voltage of 10-20 kV. For such purpose, the reclaimed powders are coated with gold to improve the image quality. The Secondary Electron Image (SEI) of SiC particle is shown in Figure 4.52; the SiC particle shows quite a rough morphology with an interfacial Al_4C_3. It can be seen from the figure that the reaction kinetics of Al_4C_3 formation varies with respect to the heat treating condition and different holding time. In Figure 4.52a, holding at 5 min limited reaction between SiC and Al takes place, and the growth of unreacted SiC and the Al_4C_3 particles are clearly seen. While increasing the holding time to 30 minutes, the interfacial reaction takes place very fast and the amount of interfacial products (see Figure 4.52b) is very much higher than that of the unreacted SiC. The 60-mins. held samples clearly reveal the hexagonal phases of Al_4C_3 particles, which are growing into unreacted SiC, and free Si cannot be revealed because of skimming out or formation of Al-Si alloy. The mechanism on the formation of Al_4C_3 particles from Al-SiC composites are clearly explained in section 4.9. The morphology of reaction product Al_4C_3 is found to be hexagonal in shape with an approximate size of 5-8μm.

4.11 Mg-1wt%Al_4C_3 MASTER ALLOY

The magnesium based Al_4C_3 master alloy is developed from reclaimed Al_4C_3 particles which is introduced into pure magnesium melting. Figure 4.53 shows the XRD pattern for Mg-1wt%Al_4C_3 master alloy. It can be observed from the figure that the peaks are identified as major Mg-peaks with the Al_4C_3 peaks indicating that the particles distributed uniformly throughout the magnesium matrix with some unreacted

SiC particles present in the master alloy. Future research needs to focus on gaining a better understanding of the effect of impurity chemistry on the nucleant particles.

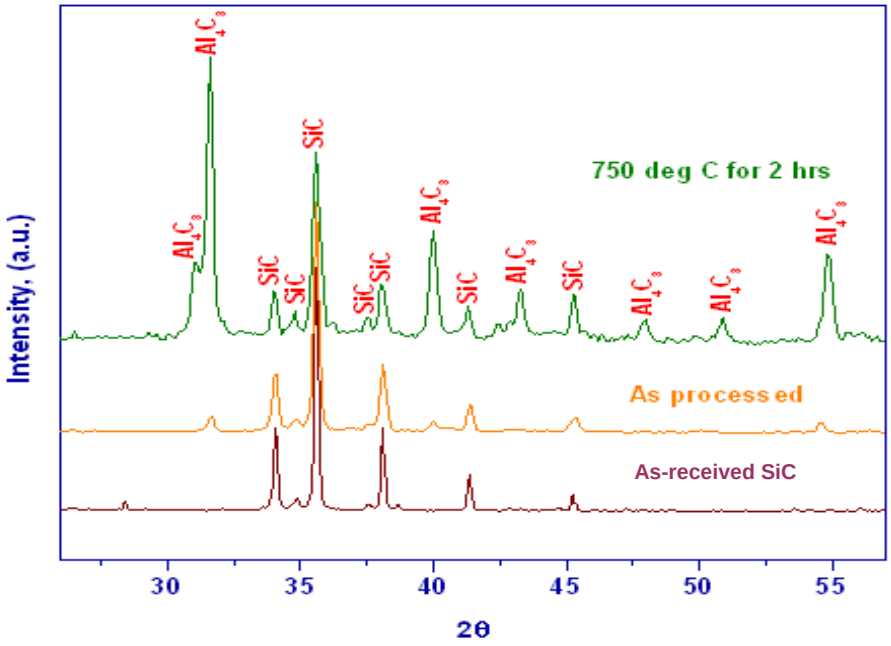

Figure 4.51: XRD showing the formation of Al_4C_3 and Si at various processing condition

To have more information on the distribution and disintegration of Al_4C_3 particle, the X-ray mapping and line scan across the particle were also carried out and given in Figures 4.54 and 4.55, respectively. These studies confirm that the concentrations of Al and C were distributed uniformly throughout the casting master alloy. The X-ray mapping of aluminium and carbon atoms in the scanning area is matches with the proportion of Al_4C_3 particles. The line scanning image shown in Figure 4.55 represents the line in particles boundary containing the down slope of curve showing the absence of Mg. The line of marked particles in Al and C slopes is upward, representing the aluminium-containing carbide particles.

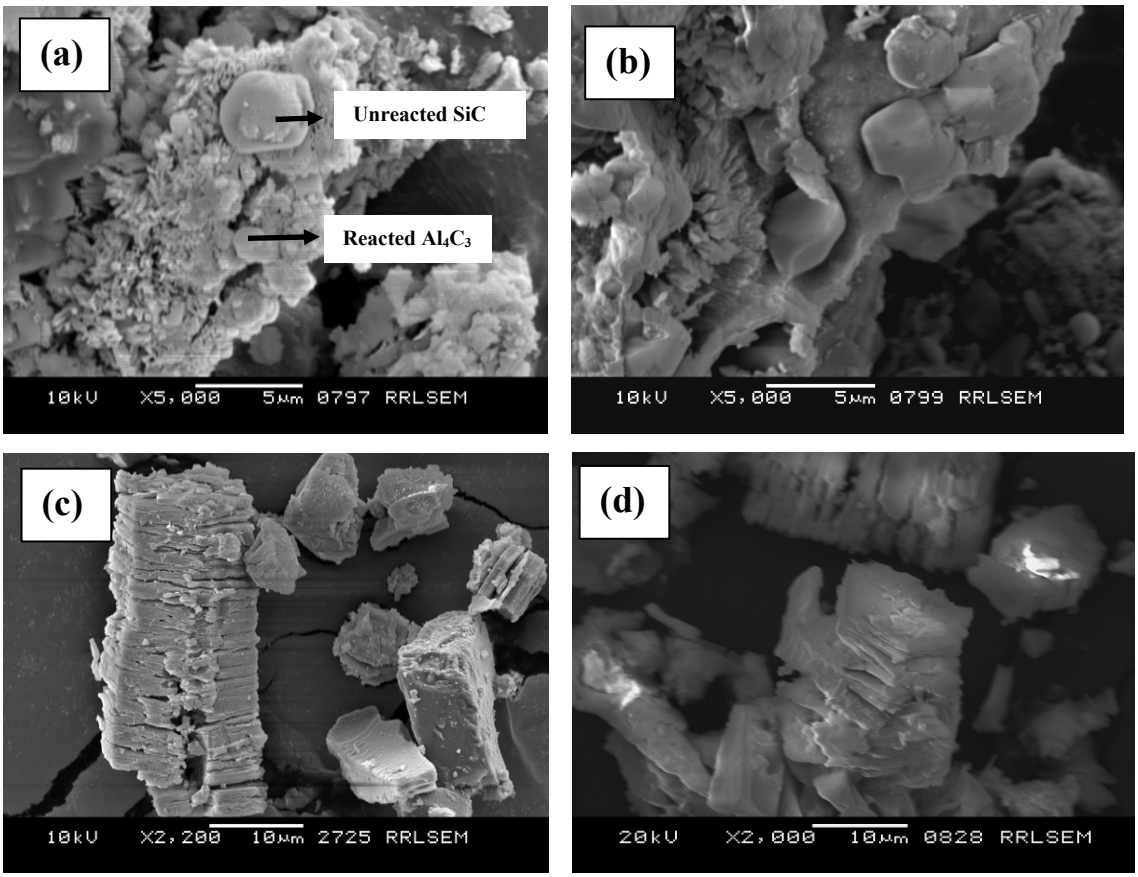

Figure 4.52: Reclaimed particles for (a) Sample conditions B (b) C (c) D and (d) E

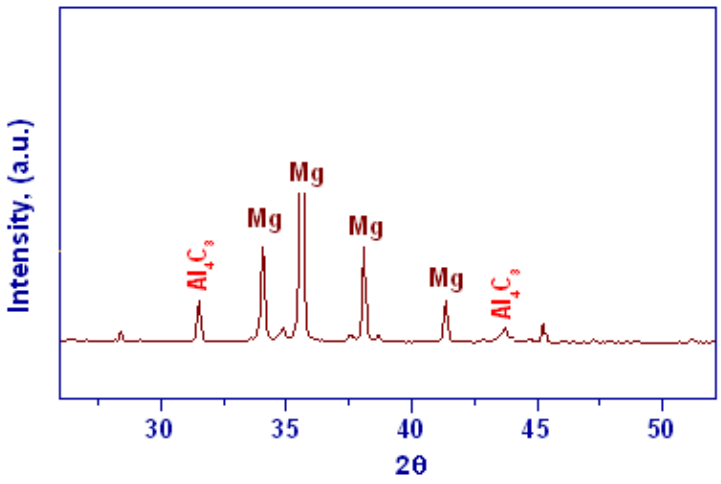

Figure 4.53: XRD pattern for Mg-1wt%Al_4C_3 master alloy

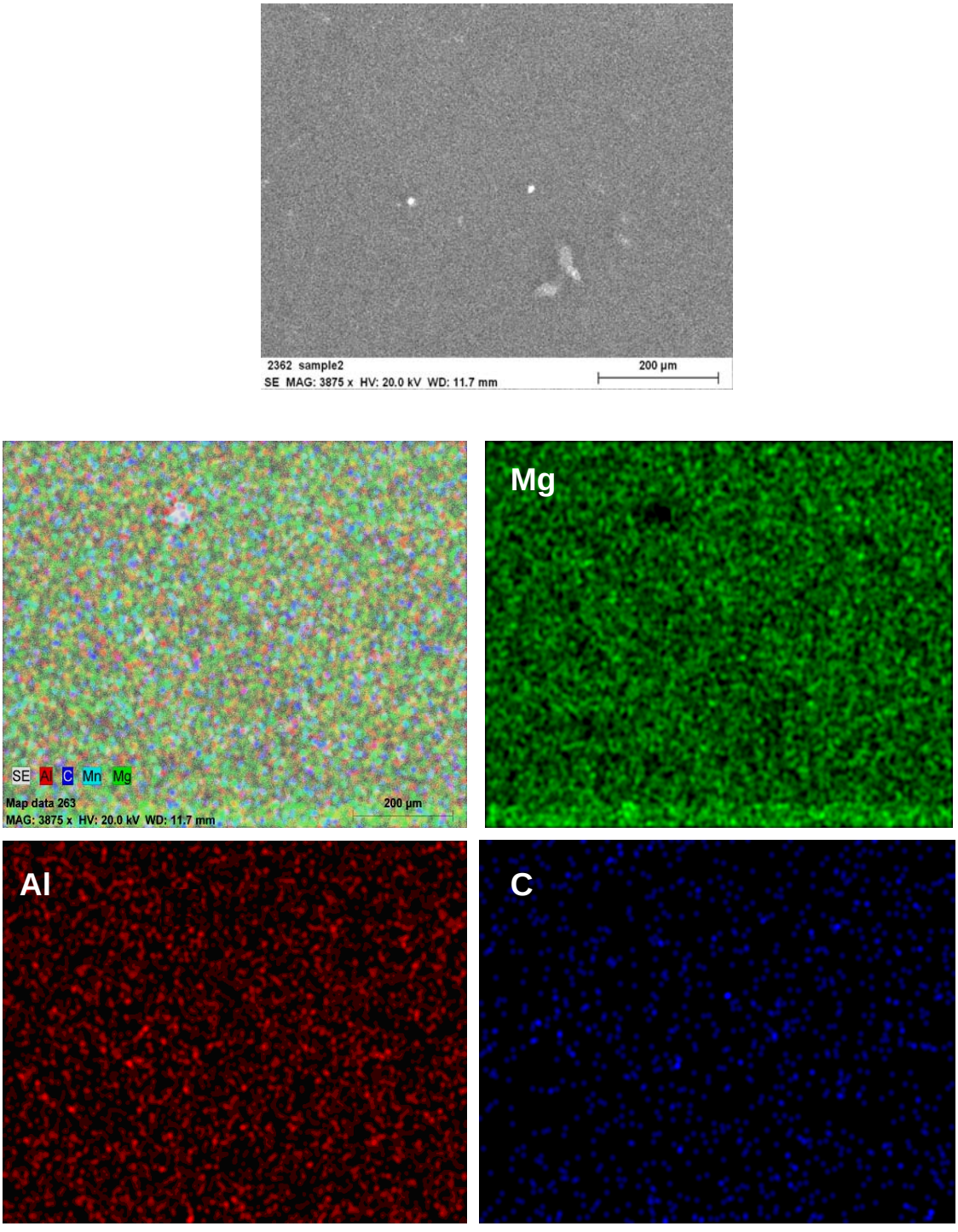

Figure 4.54: X- ray mapping taken on the Mg-1wt%Al_4C_3 master alloy

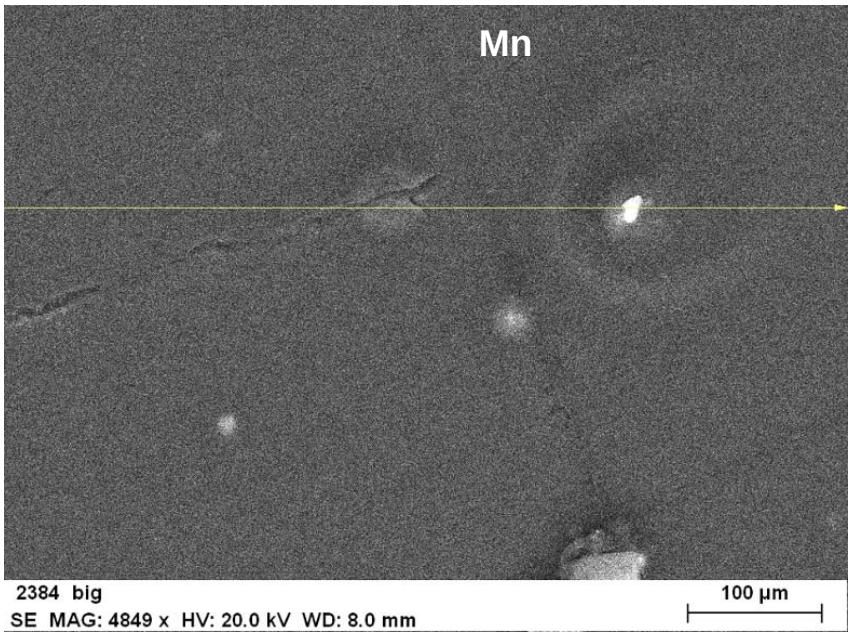

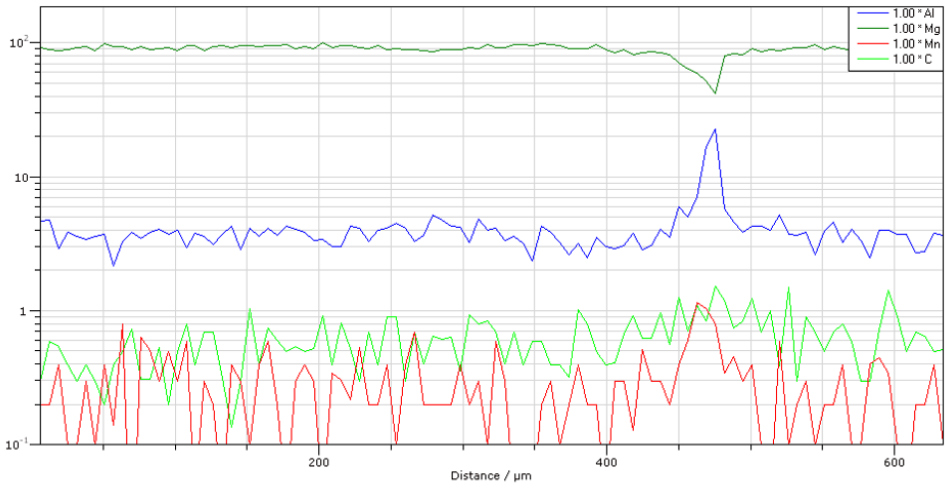

Figure 4.55: Line scanning taken across the coarse nucleant particles

From these results, it is more logical to conclude that the mapping shows, during solidification of master alloy, that the carbide particles are in structural stability and that no more chemical degradation takes place possibly because of the formation of other elemental nature. The uneven size and shape of fine particles also offer support without degrading the particles. However, more rigorous TEM studies are needed to confirm whether any particles disintegrate into other possible oxide-containing Al_4C_3 mechanism, which is included in the future course of work.

4.12 GRAIN REFINEMENT MECHANISM

The introduction of (Al_4C_3) heterogeneous nucleant by grain refiner alloy provides a large amount of substrate for nucleation of α-Mg during solidification, resulting in grain refinement. The requirements for the heterogeneous nucleant to act as an effective nucleating site are considered as follows [141]:

(1) The atomic arrangements of the nucleant particles are similar to those of any atomic planes of the matrices.
(2) It should have a melting point higher than the matrices
(3) A sufficient number of nucleating particles should be uniformly distributed
(4) It should be able to initiate the freeze at very small undercooling.

The crystallographic matching and lattice parameters between the Mg matrix and the Al_4C_3 nucleating particles are listed in Table 4.15. Al_4C_3 has a rhombohedral structure that is indexed in a hexagonal unit cell. Its lattice parameters are a=3.338Aº, c=24.996 Aº and λ=120º. Each unit cell contains 12 aluminium atoms and 9 carbon atoms. The mechanism of grain refinement by Al_4C_3 addition in magnesium alloy is related to the lattice disregistry between Mg and Al_4C_3 [238]. Both magnesium and Al_4C_3 have the same crystal structure and the lattice parameters ($a_{Mg} = 3.208A^0, a_{Al_4C_3} = 3.38A^0$) lead to low planar disregistry between the matrix and the nucleant. The grain refinement may also relate to the latent heat of crystallization.

The addition of Al_4C_3 to molten Mg decreases the latent heat leading to small undercooling and resulting in grain refinement.

Table 4.15: Crystallographic matching of Mg matrix and the Al_4C_3 nucleant

Potent Catalyst	Lattice Parameters			Space Group	Density ($g/cm^{3)}$	Crystal System	Pearson Symbol	Thermochemical Property	Planar Disregistry
	a [$\overset{0}{A}$]	c [$\overset{0}{A}$]	γ [^{0}]						
Mg	3.208	5.200	120	$P6_3$	1.738	H	hP2		
Al_4C_3	3.338	24.996	120	R-3m	2.972	H (Trimolecular)	hR7	Decomposition at about 2475K	4.05

The hypothesis for grain refinement of Al_4C_3 compound with magnesium is considering a high melting point, which can exist at normal melting temperature, and so it can be a nucleant for Mg grains. Among the hypotheses proposing to explain the mechanism of carbon inoculation refining method to Mg–Al based alloys, the Al_4C_3 nuclei hypothesis has been the most commonly accepted theory. Besides, the size of heterogeneous nuclei is a vital factor deciding nucleation potency. It is predicted that 5-8μm or less is the optimum mean particle size in the literature for high performance heterogeneous nuclei using a model based on the free growth control of grain initiation. In this article, it is believed that Al_4C_3 particles with a size 5-8μm or less are proposed to be the nucleation sites during solidification of Mg.

The potency of Al_4C_3 as a substrate for primary Mg can be further shown by crystallographic calculations. Theoretically, the interfacial free energy at the nucleating interface is believed to be a key factor controlling heterogeneous nucleation efficiency. However, a simple description of such energy is not possible as the total interfacial energy of the system is very complicated and composed of many contributory factors, such as the topographic nature of the substrate, the electrostatic potential between the

substrate and the nucleated crystal, the formation of layers at the interface, and the particle size and its distribution, respectively. Alternatively, Turnbull and Vonnegut [239] suggested that when the chemical parameters of the substrate and the nucleated crystal are similar, the only energy barrier to heterogeneous nucleation is that due to the structural aspects of the crystal/substrate interface, and this energy is at its minimum when this interface is coherent. The linear lattice disregistry, d = Da/a, was further defined to examine whether the crystal/substrate interface is coherent, where a is the lattice parameter of the crystal and Da is the difference in lattice parameters between the crystal and the substrate in a low index plane.

However, after systematic studies of heterogeneous nucleation behaviour of undercooled liquid iron on various carbides and nitrides, Bramfitt [240] suggested that the Turnbull and Vonnegut equation imposes a strict limitation on the selection of a crystallographic relationship, as only planes of similar atomic arrangement are considered. Therefore, Bramfit further modified the linear disregistry by introducing the following planar disregistry to include crystallographic combinations of two phases with planes of differing atomic arrangements:

$$\delta_{(hkl)_n}^{(hkl)_s} = \sum_{i=1}^{3} \frac{/\, d_{[uvw]_s^i} \cos\theta - d_{[uvw]_n^i}}{d_{[uvw]_n^i}} \Big/ 3$$

where subscripts s and n represent the substrate and the nucleated crystal, respectively; (hkl) is a low index plane, [uvw] is one of three low index directions in (hkl), and h is the angle between two low index directions in (hkl). It is accepted that the mismatch of crystal structures is not a unique factor controlling the favourability of nucleation, because many other factors mentioned earlier are also important. Nevertheless, this is

the only factor available to be assessed quantitatively. It is believed that good registry in crystal structures is important. On the basis of X-ray diffraction, the Al_4C_3 powder has an elongated hexagonal cell consisting of three rhomobohedral unit cells with carbon atoms on its basal planes. In Figure 4.56, the basal plane of this hexagonal cell has been superimposed on the Mg (0001) plane. According to equation, the planar disregistry between Al_4C_3 and Mg in three low-index directions on their basal planes has been calculated and is about 4.05%, which falls in the ‘‘very effective’’ range for heterogeneous nucleation. Assuming that the electronic bonding contribution to the energy of the interface is favourable, the nucleating substrate is believed to be potent if the planar disregistry is less than 12%. Therefore, according to the planar disregistry, Al_4C_3 is believed to be a very potent nucleating substrate for primary Mg. These crystallographic calculations further support the experimental observations of efficient grain refinement of primary Mg with the addition of Al_4C_3 powder.

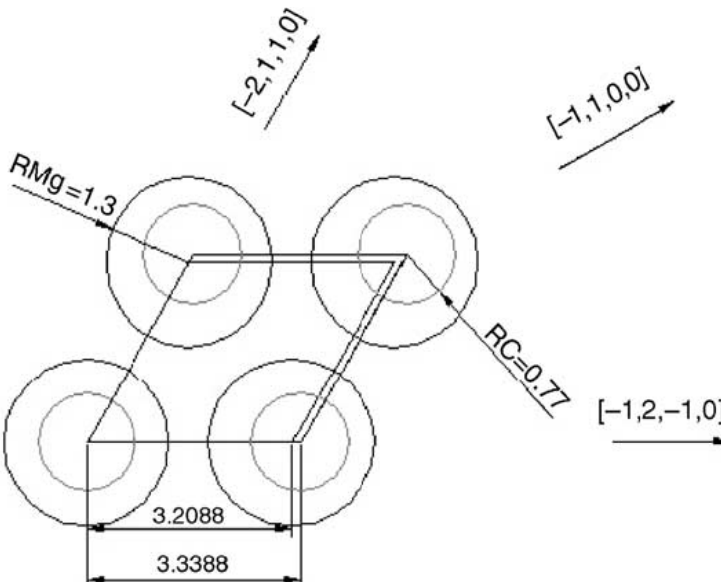

Figure 4.56: Crystallographic matching of basal plane of Mg and the Al_4C_3 particles

4.13 GRAIN REFINEMENT

The grain refinement of ZA84 alloy is based on solute segregation and the nucleant particles.. The extent of segregation is measured in terms of the growth restriction factor. The combined addition of 8%Zn and 4%Al, the GRF factor of ZA84 alloy is 59.76. If the GRF factor for a solute is large, this under-cooled zone will be large. The rate of growth is known to be inversely related to the constitutional super-cooling parameter. Most of the segregation effects have been reduced because of the formation of ternary precipitates instead of reducing the under-cooling effect of solid/liquid interface. The number of grains per unit volume N_v^G increase with the number of Al_4C_3 particles per unit volume N_v^P only up to a critical value and reach saturation beyond 0.1 wt % of Al_4C_3 particles.

The number of nucleating particles added to the magnesium alloy during the grain refinement studies depends on the addition level of the master alloy and the size of the particles. An attempt has been made theoretically to determine the quantities of Al_4C_3, particles introduced into the molten Mg by Mg-1% Al_4C_3 master alloys and the % potent nucleating sites. An attempt was also made to correlate the theoretical calculation with those obtained experimentally. The quantities of particles supplied by the master alloy at different addition levels and the % potent nucleating sites are discussed below:

The number of nucleating particles supplied by the master alloy during grain refinement can be calculated using the formula:

$$N = \left(\frac{W_{Particle}}{\rho_{Particle}}\right) / V_{Particle}$$

N = Number of particles

$W_{particle}$ = Wt% of particles in the alloy

$\rho_{particle}$ = Density of a particle

$V_{particle}$ = Volume of a particle

For 0.05 wt% particle addition:

Weight percent of particles = 0.05 wt%

Density of particle = 297200 gram/m^3

Volume of particle $= \frac{4}{3}\pi r^3$ (Radius of Particle ≈ 6 micrometer)

$= 9.0432 \times 10^{-16}$ m^3

$$N = \left(\frac{W_{Particle}(0.05)}{\rho_{Particle}(297200)}\right) / V_{Particle}(9.0432 \times 10^{-16})$$

$= 1.859 \times 10^8$ Particles

For 0.1 wt% addition:

N = 3.720×10^8 Particles

For 0.2 wt% addition:

N = 7.441×10^8 Particles

Equation to find the % potent nucleating sites (%PNS):

$$\%PNS = \frac{6v}{\pi D^3 N} x100$$

V - Volume of the melt
D - Grain size obtained experimentally

N - No. of particle

The volume of melt is 1250 grams, which is maintained constant throughout the experiments.

D- Grain size obtained experimentally (Refer Table 4.16)

Calculation for volume of ZA84+0.05Al_4C_3

Density = mass / volume

For ZA84+0.05 wt%Al_4C_3 (7.68 Zn, 3.71 Al)

Density = %of Mg (density) + %of Zn (density) + %of Al (density) + %of Al_4C_3 (density)

= 0.8856 * 1.74 + 0.078 * 7.04 + 0.0371 * 2.74 + 5E-3 * 2.972

= 2.183272

Volume of ZA84 + 0.1 Al_4C_3

= 2.187208

Volume of ZA84 + 0.2 Al_4C_3

= 2.20843

% PNS for ZA84+0.05 wt%Al_4C_3 alloy	=	49.063%
% PNS for ZA84 + 0.1 Al_4C_3 alloy	=	**88.3243%**
% PNS for ZA84 + 0.2 Al_4C_3 alloy	=	94.63318%

It can be clearly inferred from the theoretical calculations that the 3.720 x 10^8 Al_4C_3 particles for 0.1 wt% are the optimum percentage to obtain a fine grain size. Further, by increasing the percentage of Al_4C_3, the grain size reduction is not much improved. It is clearly stated that the optimum percentage for achieving the fine grain

size is 0.1wt% Al_4C_3. Table 4.16 gives summary details of grain size measurement of ZA84+xAl_4C_3 alloy. It is clearly observed from the microstructure (see Figure 4.57) that the addition of 0.05wt% of Al_4C_3 to ZA84 alloy effectively affects the grain size compared with the base alloy. The grain size of base alloy 67μm has been reduced to 27μm. The Al_4C_3 particles are sufficient in number; these particles nucleate α-magnesium in the super-cooled zone. This process repeats itself leading to a very fine grain size. Although the wt% is beyond 0.1, the number of grains per unit volume N_v^G remains constant, i.e the level beyond this content will not act as a potent nucleant.

4.14 TENSILE PROPERTIES OF ZA84+XAl_4C_3 ALLOY

Tensile samples were prepared according to the ASTM E8 standard and tests were carried out at room temperature. Five samples were tested for each alloy and the average value was reported. Strain gauge was used to get the % elongation at room temperature testing. The tensile properties, such as the ultimate tensile strength (UTS), yield strength (YS) and ductility (% of elongation) of the as-cast ZA84 alloy and ZA84+xAl_4C_3 alloy are presented in Figure 4.58. The tensile properties reported in this base alloy are in fact marginal above the reported value of the earlier research article in the same alloy. Yang [49] recently reported that the location of the sample drawn makes the difference in the properties because of the change in the thickness and the cooling rate. Therefore, the samples drawn from all the castings are maintained in the same location to uniform grain size, volume percentage of precipitates, cooling rate and porosity. From the figure, it can be seen that the strength properties of the alloy at room temperature are UTS=160 MPa, YS=115MPa and Elongation 5%. Within the margin of experimental errors, simple two- sided Student's "t" test can be used to analyze the results.

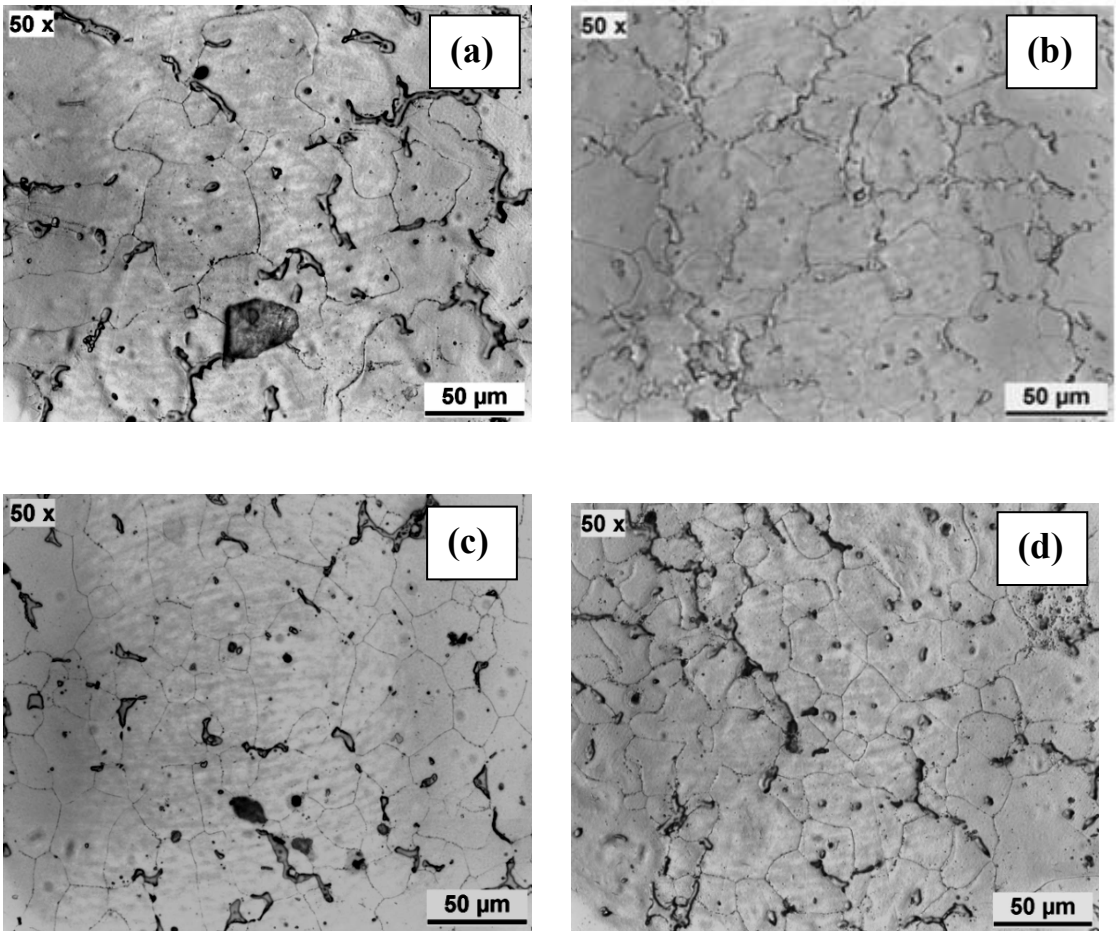

Figure 4.57: Microstructure of (a) ZA84 (b) ZA84+0.05 Al_4C_3 (c) ZA84+0.1 Al_4C_3 (d) ZA84+0.2 Al_4C_3 alloys

Table 4.16: Grain size report for ZA84+xAl_4C_3 alloy

Alloy	Grain size No	Average grain area (µm^2)	Average grain diameter (µm)	Mean intercept	Number of grains/mm
ZA84	6	1243	67	60.1	25
ZA84+0.05 Al_4C_3	8.2	430	27	18.4	55.05
ZA84+0.1 Al_4C_3	9	252	15	14.1	70.71
ZA84+0.2 Al_4C_3	9.1	190	14	12.3	72

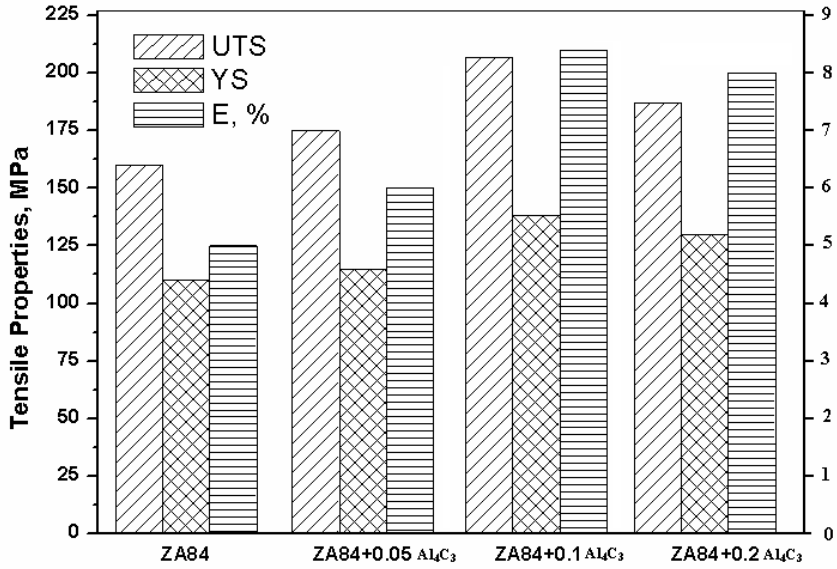

Figure 4.58: Tensile properties of ZA84 and ZA84+xAl_4C_3 alloy

The fractographs of the tensile fractured surfaces with and without grain refinement of ZA84 alloy alloys tested at ambient temperature are shown in Figure 4.59. Normally the failure of hcp structured magnesium alloys is brittle through cleavage and quasi-cleavage fracture. Figure 4.59a shows the fracture surface of ZA84 alloy, and it is seen that the surface consists of intergranular fracture with some secondary cracks (A). The presence of more cleavage planes (B in Figure 4.59 a) with constrained plastic zone (C) noticed in the structure confirms the limited ductility. In cleavage fracture, micro-cracks develop along certain crystal planes, which are mostly in the basal plane (0001) of magnesium [234]. When the load is applied, micro cracks are initiated and readily connected to grain boundaries, thereby making the failure of ZA84 alloy brittle and intergranular. The fractograph of grain refinement ZA84 alloy with 0.1Al_4C_3 shows the presence of more constrained plastic zones. The plastic zone is distributed uniformly throughout the microstructure because of very fine grain size, which increases the strength as well as ductility.

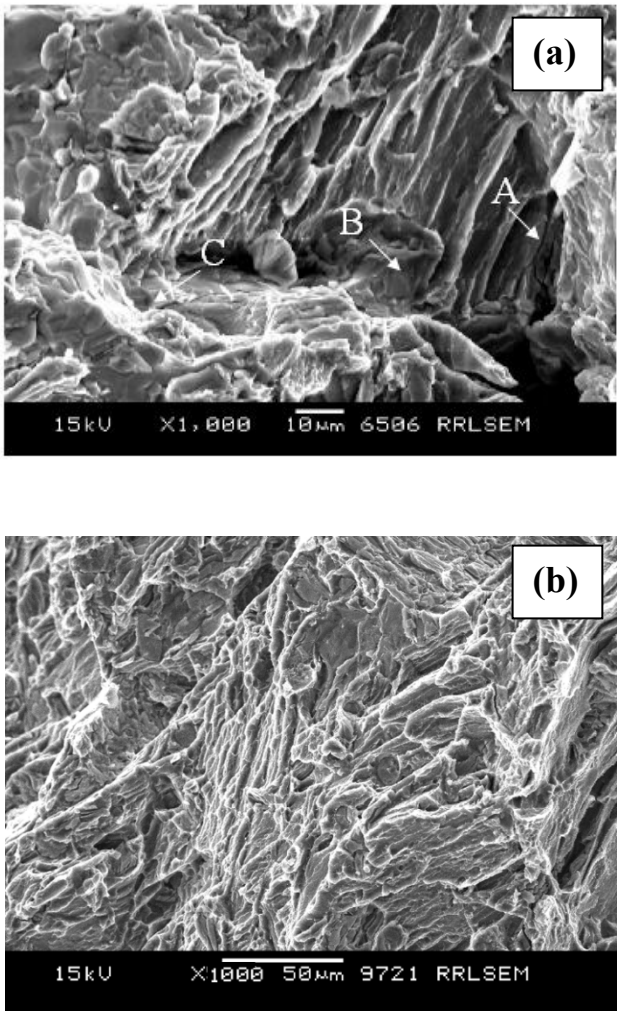

Figure 4.59: Fractograph of (a) without and (b) with grain refinement of ZA84

4.15 EFFECT OF COMBINED ADDITIONS OF Sb, Ca AND Al_4C_3

4.15.1 MICROSTRUCTURE

The optical microstructure of as-cast ZA84+0.2Sb+0.5Ca+0.1 Al_4C_3 alloy is shown in Figure 4.60. It can be observed from the figure that, between the dendrites, the precipitates are present at the grain boundaries. Further, the precipitates exist in three morphologies: continuous bone-like coarse phase called $Mg_{10}Al_6Zn_4Ca_2$; continuous without bone-like structure phase called $Mg_{32}(Al,Zn)_{49}$; and fine black Mg_3Sb_2 phases are present in the grain boundaries. The average grain size of the ZA84 alloy under the permanent mould-casting condition is 15 μm.

Further, the micro constituents of alloy are clearly seen in a scanning electron microstructure along with EDS pattern presented in Figure 4.61. It can be observed from the figure that the precipitates have different morphologies. The spectrum analysis on the phases corresponds to $Mg_{10}Al_6Zn_4Ca_2$ along with $Mg_{32}(Al,Zn)_{49}$.

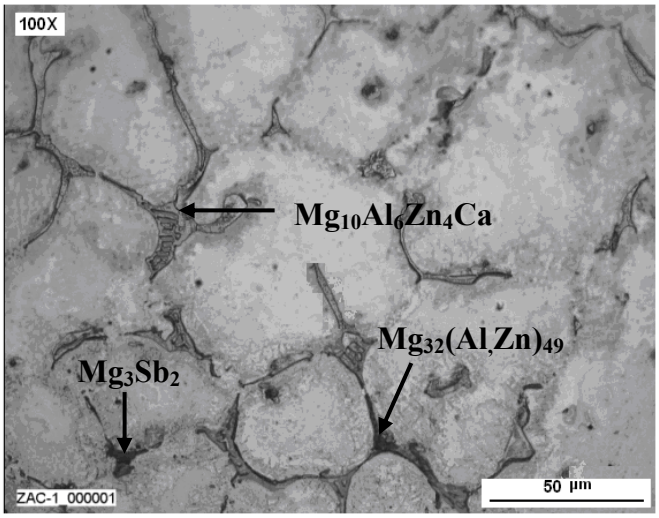

Figure 4.60: Optical microstructure of as-cast ZA84+0.2Sb+0.5Ca+0.1 Al_4C_3 alloy

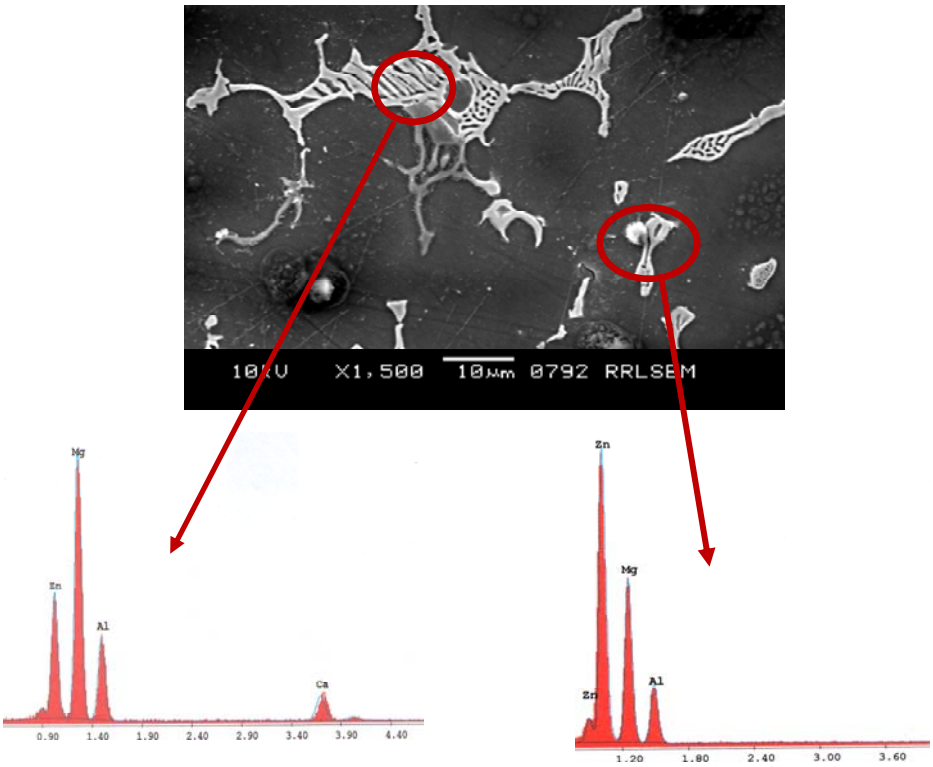

Figure 4.61: SEM microstructure and EDS of as-cast ZA84+0.2Sb+0.5Ca+0.1 Al_4C_3 alloy

4.15.2 TENSILE PROPERTIES

Tensile tests of the ZA84+0.2Sb+0.5Ca+0.1 Al_4C_3 alloy was performed at ambient and 150ºC temperatures are listed in Table 4.17. It can be seen that additions of Ca, Sb and Al_4C_3 to the base alloy have good effect on the tensile properties. The well grain refined, modified ternary $Mg_{32}(Al,Zn)_{49}$ to quaternary $Mg_{10}Al_6Zn_4Ca_2$ phases and thermally stable Mg_3Sb_2 phases in ZA84 alloy have effectively improvement in tensile properties compared to the base and individual alloying additions. It is well known that fine and modified precipitates improve the tensile properties whose intermetallic morphology also affects the tensile properties, i.e., the granular particle is in favor of the tensile properties and the fine-shaped particle does improve the tensile properties because of effective obstacle to grain boundary sliding. More dispersed precipitates for the larger quantity quaternary phase with thermally stable phase leads to the higher tensile properties.

Alloy	RT			150ºC		
	YS (MPa)	UTS (MPa)	% of Elongation	YS (MPa)	UTS (MPa)	% of Elongation
ZA84+0.2Sb+0.5Ca+0.01Al_4C_3	152	203	5	139	182	7

Table 4.17: Tensile Properties of ZA84+0.2Sb+0.5Ca+0.01Al_4C_3 alloy

4.15.3 CREEP

The creep curve of ZA84 with and without alloying additions is shown in Figure 4.62. The creep tests were conducted at 150ºC, with an initial stress of 50 MPa. It is expected that the grain size reduction due to the addition of Al_4C_3 may reduce the creep properties. However, it can be observed from the figure that the creep properties of ZA84+0.2Sb+0.5Ca alloy with and without Al_4C_3 is same. This may be due to the fact

that the creep behavior of this alloy is determined by the hard and stable precipitates. This nullifies the ill effect of the smaller grains in Al_4C_3 added alloy.

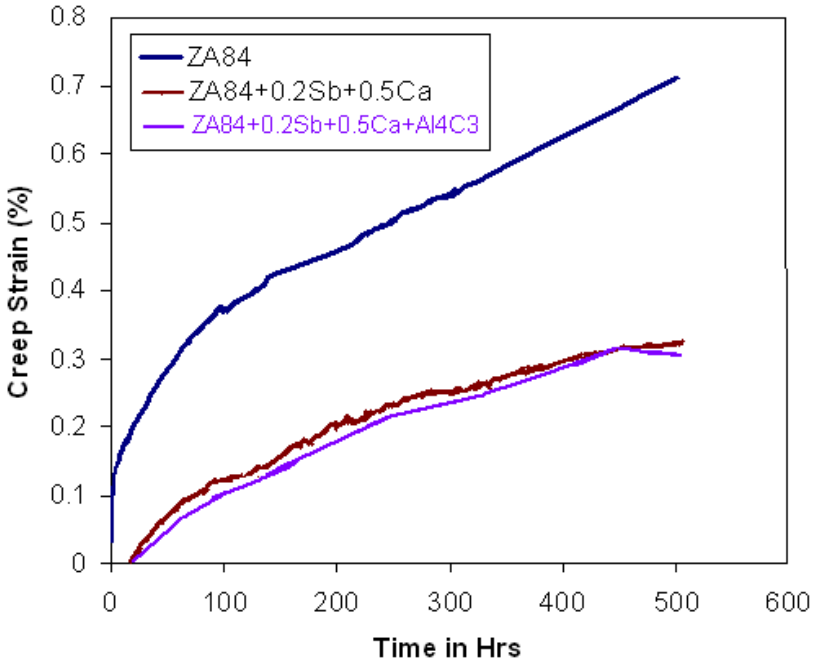

Figure 4.62: Creep curve of ZA84 with and without alloying additions

In this research work, the individual and combined additions of Sb, Ca and Al_4C_3 on the microstructure, tensile and creep properties of gravity-cast ZA84 have been investigated. Microstructure and XRD studies were carried to identify the precipitates and grain refinement. Tensile properties were evaluated both at room and high (150ºC) temperatures. Creep testing was carried out at 150ºC at an initial stress of 50MPa for 500 hrs. This chapter summarizes all the major observations and the conclusions drawn from this study as well as significant contributions of this thesis to the existing knowledge. The avenues for future work are also identified.

[1] The microstructure of ZA84 alloy consists of α-Mg matrix, continuous longer τ-$Mg_{32}(Al,Zn)_{49}$ phase and isolated ϕ-$Mg_5Al_2Zn_2$ ternary phases at the grain boundaries.

[2] The $Mg_{32}(Al,Zn)_{49}$ phase has cubic crystal structure and ϕ-$Mg_5Zn_2Al_2$ phase having primitive orthorhombic structure.

[3] Addition of Sb to ZA84 alloy refines the ternary $Mg_{32}(Al,Zn)_{49}$ precipitates, compared to that of the base alloy structure in which ternary precipitates are more continuous and longer. However, no change in the volume fraction of $Mg_{32}(Al,Zn)_{49}$ is observed with Sb addition.

[4] Added Sb combines with Mg to form a plate/needle-shaped Mg_3Sb_2 intermetallics at the grain boundary along with $Mg_{32}(Al,Zn)_{49}$ phase. Marginal grain refinement is noticed with 1%Sb addition.

[5] Ca addition leads to the formation of a new γ-$Mg_{10}Al_6Zn_4Ca$ quaternary precipitate having a bone-like structure with $Mg_{32}(Al,Zn)_{49}$ phase, however no Al_2Ca phases are observed in the microstructure.

[6] The solidification sequence of ZA84 alloy is as follows: primary α-Mg start nucleating at 593.44ºC which is monotectic reaction L (liquid)→ L_1 (liquid) + α-Mg (solid). Then grow into the melt till the second phase transformation takes place. The second phase transformation reaction in the temperature range of 346.62 and 354.22ºC. It is a mixed quasi-peritectic reaction occurs in which the following transformation takes place α-Mg + L_1→ α-Mg + τ + L_2→ α-Mg + τ + ϕ phases.

[7] When Sb is added, the following phase transformation takes place during solidification, α-Mg + L_1+ Mg_3Sb_2 → α-Mg + τ + L_2+ Mg_3Sb_2 → α-Mg + τ + ϕ + Mg_3Sb_2 phases.

[8] With Ca addition, the solidification changes from α-Mg start nucleating and grow into the melt up to 406.66ºC, where a new second transformation occurs corresponding to the reaction L_1 + α-Mg→ α-Mg+ γ + L_2. Further phase transformation occurs in the temperature 349.92ºC, corresponding to the reaction, L_1 + α-Mg + γ → α-Mg + γ + τ.

[9] For all Sb additions, improved room and elevated temperature strength properties are obtained as compared with the ZA84 base alloy with slight reduction in ductility. However, the maximum strength properties are obtained with 0.2 wt% Sb addition. Further Sb addition causes reduction in strength, which is due to the increase in the volume of coarse needle Mg_3Sb_2 precipitates.

[10] When Ca is added, marginal improvement in the room and elevated temperatures strength properties are obtained with reduced ductility.

[11] The alloying additions greatly improve the creep properties of ZA84 alloy at 150^{o}C, whereas calcium additions are more effective in improving the creep properties than Sb-added alloys.

[12] The microstructure of combined addition of Sb and Ca consists of α-Mg, quaternary $Mg_{10}Al_6Zn_4Ca$, Mg_3Sb_2 and $Mg_{32}(Al,Zn)_{49}$ phases.

[13] Marginal improvement in the tensile and creep properties is noticed for individual addition of Sb and Ca with reduced ductility. Whereas, combined additions significantly increases the tensile and creep properties because of the refined intermetallics.

[14] Aluminium carbide (Al_4C_3) particles can be successfully synthesized and fine 5-8μm particles can be reclaimed from Al-5wt%SiC composites by stir casting route.

[15] Mg-1% Al_4C_3 master alloy can be successfully prepared by flux melting method.

[16] The optimum amount of this addition is found to be 0.1%. A refined grain size of 15 micron is obtained with 0.1% Al_4C_3.

[17] For all Al_4C_3 additions, improved room temperature strength properties are obtained compared to ZA84 base alloy with enhanced ductility.

[18] Combined addition of Sb, Ca and Al_4C_3 show better room temperature tensile properties with improved ductility. However, not much improvement is obtained in the creep properties.

5.1 SIGNIFICANT CONTRIBUTIONS OF THIS INVESTIGATION TO THE KNOWLEDGE

1. A detailed microstructural analysis on ZA84 alloy with and without alloying additions has facilitated in understanding the behaviour of various intermetallics during solidification.

2. A new Mg-1wt% Al_4C_3 magnesium-based master alloy is synthesized for Mg-Al based alloys. In this work, it is found that master alloys effectively refined the grain size of an alloy, which improves the tensile properties.

3. It is well established that the alloying additions to magnesium alloys are detrimental to the ductility of the alloy. In this study, it is found that additions of grain refiner like Al_4C_3 along with Sb and Ca improves the mechanical properties without reduction in ductility.

5.2 AVENUES FOR FUTURE WORK

1. The idea adopted by various researchers either reduces the volume fraction or complete suppression in the formation of $Mg_{17}Al_{12}$ in the Mg-Al based alloys to improve the elevated performance. Based on this concept, the process of developing new cheaper magnesium alloys for high temperature applications. By adding more zinc with less aluminium content in Mg-Al alloys lead to without formation of $Mg_{17}Al_{12}$ phase. ZA84 alloy with minor modification of microstructure is leads to improved properties because of introduce thermally stable intermetallics. In this investigation, it is observed that the Sb and Ca addition is also capable of improving both the tensile and creep properties of ZA84 alloy. Therefore, it is worth studying the effect of Sb and Ca addition to Mg-Zn-Al based Mg alloys to explore the possibility of developing cost-

effective high creep resistance magnesium alloys in the different emerging applications.

2. Post- and pre-creep testing microstructure investigations need to be carried out to understand the strengthening mechanism of Sb and Ca addition in ZA84 alloy.

3. A detailed TEM investigation is required to understand the crystallographic matching between nucleant and magnesium matrix.

4. A common universal magnesium-based master alloy is developed for Mg-Al based alloys to be required for a thorough study of different aluminium-containing magnesium alloys to standardize the optimistic usage in foundry industries.

[1] B. L. Mordike and T. Ebret, Materials Science and Engineering: A, 302 (2001) p.37.

[2] http://www.vda.de/en/arbeitsgebiete/leichtbau/index.html

[3] A. Srinivasan, Ph. D Thesis, *"Influence of Si, Sb and Sr Additions on the Microstructure, Mechanical Properties and Corrosion Behavior of AZ91 Magnesium Alloy*", July 2008. Submitted to Cochin University of Science and Technology.

[4] E. F. Emley: Principle of Magnesium Technology, Pergamon press, First edition, (1966) p.124.

[5] E. Aghion and B. Bronfin, Proceedings of the First Workshop on Magnesium Platform Science and Technology, Nagaoka International City, Japan, July 27–29 (2000) p.19.

[6] X. H. Du and E L Zhang, Materials Letters, 61 (2007) p.2333.

[7] Wilson, K. Clause, M. Earlam and J. Hillis: "*Magnesium and Magnesium alloys*", A Diges of useful Technical Data from Kirk-Othmer Encyclopedia of Chemical Technology, The International Magnesium Association, McLean, PA, USA (1995) p.1.

[8] M. Henstock, "*The Recycling of Non-Ferrous Metals, International Council on Metals and Environment*", Ottawa, Ontario, Canada (1966) p.213.

[9] U.S. Geological Survey, "*Magnesium-2004*", Minerals Yearbook (2004) p.46.1.

[10] Katie Jereza, Ross Brindle, Steve Robison, John N. Hryn, David J. Weiss and Bruce M. Cox: "*Proc. Magnesium Technology 2006",* A. A. Luo, N. R. Neelameggham and R. S. Beals, eds., USA, March (2006) p.89.

[11] Statecasts Incorporated, "*AFS Metal casting Forecast and Trends 2005*", American Foundry Society, Schaumburg, IL (2004).

[12] ASM metal hand book, vol.2, 10th edition (1990) p.457.

[13] G.V. Raynor: "*The Physical Metallurgy of Magnesium and its Alloys*", Pergamon press, New York (1959) p.254.

[14] Du Wenwen, Sun Yangshan, Min Xuegang, Xue Feng, Zhu Min and Wu Dengyun, Materials Science and Engineering: A, 356 (2003) p.1.

[15] A. Srinivasan, U.T.S. Pillai and B.C. Pai, Metallurgical and Materials Transactions: A**,** 36 (2005) p.2235.

[16] Huang Deming, Chen Yungui, Tang Yongbai, Liu Hongmei and Niu Gao, Materials Letters, 61 (2007) p.1015.

[17] L. Y. Wei and G. L. Dunlop, Journal of Alloys and Compounds, 232 (1996) p.264.

[18] Hajo Dieringa, Norbert Hort and Karl Ulrich Kainer, Materials Science and Engineering: A, 510-511 (2009) p.382.

[19] Per Bakke and Hakon Westengen: Advance Engineering Materials, 5 (2003) p. 879.

[20] W.E. Marcer: II Technical Paper Series SAE Int. Congr. and Exp., SAE, Detroit, MI (1990) paper no. 900788.

[21] D.J. Sakkinen: Technical Paper Series SAE Int. Congr. and Exp., SAE, Detroit, MI (1994) p.71.

[22] H. Gjestland, G. Nussbaum, G. Regazzoni, O. Lohne and Bauger, Materials Science and Engineering: A, 134 (1991) p.1197.

[23] M.S. Dargusch, G.L. Dunlop and K.Pettersen: *Proc. Magnesium Alloys and their Application,* B.L. Mordike and K.V. Kainer, eds. Wolfsburg, German (1998) p. 277.

[24] A. Luo and M.O. Pekguleryuz: Journal of Material Science, 29 (1994) p.5259.

[25] M. Regev, E. Aghoin, A. Rosen and M. Bamberger, Metallurgical and Materials Transactions: A, 32 (2001) p.1335.

[26] F. Khomamizadeh, B. Nami, S. Khoshkhooei, Metallurgical and Materials Transactions A, Volume, 36A (2005) p.3489.

[27] A. Srinivasan, J. Swaminathan, U.T.S. Pillai, Krishna Guguloth and B.C. Pai Materials Science and Engineering: A, 485 (2008) p.86.

[28] Zhan Zhang, Alain Couture and Alan Luo, Scripta Materialia, 39 (1998) p.45.

[29] G.S. Foerster, "*Proceedings of the IMA 33rd Annual Meeting*", Montreal, Quebec, Canada, 23–25 (1976) p. 35.

[30] J.F. King, "*Magnesium alloys and their applications*", Wolfsburg, Germany April 28–30 (1998) p.37.

[31] Yingxin Wang, Shaokang Guan, Xiaoqin Zeng and Wenjiang Ding, Materials Science and Engineering: A, 416 (2006) p.109.

[32] A. Luo, T. Shinoda, "*Workshop on Magnesium Platform Science and Technology 2000*", Proceedings of the First Nagaoka International Nagaoka City, Japan, July 27–29 (2000) p.151.

[33] A. Luo and T. Shinoda, SAE Technical Paper Series, No. 980086 (1999) p.1.

[34] Z. Zhang, R. Tremblay and A. Couture, Can. Metall. Q., 39 (4) (2000) p. 503.

[35] Z. Zhang and R. Tremblay, D. Dube, Materials Science Technology, 18 (2002) p.433.

[36] S. Kamado, N. Ikeya and R. Suhardi Rudi, "*International Workshop on Magnesium Platform Science and Technology*", Proceedings of the First Nagaoka 2000, Nagaoka City, Japan, July 27–29 (2000) p.205.

[37] A. Ifeanyi, Yasuhiro Gokan, Atsuya Suzuki, Shigeharu Kamado, Yo Kojima, Suguru Takeda and Taketoshi Ishida, Materials Science and Engineering A, 380 (2004) p.93.

[38] Yang Ming-Bo, Pan Fu-Sheng, Cheng Ren-Ju and Shen Jia, Transactions of Nonferrous Metal Society China, 18 (2008) p.566.

[39] Y.P. Ren, G.W. Qin, W.L. Pei, Y. Guo, H.D. Zhao, H.X. Li, M. Jian and S.M. Hao, Journal of alloys and compounds (2009) JALCOM-19596.

[40] M. Vogel, O. Kraft and E. Arzt, Scripta Materialia, 48 (2003) p.985.

[41] Z. Zhang, R. Tremblay and D. Dube, Materials Science Technology, 18 (2002) p.433.

[42] Z. Zhang, A. Couture and A. Luo, Scripta Materialia 39 (1) (1998) p.45.

[43] Mingbo Yang, Liang Bai, Fusheng Pan and Hongjun Hu, Journal of University of Science and Technology, Beijing, 15 (2008) p.747.

[44] Ma Qian and A.Das, Scripta Materialia, 54 (2006) p.881.

[45] L.Lu, A.K. Dahle and D.H. St John, Scripta Materialia, 53 (2005) p.517.

[46] M. A. Easton and D.H. St John, Acta Materialia, 49 (2001) p.1867.

[47] Y.C. Lee, A.K. Dahle and D.H. St John, Metallurgical and Materials Transactions: A, 31 (2000) p.2895.

[48] Qudong Wang, Wenzhou Chen, Wenjiang Ding, Yanping Zhu and M. Mabuchi, Metallurgical and Materials Transactions: A, 32 (2001) p.787.

[49] Yuan Guangyin, Sun Yangshan and Ding Weiming, Materials Science and Engineering: A, 308 (2001) p.38.

[50] Ashis Mallick, Srikanth Vedantam and Li Lu, Materials Science and Engineering: A, 515 (2009) p.14.

[51] Martin Kunst, Andreas Fischersworring-Bunk, Gilles L'Esperance, Philippe Plamondon and Uwe Glatzel, Materials Science and Engineering: A, 510-511 (2009) p.387.

[52] Yizhen Lu, Qudong Wang, Xiaoqin Zeng., Wenjiang Ding, Chunquan Zhai and Yanping Zhu, Materials Science and Engineering: A, 278 (2000) p.66.

[53] Yuan Guangyin, Sun Yangshan and Zhang Weiming, Journal of Material Science Letter, 18 (1999) p.2055.

[54] C.J. Bettles, M.A. Gibson and G. Venkatesan, Scripta Materialia, 51 (2004) p.193.

[55] Sarennah J. P. Longworth: M. S. Thesis, Cambridge University, August (2001).

[56] http://www.azom.com/Details.asp? ArticleID=2417#, Applications of Magnesium.

[57] http://www.americanchemistry.com/s_plastics/hands_on_plastics/intro_to_p lastics/students.html#history.

[58] http://www.thenewsteel.com

[59] G.L. Maker and J. Kruger, International Materials Review, 38 (1993) p.138.

[60] P.D. Caton, *"Proceedings magnesium alloys and their applications"*, May (1992) B.L. Mordike and F. Hehmann eds., Germany (1992) p.367.

[61] http://www.matweb.com

[62] S.S. Sreeja Kumari, R.M. Pillai, T.P.D. Rajan and B.C. Pai, Materials Science and Engineering: A, 460-461 (2007) p.561.

[63] http://www.matweb.com/search/Datasheet.aspx? MatGUID=263886.

[64] H. Al-Kazzaz, M. Medraj, X. Cao and M. Jahazi, Materials Chemistry and Physics, 109 (2008) p.61.

[65] M. Bobby Kannan, W. Dietzel, C. Blawert, A. Atrens and P. Lyon, Materials Science and Engineering: A, 480 (2008) p.529.

[66] Z. Yang, J.P. Li, J.X. Zhang, G.W. Lorimer and J. Robson, Acta Metallurgica Sinica (English Letters), 21 (2008) p.313.

[67] T. Ryspaev, Z. Trojanová, O. Padalka and V. Wesling, Materials Letters, 62 (2008) p 4041.

[68] B.L. Mordike and T. Ebert, Materials Science and Engineering: A 302 (2001) p.37.

[69] Guanling Song and David St John, Journal of Light Metals, 2 (2002) p.1.

[70] http://www.sipreports.com/isbn--978-1-60030-664-8.html

[71] A.K. Dahle, D.H. St John and G.L. Dunlop, Materials Forum, 24 (2000) p. 167.

[72] S.A. Canney, Journal of Physics: Condensation Matter, 11 (1999) p.7507.

[73] http://www.flickr.com/photos/rous/2533296126.

[74] B.L Mordike and K.U. Kainer, "*Book-Magnesium Alloys and their Applications"*, Published by Wiley-VCH (1999) ISBN 352729936X.

[75] Lazar Leonovich Rokhlin, "*Book-Magnesium alloys containing rare earth metals: structure and properties*", Published by CRC Press (2003) ISBN 0415284147.

[76] E.F. Emley: Principle of Magnesium Technology, Pergamon press, First edition (1966) p.71.

[77] E. Hillis James and E. Mercer William, SAE Transactions, 109 (2000) p.619.

[78] Zeng Xiaoqin, Wang Qudong, Lu Yizhen, Zhu Yanping, Ding Wenjiang and Zhao Yunhu, Journal of Materials Processing Technology, 112 (2001) p.17.

[79] Tenorio JAS, Espinosa DCR, "*Oxidation of Metals*", 53 (2000) p.361.

[80] N. Balasubramani, A. Srinivasan, U.T.S. Pillai, K. Raghukandan and B. C. Pai, Indian Foundry Journal, 50 (2004) p.30.

[81] ASM hand book, Volume-15, Casting, ASM International, 4th edition (1998) p.798.

[82] Stephen. C. Erickson: Foundry Management and Technology, 126 (1998) p.38.

[83] Zeng Xiaoqin, Wang Quandang and Zhao Yhnhu, Journal of Materials Processing Technology, 112 (2001) p.17.

[84] Zeng Yi-wen, Peng Li-ming, Mao Xie-min, Zeng Xiao-qin and Ding Wen-jiang: Materials Science Forum, 488-489 (2005) p.73.

[85] You Guoqiang, long Siyuan and Zha Jili: Materials Science Forum, 488-489 (2005) p.77.

[86] H. Friedrich and S. Schumann, Journal of Materials Processing Technology , 117 (2001) p.276.

[87] M. O. Pekguleyuz, Materials Science Forum, 350-351(2000) p.131.

[88] A. Srinivasan, U.T.S. Pillai, J. Swaminathan and B.C. Pai: International Journal of Cast Metal Research, 19 (2006) p.265.

[89] A. Luo and M. O. Pekguleryuz, Journal of Materials Science, 29 (1994) p.5259.

[90] M. Avedesian and Hugh Baker, ASM International. Handbook Committee, Book- Magnesium and magnesium alloys, Published by ASM International, (1999) ISBN 0871706571.

[91] G Pettersen, H Westengen, R Høier and O Lohne, Materials Science and Engineering: A, 207 (1996) p.115.

[92] L. Lu , A.K. Dahle, D.H. StJohn, Scripta Materialia 53 (2005) p.517.

[93] M.O. Pekguleryuz and A. Luo, "*Creep Resistant Magnesium Alloys for Diecasting*," ITM Inc., International Patent Application WO 96/25529 (1996).

[94] A. Luo and T. Shinoda, "*Magnesium alloy having superior elevated-properties*," Imra America Inc., US Patent US5855697 (1997).

[95] W.A. Wood, "Creep Processes*," Proc. Symp. Creep and Fracture of Metals at High Temperature*, National Physical Laboratory, Middlesex, UK (1955) p.59.

[96] R.E. Reed-Hill, "*Physical Metallurgy Principles"*, 2nd Ed., D. Van Norstand, N.Y (1973) p.827.

[97] M.F. Ashby and D.R.H. Jones, "*Mechanisms of Creep and Creep-Resistant Materials*," Engineering Materials, Pergamon Press, England (1980) p. 172.

[98] G.V. Raynor, "*The physical metallurgy of magnesium and its alloys"*, Pregamon Press, Oxford, UK (1959) p. 247.

[99] W. Blum, B. Watzinger and P. Weidinger, "*Proceedings of Conference on Magnesium Alloys and their Applications"*, B.L. Mordike and B.L. Mordike and K.U. Kainer, Eds., Verkstoff-Informationsgesellschaft, Wolsburg, Germany (1998) p.49.

[100] F.J. Edler, G. Lagrene and R. Siepe, "*Proceedings of Magnesium and their application",* Wiley-VCH Verlag Gmbh, (2000) p.554.

[101] A. Srinivasan, U.T.S. Pillai and B.C. Pai: International Journal of Microstructure and Materials Properties, 2 (2007) p.429.

[102] F. Czerwinski, A. Zielinska-Lipiec, P.J. Pinet and J. Overbeeke: Acta Materialia, 49 (2001) p.1225.

[103] Y. Wang, G. Liu and Z. Fan, Acta Materialia, 54 (2006) p.689.

[104] http://www.arcraftplasma.com/welding/weldingdata/metalstd.htm.

[105] Polmear, "*Proceedings of Magnesium Alloys and their Applications",* B.L. Mordike and F. Hehmann, ed., Garmisch-Partenkirchen, Germany, (1992) p.201.

[106] Smithells Light Metals hand book, E.A. Brandes, G. B. Brook, eds., Butterworth-Heinemann (ISBN 0 7506 3625 4) (1998) p.86.

[107] Z.P. Luo, D.Y. Song and S.Q. Zhang: Journal of Alloys and Compounds, 230 (1995) p.109.

[108] M. Suzuki, H. Sato, K. Maruyama and H. Oikawa: Material Science and Engineering: A, 252 (1998) p.248.

[109] K. Maruyama, M. Suzuki and H. Sato, Metallurgical and Materials Transactions: A, 33 (2002) p.875.

[110] P. Abachi, A. Masoudi and K. Purazrang: Material Science and Engineering,: A, 435-439 (2006) p.653.

[111] G. Foerster, "*Proceedings of 7th International Die casting Congress"*, paper 9372 (1972) SDCE.

[112] B.R. Powell, V. Rezhets, M. Balogh and R. Waldo, "*Proceedings Magnesium Technology 2001"*, J.N. Hryned., Warrendale, PA, TMS, (2001) p.175.

[113] H. J. Fuchs: UK Patent 847992, published (1960).

[114] M.O. Pekguleryuz and A. Luo, "*Patent Cooperative Treaty application*" WO 96/25529 (1996).

[115] B.R. Powell, V. Rezhets, A. Luo, J.J. Bommarito and B.L. Tiwari: US Patent 6,264,763, 24 July (2001).

[116] M.O. Pekguleryuz and E. Baril, "*Proceedings of Magnesium Technology 2001"*, J. N. Hryned., Warrendale, PA, TMS (2001) p.119.

[117] P. Labelle, M.O. Pekguleryuz, D. Argo, M. Dierks, T. Sparks and T. Waltmate: SAE Technical Paper 2001-01-0424 (2001).

[118] P. Labelle, M.O. Pekguleryuz, M. Lefebvre and R. Bouchard: SAE Technical Paper 2002-01-0079, (2002).

[119] Jinghuai Zhang, Peng Yu, Ke. Liu, Daqing Fang, Dingxiang Tang and Jian Meng, Materials and Design, 30 (2009) p.2372.

[120] E. Evangelista, E. Gariboldi, O. Lohne, S. Spigarelli, Materials Science and Engineering: A, 387-389 (2004) p.41.

[121] A. Srinivasan, J. Swaminathan, U.T.S. Pillai, Krishna Guguloth and B.C. Pai, Materials Science and Engineering: A, 485 (2008) p.86.

[122] http://www.factsage.cn/fact/documentation/SGTE/Mg-Zn.jpg.

[123] M.O. Pekguleryuz, M.M. Avedesiaan and Sainte-Foy: "*Proceedings of* Magnesium *Alloys and their Applications"*, B.L. Mordike, F. Hehmann eds., April (1992) Germany, p.213.

[124] A.K. Dahle, Young C. Lee, mark D. Nave, Paul L. Schaffer and David H. St John: Journal of Light Metals, 1 (2001) p.61.

[125] O. Lunder, T.Kr. Aune and K. Nisancioglu, Corrosion, 43 (1987) p.291.

[126] Z. Zhang, R. Tremblay and D. Dube, Materials Science and Engineering: A, 385 (2004) p.286.

[127] Honghui Zou, Xiaoqin Zeng, Chunquan Zhai and Wenjiang Ding, Materials Science and Engineering: A, 392 (2005) p.229.

[128] Zhang Jing, Li Zhong-Sheng, Guo Zheng-Xiao and Pan Fu-Sheng, Trans. Nonferrous met. Soc. China, 16 (2006) p.452.

[129] Chris Dagger, Global Watch Mission Report, MAG TECH 1, "Magnesium alloys and processing technologies for light weight transport applications" - A mission to Europe (2004).

[130] Q.D. Wang, W.Z. Chen, X.Q. Zeng, Y.Z. Lu, W.J. Ding, Y.P. Zhu and X.P. Xu, Journal of Material Science, 36 (2001) p.3035.

[131] Yuan Guangyin, Sun Yangshan and Ding Weiming, Scripta Materialia, 43 (2000) p.1009.

[132] Kinji Hirai, Hidetoshi Somekawa, Yorinobu Takigawa and Kenji Higashi, Materials Science and Engineering: A, 403 (2005) p.276.

[133] Jihua Chen, Zhenhua Chen, Hongge Yan, Fuquan Zhang and Kun Liao, Journal of Alloys and Compounds, 461 (2008) p.209.

[134] S.F. Liu, B. Li, X.H. Wang, W. Su and H. Han, Journal of Materials Processing Technology, 209 (2009) p.3999.

[135] N. Balasubramani, A. Srinivasan, U.T.S. Pillai, K. Raghukandan and B. C. Pai, Indian Foundry Journal, 50 (2004) p.19.

[136] J. Gronder and R. Schmid Fetzer, Journal of Alloys and Compounds, 320 (2001) p.296.

[137] Sunghak Lee, Seung Hyuk Lee and Dohyang Kim, Metallurgical and Material Transactions: A, 29 (1998) p.1221.

[138] Elliot Roy, "*Eutectic Solidification Processing*", Butterworths and Co. (Publishers) Ltd., London (1983) p.73.

[139] Guan Shao-kang, Zhang Chun-xiang, Wang Li-guo, Wu Li-hong, Chen and Tang, Transactions of Nonferrous Metal Society of China, 18 (2008) p.593.

[140] M.B. Yang, J. Shen and F.S. Pan, Materials Science and Technology, 25 (2009) p.393.

[141] B.S. Murty, S.A. Kori and M. Chakraborthy, International Materials Reviews, 47 (2002) p.1.

[142] A. Ohno, and Molege, "*Solidification technology in the foundry casthouse"*, The Metals Society (1983) p.171.

[143] M. Volmer and A. Weber, Krift. Phys. Chem., 119 (1925) p. 277.

[144] K.T. Kashyap and T. Chandrashekar, Bulletin of Materials Science, 24 (2001) p.345.

[145] W. Kurz and D.J. Fisher, Fundamentals of Solidification - Switzerland: Trans Tech. Publications (1984) p. 47.

[146] C. Fleming Merton, Solidification processing, McGraw-Hill Inc (1947) p. 135.

[147] Johnson, Handbook of grain refinement, McGraw-Hill Inc (1952)

[148] M. Qian and A. Das, Scripta Materialia, 54 (2006) p.881.

[149] M. Qian, Graham D, Zheng L, D.H. St John and M.T. Frost, Materials Science and Technology, 19 (2003) p.156.

[150] M. Qian, D.H. St John and M.T. Frost, Scripta Materialia, 46 (2002) p.649.

[151] M. Qian, D.H. St John and M.T. Frost, Material Science Forum, 419-422 (2003) p.593.

[152] E. F. Emley, "*Principles of Magnesium Technology",* Oxford: Pergamon Press (1966) p.126.

[153] H. Okamoto, J Phase Equilibria, 23(2) (2002) p.198.

[154] M. Qian, D.H. St John and M.T. Frost, *"Magnesium Alloys and Their Applications"*, Kainer K U, ed., Wiley-VCH, Wolfsburg (2003) p.706.

[155] A. Aghion, B. Bronfin and D. Eliezer, Material Science Forum, 419-422 (2003) p.407.

[156] E. F. Emley, "*Principles of Magnesium Technology"*, Oxford: Pergamon Press (1966) p.257.

[157] M. Qian, D.H. St John and M.T. Frost, "*Magnesium Technology 2003"*, Kaplan H I ed., TMS (2003) p.209.

[158] M. Qian, L. Zheng, D. Graham, M.T. Frost and D.H. St John, Journal of Light Metals, 1 (2001) p.157.

[159] D.H. St John, M. Qian, M.A. Easton, P. Cao and Z. Hildebrand, Metallurgical and Material Transactions: A, 36 (2005) p.1669.

[160] E. F. Emley, "*Principles of Magnesium Technology"*, Oxford: Pergamon Press (1966) p.200.

[161] M. X. Zhang, P. M. Kelly, M. Qian and J. A. Taylor, Acta Materialia, 53 (2005) p.3261.

[162] Y. Guangyin, S. Yangshan and W. Zhen, Journal of Nonferrous Metals: Chinese, 9(12) (1999) p.779.

[163] Y. Guangyin, S. Yangshan and Z. Weimin, Foundry, 5 (1998) p.5.

[164] S. Yangshan, W. Kunzhong, and Y. Guangyin Journal of Nonferrous Metals: Chinese, 9(3) (1999) p.55.

[165] Z. Shichang, W. Bokang and L. Hantong, Journal of Nonferrous Metals: Chinese, 11(11) (2001) p.99.

[166] Q. Jin, J. P. Eom, S.G. Lim, W.W. Park and B. S. You, Scripta Materialia, 49 (2003) p.1129.

[167] Z. Shijun, L. Wenxian and Y. Kun, Foundry, 7 (2001) p.373.

[168] Y. Tamura , N. Kono and T. Motegi, Journal of Japan Institute of Light Metals, 48(8) (1998) p.395.

[169] M.A. Easton, A. Schiffl, J.Y. Yao and H. Kaufmann, Scripta Materialia, 55 (2006) p.379.

[170] D. Qiu, M-X. Zhang, J.A Taylor, Fu H-M and P. M. Kelly, Acta Materialia, 55 (2007) p.1863.

[171] C.J. Bettles, C.T. Forwood, D.H. St John,, M.T. Frost , D.S. Jones, M. Qian , G.L .Song, J.R. Griffiths and J.F. Nie, *"Magnesium Technology 2003",* San Diego, CA 2003, H.I. Kaplan ed., TMS, Warrendale, PA, (2003) p.223.

[172] P. Cao, M. Qian and D.H. St John, Scripta Materialia, 54 (2006) p.1853.

[173] Y. Liu, X. Liu and B. Xiufang, Materials Letters, 58 (2004) p.1282.

[174] R. Gunther, Hartig Ch and R. Bormann, Acta Mateialia*,* 54 (2006) p.5591.

[175] T. Motegi, E. Yano, Y. Tamura and E. Sato, Material Science Forum, 350-351 (2000) p.191

[176] E. Yang, Y. Tamura, T. Motegi and E. Sato, Journal of Japan Institute of Light Metals, 51 (2001) p.599.

[177] E. Yano , Y. Tamura , T. Motegi , and E. Sato, Material Transactions, 44 (2003) p.107.

[178] E. Yano , Y. Tamura , T. Motegi and E. Sato, Journal of Japan Institute of Light Metals, 51 (2001) p.594.

[179] Y. Tamura, Haitani Y, Yano T, T. Motegi, N. Kono and E. Sato , Material Transactions, 43 (2002) p.2784.

[180] M. Bamberger, Material Science Technology, 17 (2001) p.15.

[181] S. Boily and M. Blouin, Canadian Patent 2, 327, (2002) p. 950.

[182] N. Nishino, H. Kawahara, Y. Shimizu, and H. Iwahori, "*Magnesium Alloys and their Applications",* Kainer K U, ed., Wiley-VCH, New York, NY (2000) p.59.

[183] Farbenindustrie I G, British Patent GB359, 425 (1931).

[184] K. Achenbach, H. A. Nipper and E. Piwowarsky, *Die Giesserei,* 26 (1939) p.597.

[185] Cao P, M. Qian , and D.H. St John,: Neelameggham NR, Kaplan HI, Powell BR,ed., *Magnesium Technology 2005,* Warrendale, PA, TMS, (2005) p.297.

[186] Y. Tamura, J. Yagi, T. Haitani, N. Kono and H. Tamehiro, Material Transactions, 44 (2003) p.552.

[187] J.Y. Byun, S. Kwon, H.P. Ha and J.K. Yoon: K.U. Kainer, ed., "*Magnesium Alloys and their Applications",* Weinheim: Wiley-VCH, (2003) p.713.

[188] P. Cao, D.H. St John and M. Qian, Material Science Forum, 188-189 (2005) p.139.

[189] E. F. Emley, "*Principles of Magnesium Technology",* Oxford: Pergamon Press (1966) p.206.

[190] T. Motegi , Materials Science and Engineering: A, 413-414 (2005) p.408.

[191] P. Cao, M. Qian and D.H. St John, Scripta Materialia, 53 (2005) p.841.

[192] Q. Jin, J. P. Eom, Lim S.G, W.W. Park and B. S. You, Scripta Materialia, 52 (2005) p.421.

[193] I. G. Farbenindustrie, Belgian Patent (1942) p.757.

[194] P. Cao, M. Qian and D.H. St John, Scripta Materialia, 51 (2004) p.125.

[195] M. Qian, D.H. St John and M.T. Frost, Scripta Materialia, 50 (2004) p.1115.

[196] Y.C. Lee, A.K. Dahle and D.H. St John, Metallurgical and Material Transactions: A, 31 (2000) p.2895.

[197] Y. M. Kim, C. D. Yim and B. S. You, Scripta Materialia*,* 57 (2007) p.691.

[198] M. Qian and P. Cao, Scripta Materialia*,* 52 (2005) p.415.

[199] Lu L, A. K. Dahle and D.H. St John, Scripta Materialia, 53 (2005) p.517.

[200] I. Maxwell and A. Hellawell, Acta Met., 23 (1975) p.229.

[201] M. A. Easton, and D.H. St John,, Acta Materialia, 49 (2001) p.1867.

[202] Jae-Chul Lee, Ji-Young Byun, Sung-Bae Park and Ho-In Lee, Acta Materialia, 46 (1998) p.1771.

[203] J. C. Lee and K. N.Subramanian, Journal of Material Science, 27 (1992) p.5453.

[204] J. C. Lee, Jung-Ill and Lee Ho-In, Scripta. Materialia, 35 (1996) p.72.

[205] J. C. Lee, Jung-Ill and Lee Ho-In, Journal of Material Science Letters, 15 (1996) p.1539.

[206] D. J. Lloyd, H. Legace, A. Mcleod and P.L. Morris, Material Science and Engineering: A, 107 (1989) p.73.

[207] G. Gonzalez, L.Salvo, M.. Suery and G.L Eserance,., Scripta Materialia, 33 (1995) p.1969.

[208] F. H. Samuel, H. Liu and A. M.Samuel, Metallurgical and Material Transactions: A, 24 (1993) p.1631.

[209] Provencher, United States Patent, 4,992,241 - February 12 (1991).

[210] CRC Handbook of Chem. and Physics, 74th edn. CRC Press (1992) p.4.

[211] The Merck Index 10th edn. Merck & Co. Inc., (1983) p. 50.

[212] J. Narciso, C.Garcia-Cordovilla and E. Louis, Material Science and Engineering: B, 15 (1992) p.148.

[213] J. C. Lee, J. Y. Byun, C. S. Oh, H. K. Seok and H.-I. Lee, Acta Materialia., 45 (1997) p.5303

[214] G. H. Kim, H. S. Kim and D.W. Kum, Microstructure of Research Technology, 33 (1996) p.510.

[215] L. Salvo, M. Suery, J. G. Legour, G. I. Esperance, Material Science and Engineering: A, 135 (1991) p.129.

[216] C. F. Horng, S. J. Lin and K. S. Liu, Material Science and Engineering: A, 150 (1992) p. 289.

[217] T. Iseki, T. Kameda, and T. Maruyama, Journal of Material Science, 19 (1984) p.1692.

[218] Jian Ye and Yogeshwar Sahai, Materials Transaction of JIM, 37 (1996) p.170.

[219] Jian Ye and Yogeshwar Sahai, Materials Transaction of JIM, 37 (1996) p.175.

[220] Jian Ye and Yogeshwar Sahai, Materials Transaction of JIM, 37 (1996) p.1479.

[221] Raja R. Roy and Yogeshwar Sahai, Materials Transaction of JIM, 38 (1997) p.547.

[222] Raja R. Roy and Yogeshwar Sahai, Materials Transaction of JIM, 38 (1997) p.568.

[223] P. Moldovan, G. Popescu, M. Zsigmond, UPB Scientific Bulletin, Series B: Chemistry and Materials Science, 61 (1999) p.271.

[224] P. Moldovan, G. Popescu, I. Apostolescu, C. Popescu, Light Metals: Proceedings of Sessions, TMS Annual Meeting, Warrendale-Pennsylvania (2002) p.1019.

[225] L.A. Girifalco, R.J. Good, Journal of Physics Chemistry 61 (1957) p.904.

[226] Wiesław Apostoluk and Jan Drzymała, Journal of Colloid and Interface Science 262 (2003) p.483.

[227] Raja R Roy and T.A. Utigard, Metallurgical and Material Transactions: B, 29 (1998) p.821.

[228] K. R. Ravi, B.C. Pai, R.M. Pillai and M. Chakrabothy, International Symposium of Research Students in Materials science and Engineering, Dec 20-22, 2004, IIT-Chennai, India.

[229] JCPDS, International Centre Diffraction Data (1966) 35-0821.

[230] JCPDS, International Centre Diffraction Data (1966) 19–0029.

[231] E. F. Emley: Principle of Magnesium Technology, Pergamon press, First edition, (1966) p.945.

[232] JCPDS, International Centre Diffraction Data (1966) 71-0404

[233] E. F. Emley: Principle of Magnesium Technology, Pergamon press, First edition, (1966) p.929.

[234] ASM Metal Hand Book, vol. 9, Fractography, Atlas of Fractographs, eighth ed., Metal Park, Ohio (2000) p.64.

[235] JCPDS, International Centre Diffraction Data (1966) 75-1541.

[236] M.Bamberger Material Science and Technology, 17 (2001) p.15.

[237] W. M. Zhong,., G. L'esperance, and M. Suery, Metallurgical and Material Transactions: A, 26 (1995) p.2637.

[238] H. Ribes, M. Suery, , G. L'esperance, and T. G. Legoux,., Metallurgical and Material Transactions: A, 21 (1990) p.2489.

[239] D. Turnbull, B. Vonnegut Ind Eng Chem, 44 (1952) p.1292.

[240] B. L. Bramfitt, Materials Transaction, 1 (1970) p.1987.

LIST OF PUBLICATIONS

INTERNATIONAL JOURNALS

1. Effect of antimony addition on the microstructure and mechanical properties of ZA84 magnesium alloy, **N. Balasubramani**, A. Srinivasan, U.T.S. Pillai, K. Raghukandan, and B.C. Pai, Journal of Alloys and Compounds, 455 (2008) pp. 168-173.

2. Optimization of heat treatment parameters in ZA84 magnesium alloy, **N**. **Balasubramani**, U.T.S. Pillai and B.C. Pai, Journal of Alloys and Compounds, 457 (2008) pp.118-123.

3. Effect of Pb and Sb additions on the precipitation kinetics of AZ91 magnesium alloy, **N. Balasubramani**, A. Srinivasan, U.T.S. Pillai, and B.C. Pai, Materials Science and Engineering A, 457 (2007) pp.275-281.

4. Effect of Zn concentration on the microstructure and phase formation of Mg-5Gd alloy, **N. Balasubramani**, U.T.S. Pillai and B.C. Pai, Journal of Alloys and Compounds, 460 (2008) pp.L6-L10.

5. Observation of the suppression of $Mg_{17}Al_{12}$ formation in a La-containing AZ91 alloy, **N. Balasubramani**, M. Suresh, A. Srinivasan, U.T.S. Pillai, B.C. Pai, Journal of Mater Science 42 (2007) pp.8374–8376.

6. Microstructure and creep properties of calcium added ZA84 magnesium alloy, **N. Balasubramani**, A. Srinivasan, U.T.S. Pillai, J. Swaminathan, and B.C. Pai (to be communicated to Materials Science and Engineering: A)

7. Grain refinement of Mg-Al alloys using Mg-1wt%Al_4C_3 master alloy, **N**. **Balasubramani**, U.T.S. Pillai and B.C. Pai (Manuscript under preparation)

AWARDS

Best paper presentation award, National Seminar on "Advance materials for hostile environment - Present scenario and future perspectives" conducted by Indian Institute of Metals, Trivandrum chapter Feb 2006.

Best poster presentation award, International conference for advanced materials and composites (ICAMC-2007) "Grain refinement of ZA84 alloy by Al_4C_3" organized by National Institute for Interdisciplinary Science and Technology (CSIR), Trivandrum, Oct 2007.

NATIONAL/ INTERNATIONAL CONFERENCE PRESENTATION

1. Studies on the age hardening behavior of ZA84 magnesium alloy, **N.Balasubramani**, U.T.S. Pillai, K. Sukumaran and B.C. Pai, Proceeding of the International conference ICMPM 2005 held at BAIT-Tamilnadu, 200-206.

2. Solidification and creep behavior of Ca added ZA84 magnesium alloy, **N. Balasubramani**, U.T.S. Pillai, and B.C. Pai, Proceedings in International Symposium on Research Students (ISRS) -2006, held at IIT, Chennai, 2006, 481-486.

3. Grain refinement of Mg-3Al magnesium alloy by Al -5wt% SiC composites, **N. Balasubramani,** K.R. Ravi, U.T.S. Pillai and B.C. Pai, Proceedings in International Conference on Recent Advance Material Processing (RAMP 2006), PSG Tech. Coimbatore. 2006.

4. Study on the precipitation kinetics of age hardened Mg-6Gd-xZn alloys, **N. Balasubramani**, U.T.S. Pillai, and B.C. Pai, Proceedings in International conference THERMEC 2005, July 2006.

5. Influence of SiC particles on the microstructure and mechanical properties of AZ91 magnesium alloy, L.P. Manikandan, **N. Balasubramani**, J.T. Winowlin Jappes, U.T.S. Pillai, and B.C. Pai, Proceedings in NCSAME 2006, May 4-5, 2006.

6. Effect of alloying addition on the precipitation kinetics of magnesium alloy, **N. Balasubramani,** K.R. Ravi, U.T.S. Pillai and B.C. Pai, Presented in International Conference on Advances in Materials and Materials Processing, Feb 3-5, 2006 held at IIT- Kharagpur

7. Modeling of yield strength in Al-Si-Mg alloys, Prem E. J. Babu, **N. Balasubramani,** U.T.S. Pillai, and B.C. Pai, Proceedings in International Symposium on Research Students (ISRS) -2006, held at IIT, Chennai from Dec 18-20, 2006 pp. 481-486.

8. Effects of calcium addition on ZA84 magnesium alloy, **N. Balasubramani**, A. Srinivasan, T. Soman, K. K.Ravi kumar, U.T.S. Pillai and B.C. Pai, presented at ATM, NMD November 2005 held at IIT Madras, Chennai.

9. Study on the solidification behavior and phase constituent of Ca added ZA84 magnesium alloy, **N. Balasubramani**, P. Prabhakar Rao, Peter Koshy, U.T.S. Pillai and B.C. Pai, National conference on Electron Microscopy Society of India, April 19-21, 2006 held at RRL-Trivandrum.

10. Novel grain refiner for ZA84 magnesium alloy using Al-SiC composite, **N. Balasubramani,** K.R. Ravi, S. G. K. Pillai, U.T.S. Pillai and B.C. Pai, NMD-ATM 2006, Nov 13-16 Jamshedpur.